A Glimpse of Polarisation with Sea Urchins and Gold Nanorods

Author:
Yun Peng Li

Supervisors:
Prof. Céline Bœhm
Prof. Ken-Tye Yong
Prof. Maria Bryne

April, 2026
A thesis submitted to fulfil the requirements of the degree:
Doctor of Philosophy (Science)

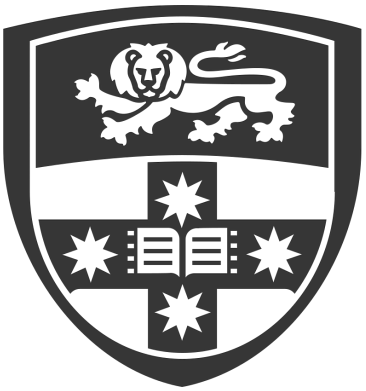

THE UNIVERSITY OF SYDNEY

The University of Sydney
School of Physics

Statement of Originality and Contribution

I, Ben Li, declare that the contents of this thesis are submitted in accordance with the requirements of the degree *Doctor of Philosophy (Science)* from the University of Sydney. I also declare that its contents are wholly my own work, unless otherwise referenced or acknowledged. This document has not been submitted for qualification at any other institution.

Signed: .....

Date: April, 2026

Statement of Generative AI

There has been no usage of any generative AI tools in this work.

Signed: .....

Date: April, 2026

Acknowledgements

To begin, I would like to acknowledge that this project was supported and funded with the Faculty of Science Research Stipend Scholarship as well as the University of Sydney - University of Glasgow Ignition Grant.

I cannot imagine any Ph.D. project being easy, but as a physicist, I certainly did not help myself delving into marine science and biomedical engineering as part of my research topic. I started this project being incredibly out of my depth and I would have sunk even further without the amazing help of my supervisors.

Firstly, I would like to show my eternal gratitude to Céline Bœhm, who has had a tremendous impact on my growth, not only as a scientist, but also as a person. From discussing crazy ideas on using sea urchins to detect dark matter to walking me through complex cross-section calculations to even our somewhat intermittent tennis session, she has capably (and quite courageously I might add) led me this wild journey, recruiting collaborators from all corners of the globe and in extremely diverse fields. I don't think this would have been possible in the slightest without her and for that I am truly grateful.

To Ken-Tye Yong, I would like to thank him for his positivity. Anytime I had a problem, he would return very quickly with several solutions and always with great enthusiasm. From letting me use his lab spaces, to helping out the procurement or synthesis of nanoparticles, and to even connecting me with knowledgable colleagues, without him, I would have been stuck at the first hurdle.

I would also like to thank Maria Bryne, whose idea helped start this whole thing. Without her, none of our sea urchin experiments would have been possible. She tirelessly toiled away, growing millions of larvae over several months (twice, I might add) just to allow me to shine some light at them.

To my collaborators: Joseph Yang, whose help and expertise on our experiments were vital; Livia Salvati Manni, who helped me not fumble at chemistry; Helena Reinardy, who made the SAMS collaboration possible; Greg Warr and Paul Fitzgerald for your help with SAXS; Paulina Selvakumaraswamy and Matthew Clements for help with the spawning of the sea urchin larvae; the SAXS/WAXS beamline team at the Australian Synchrotron, SAMS, Julien Reboud, and Filippo Menolascina for our Ignition grant collaboration; and everyone in the dark matter, biomedical, and marine science groups at Usyd, who made the passing weeks more bearable.

To all my friends thank you for being there and making life enjoyable. To Eddy, I am grateful

for all our late night gaming sessions, which kept me sane throughout the year. To Paul, I thank him for his improvisational comedy and the ability to spot all my mistakes. To my ESTA tennis team; Geogria, Mia, Ollie, and Phillipe, thank you for our (nearly) weekly hits and for putting up with my drop shots. To Melina, who has made the last few demanding months of writing a bit less stressful.

Finally, towards my family, whose support seemed endless, I am forever grateful.

Best Fishes,

Ben

Publications

As part of this thesis, 3 papers were published and 1 is in preparation. Of the 3 published 2 were as first author (chapters 2 and 4) and 1 was as second author (chapter 5). The manuscript in preparation is also as first author. The publications are listed below:

Published

- Response of the Larvae of the Sea Urchin *Centrostephanus rodgersii* Under Light and Polarisation Conditions[1] (Chapter 2)
- Towards a Novel Method of X-ray Polarimetry with Aligned Gold Nanorods [2] (Chapter 4)
- Time-Resolved In Situ Small-Angle X-ray Scattering to Determine the Kinetics of Formation of Liquid Crystalline Structure in the Core of Polymeric Nanoparticles during and after Turbulent Mixing [3] (Chapter 5)

In Preparation

- Exploring the Phototactic Response of Adult Sea Urchins to Light and Polarisation. (Chapter 3)

Contents

Chapter 1

A Journey Through Light

1.1 Introduction

Light is an essential part of the universe and for most living things, it is one of the main avenues we use to experience life. From the astonishing phenomena of sight to telecommunications to probing the entire Universe, our utilisation and manipulation of light and its interactions has not only helped us in our understanding not only biological evolution, but also the evolution of the universe and everything in between. It is therefore of vital importance that we have an understanding of the fundamentals of light and develop a model that can be used not only to explain the current behaviours of light but also use its properties to predict and examine other aspects of the natural laws of the Universe. We have a fairly robust understanding of light classically, where we can regard light as a wave with fundamental properties of wavelength, amplitude, frequency, and constant speed[1]. Light particles also behave as a single energy packet, termed photons, and our understanding of this has driven greater discovery into the interactions of light, in particular absorption and scattering. We also have extensive knowledge of the interactions of light and matter, merging special relativity and quantum mechanics with Quantum Electrodynamics (QED) [4], giving us the most complete model of light and its interactions. Not only that, but also we now realise that photons themselves are a mediator of the electromagnetic force.

There is one property of light that we will focus on in this work, namely polarisation. Polarisation is a fundamental property of light, both classically and quantum mechanically. Classical properties arise from the oscillation of all transverse waves, and quantum mechanically it comes from the spin and helicity of photons. Photons with different polarisation states are intrinsically different, not only in how they behave and interact but also in how they are created. A measurement of photon polarisation could reveal its origins, including the type of interactions which resolved in its inception. This project is an exploratory work into the development of new ways into polarisation detection. This could potentially pave the way for the development of novel polarisation detectors from visible light to γ-rays. Although polarisation detectors already exist in the visible wavelengths, improvements can be made on their sensitivity, size, cost, and complexity. We explore avenues into such ideas, using the biological process of polarisation detection that animals have been using for potentially millions of years. As primarily a physicist,

[1] Which shaped our understanding of special relativity

especially with roots in dark matter, I am motivated by the need for polarisation detection from astronomical sources. Improvement of current methods could arise from the aforementioned biological mechanisms of polarisation detection. Sensitivity to polarisation could potentially be found in sea urchins. Furthermore, I am particularly interested in the development of a high energy (X and γ ray) polarisation detector. Such a detector does not currently exist for γ rays and even hard X-rays. I explore a potential new route of detecting the polarisation of high energy photons. This would allow us to finally study the polarisation states of certain astronomical sources and potentially solve the dark matter riddle as potential dark matter interactions may produce polarised photons.

This thesis is split into 6 chapters. I will give an introduction into the interactions between light and matter in Chapter 1, with a special focus on the different types of scattering. I will also introduce the fundamental properties of light and its polarisation and how it can affect the interactions of light and matter. Next, I will delve into current methods of polarisation detection, in the visible spectrum but also with an extension into higher energy options. I will also explore the biological uses of polarisation in both air, land and sea based species with utilisations in navigation, communication, predator prey identification amongst other. I will then finish with a motivation on the development of a new type of high energy polarisation detector inspired by dark matter interactions. In Chapter 2, I will detail the work that was done on the investigation of the response to polarisation of visible light by the larvae of sea urchins. They were studied not only on their ability to detect light and polarisation, but also whether they had the ability to differentiate between different polarisation states i.e. horizontal vs. vertical or right handed vs. left handed. Chapter 3 extends this work into adult sea urchins. Sea urchins undergo a metamorphosis between the larval and adult stages of their lifecycle, giving them a completely different structure and potentially a new photo-detection mechanism. Primarily, we wanted to study whether potential polarisation sensitivity also existed for adult sea urchins. Three species were tested with the help of the Scottish Association for Marine Science (SAMS) under illumination of different light and polarisation regimes. These two projects involving adult sea urchins and larvae were done with the development of a novel technology of visible light polarisation detection in mind. This detector would be based on the mechanism that the sea urchins use to detect the polarisation of light, motivated by their potential ease of production and their massive decrease in size compared to current detectors. However, this detector being biological based, would not be sufficient for higher energy photons such as X-rays and γ-rays as biological tissue would suffer structural damage in the face of such high energies. We addressed this in Chapter 4, with a new development of using gold nanorods to detect the polarisation of X-rays. We tested for possible anisotropic scattering of polarised X-rays and aligned gold nanorods. We found that the distribution of the scattered X-rays depended on the orientation of the aligned nanorods compared to the polarisation direction of the X-rays. This phenomenon, in theory, would be able to be used to infer the polarisation state of incident X-rays and potential γ-rays, paving the way into a new type of high energy polarisation detector. In fact, such detectors are not only in rare supply, but are massive and costly. They also suffer from sensitivity issues and have a limited energy range in which they function. Additionally, there does not currently exist a functioning γ-ray detector above 10 MeV. Chapter 5 details some partial involving some contributions to the experimental work done at the Australian Synchrotron. This was used as experience training for my own synchrotron experiments. Finally I will finish with a quick conclusion in Chapter 6.

1.2 Electromagnetic Radiation

Historically it was known that light has both wave-like and particle-like properties and two competing theories emerged as a result.Newton's corpuscular theory of light argued that light is made up of many corpuscles or little particles. They travelled with finite velocity in straight lines and light was viewed at the time to be very ray-like. He was able to explain properties such as reflection and refraction in terms of particle interactions [5] with particles bouncing symmetrically off a surface for reflection and that these particles are being attracted to a denser medium being the cause of refraction. In fact, at that time, polarisation was supporting evidence for the particle nature of light [6]. Not long after, however, Huygens proposed a wavelike model of light [7]. Not only was he able to explain reflection and refraction in terms of waves, but he was also able to propose a mechanism of diffraction and interference with the Huygens–Fresnel principle [8]. Through it, they were able to explain light propagation in terms of wavefronts, and each point on a wavefront being itself a source of a new light wave. They were so successful in their modelling that a wave-like nature of light was the main supported model for the next two centuries. It wasn't until very recently, through the works of Planck, Einstein, Bohr, de Broglie amongst others, that championed quantum mechanics that we realise the wave-particle duality of not just light, but of matter itself.

The wavelike properties of light can be explained by electromagnetism, where light propagates through space as electromagnetic (EM) waves. EM waves are progressive transverse waves that propagate due to an oscillating electric field ($\vec{E}$) coupled to an oscillating magnetic field ($\vec{B}$). Unlike mechanical waves, EM waves do not require a medium to propagate. The luminiferous aether was briefly considered to be the medium of light, but this was debunked by the Michelson and Morley experiment in 1887[2][9]. Thus, light is the only form of energy that does not require a medium to transfer through space. The oscillating $\vec{E}$ and $\vec{B}$ fields will in turn induce oscillating $\vec{B}$ and $\vec{E}$ fields, as described from Maxwell's equations, which allows for their continued propagation. In fact, using his laws of electromagnetism, Maxwell was able to predict the existence of the whole spectrum of electromagnetic waves as well as their speed, which he also calculated to be fixed [10]. It is this propagation of the $\vec{E}$ and $\vec{B}$ fields which allows for light to travel without the requirement of a medium as $\vec{E}$ and $\vec{B}$ fields also not require a medium to exist. Maxwell's calculated speed of light is as follows:

$$\begin{aligned} c &= \frac{1}{\epsilon_0 \mu_0} \\ c &= 299,792,458 \text{ m/s} \end{aligned} \tag{1.1}$$

where the constants ϵ_0 is vacuum permittivity and μ_0 is the vacuum permeability. The $\vec{E}$ and $\vec{B}$ fields oscillate perpendicularly to each other, and both are perpendicular to the direction of propagation of the EM wave [11] (see Figure 1.1).

Electromagnetic waves exist as a continuous spectrum of wavelengths and frequencies, going from radio waves, microwaves, infra-red, visible light, ultraviolet, X-rays and finally to γ-rays (see Figure 1.2). As the speed of light is constant, $c = \lambda f$, the wavelength, λ, and the frequency, f, of light are directly inversely proportional to each other. Radio waves thus have low frequency and large wavelengths and on the other end of the spectrum, γ-rays have high frequency and

[2]The experiment obtained a null result, rather than a negative result

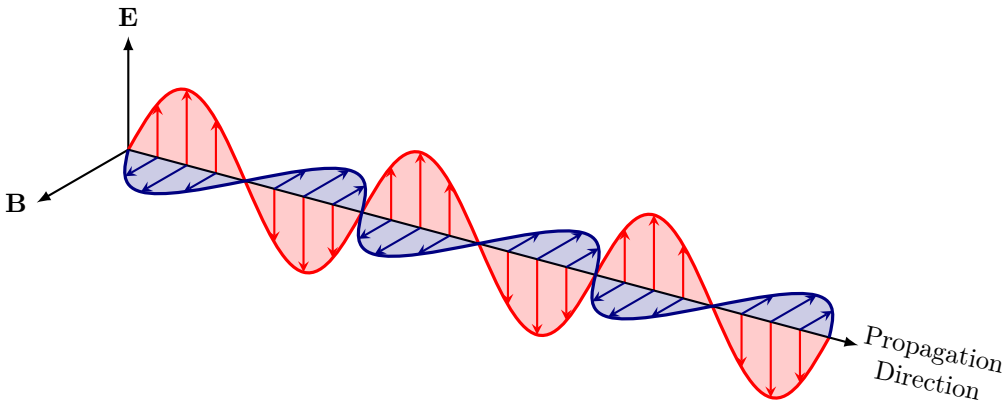

Figure 1.1: Propagation of an electromagnetic wave, oscillations of the electric and magnetic fields are perpendicular to each other and also perpendicular to the direction of propagation.

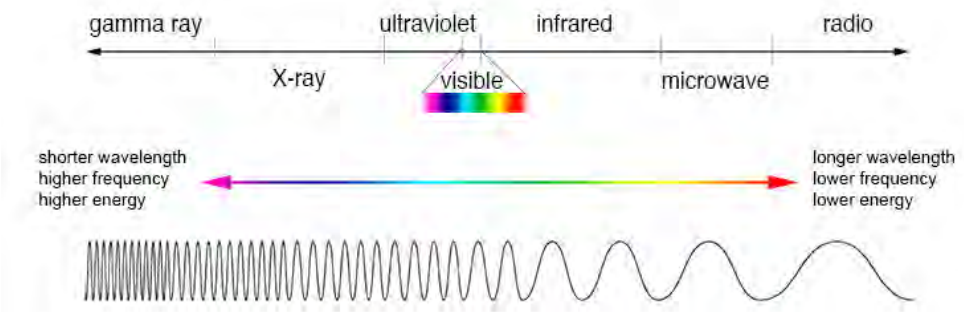

Figure 1.2: Electromagnetic Spectrum. Credit: NASA's Imagine the Universe [12].

small wavelengths. The frequency of light is related to the speed of oscillation of their $\vec{E}$ and $\vec{B}$ fields, and the wavelength is the distance of one cycle of their oscillations. Each EM wave is also associated with an energy. This introduces the particle model of light, where light is described as packets of energy called photons. Historically, the idea of a photon of light was needed to solve the ultraviolet catastrophe [13]. For a blackbody, such as stars, the intensity of the emitted blackbody radiation can be classically described using the Rayleigh-Jeans law.

$$B_\lambda = \frac{2ck_BT}{\lambda^4} \tag{1.2}$$

where B_λ is the intensity of the blackbody radiation, c is the speed of light, k_B is the Boltzmann constant[3], T is the temperature and λ is the wavelength of the emitted light. From Equation 1.2 we can see that as the wavelength λ approaches 0, the intensity of the emitted blackbody radiation approaches infinity. In fact, as the wavelength of the emitted light reaches the UV

[3] 1.380649×10^{-23} J/K

wavelengths, the intensity of radiation emitted, and thus the energy emitted, approaches infinity (see Figure 1.3). This is clearly unphysical, and at the time was a huge black mark against the classical wave-like treatment of light. It was not until Max Planck came up with the idea that light existed as separate quantised energy packets, rather than a continuous source of energy, that this problem was solved[4]. Planck described light as packets of energy with their energies related to their wavelengths: [14]:

$$\begin{aligned} E &= hf \\ E &= \frac{hc}{\lambda} \end{aligned} \tag{1.3}$$

where h is Planck's constant[5]. Using this, the emission intensities of for a blackbody is modified to be:

$$B_\lambda = \frac{2hc^2}{\lambda^5} \frac{1}{e^{hc/\lambda k_B T} - 1} \tag{1.4}$$

From Equation 1.4 we can see now as, λ approaches 0, the limit of B_λ also is 0 and thus, solving the ultraviolet catastrophe.

This brings together the idea of wave-particle duality for a model of light, with light having both wave-like and particle-like properties and has been extensively studied since the idea's conception [15–19].

1.3 Light Interactions with Matter

The interactions of light and matter are fundamental in how we perceive the universe. The reflections of light off materials give rise to their colour and the absorption of light by our photoreceptors allows us to see those objects. And that is just the visible spectrum. Many modern technologies rely on understanding and using the interactions of light and matter such as wireless communication [21], imaging and sensing [22–26], medical treatments [27–29], renewable energy [30], spectroscopy [31, 32], astrophysics [33–35] and many more.

The fundamentals of light and matter interactions boil down to four main types of interactions; absorption, emission, transmission, and reflection [36]. However, for the purposes of this work, we will focus on the absorption of light and the scattering of light, which involve the absorption and re-emission of light.

Absorption

When a photon is incident on an atom, it is possible for the photon to be absorbed by an atomic electron. The electron absorbs all the energy of the photon $E = hf$ as partial absorption cannot occur, and is excited to a higher energy orbital. Only photons that correspond exactly to the energy difference between two electron orbitals are absorbed [37] with;

$$hf = E_1 - E_2 \tag{1.5}$$

[4] In fact Max Planck first didn't believe his model of the quantised nature of light

[5] 6.626×10^{-34} Js

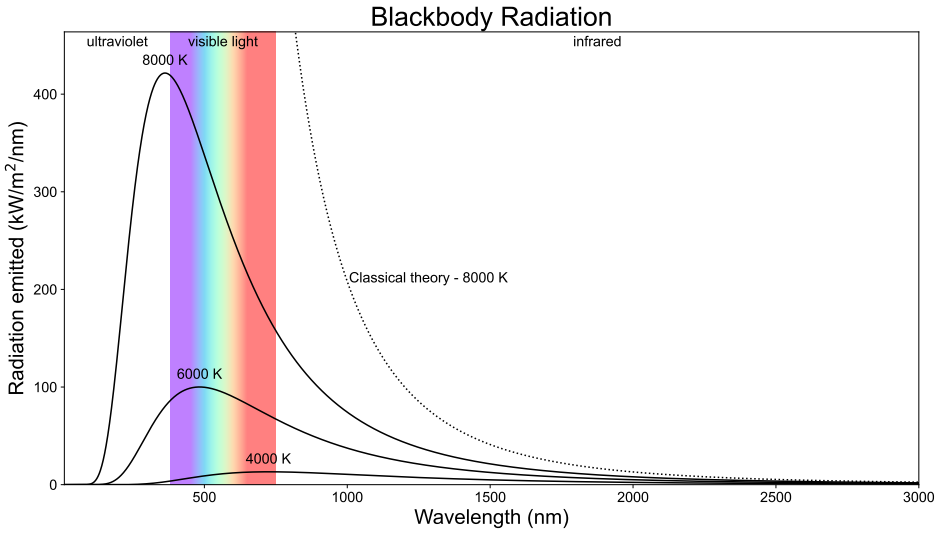

Figure 1.3: Ultraviolet catastrophe using a classical treatment of light results in infinite emitted energy at the UV wavelengths of a blackbody. Credit: IAU OAE/Niall Deacon [20].

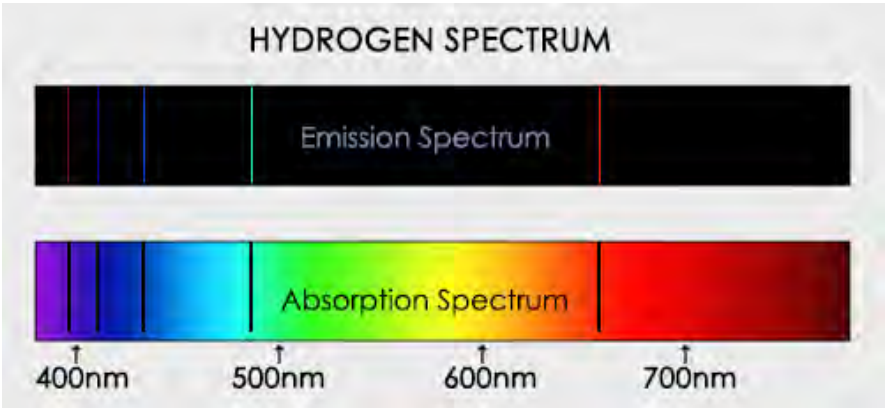

Figure 1.4: Absorption (botton) and emission (top) spectra of hydrogen. Credit CESAR [39].

where E_1 and E_2 are the energies of the electron orbitals and h is Planck's constant and f is the frequency of light as stated before. Thus, a particular atom can only absorb photons of certain wavelengths, which gives rise to the absorption spectra as first described by Niels Bohr for hydrogen [38]. In the same vein, the emission spectra of an atom is the opposite process, where excited electrons fall from a higher orbital back into its original electron shells. Thus, the wavelengths of the absorption and emission spectra match exactly. Figure 1.4 showcases the absorption and emission spectra for hydrogen. Note that the absorption and emission lines line up at the same wavelengths, giving credence to Bohr's model of the hydrogen atom.

If the incident photon has high enough energy, i.e. greater than the binding energy or the work function of the electron strikes a material, then it would be possible for electrons to be emitted from the surface. This process is known as the photoelectric effect [40]. Once again, the energy transfer of the photon to the electron has to be complete, and it cannot be partial. This phenomenon was famously used by Einstein to explain the quantum nature of light, since only a photon with sufficiently enough energy would be able to create photoelectrons [41]. In addition, the kinetic energy of the photoelectrons did not depend on the intensity of the incident light, it only depends on the energy of the photon and the work function of the material with;

$$E_{\text{electron}} = hf - \phi \tag{1.6}$$

where E_{electron} is the kinetic energy of the photoelectron and ϕ is the work function of the material.

Rayleigh Scattering

Rayleigh scattering occurs when the photon energy is small compared to the ionisation energy of the atom or when the diameter of the atom is smaller than a tenth of the photon wavelength [42]. Rayleigh scattering is most famously responsible for giving the sky its blue colour. For larger objects, the elastic scattering process is described by Mie scattering [43]. Classically, Rayleigh scattering occurs when an incident photon collides with a strongly bound atomic electron. The electron begins to oscillate with the same frequency as the incident radiation. This in turn causes the now oscillating electrons to re-emit radiation with that same exact frequency. Because the frequencies of the incident and emitted photons are identical, they have the same energy. As neighbouring atoms oscillate in sync with each other, the emitted photons have the same wavelengths and frequencies, and so the scattering light from a sample is known to be coherent[6] and has the ability to form interference patterns.

Treating a particle as a dielectric[7] sphere of radius r and relative permittivity ϵ[8], the probability that the sphere scatters a photon at angle θ is determined by the differential cross section $\frac{d\sigma_{\text{Rayleigh}}(\theta)}{d\Omega}$ with:

$$\frac{d\sigma_{\text{Rayleigh}}(\theta)}{d\Omega} = \frac{1}{2}\frac{2\pi n_0}{\lambda} r^6 \left(\frac{\epsilon - \epsilon_0}{\epsilon + 2\epsilon_0}\right)^2 (1 + \cos^2\theta) \tag{1.7}$$

where ϵ_0 is the permittivity of a vacuum and n_0 is the refractive index of the medium [44], λ is the wavelength of the photon, and Ω is the solid angle. Integrating over the solid angle Ω we can obtain the total cross section for unpolarised light:

$$\sigma_{\text{Rayleigh}} = \frac{8\pi}{3}\left(\frac{2\pi n_0}{\lambda}\right)^4 r^6 \left(\frac{\epsilon - \epsilon_0}{\epsilon + 2\epsilon_0}\right)^2 \tag{1.8}$$

with intensity of the scattered light being;

$$I_{\text{Rayleigh}} = I_0 \left(\frac{2\pi n_0}{\lambda}\right)^4 \frac{r^6}{2d^2} \left(\frac{\epsilon - \epsilon_0}{\epsilon + 2\epsilon_0}\right)^2 (1 + \cos^2\theta) \tag{1.9}$$

[6] same frequency, wavelength and phase
[7] high polarisability
[8] dielectric constant

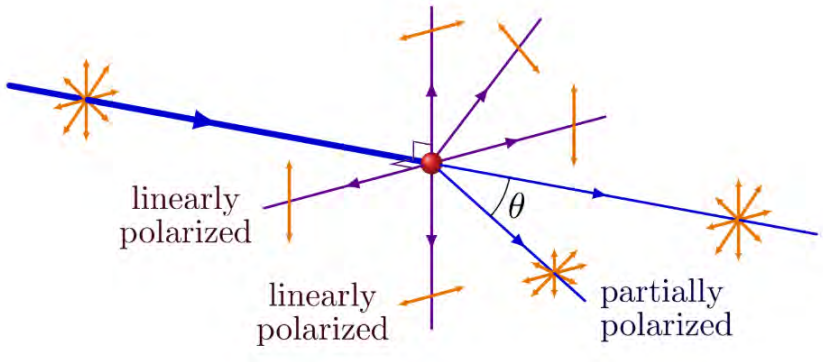

Figure 1.5: Rayleigh scattering of unpolarised light results in fully linearly polarised light when the scattering angle is 90° and is partially linearly polarised at other angles. Credit: Izaak Neutelings [45].

with I_0 being the intensity of the incident light and d being the distance between the particle and the detector.

The polarisation of photons is also important in Rayleigh scattering as scattered light that is perpendicular to the direction of the incident light is fully linearly or plane polarised. The scattering of light at other angles is partially linearly polarised. The polarisation of the scattered light is also perpendicular to the direction of propagation of the incident and scattered photons (see Figure 1.5).

Raman Scattering

Whilst Rayleigh scattering is elastic, Raman scattering, on the other hand, is inelastic. In Raman scattering, the photon is first absorbed and re-emitted with a change to its energy [46]. The Raman effect involves the vibration energy of the molecule with which the photon interacts, which causes a splitting of the quantum electronic energy levels and also the same splitting of the virtual electronic orbital levels. Unlike defined electronic orbital energy levels, which are fixed and quantised, these virtual states are continuous and are determined by the energy of the source radiation and are not restricted by the energies of the real molecular quantum states [47].

The excitement of the electron from the ground states is still governed by the energy difference between the two real quantised energy electron orbitals. Once excited, a ground state electron is excited into the first excited energy level. This electron can fall back into its original ground state and release a photon that has the same energy as the original incident photon, resulting in Rayleigh scattering. However, the electron can also enter an excited vibrational energy state of the ground state, so the energy difference between these two electronic states is no longer the same as the energy difference between the original two energy levels. Therefore, the released photon would have a different energy and thus also have a different wavelength (see Figure 1.6). This is known as Stokes scattering, where the emitted photon has less energy

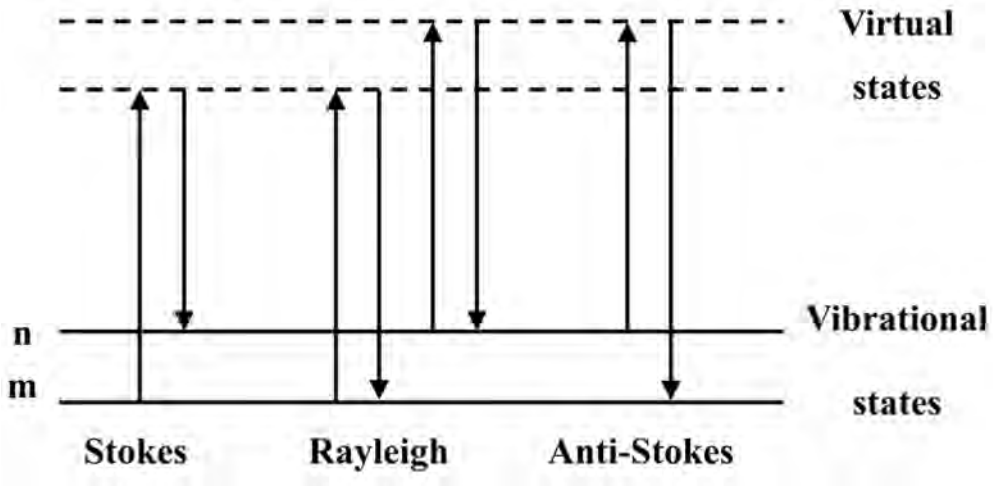

Figure 1.6: Raman Scattering showing Stokes and Anti-Stokes scattering [50].

and a longer wavelength and causes a redshift [48] to the light. Anti-Stokes scattering can also occur when a ground-state electron that is already in an energised vibrational ground state is excited to an energised vibrational first electronic state. The molecule can then relax, which would cause the electron to fall back into an unenergised ground state, once again releasing a photon with an energy different from the original photon, this time with a higher energy and a shorter wavelength, or a blueshift [49].

The result of this is that the wavelengths of the Raman scattered light can continuously change with the wavelength of the incident light. The Raman effect is inherently weaker than Rayleigh scattering (1,000 to 10,000 times weaker) [51].

Similarly to Rayleigh scattering, Raman scattering is also sensitive to polarisation as it depends on the direction of molecular vibrations [52]. Light is preferentially absorbed if its polarisation is parallel to the vibration of the molecule. Hence, looking at the depolarisation ratio or the intensity of the parallel polarised light against the perpendicularly polarised light can give information about the molecular vibrational modes.

Thomson Scattering

Thomson scattering is the elastic scattering that occurs between an electromagnetic wave and a charged particle that is not bound to an atom, or, in other words, a free electron. During the scattering process, the photon exchanges momentum with the charged particle, which then causes it to recoil. When the energy of the photon is comparable or greater than the energy of the particle, this recoil changes the momentum of the particle, and this is known as Compton scattering (see Figure 1.7). When the photon energy is much lower than the particle energy, the momentum of the particle is conserved [53] (seeFigure 1.6). Note that this is an extremely simplified view of Thomson scattering, where in reality, some energy and momentum will always be exchanged from the photon to the electron. Thus, Thomson scattering is the nonrelativistic[9]

[9]Low energy

limit of Compton scattering and occurs when $hf << mc^2$. Here h is Planck's constant, f is the frequency of the photon, and m is the mass of the particle [54].

We will begin with a classical interpretation of Thomson and Compton Scattering. However, for a complete picture, Thomson scattering as well as Compton scattering are described by quantum electrodynamics. We will go through those derivations later in this chapter and show how to obtain the classical results from the quantum field theory formalism, linking the two together.

Classically, Thomson scattering can be viewed as the scattering caused by the Coulomb force between the charged particle and the electromagnetic field of the incident photon. The differential cross section of Thomson scattering for unpolarised or randomly polarised light $\frac{d\sigma_{\text{Thomson}}}{d\Omega}$ for a free electron is:

$$\frac{d\sigma_{\text{Thomson}}}{d\Omega} = r_{\text{electron}}^2 \sin^2 \psi \tag{1.10}$$

where $r_{\text{electron}} = \frac{q^2}{4\pi\epsilon_0 m_e c^2}$[10] is the classical radius of an electron and ψ is the angle made by the scattered photon and the acceleration on the electron [55]. For a polarisation vector of the photon $\hat{e}$ and the direction of the scattered photon $\hat{n}$, we have $\hat{e} \times \hat{n} = \cos\psi$. Letting $\hat{k}$ be the direction of the incident photon, we can choose a coordinate basis with unit vectors $\hat{e}, \hat{k}$ and $\hat{e} \times \hat{k}$. This means that $\hat{n}$ can be defined as the following:

$$\hat{n} = \sin\phi\cos\theta\hat{e} + \sin\theta\cos\phi\hat{e} \times \hat{k} + \cos\phi\hat{k} \tag{1.11}$$

where ϕ is the angle subtended by the direction of the incident photon and the angle of the scattered photon. and θ is the azimuth angle that specifies the polarisation vector in the plane perpendicular to $\hat{k}$. It can be now shown that:

$$\cos\psi = \hat{e} \times \hat{n} = \cos\theta\sin\phi \tag{1.12}$$

$$\sin\psi = 1 - \cos^2\theta\sin\phi \tag{1.13}$$

Since this is for unpolarised light, we need to average out over all possible polarisation giving us:

$$\begin{aligned} \overline{\sin^2\psi} &= 1 - \overline{\cos^2\theta}\sin^2\theta \\ &= 1 - \frac{\sin^2\theta}{2} \\ &= \frac{1+\cos^2\theta}{2} \end{aligned} \tag{1.14}$$

Thus, the differential cross section for unpolarised Thomson scattering is:

$$\begin{aligned} \frac{d\sigma_{\text{Thomson}}}{d\Omega} &= r_{\text{electron}}^2 \overline{\sin^2\psi} \\ &= r_{\text{electron}}^2 \frac{1+\cos^2\theta}{2} \end{aligned} \tag{1.15}$$

[10] $r_{\text{electron}} = 2.818 \times 10^{-15}$ m

Integrating over the solid angle of the polar angle θ and the azimuthal angle ϕ we get:

$$\begin{aligned}\sigma_{\text{Thomson}} &= \int_0^{2\pi}\int_0^{\pi} \frac{d\sigma_{\text{Thomson}}}{d\Omega}\sin\theta d\theta d\phi \\ &= \frac{8\pi}{3} r_{\text{electron}}^2 \\ &= 6.65 \times 10^{-29}\text{m}^2\end{aligned} \tag{1.16}$$

We can see from Equation 1.15 that the Thomson cross section is independent of the photon energy.

The Thomson cross section of a charged particle with charge q and mass m is:

$$\sigma_{\text{Thomson}} = \frac{8\pi}{3}\left(\frac{q^2}{4\pi\epsilon_0 mc^2}\right)^2 \tag{1.17}$$

Thus, the Thomson cross section for protons and other heavy charged particles such as nuclei is negligible when compared to electrons and their masses are approximately 2000 times greater than that of the electron.

The permittivity of free space ϵ_0 in natural units is:

$$\epsilon_0 = \frac{e^2}{4\pi\alpha} \tag{1.18}$$

and so the Thomson cross section for an electron in natural units is:

$$\sigma_{\text{Thomson}} = \frac{8\pi}{3}\frac{\alpha^2}{m^2} \tag{1.19}$$

Compton Scattering

In the instance where the incident photon's energy is comparable or greater than the energy of the charged particle with which it interacts, i.e. $hf \geq mc^2$, Compton scattering may occur. Unlike Thomson scattering, Compton scattering is inelastic, meaning that the energy of the scattered photon is different from that of the initial photon. In the case where the energy of the photon is greater than the energy of the particle, the scattering photon imparts some of its energy to the particle. The scattering photon thus has lower energy and a longer wavelength compared to the incident photon, and the recoiled particle now has gained the same amount of energy that the photon has lost. In the instance where the charged particle started with more energy than the photon, the opposite occurs where the scattered photon gains energy. This process is known as inverse Compton scattering [56]. The change in the wavelength of the scattered photon is known as the Compton shift.

Whilst Compton scattering could theoretically work with any charged particle such as the proton, the majority of instances where Compton scattering occurs are with free electrons, partially due to their abundance and lifetimes compared to other charged particles. For the following derivation I will introduce the concept of 4-momentum. This allows use to write out the energy and classical 3-momentum (relativistic momentum in 3 dimensions) together as a 4-vector s.t. the 4-momentum $p = (E/c, \vec{p})$ where E is the energy of the particle, and $\vec{p} = (p_x, p_y, p_z)$ are the spatial relativistic momenta.

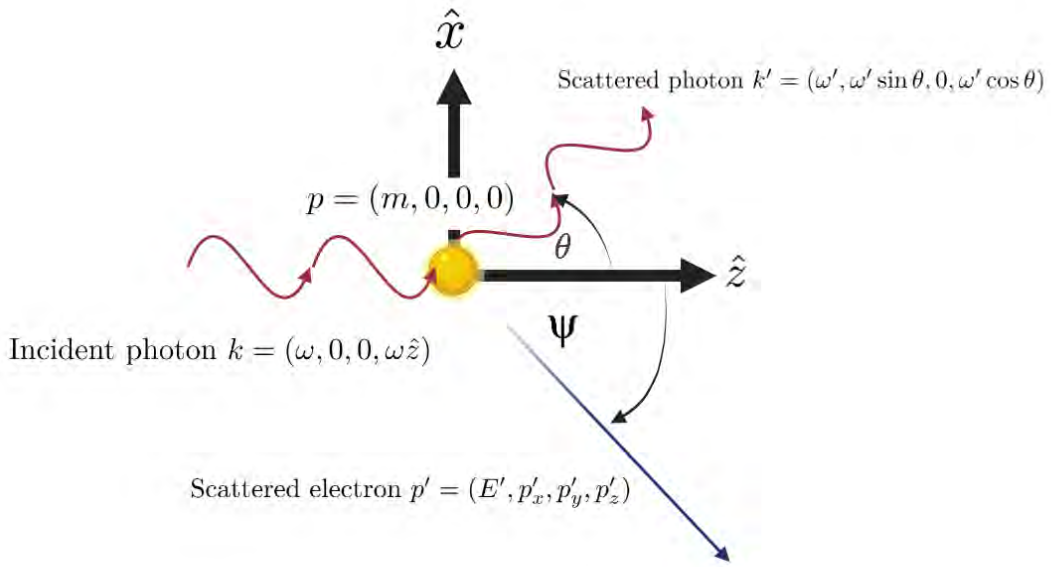

Figure 1.7: Compton scattering of incident photon with 4-momentum k with a stationary electron with 4-momentum p. After collision, the photon scatters at an angle of θ with a 4-momentum of k' and the electron scatters with a 4-momentum of p'

When an incident photon with 4-momentum $k = (E_\gamma/c, \vec{p_\gamma})$ interacts with an electron at rest with 4-momentum $p = (m_e c, \vec{0})$, the photon scatter off the electron at some angle θ. The 4-momentum of the scattered photon is now $k' = (E'_\gamma/c, \vec{p_\gamma}')$ and the 4-momentum of the scattered electron is $p' = (E'_e/c, \vec{p_e}')$. In this system, we have conservation of 4-momentum. This is another way of saying conservation of energy and momentum. Since the photon scatters at angle θ we have:

$$\vec{p_\gamma} \cdot \vec{p_\gamma}' = |\vec{p_\gamma}||\vec{p_\gamma}'| \cos\theta \tag{1.20}$$

From conservation of 4-momentum we have:

$$\begin{aligned} k + p &= k' + p' \\ k - k' &= p' - p \end{aligned} \tag{1.21}$$

Squaring both sides leads to:

$$k^2 - 2k \cdot k' + k'^2 = p'^2 - 2p' \cdot p + p^2 \tag{1.22}$$

We define the inner product using the Minkowski (flat space-time) metric s.t. for $x = (x_0, x_1, x_2, x_3)$ and $y = (y_0, y_1, y_2, y_3)$

$$x \cdot y = x_0 y_0 - x_1 y_1 - x_2 y_2 - x_3 y_3 \tag{1.23}$$

We can use $k^2 = k \cdot k = E_\gamma^2/c^2 - \vec{p_\gamma}^{\,2} = m_0^2 c^2$. m_0 is the rest mass of the photon, which is 0. Thus, we have $k^2 = 0$ and also $E_\gamma^2/c^2 = \vec{p_\gamma}^{\,2}$. Similarly, we have $p^2 = m_e^2 c^2$. We also find that $k'^2 = 0$ and $p'^2 = m_e^2 c^2$.

Plugging these values back into Equation 1.23 we can obtain:

$$\begin{aligned} -2k \cdot k' &= 2m_e^2 c^4 - 2p' \cdot p \\ k \cdot k' &= p' \cdot p - m_e^2 c^2 \\ \frac{E_\gamma E'_\gamma}{c^2} - \vec{p} \cdot \vec{p'} &= E'_e m_e - m_e^2 c^2 \\ \frac{E_\gamma E'_\gamma}{c^2} - |\vec{p_\gamma}||\vec{p_\gamma}'| \cos\theta &= E'_e m_e - m_e^2 c^2 \end{aligned} \tag{1.24}$$

We can now use $|\vec{p_\gamma}| = E_\gamma/c$ for photons to obtain:

$$\frac{E_\gamma E'_\gamma}{c^2}(1 - \cos\theta) = E'_e m_e - m_e^2 c^2 \tag{1.25}$$

We can now use conservation of energy to see that

$$E'_e = E_e + E_\gamma - E'_\gamma \tag{1.26}$$

Putting this into Equation 1.25 and using $E_e = m_e c^2$, we can get:

$$\frac{E_\gamma E'_\gamma}{c^2}(1 - \cos\theta) = (E_\gamma - E'_\gamma) m_e \tag{1.27}$$

Here we can use $E_\gamma = hc/\lambda$ to finally obtain:

$$\begin{aligned} \frac{h^2}{\lambda\lambda'}(1 - \cos\theta) &= hc\left(\frac{1}{\lambda} - \frac{1}{\lambda'}\right) m_e \\ \lambda' - \lambda &= \frac{hc}{m_e}(1 - \cos\theta) \\ \Delta\lambda &= \lambda_c(1 - \cos\theta) \end{aligned} \tag{1.28}$$

Here $\Delta\lambda$ is the Compton shift of the photon and $\lambda_c = 2.43$ pm is the Compton wavelength of an electron[11]. From Equation 1.28 we can see that the maximum Compton shift occurs when $\theta = 180°$, i.e. the photon scatters back in the direction of the incident photon and the minimum Compton shift occurs when the photon is not deflected. For the Compton effects of photon collisions with other charged particles, the rest mass of the electron m_e can be replaced with the rest mass of the charged particle. However, for protons and atomic nuclei, the effect is ≥ 4 orders of magnitude lower and thus can be ignored.

Quantum Field Theory formulation of Compton Scattering

For a proper derivation of Compton scattering we must look towards the quantum electrodynamics (QED) of electron photon interactions described in quantum field theory (QFT). A Compton interaction can be described by the Feynman diagrams shown in Figure 1.8

[11] Wavelength of a photon that has equal energy to the rest mass of an electron

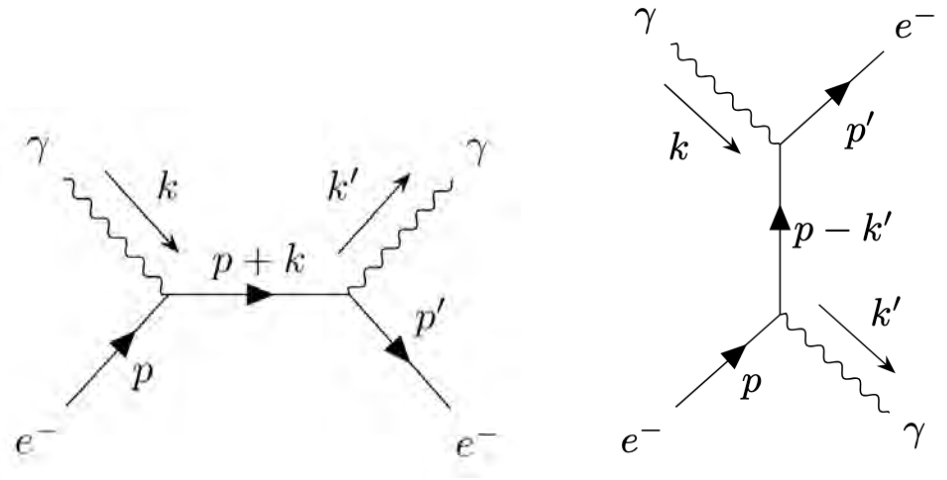

(a) s-channel (b) u-channel

Figure 1.8: Tree (Lowest) Level Diagrams for Compton Scattering.

Feynman Rules

To find the cross section of these interactions, we need to calculate the matrix elements $\mathcal{M}$. For that we can use the Feynman rules on Feynman diagrams. I will not go through all the Feynman rules, just the necessary ones required for this calculation. The matrix element can be calculated by looking at the incoming and outgoing particles for each vertex on a Feynman diagram. The contribution of each vertex is multiplied together to obtain the final matrix element. Each contribution is listed in the following:

- For a fermion, such as e^-, with momentum p heading into a vertex, multiply by $u(p)$.
- For n fermion with momentum p, heading away from a vertex, multiply by $\bar{u}(p)$.
- For each vertex multiply by $-ie\gamma^\mu$
- For a photon γ with momentum k, heading into a vertex multiply by $\epsilon_\mu(k)$
- For a photon γ with momentum k, heading away from a vertex multiply by $\epsilon^*_\mu(k)$
- For a fermion propagator (between vertices) with momentum p and mass m, multiply by $\dfrac{i(\not{p} + m)}{p^2 - m^2}$

with u and ϵ being the polarisation vectors of the electron and the photon respectively. Additionally, γ^μ are the Dirac matrices with:

$$\gamma^\mu \gamma_\mu = 4I_4 \tag{1.29}$$

where I_4 is the 4 dimensional identity matrix. $\not{p}$ is the Dirac slash notation with:

$$\not{p} = \gamma^\mu p_\mu \tag{1.30}$$

Cross Section Calculation

We can use the aforementioned Feynman rules to write out the matrix element $\mathcal{M}$ with for the s-channel with:

$$i\mathcal{M} = \bar{u}(p')(-ie\gamma^\mu)\epsilon^*_\mu(k')\frac{i(\not{p}+\not{k}+m)}{(p+k)^2-m^2}(-ie\gamma^\nu)\epsilon_\nu(k)u(p) \tag{1.31}$$

where $\epsilon_\nu(k)$ and $\epsilon^*_\mu(k')$ describes the polarisation vectors of the initial and final photons. The matrix element for the u-channel can be written out similarly with:

$$i\mathcal{M} = \bar{u}(p')(-ie\gamma^\mu)\epsilon_\nu(k)\frac{i(\not{p}-\not{k}'+m)}{(p-k')^2-m^2}(-ie\gamma^\nu)\epsilon^*_\mu(k')u(p) \tag{1.32}$$

The total matrix element is just the addition of Equation 1.31 and Equation 1.32 to obtain:

$$i\mathcal{M} = -ie^2\epsilon^*_\mu(k')\epsilon_\nu(k)\bar{u}(p')\left[\frac{\gamma^\mu(\not{p}+\not{k}+m)\gamma^\nu}{(p+k)^2-m^2}+\frac{\gamma^\nu(\not{p}-\not{k}'+m)\gamma^\mu)}{(p-k')^2-m^2}\right]u(p) \tag{1.33}$$

To simplify Equation 1.33 we note that $p^2 = m^2$ and $k^2 = 0$ as the mass of the photon is 0, which means that:

$$\begin{aligned}(p+k)^2-m^2 &= 2p\cdot k\\ (p-k')^2-m^2 &= -2p\cdot k'\end{aligned} \tag{1.34}$$

We can also show, using Dirac algrebra, that:

$$\begin{aligned}(\not{p}+m)\gamma^\nu u(p) &= (2p^\nu-\gamma^\nu\not{p}+\gamma^\nu)u(p)\\ &= 2p^\nu u(p)-\gamma^\nu(\not{p}-m)u(p)\\ &= 2p^\nu u(p)\end{aligned} \tag{1.35}$$

Using Equation 1.34 and Equation 1.35 we can simplify Equation 1.33 to now obtain:

$$i\mathcal{M} = -ie^2\epsilon^*_\mu(k')\epsilon_\nu(k)\bar{u}(p')\left[\frac{\gamma^\mu\not{k}\gamma^\nu+2\gamma^\mu p^\nu}{2p\cdot k}+\frac{-\gamma^\nu\not{k}'\gamma^\mu+2\gamma^\nu p^\mu}{-2p\cdot k'}\right]u(p) \tag{1.36}$$

We want to sum over the electron ($u(p)$) and photon ($\epsilon_\nu(k)$) polarisations with:

$$\sum_{\text{polarisations}} u(p)\bar{u}(p) = \not{p}+m \tag{1.37}$$

and

$$\sum_{\text{polarisations}} \epsilon^*_\mu\epsilon_\nu \to -g_{\mu\nu} \tag{1.38}$$

where $g_{\mu\nu}$ is the metric tensor and for a flat spacetime metric (Minkowski metric):

$$g_{\mu\nu} = \begin{pmatrix}-1 & 0 & 0 & 0\\ 0 & 1 & 0 & 0\\ 0 & 0 & 1 & 0\\ 0 & 0 & 0 & 1\end{pmatrix} \tag{1.39}$$

Now finally we are able to sum over the polarisation states of the electron and the photon, giving us:

$$\begin{aligned}\frac{1}{4}\sum_{\text{spins}}\left|\mathcal{M}^2\right| = \frac{e^4}{4}g_{\mu\rho}g_{\nu\sigma}\cdot\text{tr}\Bigg\{(\not{p}'+m)\left[\frac{\gamma^\mu \not{k}\gamma^\nu + 2\gamma^\mu p^\nu}{2p\cdot k} + \frac{\gamma^\nu \not{k}'\gamma^\mu - 2\gamma^\nu p^\mu}{2p\cdot k'}\right] \\ \cdot(\not{p}+m)\left[\frac{\gamma^\sigma \not{k}\gamma^\rho + 2\gamma^\rho p^\sigma}{2p\cdot k} + \frac{\gamma^\rho \not{k}'\gamma^\sigma - 2\gamma^\sigma p^\rho}{2p\cdot k'}\right]\Bigg\}\end{aligned} \tag{1.40}$$

$$\frac{1}{4}\sum_{\text{spins}}\left|\mathcal{M}^2\right| = \frac{e^4}{4}\left[\frac{A}{(2p\cdot k)^2} + \frac{B}{(2p\cdot k)(2p\cdot k')} + \frac{C}{(2p\cdot k')(2p\cdot k)} + \frac{D}{(2p\cdot k')^2}\right] \tag{1.41}$$

where A, B, C and D are substituted for the traces. For the traces $B = C$ and A is the same as D but with k replaced by $-k'$.

For A we have:

$$\begin{aligned}A &= \text{tr}\left[(\not{p}'+m)(\gamma^\mu \not{k}\gamma^\nu + 2\gamma^\mu p^\nu)(\not{p}+m)(\gamma_\nu \not{k}\gamma_\mu + 2\gamma_\mu p_n u)\right] \\ &= 16(4m^4 - 2m^2 p\cdot p' + 4m^2 k\cdot k - 2m^2 p'\cdot k + 2(p\cdot k)(p'\cdot k))\end{aligned} \tag{1.42}$$

To simplify further, we can introduce the Mandelstam variables defined as:

$$\begin{aligned}s &= (p+k)^2 = 2p\cdot k + m^2 = 2p'\cdot k' + m^2 \\ t &= (p'-p)^2 = -2p\cdot p' + 2m^2 = -2k\cdot k' \\ u &= (k'-p')^2 = -2k'\cdot p = -2k\cdot p' + m^2\end{aligned} \tag{1.43}$$

Using Equation 1.43, we can obtain the following:

$$A = 16\left(2m^4 + m^2(s-m^2) - \frac{1}{2}(s-m^2)(u-m^2)\right) \tag{1.44}$$

Then we can switch k with $-k'$ to get:

$$D = 16\left((2m^4 + m^2(u-m^2) - \frac{1}{2}(s-m^2)(u-m^2)\right) \tag{1.45}$$

And we have:

$$B = C = -8(4m^4 + m^2(s-m^2) + m^2(u-m^2)) \tag{1.46}$$

We can put A, B, C and D back into Equation 1.41 to finally obtain:

$$\frac{1}{4}\sum_{\text{spins}}\left|\mathcal{M}^2\right| = 2e^2\left[\frac{p\cdot k'}{p\cdot k} + \frac{p\cdot k}{p\cdot k'} + 2m^2\left(\frac{1}{p\cdot k} - \frac{1}{p\cdot k'}\right) + m^4\left(\frac{1}{p\cdot k} - \frac{1}{p\cdot k'}\right)^2\right] \tag{1.47}$$

To turn it into a cross section, we have to chose a frame of reference. We chose the lab frame where the electron is initially at rest with a 4-momentum $p = (m, 0, 0, 0)$. It is struck by an incident photon travelling in the z direction with a 4-momentum $k = (\omega, 0, 0, \omega\hat{z})$. After collision,

the photon scatters at some angle θ with a new 4-momentum $k' = (\omega', \omega' \sin\theta, 0, \omega' \cos\theta)$ and imparts some energy and momentum to the electron such that its new 4-momentum is $p' = (E', \mathbf{p}')$ (see Figure 1.7). We also have:

$$\begin{aligned} m^2 = (p')^2 &= (p + k - k')^2 = p^2 + 2p \cdot (k - k') - 2k \cdot k' \\ &= m^2 + 2m(\omega - \omega') - 2\omega\omega'(1 - \cos\theta) \end{aligned} \tag{1.48}$$

and we can obtain

$$\frac{1}{\omega'} - \frac{1}{\omega} = \frac{1}{m}(1 - \cos\theta) \tag{1.49}$$

We can see that with $\lambda = \dfrac{1}{\omega}$ for a photon with momentum ω in Natural units we obtain:

$$\lambda' - \lambda = \frac{1}{m}(1 - \cos\theta) \tag{1.50}$$

which is just the Compton shift formula (Equation 1.28) in Natural units.

We can also use Equation 1.49 to solve for ω' with:

$$\omega' = \frac{\omega}{1 + \frac{\omega}{m}(1 - \cos\theta)} \tag{1.51}$$

to give us the phase space integral in the lab frame:

$$\begin{aligned} \int d\Pi_2 &= \int \frac{d^3k'}{(2\pi)^3} \frac{1}{2\omega'} \frac{d^3p'}{(2\pi)^3} \frac{1}{E'} (2\pi)^4 \delta(k' + p' - k - p) \\ &= \int \frac{(\omega')^2 d\omega' d\Omega}{(2\pi)^3} \frac{1}{4\omega' E'} \times 2\pi\delta(\omega' + \sqrt{m^2 + \omega^2 + (\omega')^2 - 2\omega\omega'\cos\theta} - \omega - m) \\ &= \int \frac{d\cos\theta}{2\pi} \frac{\omega'}{4E'} \frac{1}{\left|1 + \frac{\omega' - \omega\cos\theta}{E'}\right|} \\ &= \frac{1}{8\pi} \int d\cos\theta \frac{\omega'}{m + \omega(1 - \cos\theta)} \\ &= \frac{1}{8\pi} \int d\cos\theta \frac{(\omega')^2}{\omega m} \end{aligned} \tag{1.52}$$

where δ is the Dirac-Delta function and Ω is the solid angle. Using Equation 1.52, we can find an expression for the cross section σ_{Compton} for Compton scattering:

$$\frac{d\sigma_{\text{Compton}}}{d\cos\theta} = \frac{1}{\omega}\frac{1}{2m} \cdot \frac{1}{8\pi}\frac{(\omega')^2}{\omega m} \cdot \left(\frac{1}{4}\sum_{\text{spins}} \left|\mathcal{M}^2\right|\right) \tag{1.53}$$

$\dfrac{1}{4}\displaystyle\sum_{\text{spins}} \left|\mathcal{M}^2\right|$ is from Equation 1.47 noting that $p \cdot k = m\omega$ and $p \cdot k' = m\omega'$ to obtain:

$$\frac{d\sigma_{\text{Compton}}}{d\cos\theta} = \frac{\pi\alpha^2}{m^2}\left(\frac{\omega'}{\omega}\right)^2 \left[\frac{\omega'}{\omega} + \frac{\omega}{\omega'} - \sin^2\theta\right] \tag{1.54}$$

where α is the fine structure constant. This is the *Klein-Nishina* formula which details the differential cross section of photons scattered from a single free electron.

We see that in the limit of low photon energy such that $\omega \to 0$, we have, from Equation 1.51 $\omega'/\omega \to 1$ and the cross section becomes.

$$\frac{d\sigma_{\text{Compton}}}{d\cos\theta} = \frac{\pi\alpha^2}{m^2}(1+\cos^2\theta) \tag{1.55}$$

which gives

$$\sigma_{\text{total}} = \frac{8\pi\alpha^2}{3m^2} \tag{1.56}$$

which is the classical Thomson scattering cross section off an electron as seen in Equation 1.19.

Pair Production from Nuclear Interactions

When the energy of a photon exceeds twice the rest mass energy of an electron, that is, $hf > 2m_0c^2 = 1.022$ MeV, it becomes possible for the photon to be transformed and create an electron and positron pair [57]. As energy and momentum need to be observed, a single photon cannot spontaneously decay into an electron and a positron[12].

The electron-positron pair produced will travel in opposite directions in the electron-positron rest frame, and, as they have exactly the same mass, their total momentum must be zero. However, the momentum of a photon is $p = \dfrac{E}{c}$, which would require the photon energy to be 0 to have zero momentum. Thus, in a vacuum, two photons with momenta equal in magnitude but opposite in direction are required such that:

$$\vec{k}_1 + \vec{k}_2 = \vec{p}_e + \vec{p}_p \tag{1.57}$$

where $\vec{k}_1$ and $\vec{k}_2$ are the momenta of the photons and $\vec{p}_e$ and $\vec{p}_p$ are the momenta of the electron and positron respectively.

However, in the presence of an atomic nucleus, Z, a virtual photon can be created, which would allow the decay of this virtual photon and a photon into an electron-positron pair [58] (see Figure 1.09). The cross section of pair production near an atomic nucleus in the relativistic limit is:

$$\sigma \propto \alpha r_e Z^2 \tag{1.58}$$

where Z is the atomic number, r_e is the classical electron radius and $a = \dfrac{1}{4\pi\epsilon_0}\dfrac{e^2}{\hbar c}$ is the fine structure constant [60]. The cross section of photon-matter interactions as a function of photon energy and atomic number can be seen in Figure 1.10 dominates photon-matter interactions. When a threshold energy is reached, Compton interactions start to occur, and its cross section is relatively constant for photon energy afterwards. However, as the atomic number increases, the Compton scattering for inner shell electrons also increases [61]. Above the threshold energy of 1.022 MeV, pair production becomes possible and increases approximately with the logarithmic of the cube of the photon energy and the square of the atomic number.

[12] Antimatter version of the electron

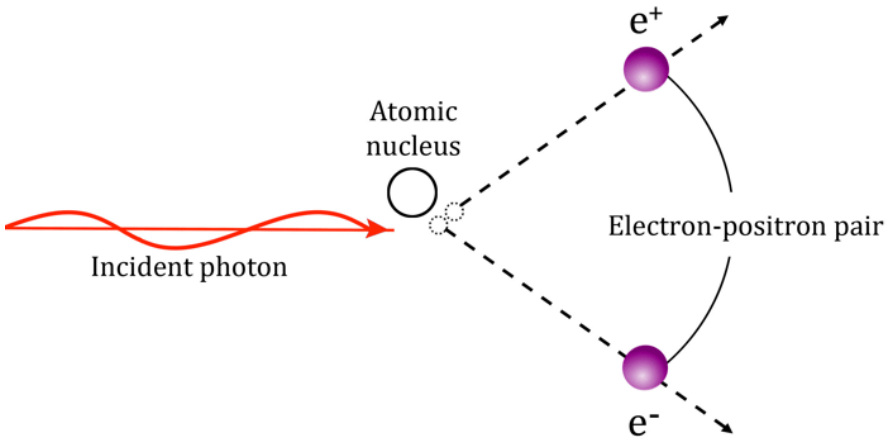

Figure 1.9: A cartoon showcasing the pair production process of a photon near an atomic nucleus, Z [59]. The real photon interactions with a virtual photon created by the nucleus, which allows it to decay into an electron and positron, provided the photon energy is greater than twice the rest mass energy of an electron.

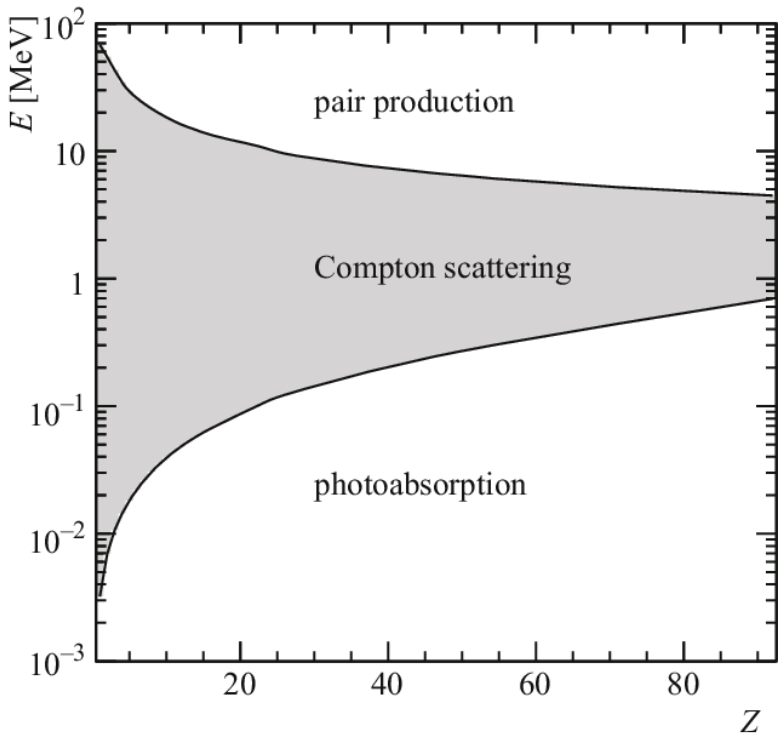

Figure 1.10: Photon matter interactions as a function of photon energy and atomic number. Credit: Hans Bichsel and Heinrich Schindler [57].

1.4 Polarisation

The wave description of light are synchronised, coupled fluctuating electric and magnetic fields, which self propagate through space (Figure 1.1). The direction of oscillations of the electric and magnetic fields as well as the direction of propagation are all orthogonal to each other. The polarisation of light is usually defined as the direction of its electric-field oscillation, or its E-vector.

For any given direction of light propagation, the only conditions on the oscillations of the electric and magnetic fields are that they must be orthogonal to each other and also the direction of propagation. Thus, for light propagation in a specific direction, its E-vector can be any direction on a plane[13]. A random distribution of E-vectors in that plane for a beam of light is said to be unpolarised.

There are three types of polarisations; linear, circular, and elliptical (see Figure 1.11). To understand the different polarisations of light, we can think of splitting the electric field oscillation vector into its two orthogonal components. Without loss of generality, we will set these two components as the horizontal and vertical components. Both components can oscillate independently of each other, with their own phase and amplitude; however, their periods are the same. Linear polarisation occurs when the amplitude of one of the components is set to 0. For horizontally polarised light, the amplitude of the vertically oscillating electric field goes to 0, and vice versa for vertically polarised light. Linear polarisation in any direction in between the horizontal and vertical directions is caused by both the horizontal and vertical electric field components being in phase and non-zero.

In the case where the vertical and horizontal electric fields have equal amplitudes but are out of phase by 90 degrees, the light is said to be circularly polarised. This occurs because the magnitude of the electric field is strongest for the vertical component when the magnitude of the horizontal component is at its weakest. Over time, the vertical component decreases, whilst the horizontal component increases until the magnitude of the horizontal component is at its maximum, with the vertical component at its minimum. This cycle repeats continuously. If one were to look directly at the source of light, it would appear that the electric field is rotating in a circle, giving rise to a rotational E-vector and thus to circular polarisation. This rotation may appear to be clockwise, which would result in left-handed circular polarisation, or counter clockwise, which results in right-handed circular polarisation.

In the instance where the horizontal and vertical electric fields are out of phase by 90 degrees but their maximum amplitudes are not equal, instead of a circular rotation, the electric field would appear to trace out an ellipse. This is known as elliptical polarisation of light, and once again there are two modes, namely right-handed and left-handed elliptical polarisations. This is the most general polarisation state of light, with linear and circular polarisations being special cases of elliptical polarisation [62].

A mathematical description for the polarisation of light can be characterised by four intensity parameters, introduced by George Gabriel Stokes [64], known as the Stokes parameters. The two orthogonal components of the electric field, in the $(\hat{x}, \hat{y})$ basis, described previously, can be

[13]The plane is perpendicular to the direction of propagation

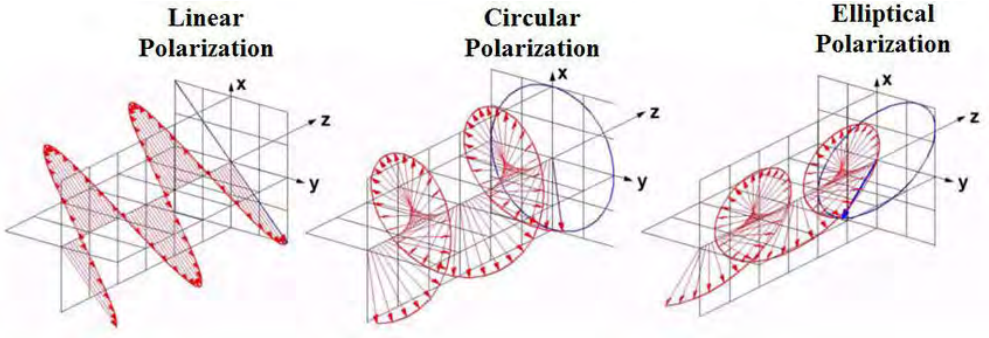

Figure 1.11: Linear, circular and elliptical polarisation modes of light. Credit: Ali Siblini [63]

expressed as:

$$\begin{aligned} E_x &= E_{0x}\cos(\omega t - kz - \delta_x), \\ E_y &= E_{0y}\cos(\omega t - kz - \delta_y) \end{aligned} \tag{1.59}$$

where E_{0x} and E_{0x} are the maximum amplitudes of their respective electric fields, ω is the angular frequency, $k = \dfrac{2\pi}{\lambda}$ is the wavenumber, and δ_x and δ_y are the phases, with $\delta = \delta_y - \delta_x$ being the phase difference.

With that in mind, we can define 4 parameters S_0, S_1, S_2 and S_3 as the following:

$$\begin{aligned} S_0 &= E_{0x}^2 + E_{0y}^2 \\ S_1 &= E_{0x}^2 - E_{0y}^2 \\ S_2 &= 2E_{0x}E_{0y}\cos\delta \\ S_3 &= 2E_{0x}E_{0y}\sin\delta \end{aligned} \tag{1.60}$$

We can also see that

$$S_0^2 = S_1^2 + S_2^2 + S_3^2 \tag{1.61}$$

These four Stokes parameters can be combined to form the Stokes vector [65]:

$$\vec{S} = \begin{pmatrix} S_0 \\ S_1 \\ S_2 \\ S_3 \end{pmatrix} = \begin{pmatrix} I \\ Q \\ U \\ V \end{pmatrix} \tag{1.62}$$

where $I = S_0$ can be seen as the summation of the intensity of x and y components of the electric field and thus is the total intensity. Q can be interpreted at the polarisation in the $\hat{x}$ and $\hat{y}$ directions. When $E_{0x}^2 = 1$ and $E_{0y}^2 = 0$, there is an electric field oscillating only in the x direction and is thus horizontally polarised. When $E_{0x}^2 = 0$ and $E_{0y}^2 = 1$, there is an electric field that oscillates only in the y direction and is only vertically polarised. Therefore, we can see that $Q = 1$ for horizontally polarised light and $Q = -1$ for vertically polarised light.

U can be seen at the mixing of the two linearly polarisation modes, with δ being the phase difference between the two electric field components E_{0x} and E_{0y}. For linear polarisation, the phase difference is 0, i.e. $\delta = 0$ or $\delta = \pi$, with $E_{0x} = E_{0y} = 1/\sqrt{2}$. Thus we have $U = 1$ being linearly polarised in $+45°$ and $U = -1$ being linearly polarised in $-45°$. The values of Q and U between describe elliptical polarisations. Together, Q and U describe the shape and orientation of the polarisation ellipse, taking up values between 1 and -1. V is related to the chirality of the polarisation vector and can also be described as $V = E_{0r}^2 - E_{0r}^2$ where E_{0r}^2 is the intensity of right-handed polarised photons and E_{0l}^2 is the intensity of left-handed photons. Thus, we can see that $V = 1$ for right-handed polarisations and $V = -1$ for left-handed polarisations. Together, these four vectors describe all possible polarisation modes of the light and can be illustrated on a Poincare spheré [66] (see Figure 1.12). Equation 1.63 summarised the Stokes parameters for special cases of polarisations, noting that $I = Q^2 + U^2 + V^2$.

$$(I, Q, U, V) = \begin{cases} (1, 1, 0, 0) & \text{Horizontal Linearly polarised} \\ (1, -1, 0, 0) & \text{Vertically Linearly polarised} \\ (1, 0, 1, 0) & \text{Linearly polarised at + 45°} \\ (1, 0, -1, 0) & \text{Linearly polarised at - 45°} \\ (1, 0, 0, 1) & \text{Right-handed Circularly polarised} \\ (1, 0, 0, -1) & \text{Light-handed Circularly polarised} \\ (1, 0, 0, 0) & \text{Unpolarised} \end{cases} \tag{1.63}$$

1.5 Polarisation of light

Unpolarised light can be polarised through its interactions with matter, and have led to the development of polarisers, which are optical filters which only lets through a specific polarisation of light through, thus turning unpolarised light into polarised light. There are several mechanisms that allow for the polarisation of electromagnetic waves including; dichroism, birefringence, reflection and scattering [68]. As we have already talked about how scattering can lead to polarisation, thus we will now focus on the other three methods.

Dichroism

Dichroism is the phenomenon where the absorption of light in a material is dependent on its polarisation. This is possible since the horizontal and vertical polarisation components have different extinction coefficients. Dichroism can only occur in anisotropic systems, where the anisotropic molecular arrangement of the material changes its absorption coefficients [69]. The main process by which light is absorbed as it passes through a material is by atomic electrons of the material. The polarisation of light determines its electric field oscillations, and the electrons that absorb light also pick up such oscillations. Thus in materials where one direction of electron oscillation is preferred over another, one polarisation of photons is preferentially absorbed, leading to linear dichroism [70]. Common dichroic materials including Polaroid sheets, which uses herapathite crystals [71] and liquid crystals [72]. The degree of linear dichroism (LD) is defined to be:

$$\text{LD} = A_{\parallel} - A_{\perp} \tag{1.64}$$

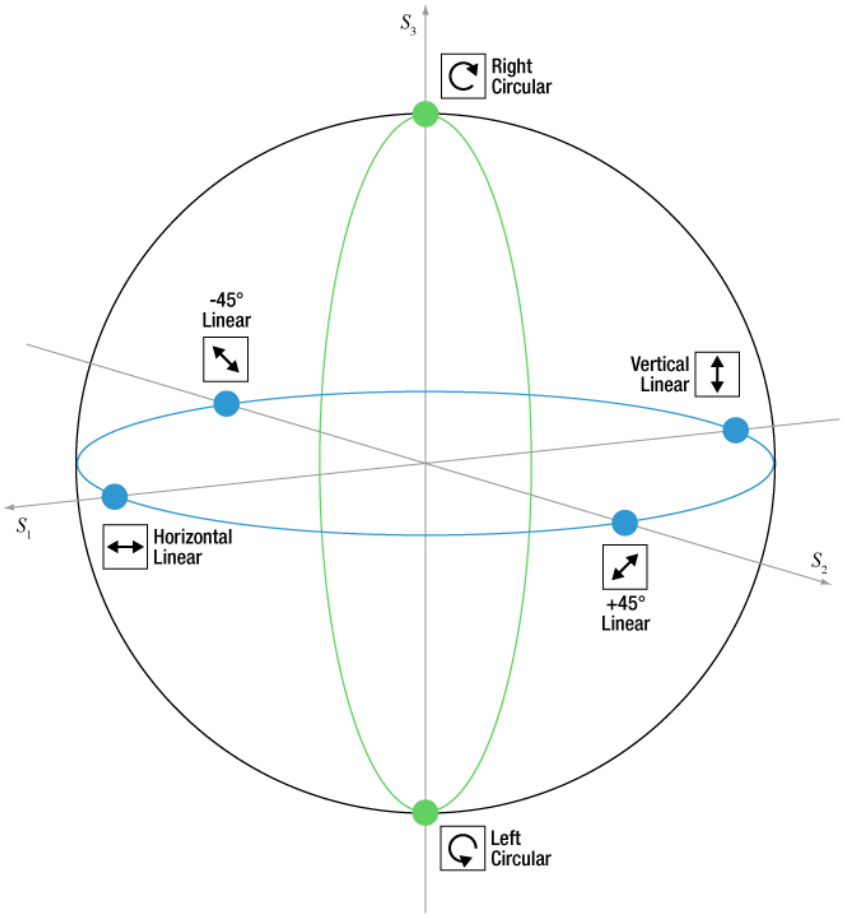

Figure 1.12: Poincare spheré showing the polarisation states, described by a sphere with radius S_0 or I and axes of $\{S_1, S_2, S_3\}$ or $\{Q, U, V\}$. Credit: Thorlabs [67]

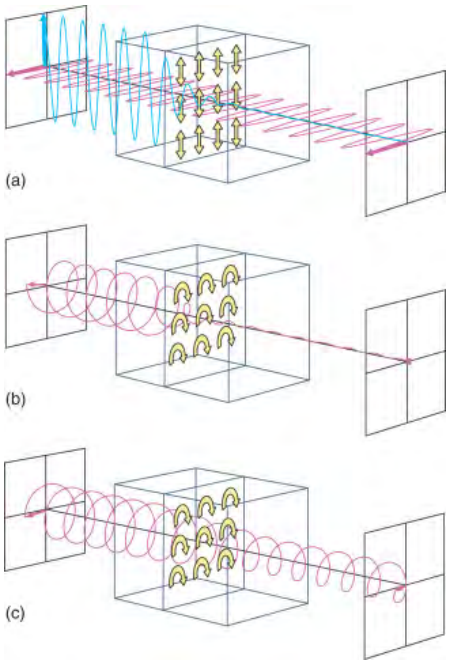

Figure 1.13: (a) Linear dichroism. (b) and (c) Circular dichroism [69]. This showcases that a material biased towards a particular polarisation will only allow that polarisation to be transmitted and absorbs light with all other polarisations. Credit: Schattschneider et al. [73].

where $A_{\parallel}$ is the absorption of linearly polarised light in a parallel direction and $A_{\perp}$ is the absorption of linearly polarised light in a perpendicular direction. Materials that exhibit circular dichroism (CD) also exist, being composed of chiral molecules. The chirality of an object is the property that its mirror images cannot be superimposed on each other, handedness being a prime example[14]. Materials with CD absorb one circular polarisation mode more than the other mode, with the degree of CD being:

$$CD = |A_l - A_r| \tag{1.65}$$

where A_l is the absorption of left-handed polarised light and A_r being the absorption of right-handed polarised light. The two types of dichroisms (LD, CD) can be seen in Figure 1.13

Birefringence

Birefringence is the property of a material having a refractive index that changes with the polarisation and propagation directions of light. Light propagating through a birefringent material will be decomposed into its two linearly polarised orthogonal components, one parallel and one perpendicular to the optical axis [74]. Light propagating along the optic axis will experience the

[14]Left-handed and right-handed being used to describe the orientation of chiral objects

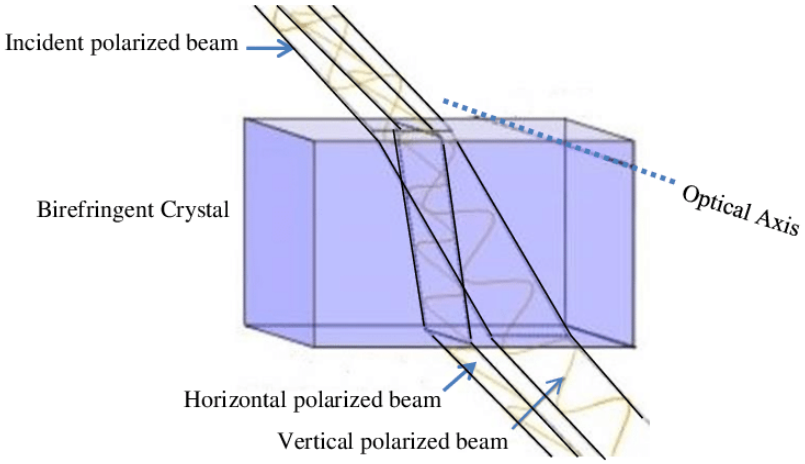

Figure 1.14: Birefringent material showing refractive indices dependent on the polarisation of the incident light. Credit: Sherif Hindi [79].

ordinary refractive index (n_o) which is polarisation independent. In contrast, light propagating perpendicularly to the optical axis will experience a refractive index that is dependent on its polarisation, called the extraordinary refractive index (n_e) (see Figure 1.14). Birefringence, like dichroism, is caused by the anisotropy of the molecular arrangement and molecular shape in a material. This causes light that is polarised parallel and light that is polarised perpendicularly to the optical axis to travel through the material with different velocities, as caused by different absorption and re-emission of light [75]. The refractive index is related to the speed of light through a medium by:

$$n = \frac{c}{v} \tag{1.66}$$

where n is the refractive index and v is the speed of light in that medium. This is the cause of the different refractive indices for birefringent materials. Birefringent materials include certain uniaxial crystals, such as borate [76] and liquid crystals [77].

The end result is a phase shift between the two components. In materials where the phase shift is exactly 90°, incident linearly polarised light will be outputted as circularly polarised light. These are known as quarter-wave plates and are used to convert linear polarisation to circular polarisation and vice versa [78].

Reflection

Light can also be polarised via reflection. Reflection of light occurs when light is incident upon a smooth surface with a different refractive index and bounces off at the same angle. Reflection is caused by the motion of electrons in the medium as a result of the absorption of incident light. The oscillations of the electrons can emit an EM wave in any direction except for the direction of its oscillation. Thus, the reflected beam of light will depend on the motion of the dipoles in the material from the incident beam. As the reflected angle and the incident angle must be the same, there is an angle where only polarisations that are normal to the incident plane

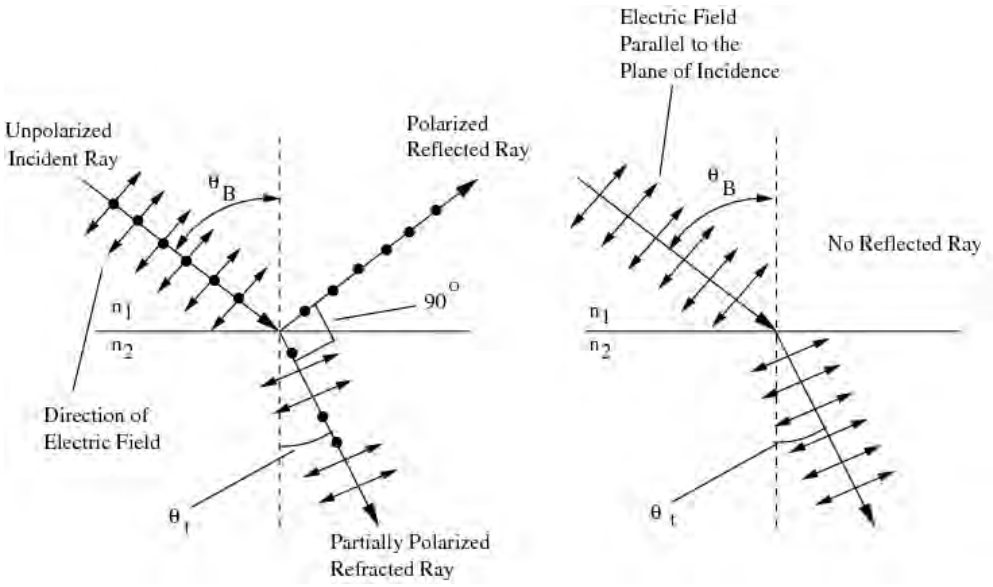

Figure 1.15: Reflection at Brewster's angle causing the reflected ray from a unpolarised beam to be polarised. Additionally a beam polarised parallel to the incident surface will not be reflected [82].

or parallel to the surface can be reflected, with the reflected ray being completely horizontally polarised, or polarised parallel to the surface [80]. This angle is known as Brewster's angle, with the condition that the reflected and transmitted rays are perpendicular [81] (see Figure 1.15). Brewster's angle θ_B is defined to be:

$$\theta_B = \arctan \frac{n_2}{n_1} \tag{1.67}$$

where n_1 and n_2 are the refractive indices of the two media. Reflections at any other angle will result in partially polarised light.

1.6 Polarisation Detection

Visible spectrum

Current methods for detecting polarisation for visible light involve the use of adjustable polarising films [83], polarisation diffraction gratings [84], birefringent materials [85], among others.

The basic principle is to use a polarising filter on polarised light. A polarising filter only allows light with polarisation parallel to the filter through, whilst blocking light polarised perpendicularly. For unpolarised light, it cuts the intensity by half:

$$I = \frac{1}{2} I_0 \tag{1.68}$$

where I_0 is the initial intensity and I is the intensity of the transmitted beam. When a beam of polarised light hits the filter, the amount of light that passes through it is determined by the angle between the filter and the polarisation of the EM wave, known as Malus's law [86]:

$$I = I_0 \cos^2 \theta \tag{1.69}$$

where θ is the angle subtended by the E-vector of the EM wave and the polarising filter. From Malus's law we can clearly see that when $\theta = 0^\circ$ i.e. the polarisation is parallel to the filter, the amount of light let through is at its maximum. When $\theta = 90^\circ$, i.e., the polarisation is perpendicular to the filter, no light is let through. Thus, the polarisation of light can be determined by measuring the intensity of polarised light passed through a polarising filter, whilst rotating the filter and noting orientation of the filter for the maximum intensity passed through. That orientation is also the polarisation of the beam. Circular polarisation can be measured using circular polarising filters or converting the circular polarisation into linear by passing it through a quarter-wave plate. This can convert circular polarisations to linear polarisations and then the same principle of measuring linear polarisations can apply.

X-rays and γ-rays

Such methods, unfortunately, do not work for high-energy photons such as X-rays and γ rays. Recent developments have made it possible to detect the polarisation of high-energy photons using the photoelectric effect, where the photoelectron is emitted preferentially in the direction of the E-vector (polarisation vector) of the incident X-ray [87, 88]. One such example is the time project chamber polarimeter (TPC) [89] along with the photoelectric effect. The main idea behind this instrument is to create photoelectrons in a gas chamber with polarised X-rays. The electrons are preferentially emitted in the direction of the E-vector of the X-ray with a $\sin^2\theta\cos^2\phi$ distribution, where θ is the angle that the photoelectron makes with the direction of the X-ray propagation and ϕ is the azimuthal angle with respect to the polarisation of the X-ray. A drift electric field is made with a drift electrode and a gas electron multiplier (GEM), which contains strips of electrodes. As the photoelectrons ionise the gas along its trajectory, the ionised electrons then drift with a constant velocity to the GEM, where their charge is multiplied and collected on the strips (Figure 1.16). The ionised electron path can be reconstructed and the polarisation of the original X-ray can be calculated. However, there are sensitivity problems related to the reconstruction of photoelectron paths[90]. Another constraint is that this technique relies on the photoelectric effect to function. The photoelectric effect is most effective at energies below approximately 100 keV.

For higher energy photons, approximately 100 keV - 10 MeV, Compton scattering can be used [91]. The Compton cross section for polarised incident photons follows the Klein-Nishima formula:

$$\frac{d\sigma}{d\Omega} = \frac{1}{2} r_e^2 \left(\frac{E'}{E}\right)^2 \left[\frac{E}{E'} + \frac{E'}{E} - 2\sin^2\theta\cos^2\phi\right] \tag{1.70}$$

where E' represents the energy of the scattered photon and E represents the energy of the incident photon. The radius, $r_e = 2.818 \times 10^{-15}$ m is once again the classical electron radius. θ is the polar scattering angle and ϕ is the azimuthal scattering angle with respect to the polarisation of the incident photon (see Figure 1.17).The polarisation dependence is shown in the last term

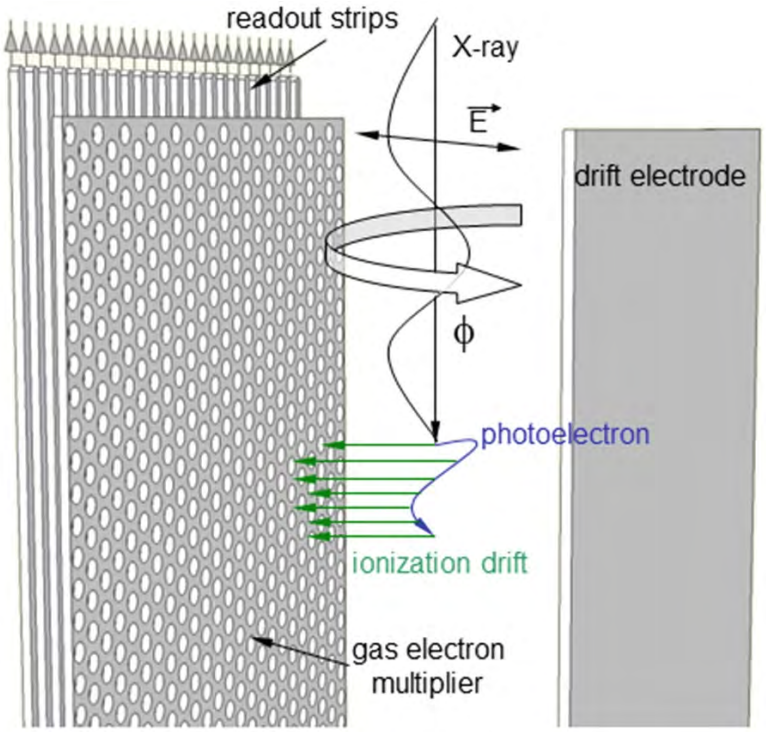

Figure 1.16: Time Project Chamber Polarimeter [89]

with $\cos^2\phi = \frac{1}{2}(\cos 2\phi + 1)$. This has a period of π, which indicates that the scattering has an π angular symmetry. This is expected as the scattering at $\phi = 0°$ and $\phi = 180°$ is both in line with the polarisation vector. This polarisation sensitivity is strongest when $\sin\theta = 1$ or when $\theta = \pi/2$, that is, when the photon is scattered perpendicularly compared to the incidence. Therefore, it is ideal to place detectors that are perpendicular to the scattering event.

As this cross section is also dependent on the energies of the incident and scattered photons, there is a range of energies where this is most effective (see Figure 1.18). We can see that the effect of the change in azimuthal angle is most apparent (comparing 0° to 90°) when the energies are between 100 keV and approximately 1 MeV, which is the energy range in which detectors that use this technique are most effective.

At even higher energies, i.e. in the MeV and GeV ranges, where we start to go into the hard γ-ray wavelengths, another approach must be taken. There are no current detectors that have the capacity of detecting such high energy polarisation [94]. There is a proposed method which makes use of the E-vector dependence of pair production, where the directions of the created and emitted electron and positron are sensitive to the polarisation of the photon. They have their ejected plane tending to be parallel to the E-vector of the incident photon [95]. The cross section of polarised pair production is dependent on the polar and azimuthal angles of the electron: θ_- and ϕ_- and of the positron: θ_+ and ϕ_+ (see Figure 1.19). It also depends on the ratio of energy of the produced positron E_+ compared to that of the incident photon

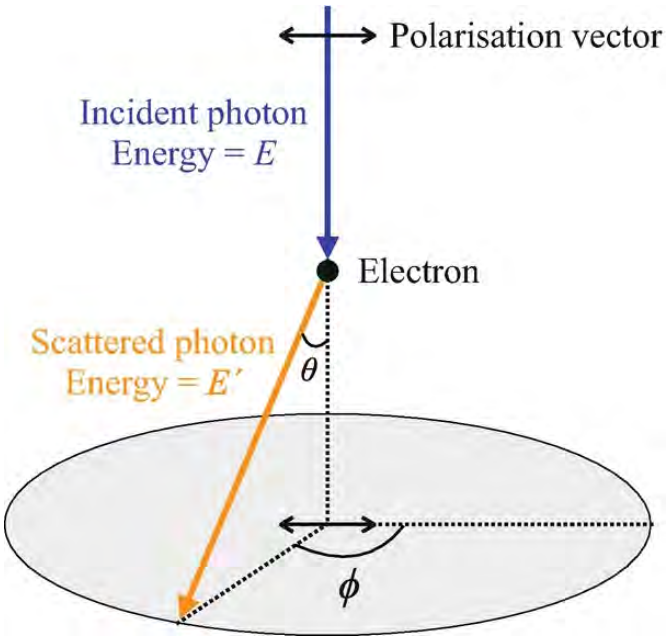

Figure 1.17: Schematic of Compton scattering of polarised photons according to the Klein-Nishima equation [92]. θ represents the polar scattering angle and ϕ is the azimuthal angle relative to the polarisation of the incident photon.

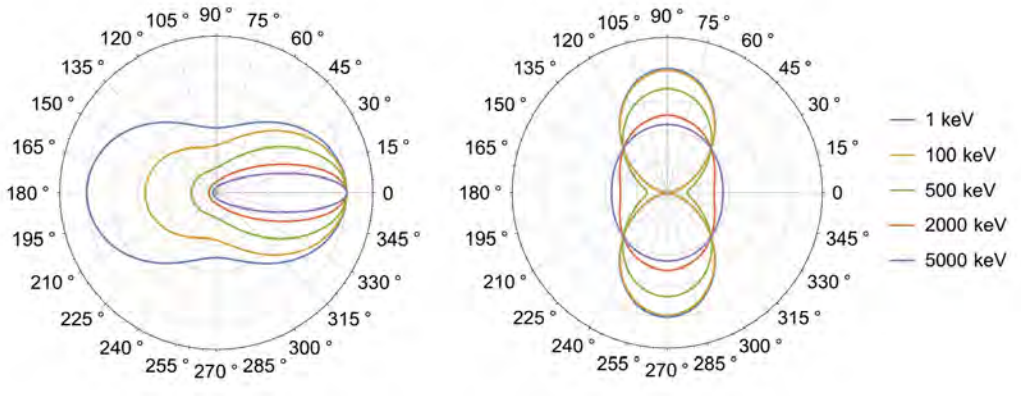

Figure 1.18: Compton scattering at various energies for polar scattering angle θ (left) and azimuthal angle relative to the polarisation (right)[93]

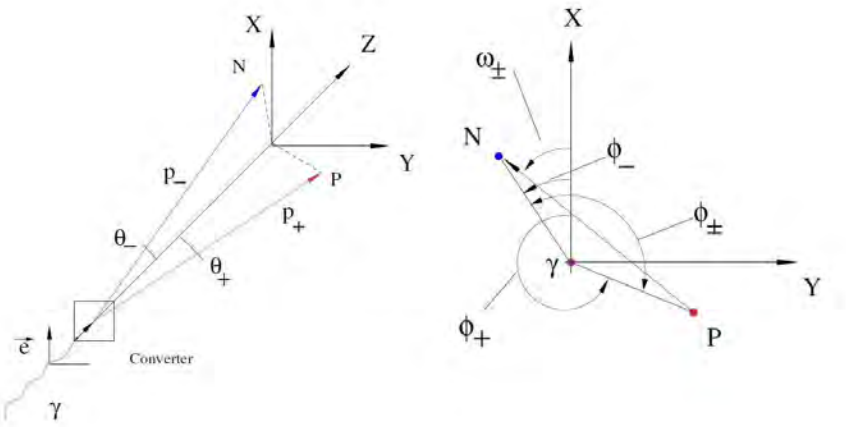

Figure 1.19: Schematic of the pair production mechanism from a polarised photon with E-vector $\vec{e}$, parallel to the X axis. The photon is incident along the Z axis. ϕ_+ and ϕ_- are the angles between the photon polarisation plane and the directions of the positron and electron respectively. $\phi_\pm$ is the co-planarity angle and is the angle subtended by the directions of the positron and the electron. $\omega_\pm$ is the azimuthal angle between the polarisation plane and the vector formed by the positron and the electron. [97]

(E_γ). E_+/E_γ [15]. The creation of an electron and positron pair from a polarised photon is asymmetrical in their azimuthal angle ϕ with:

$$\frac{dN}{d\phi_\pm} \propto (1 + A.P\cos 2(\phi_+ + \delta)) \tag{1.71}$$

where δ is the angle of the photon polarisation relative to the detector, P is the degree of polarisation ($0 \leq P \leq 1$) and A is the polarisation asymmetry and is a function of the photon energy with [96]:

$$A = \left[\frac{4}{9}\ln(2E_\gamma) - \frac{20}{27}\right] / \left[\frac{28}{9}\ln(2E_\gamma) - \frac{218}{27}\right] \tag{1.72}$$

For energies greater than approximately 20 MeV, this asymmetry follows Equation 1.72 [93].

Figure 1.20 shows the pair production γ-ray polarimetry distribution of the azimuthal angle $\phi_\pm$ with the HARPO time projection chamber with energy of 12 MeV [98]. We can see that there is a difference in scattered directions for fully polarised ($P = 100\%$) and unpolarised ($P = 0\%$) incident γ-rays. The largest differences occur at an azimuthal angle of $0, \pi/2$ and π radians, that is, when the positron and electrons are either on the same plane or are perpendicular to each other.

[15] By conservation of energy, this is also dependent on the electron energy

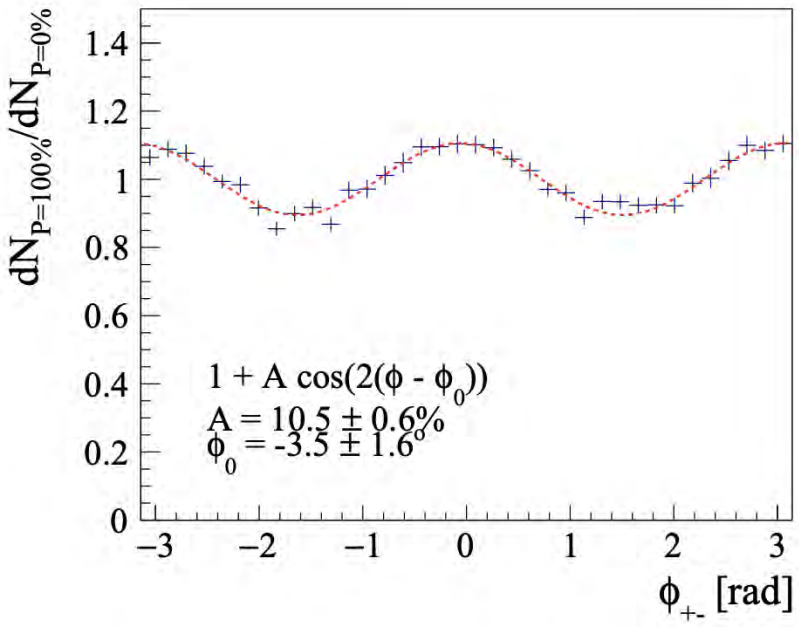

Figure 1.20: Pair-production γ ray polarimetry distribution of the azimuthal angle $\phi_{\pm}$ with the HARPO time-projection chambre with energy of 12 MeV [98]. It showcases the difference in ratio of 100% linearly polarised photons vs unpolarised photons.

1.7 Biological Detection of Polarisation

Using Polarisation

Linear polarisation of light has been shown to be used by animals such as the African dung beetle, *Scarabaeus zambesianus* & *Escarabaeus satyrus*, which uses the polarisation of moonlight to navigate at night [99–101]. When the dung beetle finds a source of food, i.e. dung, they roll the ball of dung away for safekeeping. The most efficient paths are straight radial ones directly outward. These are the paths taken by the dung beetle under a clear moonlit sky. However, when it was cloudy or when the moonlight was blocked, the dung beetle's paths were more sporadic and no longer straight and radially outward. Furthermore, when a polarisation filter was placed above the dung beetle such that it rotated the polarisation by 90°, so did the paths taken by the dung beetle (see Figure 1.21). More examples of using linear polarisation include species such as migrating monarch butterflies [102, 103], crickets [104, 105] and desert locusts [106], which have specialised areas of eyes called the dorsal rim area (DRA) which have adapted to use polarisation of the light from the Sun and the Moon as a compass [107].

There have also been instances of animals using circular polarisation in nature. The telson keel[16] of mantis shrimp reflect the two modes of circularly polarised light differently (see Figure 1.22). This potentially can be used as a unique channel of communication as other marine

[16] tail

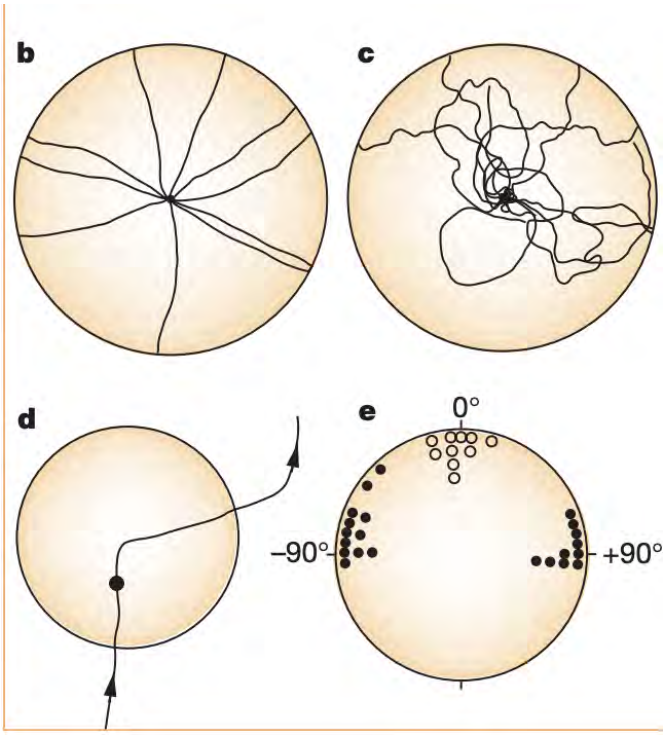

Figure 1.21: Paths taken by dung beetles; (b) under moonlight, (c) without moonlight, (d) under a 90 degree polarisation filter (e) average angle under the same filter. Credit: Marie Dacke [99].

species cannot detect polarisation.

The eyes of mantis shrimp contain specialised cells that act as quarter-wave plates (see Figure 1.23). These transform circularly polarised light into linearly polarised light by shifting the phases of the two orthogonal components of the electric field of light by 45°. Not only that, it also differentiates between left-handed polarisation and right-handed polarisation by converting them into horizontal and vertical modes of linear polarisation[17], after which the polarisation is detected normally.

Chromophores

Biological photoreceptors have molecules called chromophores, which allow absorption and thus detection of light[110]. In humans, the molecule responsible for this process is called the retinal[18] molecule [111]. Retinal contains a long chain of carbon carbon bonds, the most important to light detection being the double bond between the 11th and 12th carbons in the chain. Retinal

[17] The reversed modes of linear polarisation is also possible, depending on the setup of the quarter-wave plate
[18] Also known as retinaldehyde

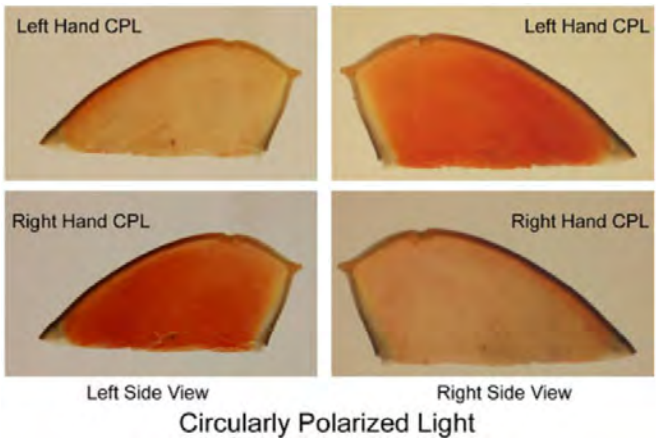

Figure 1.22: Chitin of Mantis Shrimp reflecting different circular polarisations. Credit: Cronin et al. [108].

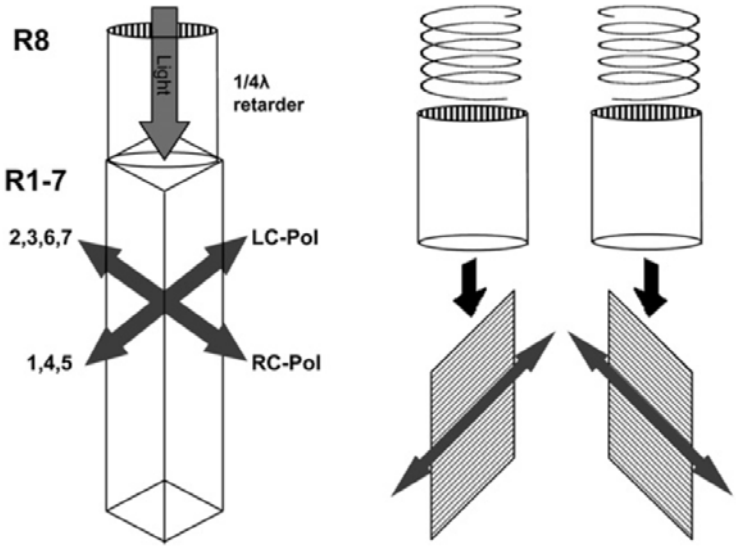

Figure 1.23: Specialised cell in stromatopods acting as a quarter wave plate [109]

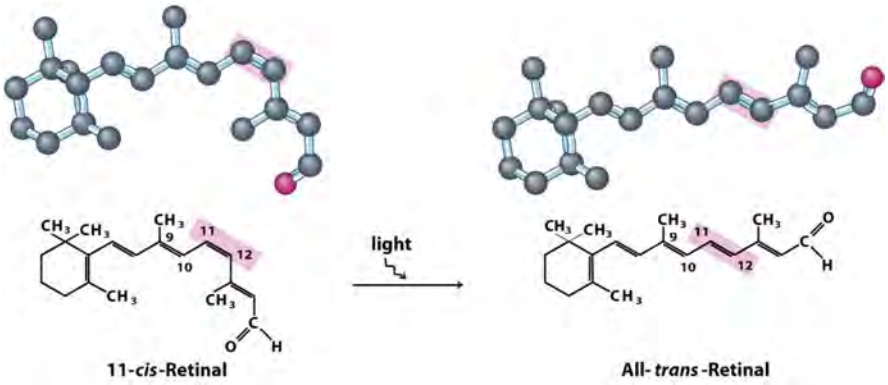

Figure 1.24: 11-*cis*-retinal absorption of a photon which causes a conformal change to the all-*trans*-retinal. Credit: Lehninger Principles of Biochemistry [113].

has diastereomer states[19] of 11-*cis*-retinal and the all-*trans*-retinal. Before an interaction with light at the appropriate wavelengths, the retinal molecule is in the 11-*cis*-retinal state. When an incident photon in the visible domain hits the molecule, it is absorbed by the double bond between the 11th and the 12th carbons in the chain. This energises a bonding pair of electrons, more specifically, the pi-bond. This causes the pi-bond to temporarily break, which results in there now being only a single sigma bond between the 11th and 12th carbons. This allows the molecule to rotate now around the single sigma bond, until it reaches the all-*trans*-retinal configuration, at which point the electrons relax and reform the pi-bond [112] (see Figure 1.24). This conformal change in the molecule causes an electric signal to be sent down the optic nerve to be processed by the brain, and thus this is how light is detected.

The retinal molecule is also bound to an opsin protein to form rhodopsin[114] in rods and iodopsins in cones[115], which are the basis of photoreceptors in humans (see Figure 1.25). Rhodopsin can absorb light with a wavelength of 500 nm, or in the blue-green part of the visible spectrum[117]. Iodospins are pigments found in cones that are responsible for their absorption of light, and contain chromophores[20]. They come in three varieties, called erythrolabe, chlorolabe, and cyanolabe. These different pigments have different peak absorption wavelengths. Erythrolabe has a peak wavelength of 565 nm, or red light, chlorolabe has a peak wavelength of 535 nm, or green light, and cyanolabe has a peak wavelength of 440 nm, or blue light[118] (see Figure 1.26). Our perception of colour is therefore based on the mixing of the signals of the rods and cones, and is the origin of human trichromatic[21] vision[119].

Photoreceptors and Polarisation

Now that we have established the mechanism of the photoabsorption process in photodetectors, how does polarisation sensitivity arise? The absorption process of light by a chromophore is inherently sensitive to polarisation. Light with its E-vector aligned with the carbon carbon

[19] chiral molecules
[20] Retinal in humans
[21] 3 coloured

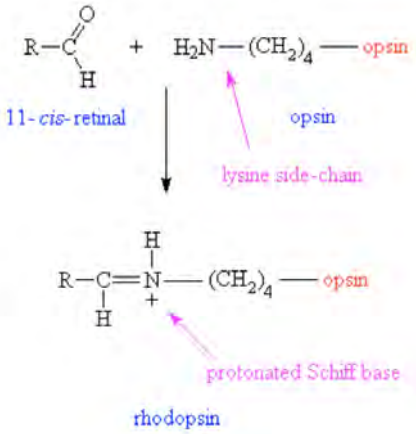

Figure 1.25: Retinal bound to opsin to form rhodopin. Credit: University of Pennsylvania [116]

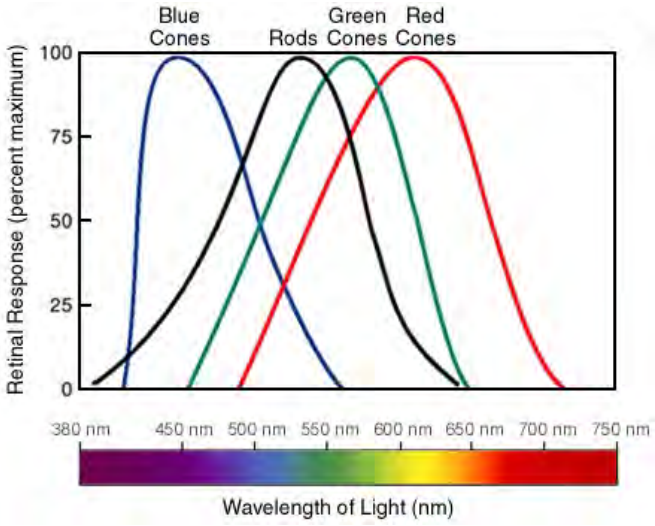

Figure 1.26: Peak wavelengths of rods and the three different types of cones. Credit: Al-Bahadly[120]

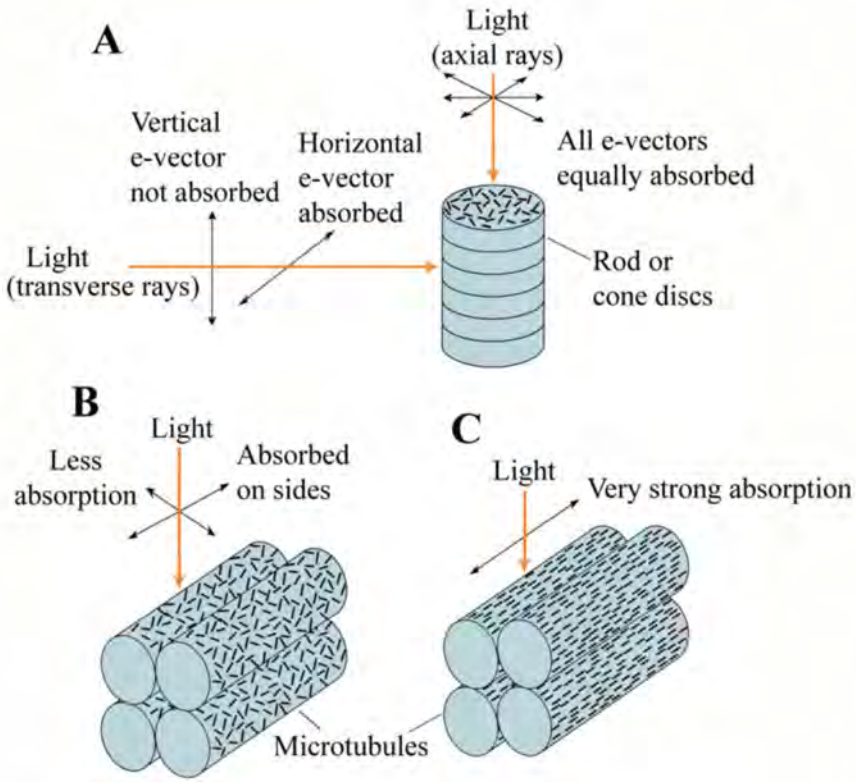

Figure 1.27: Sensitivity to polarised light in rhabdomeric and ciliary photoreceptors. Credit: Bradbury and Vehrencamp [124].

double bond of the chromophore is preferentially absorbed compared to light with its E-vector not aligned to the bond[121]. Thus, each individual chromophore is sensitive to the polarisation of light. However, if the chromophores are arranged randomly, like in the eyes of humans, then there is no overall sensitivity to polarisation, as all E-vectors are absorbed equally. However, when rhabdomeric and ciliary photoreceptor cells [122] form microvilli tubules or microtubules, a general preference for certain E-vectors can arise, when the microvilli are aligned[123]. Alignment of the photoreceptors and, by extension, of the chromophores means that there is a global sensitivity to polarisation. As each individual chromophore is sensitive to polarisation, having all chromophores aligned means that all light-absorbing double bonds of the chromophores are aligned and light with its E-vector parallel to the double bond will be absorbed and light that has its E-vector perpendicular will not be (see Figure 1.27).

Rayleigh Sky Model

Now that we know how polarisation sensitivity can arise in animals, how does it help them navigate? As visible light travels from the Sun through the Earth's atmosphere, it scatters

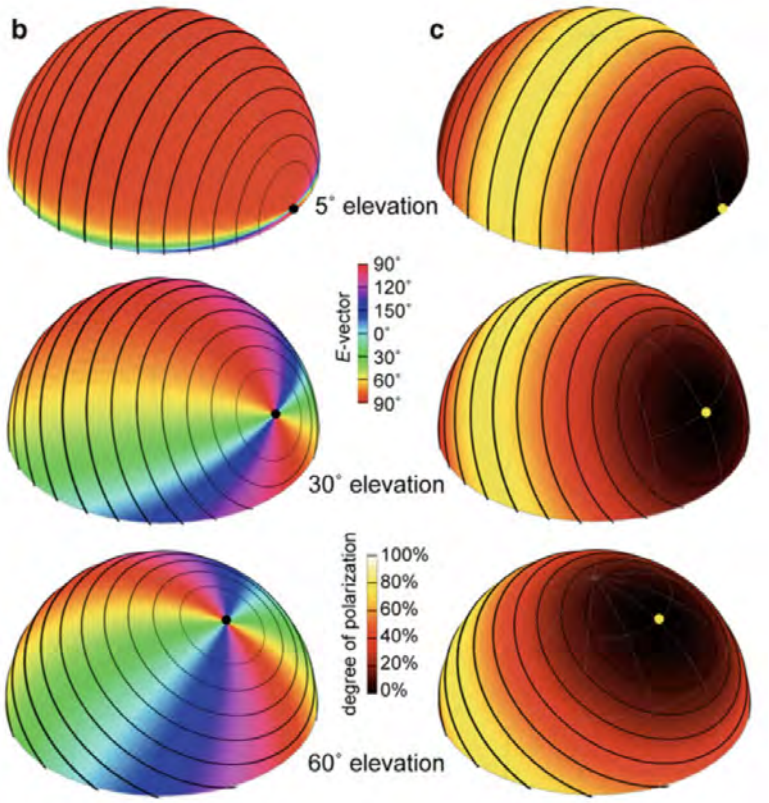

Figure 1.28: Rayleigh Sky Model of linearly polarised light from the Sun, showing the E-vector and the degree of polarisation at different locations on the planet at different positions of the Sun. Credit: Heinze [102].

elastically off atmospheric molecules. This process is called Rayleigh scattering, as previously mentioned. In addition, the direction of scatter can polarise the incident light, with the perpendicular scattering fully polarised and the parallel scattering remaining unpolarised [125] (see Figure 1.5). Therefore, when sunlight travelling parallel to the ground scatters perpendicularly off a particle so that it is now travelling down to the surface of the planet, it will be fully linearly polarised (horizontally polarised). In fact, the degree of polarisation and the E-vector of light that impacts the surface of the planet are determined by the location of the Sun and position of the observer on the planet. It also depends on the time of day and the time of year[126]. This is known as the Rayleigh sky model. Thus, measuring the polarisation of sunlight allows animals to track their current position on the planet (see Figure 1.28) and allows them to navigate around the globe.

1.8 Towards Higher Energy

As discussed in the previous sections, chromophores give photoreceptors their sensitivity to light and are individually inherently also sensitive to polarisation. However, the mechanism for light detection is through the use of photon absorption, the excitation of an electron from its ground state to an excited state[127]. This means that the potential energies of the absorbed photon are subject to the available energy levels of the bound electron. While there are chromophores that can absorb photons in the infra-red wavelengths[22][128–130], or the ultraviolet wavelengths[23][131, 132], the majority of chromophores absorb light in the visible wavelengths[24][133, 134]. Whilst this is beneficial from an evolutionary and biological point of view, it means that the use of chromophores to detect the polarisation of light is limited. If a high energy photon is absorbed by the organic compound, then the electron will be ionised instead of energised. This can cause irreversible damage to the molecule[135] and restrict their detection mechanism as the photon-absorbing bond is now damaged and cannot absorb another. Thus, to have the ability to detect the polarisation of high-energy photons such as X-rays and γ-rays, we must look towards other detection techniques.

One method is the use of semiconductors, especially organic-based semiconductors (OSCs). OSCs are polymers consisting of double-bonded carbon-carbon building blocks, i.e. with a sigma and a pi bond [136]. This is very similar to the double bonding of carbons in a chromophore; in fact, the absorption of a photon by the double bond is also preferential to photons whose E-vector is parallel to the bond and is thus inherently sensitive to polarisation. However, unlike in a chromophore, ionisation of the bonding electrons will not limit the molecule's ability to absorb more photons, as there are many identical carbon-carbon double bonds. Any of these is available to absorb another photon. Absorption of a high-energy photon ionises the bonding electron and creates a free radical (unpaired electron) and an electron hole. This electron hole can be filled by a bonding electron from a neighbouring carbon atom, reforming the bond. However, this now means that the neighbouring carbon has lost a bonding electron and it now has an electron hole. This "positively" changed electron hole propagates along the polymer and thus forms a current, which can then be detected (see Figure 1.29). Thus, an organic semiconductor can be used to detect the polarisation of high energy photons if the organic semiconductor is anisotropic[137]. Therefore, there is a potential application of using organic semiconductors as X-ray polarisation detectors, especially for soft X-rays [138]. However, because of the damaging nature of high energy photons to organic bonds, hard X-rays, and γ-rays in the MeV and GeV energies, OSCs will still be insufficient. This is especially true if the photon source has a high flux, ionising the carbon-carbon double bonds before they can regenerate or also breaking the sigma bond and this breaking apart the molecule. For such sources, a more robust method is required, one that does not rely on bonding electrons and has more electrons to spare. Thus, metallic detectors have great potential for the detection of high-energy photons.

[22] > 700 nm
[23] < 400 nm
[24] $400 - 700$ nm

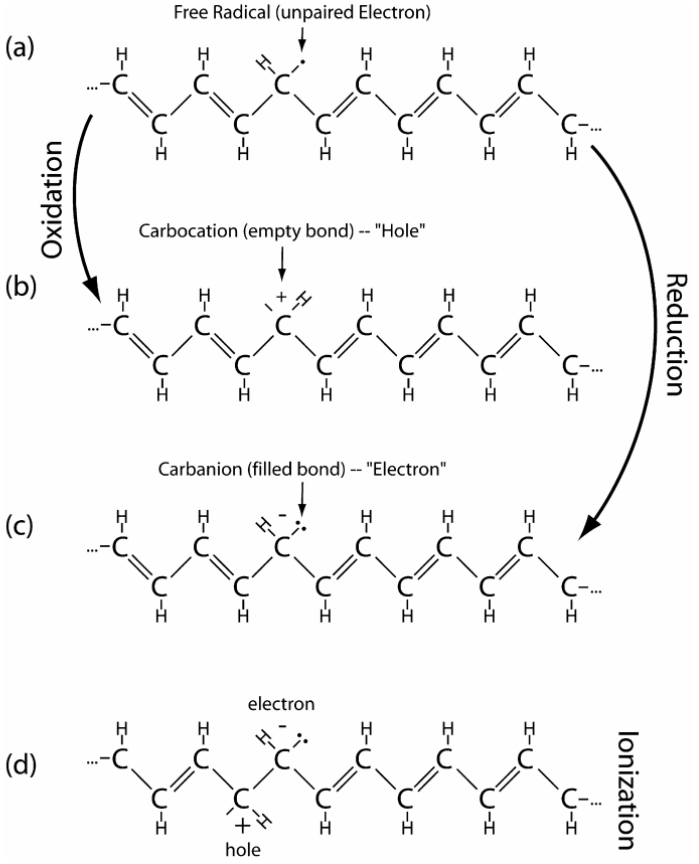

Figure 1.29: Incoming photons can hit the organic polymer and ionise the molecule. This can create electron free radicals or electron holes allowing it to now act as a semiconducting material [139].

1.9 Exploration into the Unknown

Polarisation is a fundamental property of visible light and all electromagnetic radiation, with applications spanning across many different fields of research, often interdisciplinary. It has implementations in biomedical and clinical imaging, to characterise complex tissue samples [140–143] and for diagnostics [144–146]. There are also potential therapeutic applications of using polarised light in tissue healing [147–150], immunomodulation [151] and photobiomodulation [152]. Outside the field of medicine, polarisation microscopy can reveal information very quickly about the orientations of molecules, including collagen fibres [153, 154], proteins, cellular structures [155] and liquid crystals [156]. Polarisation also has many everyday technological uses, such as improving the efficiency in liquid crystal displays (LCDs) [157, 158], increasing the contrast in photography in cameras but also in the retina [159] as well as the reduction of glare [160].

Recently, the importance of polarisation in the animal kingdom has increasingly come to

the fore. From navigation in arthropods [161–165] to communication in cephalopods and stromatopods [166], the latter being currently the only species that appears to use circular rather than linear polarisation. In addition, polarisation is also used in the identification of predators and prey and in the responses in certain species of fish [167, 168]. Furthermore, it is utilised for habitat selection of semiaquatic insects [169] as well as to facilitate shore flight responses in water fleas [170]. Polarisation is significant in the study of plant development, resulting in better growth rates of maize and white lupin under linearly polarised light [171, 172] and higher germination rates of Arabidopsis and lettuce under circularly polarised light [173].

At higher energies, polarised X-rays are at the heart of many X-ray imaging techniques such as magnetic X-ray diffraction [174], magnetic Compton scattering [175] and X-ray circular dichroism [176] which are used to study materials interacting with a magnetic field. Additionally, X-ray polarisation can also be used to study the magnetic sub-levels of charged particle collisions [177–179]. The polarisation of γ-rays is also relevant in astrophysics in order to understand the nature of astrophysical sources [180, 181], the origin of cosmic rays [182], the properties of black holes and their role in the evolution of galaxies [183–185] amongst many other uses. Furthermore, X-rays have many important modern uses such as radiography [186–188], radiotherapy [28, 189, 190], computed tomography (CT) scans [191, 192], X-ray diffraction [193, 194], small-angle X-ray scattering (SAXS), and wide-angle X-ray scattering (WAXS) [195–197]. Such techniques currently do not consider polarisation. However, polarisation could provide additional information on the properties of X-ray interactions with matter in terms of structural orientation of samples in 3-dimensions as well as provide information on the direction of scattered photons [198]. Therefore, introducing polarisation into such applications could be a potential avenue into their improvement and enhancement, allowing for a more comprehensive image.

Realisation of the effects and applications of polarised light requires its characterisation. This is normally done via the use polarisation detectors. Current detection methods of polarised electromagnetic waves spanning from infrared to visible to ultraviolet (UV) light generally include the use of polarisers or polarising filters. From Malus's law the transmitted intensity of polarised light through a linear polariser is:

$$I = I_0 \cos^2 \theta \tag{1.73}$$

where I is the transmitted intensity, I_0 is the intensity of incident polarised light, and θ is the angle between the direction of polarisation and the transmission axis of the polariser. In short, light with its polarisation parallel to the transmission axis is allowed through the polariser, and light with its polarisation perpendicular to the transmission axis is blocked. This can be used to characterise the polarisation of an unknown source by rotating the polariser until the measured intensity matches the incident intensity [199]. For circularly polarised light, the inclusion of a quarter waveplate, which converts circularly polarised light to linearly polarised light, allows the determination of left-handed or right-handed polarisation states. However, such methods can only determine the polarisation state indirectly by measuring the intensity of light transmitted through a polariser. This additional optical filter adds to the complexity, size and costs associated with such polarimetric photodetectors and can also cause a loss of sensitivity and responsiveness of the photodetector [200]. This calls for methods of direct detection of polarisation to mitigate such restrictions. Current research into alternatives include inorganic semiconductors [200, 201], carbon nanotubes [202, 203] and inorganic nanowires [204, 205].

In this project, we explored a novel method of the detection of polarisation using the biological mechanisms of animal sensitivity to polarisation. Polarisation sensitivity in some animals arises due to their photodetection mechanism, using chromophores. Chromophores are naturally dichroic, and polarisation sensitivity is due to the ordering of chromophore molecules [121, 123]. This mechanism can be exploited to possibly create a device that can directly detect the polarisation state of light, without the need to a separate filter, enhancing their sensitivity and resolution. Furthermore, the optical properties of chromophores have been well documented and studied, especially their peak wavelengths [128, 134, 206]. A polarimetric photodetector based on chromophores could potentially be extremely tunable to measure different wavelengths by switching out the base chromophore.

We were especially interested in sea urchins due to the calcite in their skeletons and tube feet [207, 208], where their photorecptors reside. Calcite interacts anisotropically with different polarisations of light [207] since calcite has high birefringent properties [209]. Coupled to the photoreceptors, this could potentially lead to both linear and circular polarisation sensitivity in sea urchins, which uses both the birefringent properties of calcite and polarisation sensitivity of aligned chromophores. Any polarisation detection could pave the way to the possible development of a novel polarimetric photodetector. This would utilise the same mechanism that these sea urchins use to detect polarisation, which would not only directly measure the polarisation state of light but would also help miniaturise the technology.

Additionally, despite the importance of polarisation, its detection at high energies are currently also very limited. Generally speaking, current X-ray and γ-ray polarimetry detection can be classified into two main techniques. The first relies on the dependence of polarisation on the direction of photoelectron emission [89]. This method is used by the IXPE (Imaging X-ray Polarimetry Explorer) [210, 211], which is currently the only X-ray polarisation detector in use. There are several proposals [212, 213] including the HypeX project which uses the same concept with improved resolution and effective X-ray energy range is currently in development [214].

The second method uses the anisotropy of Compton scattering [91, 215, 216]. Current γ-ray polarisation detection projects includes; Polar-2 [217], GAP [218], Astrosat-CZTI (Cadmium-Zinc-Telluride Imager) [219], COSI (Compton Spectrometer and Imager) [220] and INTEGRAL (INTErnational Gamma-Ray Astrophysics Laboratory) [221].

The photoelectron detection method has difficulties associated with the sensitivity of the instrument and the reconstruction of photoelectron tracks [90]. The Compton detection method requires detailed comparison to Monte Carlo simulations, in which the projected azimuthal scattering angle is highly dependent on the orientation of the instrument as well as on multiple scattering events. Thus, instruments which utilises one of these two techniques are generally quite large and have complex electronics to achieve the sensitivity required to accurately determine the polarisation of the incident photons. Furthermore, both the photoelectric effect and Compton scattering are effective at different energies [222, 223]. This means that the current and proposed detectors mentioned above are limited in ranges for incident photon energies; and that one detector that is effective in one energy range would not be in the other energy range. Additionally, there is no current instrument capable of high-energy γ-ray polarimetry (> 10 MeV). Methods such as those proposed by Wojtsekhowski et al. [224] which makes use of the E-vector dependence of pair production. In pair production, the directions of the created electron and positron are sensitive to the polarisation of the photon, their plane tending to be parallel to the polarisation vector of the incident photon [95]. However, multiple scattering of the produced particles need to be considered to accurately determine the photon polarisation

and this presents a tremendous challenge [93].

Any novel polarisation detection mechanisms could pave the way to the possible development of a novel polarimetric photodetector. In this project we explored such new ideas in biomimicry, using sea urchins and using anisotropic scattering of X-rays and aligned gold nanorods. We delved into the possibility of polarisation detection that would not only directly measure the polarisation state of light but would also help miniaturise the technology with greater ease of production in both costs and scale.

This could have long lasting applications in cosmology, astrophysics, medical science, and X-ray and γ-ray imaging.

1.10 Thesis Structure

This thesis consists of 6 chapters. This is currently the end of Chapter 1 where I summarised the theory leading up to the idea of needing a novel type of polarimetric photodetector, capable of quick, efficient, and cost effective direction detection of the polarisation of light. I started with a brief overview of the theory of light matter interactions, particularly how polarisation has a big impact on these fundamental interactions. I then delved into the current methods of polarisation detection, particularly for visible light and X-rays, and explored the limitations of current technology and their deficiencies that this work would cover, motivating the search for new ways of polarisation detection.

This leads up into Chapter 2 where potential polarisation of light by marine animals is explored, specifically in those of sea urchin larvae. We tested for their responses under different polarisation modes and found that they had different behavioural responses that depended on the polarisation of the incident light.

Chapter 3 follows this result, as we wonder if this polarisation sensitivity persists in sea urchins as they mature into adulthood. Sea urchins undergo a physical metamorphosis from the larvae stage to the adult stage, and persistent polarisation detection may give us hints on the types of photodetector structure they have, as well as any light altering components that they have. Furthermore, this allows for more precise future imaging such as with PET (positron emission tomography) scans and serial block SEM (scanning electron microscope) scans, as well as searches into the specific DNA sections that are responsible for polarisation sensitivity.

Chapter 4 diverges into polarisation of higher energy photons such as X-rays and γ-rays, motivated cosmic searches. In this chapter, we looked at the scattering between polarised X-rays and aligned gold nanorods. We noticed that the diffraction patterns were dependent on the angle subtended by the orientation of the gold nanorods and the polarisation vector of the X-rays. This new mechanism is potentially a novel method for determining the polarisation of any incident X-rays by reverse engineering.

Chapter 5 involves some preliminary experimental experience that I had at the synchrotron where I learnt vital skills to carry out my own synchrotron experiences. This involves sample preparation and loading as well as result analysis.

Finally, I conclude the whole work in Chapter 6.

Chapter 2

Sea Urchin Larvae under Light and Polarisation

The following work is an adaptation of a submitted manuscript titled: "Response of the Larvae of the Sea Urchin *Centrostephanus rodgersii* Under Light and Polarisation Conditions" by Ben Li, Matthew Clements, Paulina Selvakumaraswamy, Zhenxu Yang, Ken-Tye Yong, Maria Byrne and Céline Bœhm.

Author Contributions:

- Ben Li: Conceptualisation (main[1]), Methodology (main), Investigation (main), Data Analysis (main), Writing (original draft), Sea Urchin Rearing[2] (supporting[3]).
- Matthew Clements: Investigation (supporting), Writing (review), Sea Urchin Rearing (supporting).
- Paulina Selvakumaraswamy: Sea Urchin Rearing (supporting)
- Zhenxu Yang: Writing (review).
- Ken-Tye Yong: Supervision (supporting).
- Maria Byrne: Conceptualisation (supporting), Methodology (supporting), Writing (review and editing), Sea Urchin Rearing (main), Supervision (supporting).
- Céline Bœhm: Conceptualisation (supporting), Methodology (supporting), Writing (review and editing), Supervision (main).

This chapter outlines the work done on the response of the larvae of the sea urchin *Centrostephanus rodgersii* to light and polarisation. The conceptualisation for this project seemed to be, by coincidence, a random meeting between an astroparticle physicist and a marine biologist who were both interested in polarised light, albeit for different reasons. It culminated into an interesting idea; could the larvae of sea urchins see light and, more interestingly, could

[1] Involved in its entirety
[2] Spawning and housing of sea urchin larvae
[3] Partial involvement

they see polarisation. The following detail the process in which we set out to find the answers to those two questions. The larvae of *C. rodgersii* were subjected to different lighting regimes, namely; unpolarised halogen light, darkness, as well as polarised (linear, circular and elliptical) halogen light. The larvae exhibited positive phototaxis, that is, swimming toward the light source, when exposed to unpolarised, horizontally polarised, elliptically polarised and circularly polarised light. However, they did not respond to vertically polarised light with any sort of phototaxis. In fact, larval swimming behaviour after exposure to vertically polarised light was the same as keeping them in the dark, there was no overall bias in their swimming direction. These findings indicate that not only can the larvae of the sea urchin *C. rodgersii* have photoreceptors capable of detecting light in the visible spectrum but they may also possess the capacity to differentiate between horizontally and vertically polarised light, which could help them navigate. A mechanism for polarisation detection suggests the possibility of aligned photoreceptors in these larvae, commonly seen in insects such as locusts and butterflies. In addition, it was found that these sea urchin larvae respond to circularly polarised light with positive phototaxis. This result is notable because there are few documented cases of circular polarisation sensitivity in animals, the most known case being in stomatopod vision. As they did not appear to have a preference between the left and right handed polarisations, one would need to study their photoreceptor cells to determine the mechanism by which they can detect circular polarisation. The understanding behind the mechanism of their polarisation sensitivity could pave the way for the development of new polarisation detectors based on biological mechanisms.

2.1 Introduction

Sea urchins are ecologically important algal grazers and, in large numbers, can have detrimental effects on kelp forest ecosystems [225, 226]. Some sea urchin species develop ciliated appendages used for swimming and feeding. Swimming behaviour in response to environmental stimuli can affect larvae distribution and dispersion and thus the end location of adult sea urchins [227]. As such, it is important to understand the environmental factors that influence their behaviour during development.

One of such factors is visible light. In Ref.[228], the authors show that the larvae of *Hemicentrotus pulcherrimus* and *Temnopleurus reevesii* reversed their swimming direction under photoirradiation, indicating that light can influence their displacement and that they therefore possess photo-receptors. In fact, sea urchin larvae appear to have photoreceptor expressing cells as part of their digestive system [229]. Furthermore, opsin2 (a protein found in photoreceptors) was present in their arms [230]. Ref. [231] also found that the skeletons of sea urchin larvae are birefringent. Since other species with birefringent skeletons exhibit polarisation sensitivity, it seems natural to expect that sea urchin larvae may also be sensitive to polarisation, in addition to being sensitive to light.

Animal species use polarisation for a range of purposes. One of such is navigation. For example, the African dung beetle *Scarabaeus zambesianus* uses the polarisation of moonlight to roll a ball of dung in a straight line radially away from the source, to escape aggressive competition for food foraging inside the dung ball [99, 100]. Other insect species such as migrating monarch butterflies [102, 103], crickets [104, 105] and desert locusts [106] use a skylight compass [103, 106, 232, 233] to navigate under a variety of atmospheric conditions. Polarisation may also be used for communication purposes, such as in the case of stromatopods who may be using circularly polarised light to potentially seek out partners [108, 234, 235] or in the case of butterflies to seek out mating signals [236] or to enhance contrast and visibility through the polarisation angle of light reflected from shiny surfaces [237] or from water surfaces [238]. Underwater polarisation vision is also quite widespread in nature (see, e.g., cephlapods [168], anchovies [239], damselfishes [240] and rainbow trout [241]) and is often used for contrast enhancement or predator/prey responses.

Polarisation arises when sunlight passes through the atmosphere and scatters off air molecules. This phenomenon is called Rayleigh scattering. The intensity of the scattered light is proportional to $I \propto \lambda^{-4}\ (1 + \cos\theta^2)$, with λ the wavelength of the incident light and $\cos\theta$ the angle between the incident and scattered light[4]. The intensity of the scattered light is the strongest in the direction (and opposite direction) of the incident light, and the degree of horizontality and polarisation can be predicted. The same is true as light passes through the water and interacts with water molecules. In both cases, the polarisation pattern can be affected by Mie scattering[5]. Mie scattering occurs in the presence of cloudy atmospheric conditions or turbid waters [242–246]. However, Ref. [247] showed that, even under these conditions, the polarisation pattern can still be recognisable enough to be used as a navigational tool. Given the above and since the Mie cattering coefficient of the ions found in pure seawater is extremely small ($<<\mathrm{m}^{-1}$), Rayleigh scattering is more likely to influence sea larvae urchins than Mie scattering, if at all.

[4]Rayleigh scattering is only valid when the particle sizes are smaller than the wavelength of the incident light.

[5]Mie scattering differs from Rayleigh scattering in that it has a weaker dependence on the incident wavelength and its intensity is the strongest in the forward direction.

Just below the surface of the water, light is generally found to be horizontally polarised, with a relatively high degree of polarisation [248]. Scattering events underwater also tend to create more horizontally polarised light [249]. Internal reflections are also more horizontally polarised [250]. Although the prominence of horizontal and vertical components is expected to change with the depth of the water column due to changes in density and in turbid conditions, previous studies have shown that marine animals can use polarisation at depths up to 15 m [251] and could exist up to 200 m [252, 253]. Since sea urchin larvae reside in the plankton (unlike sea urchin adults who live on the ocean floor), they may be particularly sensitive to polarised light and one may be tempted to speculate that horizontally polarised light may generate a stronger behavioural response in sea urchin larvae when compared to vertically polarised light exposure.

We note, in addition, that some species may be sensitive to circular polarisation (CP) as well. For example, the aforementioned mantis shrimp and the larvae of fireflies *P. lucicrescens* and *P. versicolor* emit weak left and right circularly polarised bioluminescent light [254] while the light passing through the body of certain dinoflagellates is also circularly polarised [255]. Thus, one may ask whether sea urchin larvae are also sensitive (or respond to) circularly polarised light.

We addressed the question as to whether the larvae of the sea urchin *C. rodgersii* change the course of their swimming direction under both unpolarised and polarised light. A positive response, exhibited by swimming towards the light source (positive phototaxis), would indicate their sensitivity to these environmental factors, and could bring a wealth of information about the sea urchin larvae displacement. This might be useful for the detection of potential photoreceptors and the design of new biodetectors.

In Section 2.2, we present the species and our experimental setup and our results in Section. 2.3, along with the data analysis in Section. 2.4. The discussion can be found in Section. 2.5 and our conclusion is given in Section. 2.6.

2.2 Experimental setup

Our goal is to determine whether sea urchin larvae exhibit phototaxis. While it is known that, in their natural habitat, sea urchins exhibit Diel Vertical Migration (DVM) [256, 257], one still needs to demonstrate that such a motion is the result of their response to the sunlight rather than other factors (e.g. temperature, pressure). For this reason, we do not to test for vertical motion with our setup, i.e., we do not illuminate the sea urchin *Centrostephanus rodgersii* from above. Instead, we study whether they exhibit phototaxis behaviour when light is directed from the side of the water chamber.

The other reason to not shine the light from above is that this helps to test their sensitivity to the different polarisation modes. Indeed, when the light is shone from above, the larvae, which are free to rotate but not flip in the water column, can always orient themselves to perceive both linear polarisations modes in the same way. However, when the light is shone from the side, this orientation symmetry is broken, allowing us to test whether they exhibit a preference for a particular polarisation mode (see Figure 2.1). Thus for the purposes of testing for polarisation sensitivity, we need to ensure that the sea urchins perceive the two polarisaiton modes as different.

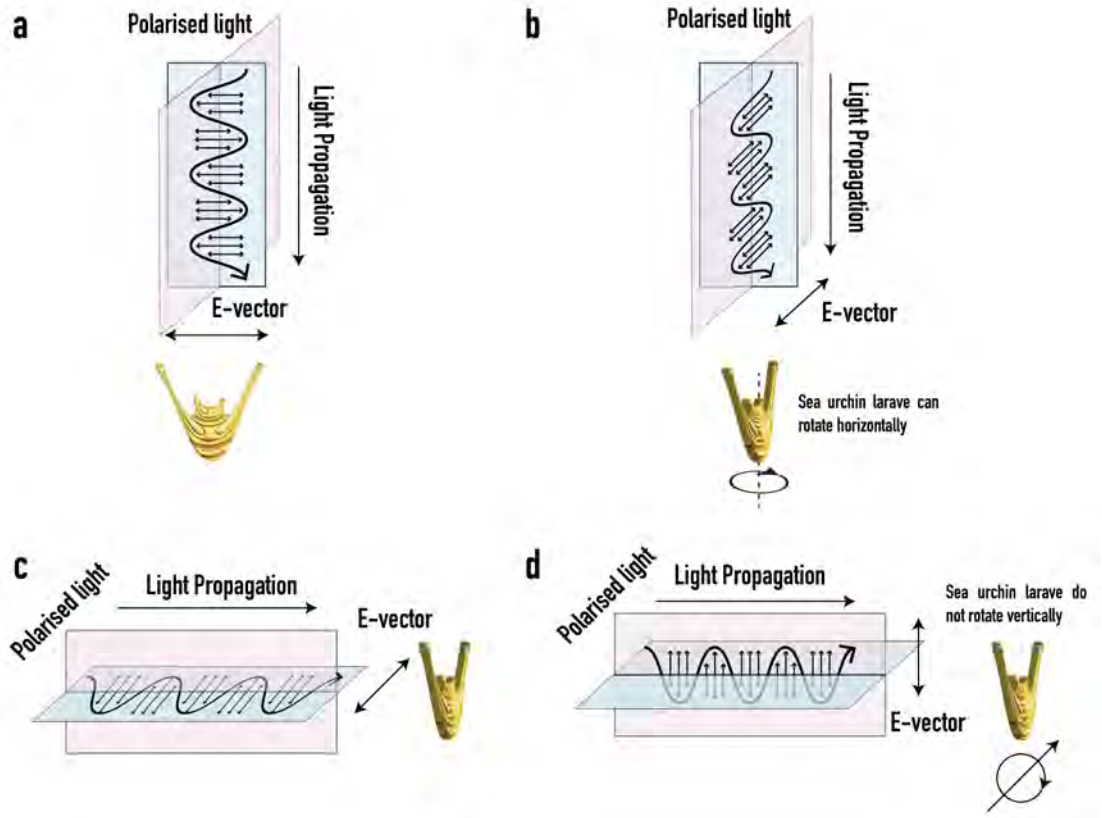

Figure 2.1: In images (a) & (b) we have sea urchins subjected to different polarisations of halogen light incident from above. As the sea urchins are free to rotate along the horizontal plane, they can see both polarisation modes as the same. In images (c) & (d) we have sea urchins subjected to different polarisation modes of halogen light incident from the side. The sea urchins are not free to rotate along the vertical plane (i.e flip), thus they cannot perceive the two polarisations as the same.

To determine whether *C. rodgersii* larvae are sensitive to skylight, we performed two sets of experiments: in the first set of experiments, the larvae were exposed to halogen light to mimic sunlight while in the second set of experiments, the larvae were kept in the dark. Their swimming response was recorded using a 12-megapixel Iphone 13 pro camera using the wide f/1.5 aperture. We note that the larvae were never directly exposed to sunlight during the experiments as there are various environmental factors associated to sunlight (such as flux, temperature, and angle of incidence) that could not be controlled to take meaningful measurements.

The spectrum of our halogen lamp ranges from 400 nm to 1000 nm with a wide peak from 480 nm to 750 nm, meaning that it contains visible light and some infrared components, while the sunlight spectrum ranges from 250 nm to 2500 nm. Hence, both the halogen and the sunlight spectra are similar in terms of shape and location of the peak in the visible spectrum. Even though the halogen lamp does not include as much as infrared light as the solar radiation, we

do not expect this to be a problem as sea-urchins are not expected to be sensitive to those wavelengths [258]. Also, whilst ultra-violet light exists in the sunlight spectrum and is mostly absent in the halogen spectrum, it only makes up about 9% of the total energy from the sun. Hence its absence from the halogen lamp spectrum should not impact the larval swimming pattern. We also note that IR, UVB, and UVC lights are absorbed at a greater rate underwater than the visible spectrum, so their influence on larval behaviour should be negligible. However, there would normally be UVA light present in the natural habitat of sea urchins. Nonetheless, the proportion of UVA light compared to visible light is very low [259]. We can therefore safely use the halogen light to simulate the light that sea urchin larvae would normally be exposed to in their natural habitat.

A subsequent set of experiments were carried out to study the sensitivity of C. rodgersii to polarised light. The following experiments were done with polarised sunlight in mind, as that is the type of light that sea urchins would be most exposed to, but it is worth noting that moonlight creates the exact same polarisation pattern as sunlight, although it is up to 1 million times dimmer [249, 260]. In these new sets of experiments, the sea urchin larvae were in turn be exposed to vertically and horizontally polarised halogen light as well as elliptically and circularly polarised halogen light. Their swimming response was recorded using the same camera as described before.

Species

C. rodgersii (test diameter 6 - 12 cm) were collected (1 - 2 m depth) from Camp Cove, Sydney in July 2022 when the sea temperature was 17°C. They were maintained in aquaria at 17–18°C. The urchins were used for spawning within 4 days of collection. Spawning was induced by injection of 1 mL of 0.5 M KCl through the peristome. Three fertilizations were done each obtaining gametes from two to three males and females, were used to generate embryo populations. Sperm was collected dry directly from the gonopores using a glass pipette, pooled in equal portions from each male and stored at 4°C until use ($<$ 30 min). Egg quality was checked microscopically to select the best egg sources. Sperm from individuals were checked and quality assessed for motility. Eggs from selected females were pooled in 500 - 1000 mL beakers of filtered (1 μm) seawater (FSW, Millipore) at 18°C. The eggs were fertilised (104 sperm per mL) and microscopic examination after 10 min revealed $>$ 90% fertilization as indicated by the presence of the fertilization envelope. The eggs were then rinsed to remove excess sperm and the FSW renewed. The density of the embryos was determined from an average of five counts of 10 μL aliquots using Sedgwick Rafter Counting Chamber and placed in 5 L beakers at 10 to 20 embryos mL^{-1}. After hatching the larvae were reared in 5 L beakers at a density of 10 mL^{-1}. The cultures were gently bubbled to keep the larvae in suspension and the water was changed by reverse aspiration every $2-3$ days. After the water was changed, the larvae were fed *Proteomonas sulcata* (20,000 cells per mL^{-1}).

A sample of 250 mL of the larval culture (4-20 larvae per mL) was taken from the culture and 250 mL of 1 μL FSW was added. The larvae used for testing in the different lighting regimes were between the ages of 3-6 weeks after spawning (see Figure 2.2). The larvae were then placed in the observation chambers. These chambers were made using a high purity borosilicate glass to reduce light scattering as as well increased durability. The chambers were shaped as a square prism with dimensions of 5 cm $\times$5 cm$\times$30 cm (see Figure 2.3).

Figure 2.2: Image of a larvae of the sea urchin species *C. rodgersii*. Note their ciliated appendages (arms) which are used for feeding and swimming.

Setup

The chambers with the larvae were placed on a table in a dark room and in front of a halogen light source whose distance to the chamber could be adjusted. The larvae were exposed to different light conditions from various directions and their overall swimming behaviour within the water chamber in the camera's FOV was recorded at 0 min, 5 min, 10 min, 20 min, 30 min, 45 min and 60 min of light exposure. The halogen light conditions included:

- Unpolarised light. The halogen lamp was aligned with the center of the water column, at an arbitrary distance of 85 cm. The lamp was then moved horizontally so that the light could shine incident either from the left or right sides of the water chamber in separate runs. This allowed us to test if the response was dependent on the physical direction of the incident light[6]. The flux (which was measured with a light meter) was approximately 1750 lux at the center of the water column.
- Darkness – the halogen light was switched off.
- Horizontally and vertically polarised light. The halogen lamp was again aligned with the center of the water column at a distance of 85 cm. A Hoya 77 mm linear polarising filter was placed in front of the halogen lamp in the vertical and horizontal orientations to reproduce the two polarisation modes. The larval swimming response recorded accordingly.

[6]The orientation of the water chambers stay the same.

The flux of photons at the centre of the water column and with the linear polarising filter in place was approximately 400 lux. We note that Hoya claims that their polarising filters have a $40\% - 29\%$ transmission rate whereas we measured a transmission rate of 23%. However the difference may be accounted for via the reduced reflections of the walls of the experimental room with the polarising filter in place. The filter is rated to have a polarising efficiency of $> 99.9\%$. Whilst there may be some scattering off various objects and and off the walls of the room that may change the polarisation of the incident light onto the larvae, the flux would be much smaller comparatively to the flux of the direct incident light with the desired polarisation. Thus the effects of random scattering events should be negligible and we can expect a high degree of polarisation.

– Elliptical polarised light. The halogen lamp was moved to a point 125 cm away from center of the water column to create a $\approx 45^{\circ}$ above the horizontal. The polarising filter was once again used in the 'horizontal' and 'vertical' orientations. The photon flux in this configuration was approximately 290 lux since the source is further away.

– Circularly polarised light. To test the effects of circular polarisation, a circular polariser (CP42HE and CP42HER from Edmund Optics with diameter of 50mm) was placed in front of the halogen lamp, which was aligned with the center of the water column at a distance of 85 cm. The efficiency of these polarisers is supposed to be greater than 99.9% so there should not be a large component of linearly polarised or unpolarised light going through. The effects of both left handed and right handed polarisations on the larval swimming responses were tested. The flux of photons at the centre of the column in this configuration was approximately 600 lux. Whilst random scattering events may effect the polarisation of the incident light, we expect it to be negligible. Edmund optics claim a transmission rate of 42% for wavelengths of 400 nm-700 nm whereas we measured a transmission rate of 34% but this could also be due to the reduced reflections from the walls of the room.

The experiment with each light regime was repeated 3 times. We observed that the response of the larvae was evident after 10 minutes of exposure and less apparent at 60 minutes as the larvae tend to sink to the bottom after long exposure times. Hence further images were taken at the 10 minute mark only.

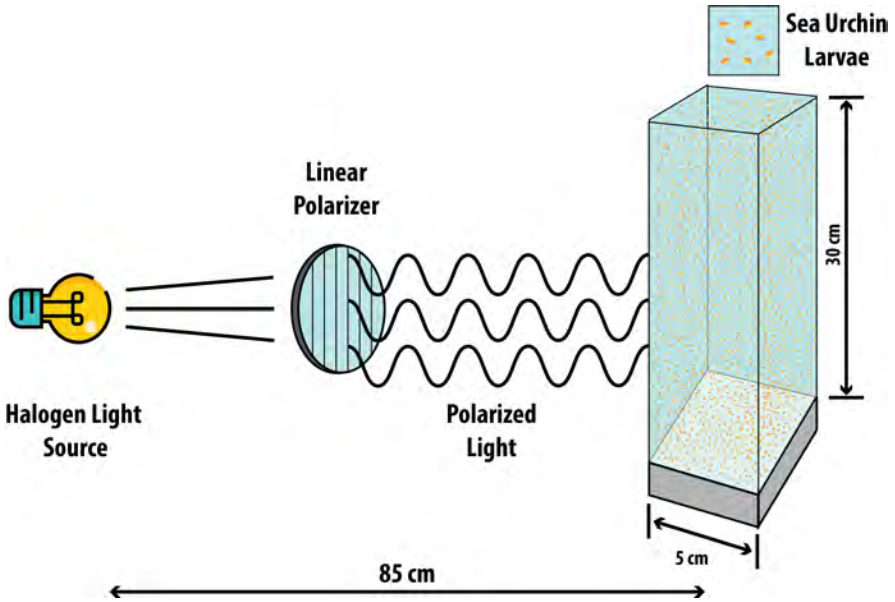

Figure 2.3: Schematic of the setup. In this configuration the halogen light source was level with the midpoint of the water chamber and a linear polarising filter was placed in front of the halogen lamp. This same setup was also used for left and right circular polarisations, using circular polarisers. For elliptical polarisation, the halogen lamp was moved further away and vertically upwards so that it made a $\approx 45^{\circ}$ to the horizontal plane and the linear polariser was placed in front of the lamp.

2.3 Results

The time progression of the larvae response to different lighting regimes: (a) no light or darkness, (b) unpolarised halogen light, (c) horizontally polarised halogen light and (d) vertically polarised halogen light can be seen in Figure 2.4. We can see by the 10 min mark (see Figure 2.5), the movements (or lack thereof) of the larvae are already very apparent. Under both unpolarised and horizontally polarised halogen light, there was positive phototaxis[7] exhibited by the larvae. For darkness and vertically polarised halogen light, there was no overall trend in the movements of the larvae.

[7]Swimming towards the light source.

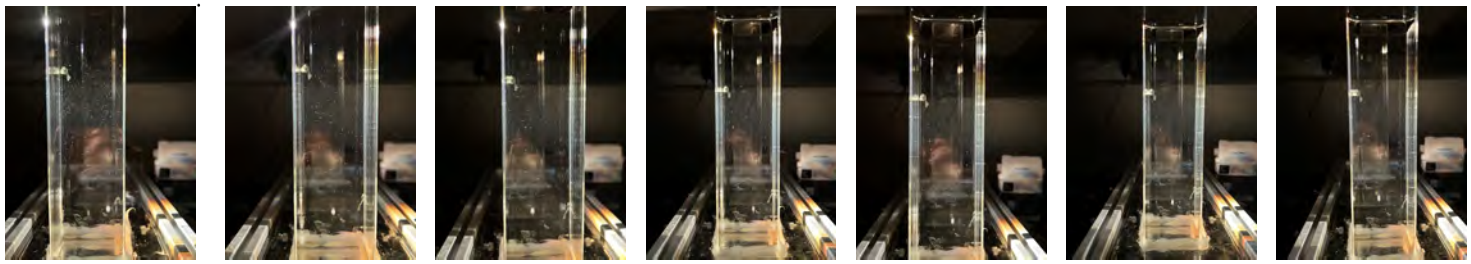

(a) Larvae response to no light at (left to right) 0 min, 5 min, 10 min, 20 min, 30 min, 45 min and 60 min.

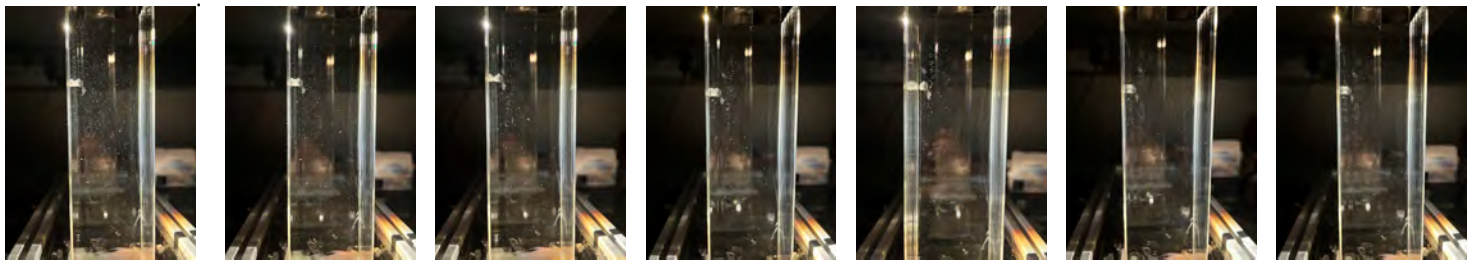

(b) Larvae response to unpolarised light at (left to right) 0 min, 5 min, 10 min, 20 min, 30 min, 45 min and 60 min.

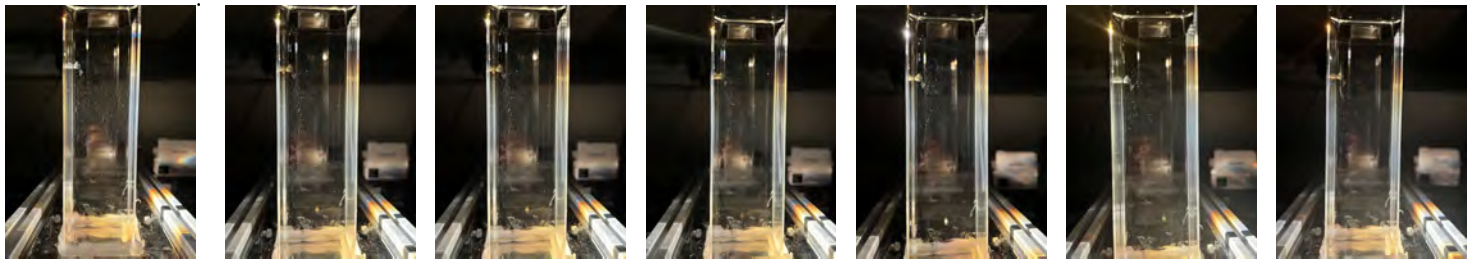

(c) Larvae response to horizontally polarised light at (left to right) 0 min, 5 min, 10 min, 20 min, 30 min, 45 min and 60 min.

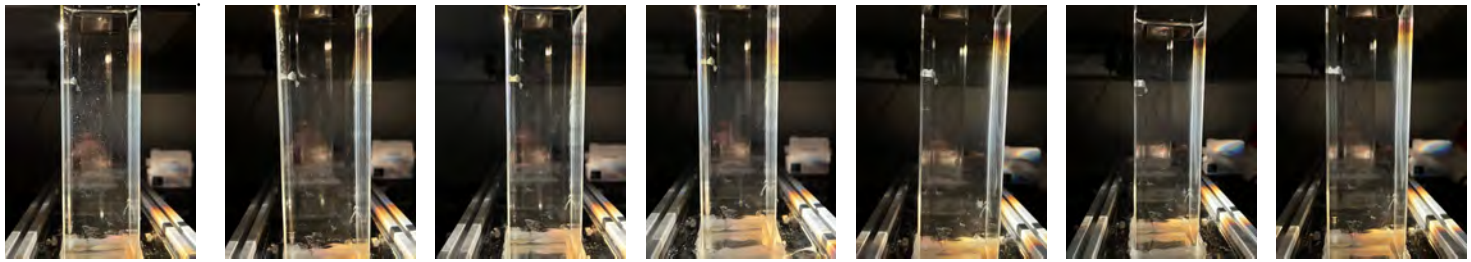

(d) Larvae response to vertically polarised light at (left to right) 0 min, 5 min, 10 min, 20 min, 30 min, 45 min and 60 min.

Figure 2.4: Sea urchin larvae response to different lighting regimes; (a) dark, (b) unpolarised, (c) horizontally polarised, (d) vertically polarised at 0 min, 5 min, 10 min, 20 min, 30 min, 45 min and 60 min. By the 10 minute mark, it was visible of the larvae reacted to the light or not.

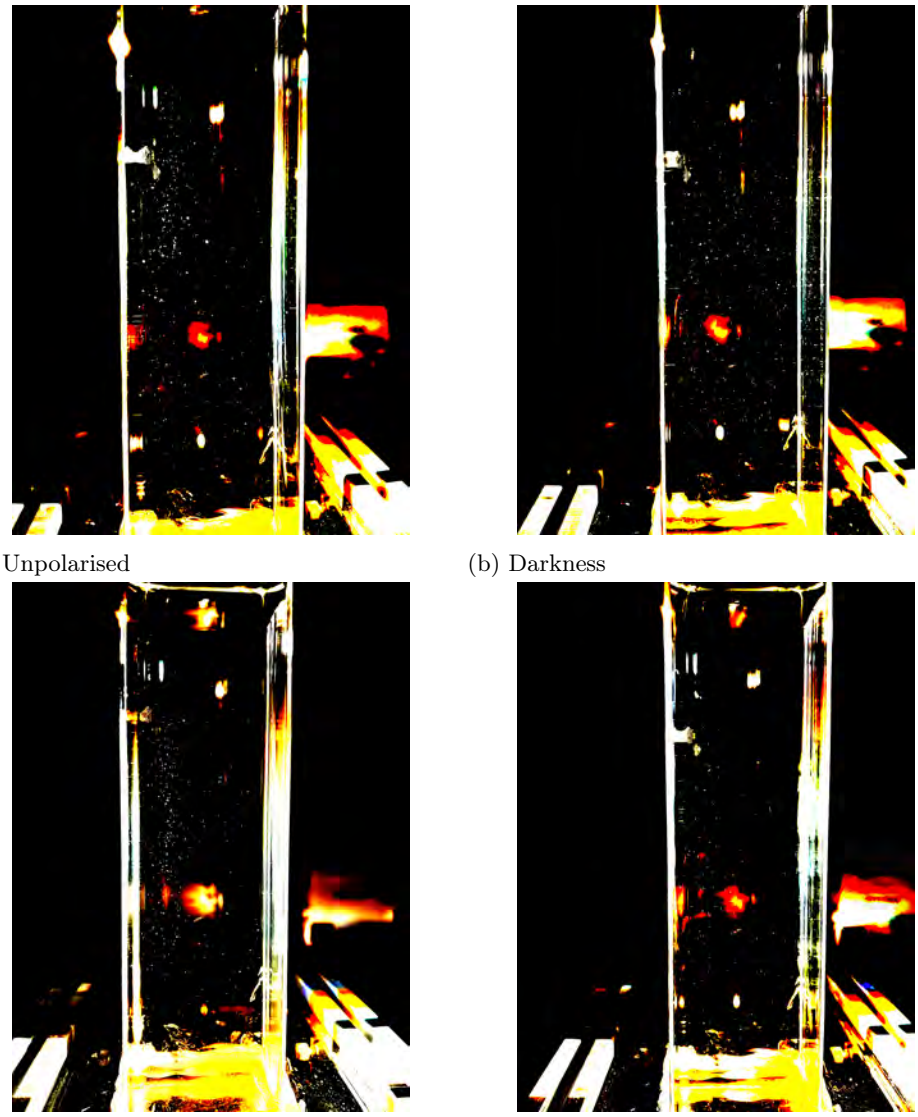

(a) Unpolarised (b) Darkness

(c) Horizontal Polarisation (d) Vertical Polarisation

Figure 2.5: Swimming responses of larvae after 10 minutes of exposure to different light regimes. The contrast has been increased in these images to make the larvae (white dots) more visible. In all of them, unpolarised halogen, horizontally polarised and vertically polarised halogen light was shining from the left. We can see that for unpolarised and horizontally polarised light, the larvae swam towards the light source (left) and for vertically polarised light and darkness the larvae were more spread out.

The larvae and their motion were detected using the software ImageJ (version 1.54i) [261]. To minimise the counting of objects that were not larvae, we assumed a size between 20-300

pixels which covers most larval sizes while excluding most contaminants. Although each larva was meant to be counted individually by the software, the glare that accompanied the reflection of light off the glass made this difficult. Indeed, ImageJ counts all visible objects in the water tank with a size and luminosity consistent with that of the larvae. As the glare saturates the luminosity in that part of the tank, the identification of the larvae becomes less accurate.

To make the larvae more visible, the image contrast was increased (see Figure 2.6). However, since this also made the glare more apparent, the ROI had to be cut again, thus leading to a smaller ROI. The total number of counts found by ImageJ is therefore a compromise between larvae visibility and the size of the ROI needed to get a decent number of counts. The percentage distributions of larvae was calculated for each light conditions after the number of larvae on both sides of the ROI was returned by ImageJ.

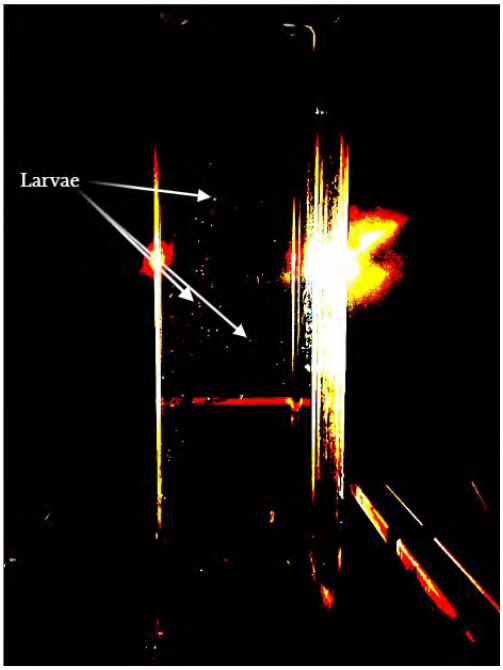

Figure 2.6: In this example, the larvae (see arrows) were exposed to horizontally polarised light from the left and we use ImageJ for the counts after increasing the contrast.

To minimise the number of false counts, we explicitly cut the part of the image where the glare occurred (see Figure 2.7) and defined a region of interest (RoI) accordingly. The cut was performed manually for each image since the extent of the glare varied from image to image. As a result, the RoI's sizes and positions vary across the set of images. We mitigated this effect in our data analysis by considering two approaches: one was based on the number of counts and the other one based on the counts density of larvae per ROI.

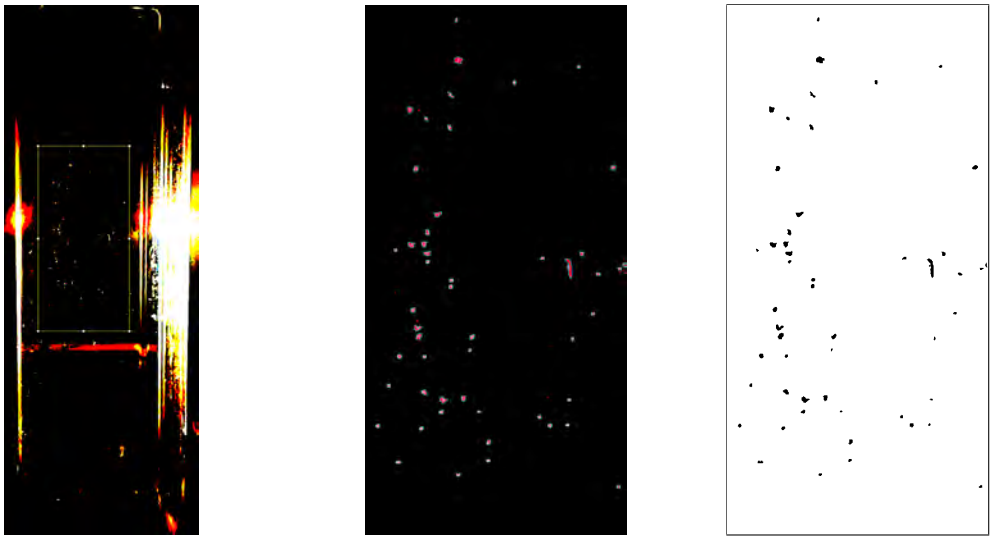

(a) Choosing a ROI (b) ROI (c) Counted Larvae

Figure 2.7: Example of a region of interest for larvae analysis whilst minimising the effects of unwanted counts. This particular example was for larval response to horizontally polarised light. By imposing specific objects size and luminosity restrictions, we could eliminate unwanted counts. Left: Area that was used for the larvae distribution analysis. Middle: Outlines of the selected larvae (indicated by dots) in the ROI. Right: Remaining larvae after cut and ROI selection to avoid glare which were used for the analysis.

In the first approach (where we used the total number of counts), each image's ROI has a different volume and is cut into two equal parts from the centre of the ROI to define a number of counts in the left and right sides. In the second approach (where we used densities), the centre of the water column was kept as a reference point for defining the left and right sides, meaning that the volumes enclosed in each sides of the ROI were no longer equal. As a volume asymmetry could affect our conclusions (especially when it comes to performing statistical tests of the impact of polarisation), we used the density of counts in each side, instead of the number of counts, to perform our analysis. The results displayed in Table 2.1, Table 2.2, Table 2.3, Table 2.4 and Figure 2.13 are only for the counts approach and the results in Table 2.5, Table 2.6, Table 2.7 and Figure 2.14 are for the density method.

The datasets corresponding to the incident light from the left and right sides for the different lighting conditions were analysed separately. This allowed us to assess not only whether the larvae responded to light, but also whether they swam in a preferred direction, independent of the location of the light source. To perform statistical analysis, an arcsine transformation was first applied to the data to stabilise the variances [262] and then a one-way analysis of variance (ANOVA) test was performed, after verifying the assumptions of normality (Shapiro–Wilk test) and homogeneity of the variances (Bartlett test). The ANOVA test that compares unpolarised light, horizontally and vertically polarised light with light incident from the left and from the right gave $F(5,18) = 3.098$, $P = 0.0343$ for the counts method and $F(5,18) = 6.472$, $P = 0.0013$ for the density method. Both processes of dividing the ROI show a statistically significant

difference between the means of some of the datasets, see Table 2.3 for the counts method and Table 2.6 for the density method. The post-hoc Tukey's multiple comparison tests of all the different set-ups was then performed to determine if any two lighting conditions were statistically similar and whether the larvae had a preferred swimming response to the different light conditions. We compared the larvae swimming response to the light source incident from the left and right sides of the water chamber to determine whether the source position had an influence of their response. Any differences in swimming response to exposure to horizontal versus vertical polarisation and unpolarised light versus darkness were also tested. It was found that, under the same lighting regimes, the larvae distribution was always consistent relative to the location of the incident light (p-values of 0.9614, 0.9988 and > 0.9999 respectively for horizontally, vertically polarised light and unpolarised light). Therefore the two data sets were combined and after combination we have 8 sets of 10 min runs for larvae under exposure of unpolarised light, horizontally and vertically polarised light and 4 sets of 10 min runs for larvae in darkness (since in the absence of a light source, there is no left side or right side positions). Thus a new ANOVA with Welch's correction was done to account for the number of repetitions (once again, the datasets met the assumptions of normality and homogeneity of variances). The ANOVA test between unpolarised light, horizontally and vertically polarised light and darkness gave $F(3,24) = 17.05$, $P < 0.0001$ for the counts method (Table 2.4), and $F(3,24) = F(3,24) = 17.00$, $P < 0.0001$ (see Table 2.7). Once again, this shows that there is a statistical difference in the means between datasets.

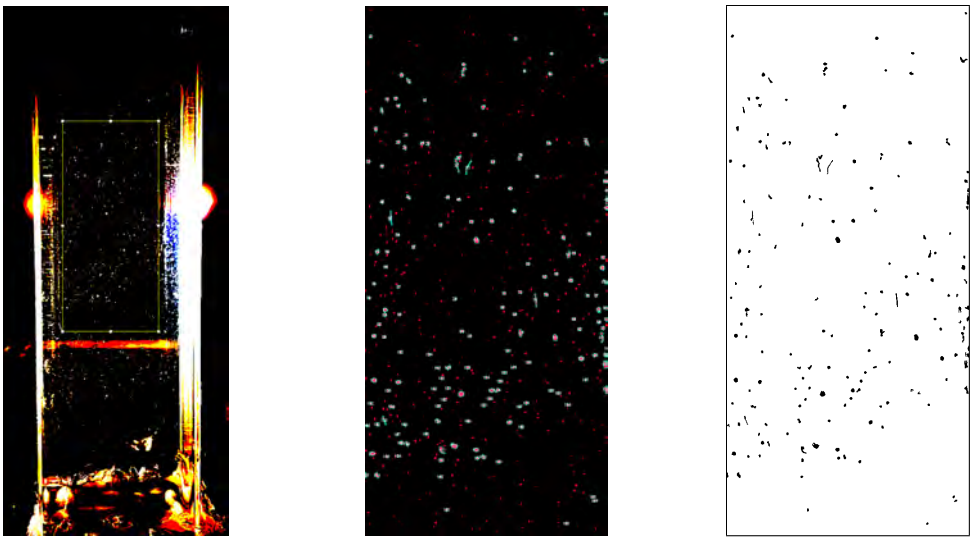

(a) Choosing a ROI (b) ROI (c) Counted Larvae

Figure 2.8: Example of choosing a ROI for larval response to vertically polarised light. Left: Area that was used for the larvae distribution analysis. Middle: Outlines of the selected larvae (indicated by dots) in the ROI. Right: Remaining larvae after cut and ROI selection to avoid glare which were used for the analysis.

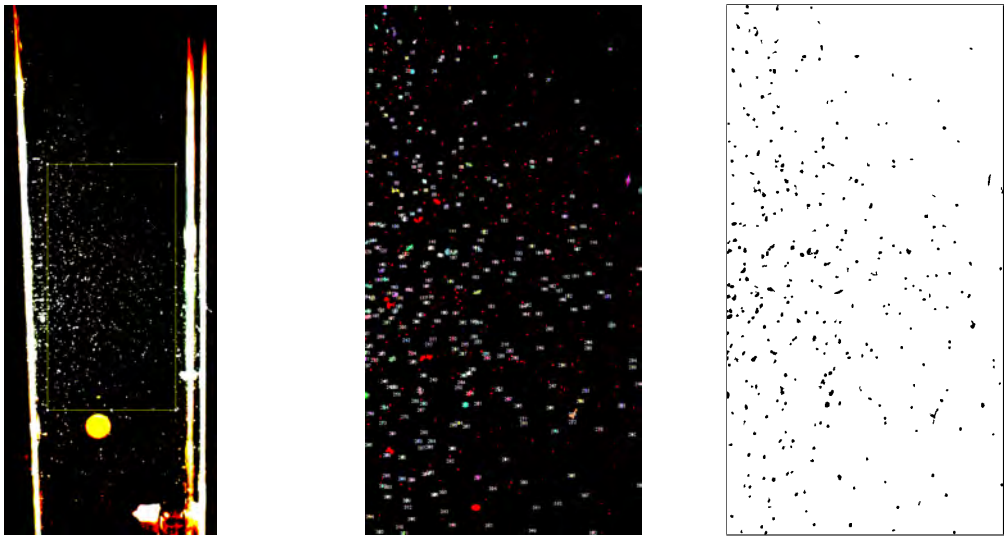

(a) Choosing a ROI (b) ROI (c) Counted Larvae

Figure 2.9: Example of choosing a ROI for larval response to unpolarised halogen light. Left: Area that was used for the larvae distribution analysis. Middle: Outlines of the selected larvae (indicated by dots) in the ROI. Right: Remaining larvae after cut and ROI selection to avoid glare which were used for the analysis.

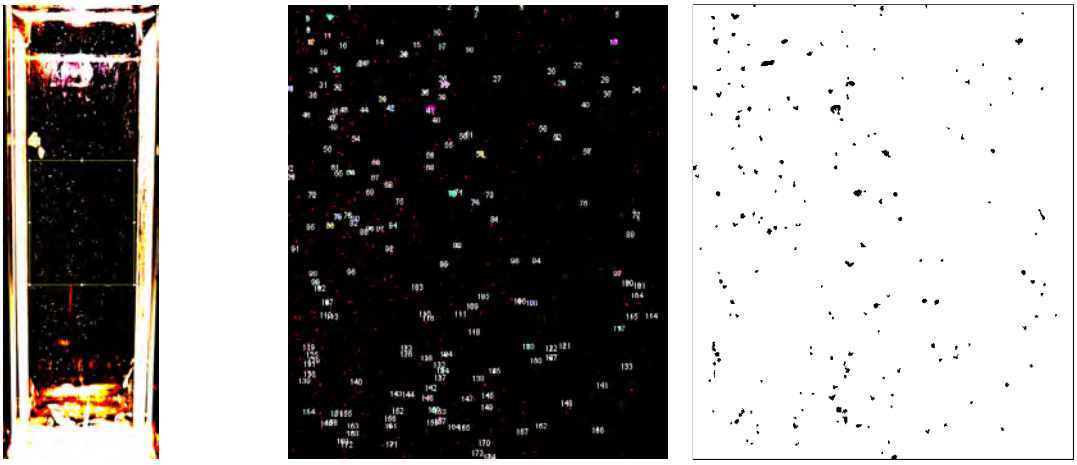

(a) Choosing a ROI (b) ROI (c) Counted Larvae

Figure 2.10: Example of choosing a ROI for larval response no light (darkness). Left: Area that was used for the larvae distribution analysis. Middle: Outlines of the selected larvae (indicated by dots) in the ROI. Right: Remaining larvae after cut and ROI selection to avoid glare which were used for the analysis.

In Figure 2.5, we see that after 10 minutes of unpolarised halogen light, the larval distribution was more skewed towards the light source compared to 10 minutes of darkness, thus displaying positive phototaxis. It is also evident that the distribution of larvae is more toward the light after 10 minutes of horizontally polarised halogen light exposure than after 10 minutes of vertically polarised light exposure.

Figure 2.7 outlines (a) the process of choosing an ROI that minimises the effects of the glare and scattered light while also maximising the number of larvae, (b) shows the objects within the chosen ROI and applying the restriction for counted larvae, and finally we have (c) which showcases the remaining objects to be counted. These counts are what is used for the counts and densities method of larvae comparison. This example is for the larvae response under horizontally polarised halogen light. Figure 2.8 showcases an example of this method for vertically polarised light, Figure 2.9 is an example of unpolarised halogen light, and Figure 2.10 is for darkness.

Figure 2.11 shows the response of the larvae when the halogen lamp was moved to a higher position allowing for elliptical polarisation. We found that under both configurations of the linear polarising filter, the distribution of larvae after 10 minutes were skewed towards the light source, thus displaying no visible difference with the horizontally polarised light case, despite a smaller flux. As elliptical polarisation features both vertical and horizontal polarisation, it is likely that the larvae are actually responding to the horizontal component.

(a) Polarising filter placed in the horizontal configuration

(b) Polarising filter placed in the vertical configuration

Figure 2.11: Swimming response of larvae after 10 min of exposure to elliptically polarised light incident from the left. The contrast of the images were adjusted to better visibility of the larvae. There was a positive phototaxis response to both elliptical polarisations.

Figure 2.12 shows the larvae response to circularly polarised light, both left handed and right handed. In both instances, the larvae showed positive phototaxis. This sensitivity to

circularly polarised light could indicate that they possess optical filters (e.g. quarter-waveplates) to transform the circularly polarised light into a linearly polarised signal (assuming that photoreceptors can only detect linear polarisation). They did not show a preference for left versus right handed circular polarisations.

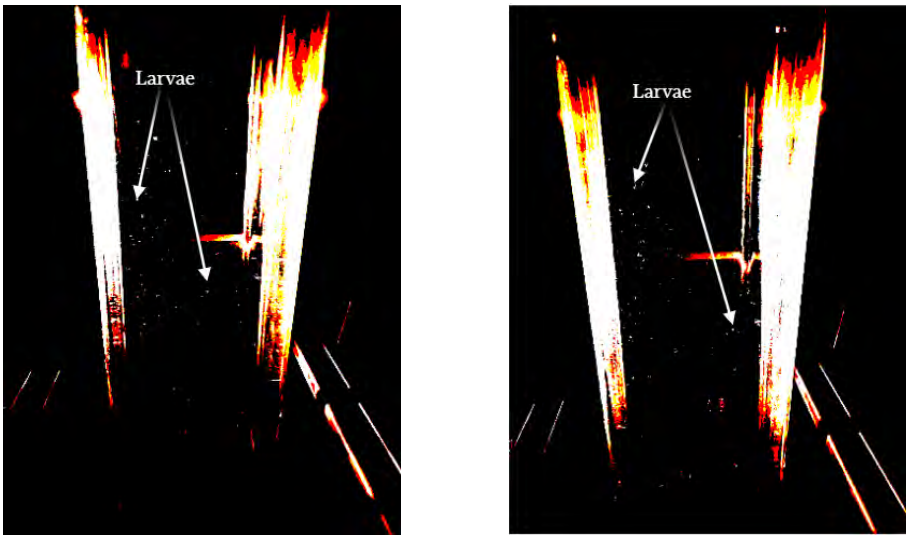

(a) Larvae response after exposure to 10 min of right-handed circularly polarised light.

(b) Larvae response after exposure to 10 min of left-handed circularly polarised light.

Figure 2.12: Swimming response of larvae after 10 min of exposure to circularly polarised light incident from the left. The contrast of the images were adjusted to better visibility of the larvae. There was a positive phototaxis response to both left handed and right handed circularly polarised light.

Table 2.1 shows the mean number of larvae in the different lighting treatments, and the arcsine transformed data is shown visually in Figure 2.13 for the counts method and Figure 2.14 for the density method . When comparing horizontal polarisation versus vertical polarisation as well as unpolarised light versus darkness (using an Anova test plus a post-hoc Tukey's test), we found that a significant difference in the proportion of larvae in the left and right sides of the chamber (p values of 0.0216 and 0.0234 respectively). There was no difference between unpolarised light and horizontal polarisation setups nor darkness versus vertical polarisation setups. The post hoc Tukey's test can be seen in Table 2.2 and the ANOVA test prior to the combination of data for light incident from the left and the right can be seen in Table 2.3, and after the combination in Table 2.4[8].

[8]After it was deemed lighting incidence made no difference to the relative phototaxis of the larvae

Light Regime	Mean	Standard Deviation	n
Horizontal Polarisation	0.72373	0.05228	8
Vertical Polarisation	0.62502	0.06294	8
Halogen Light	0.73811	0.06472	8
Dark	0.51330	0.08842	4

Table 2.1: Proportion of larvae for each light setup in the half of the ROI closer to the light source compared to the half further away for the horizontally, vertically polarised and unpolarised light. For darkness, the proportion was obtained using the left half versus the right half of the ROI (defined so as to remove external objects to the chambers), given the absence of light source, noting that the comparison of the proportions in the right half to left half of the ROI would give the inverse result. There were $n = 8$ repeats for horizontally, vertically polarised and unpolarised light and $n = 4$ for darkness.

Comparison	P value	Statistical Difference
Horizontal vs. Vertical	0.0216	Yes
Horizontal vs. Halogen	0.9947	No
Horizontal vs. Dark	0.0366	Yes
Vertical vs. Halogen	0.0182	Yes
Vertical vs. Dark	0.4969	No
Halogen vs. Dark	0.0234	Yes

Table 2.2: Paired comparison of the different light regimes after performing a posthoc Tukey's multiple comparison test using the counts method

Source of Variations	Sum of Squares	d.o.f	Mean Squares	F(DFn,DFd)	P value
Between Datasets	0.07564	5	0.01513	F(5,18) = 3.098	0.0343
Within Datasets	0.08789	18	0.004883		
Total	0.1635	23			

Table 2.3: ANOVA test for comparison of sea urchin distribution for horizontally, vertically polarised and unpolarised light for the light incident from the left separately from the light incident from the right, using the counts method. DFn is the number of datasets minus one and DFd is the number of datapoints minus the number of datasets.

Source of Variations	Sum of Squares	d.o.f	Mean Squares	F(DFn,DFd)	P value
Between Datasets	0.2218	3	0.07393	F(3,24) = 17.05	$< 10^{-4}$
Within Datasets	0.1041	24	0.004335		
Total	0.3258	27			

Table 2.4: ANOVA test for comparison of sea urchin distribution after combining left and right incident light datasets for each light environment plus darkness, using the counts method.

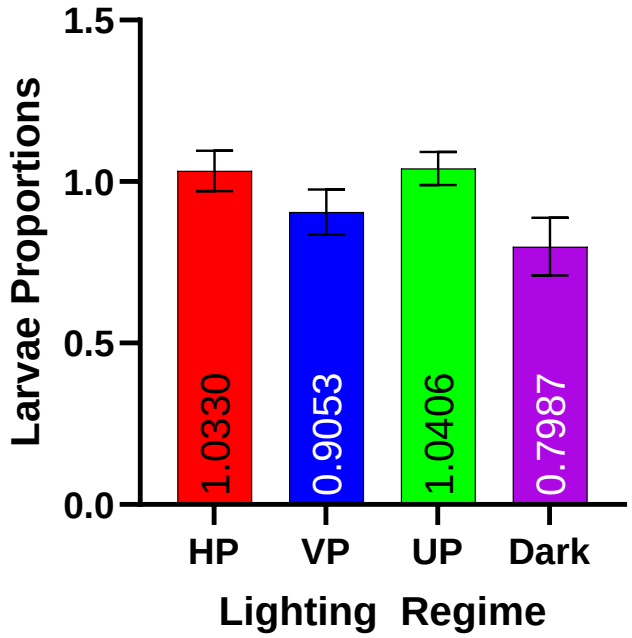

Figure 2.13: Larvae proportions for each light regime after an arcsine transformation for the counts method. The numbers indicated on each bar are obtained from Table. I for the horizontally polarised (HP), vertically polarised (VP), unpolarised light (UP) and darkness (Dark).

A comparison was made once again for the larval distribution, this time using the density method. We can see the statistical comparison of the post hoc Tukey's test in Table 2.5. The larvae response to horizontal polarisation versus vertical polarisation as well as unpolarised light versus darkness was studied and, we found that a significant difference in the proportion of larvae in the left and right sides of the chamber (p values of 0.0026 and < 0.0001 respectively). Once again, there was no statistical difference between unpolarised light and horizontal polarisation

setups nor darkness versus vertical polarisation setups. The ANOVA test prior to the combination of data for the incident light from the left and right can be seen in Table 2.6 and after the combination in Table 2.7 and the arcsine transformed values are represented in a column graph in Figure 2.14.

Comparison	P value	Statistical Difference
Horizontal vs. Vertical	0.0026	Yes
Horizontal vs. Halogen	0.9981	No
Horizontal vs. Dark	<0.0001	Yes
Vertical vs. Halogen	0.0017	Yes
Vertical vs. Dark	0.2090	No
Halogen vs. Dark	<0.0001	Yes

Table 2.5: Paired comparison of the different light regimes after performing a posthoc Tukey's multiple comparison test using the density method

Source of Variations	Sum of Squares	d.o.f	Mean Squares	F(DFn,DFd)	P value
Between Datasets	0.1791	5	0.03582	F(5,18) = 6.472	0.0013
Within Datasets	0.09963	18	0.005535		
Total	0.2787	23			

Table 2.6: ANOVA test for comparison of sea urchin distribution for horizontally, vertically polarised and unpolarised light for the light incident from the left separately from the light incident from the right, using the density method.

Source of Variations	Sum of Squares	d.o.f	Mean Squares	F(DFn,DFd)	P value
Between Datasets	0.3430	3	0.1143	F(3,24) = 17.00	$< 10^{-4}$
Within Datasets	0.1614	24	0.006724		
Total	0.5043	27			

Table 2.7: ANOVA test for comparison of sea urchin distribution after combining left and right incident light datasets for each light environment plus darkness, using the counts method.

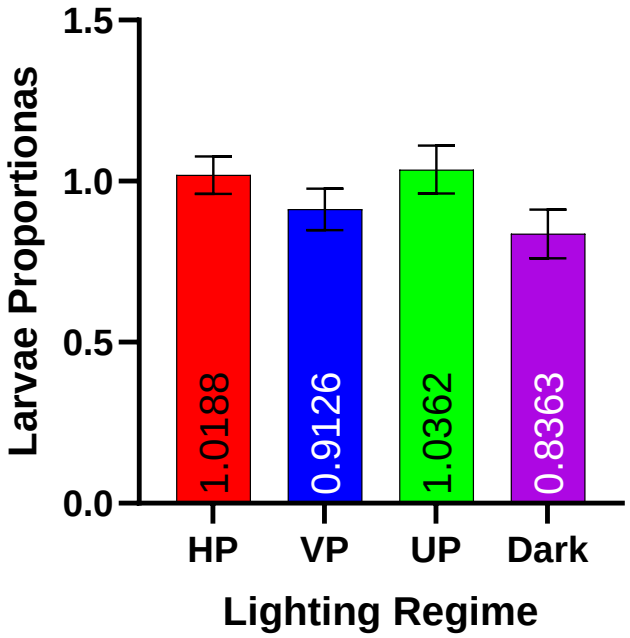

Figure 2.14: Larvae proportions for each light regime after an arcsine transformation for the density method. The numbers indicated on each bar are obtained from Table 2.1 for the horizontally polarised (HP), vertically polarised (VP), unpolarised light (UP) and darkness (Dark).

For the elliptical polarisations, there was no difference in the response of the larvae to the 'horizontal' and 'vertical' orientations of the polarising filter. The larvae showed positive phototaxis to both configurations ($F(2, 17) = 0.1290$ and $P = 0.8798$, see Table 2.8 and Table 2.9). For circular polarisations, larvae also showed positive phototaxis for both left-handed and right-handed polarisations ($F(2, 17) = 0.8498$ and $P = 0.4449$, see Table 2.10 and Table 2.11).

2.4 Data Analysis

The comparison of the mean values of horizontally polarised light, vertically polarised light, and unpolarised light incident from the left vs. the right of the water chamber was performed using a Tukey test, allowing for pairwise comparisons. Figure 2.15 for the counts method Figure 2.17 for the density method both shows that for horizontally polarised light, vertically polarised light and unpolarised light and, there is no statistical difference between the larval distributions with the light incident from the left vs. the right.

A Tukey test was also performed after the combination of the results of the light incident from the left and the right, this time incorporating the data for no light exposure. We can see in Figure 2.16 for the counts method and in Figure 2.18 for the denstiy method, there is a

clear difference in the means of vertical polarisation when compared to horizontal polarisation. There is also a difference between unpolarised light and darkness, unpolarised light and vertical polarisation, and darkness and horizontal polarisation. Note that there is no statistical difference between horizontal polarisation and the halogen lamp, as well as no difference between dark and vertical polarisation.

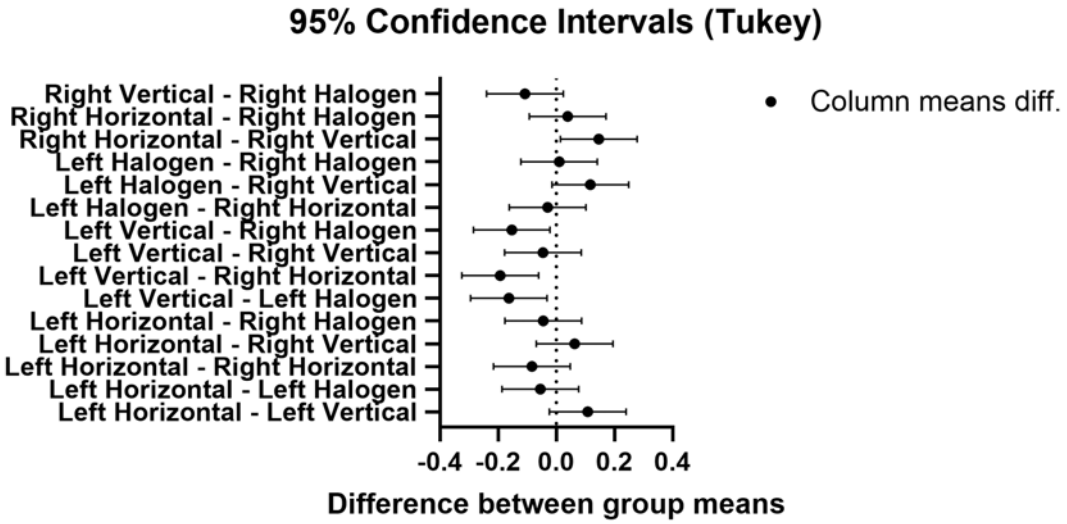

Figure 2.15: Tukey test of the counts method for light sources of horizontally polarised, vertically polarised and unpolarised light with incident light coming from the left and right of the water chamber. In particular, we can see that there was no statistical difference between left horizontally vs. right horizontally polarised light, left vertically vs. right vertically polarised light and left unpolarised vs. right unpolarised light.

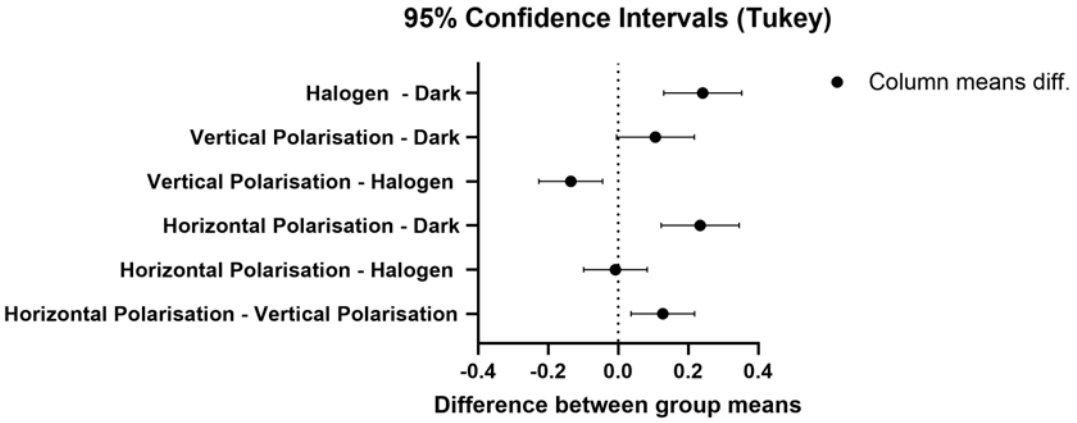

Figure 2.16: Tukey test of the counts metho dafter combining left and right incident light sources. We can see that there is a statistical difference between horizontal polarisation and vertical polarisation. Interestingly there is no statistical difference between unpolarised light and horizontally polarised light as well as between vertically polarised light and darkness.

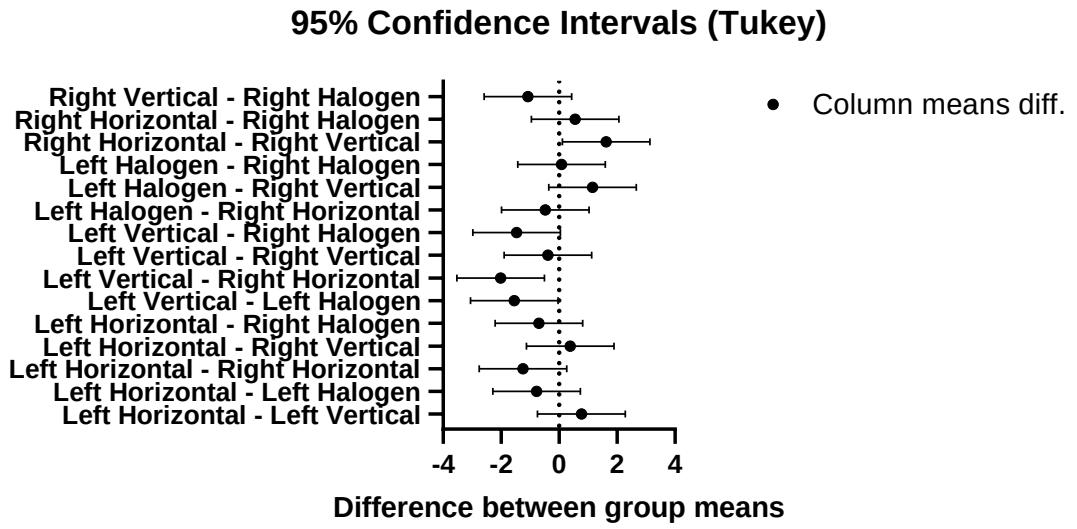

Figure 2.17: Tukey test of the density method for light sources of horizontally polarised, vertically polarised and unpolarised light with incident light coming from the left and right of the water chamber.

In Table 2.8, we display the proportions of the larvae in the half of the ROI closer to the

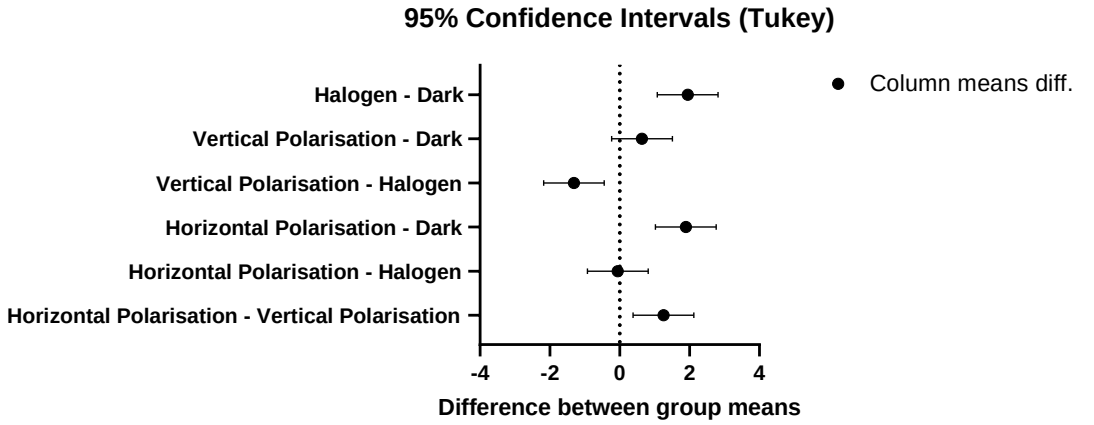

Figure 2.18: Tukey test of the density method after combining left and right incident light sources.

light source compared to the half further away after an arcsine transformation, for the elliptical polarisations as well as for unpolarised halogen light. Table 2.9 is the corresponding ANOVA table. We find $F(2, 17) = 0.1290$ and a p-value of 0.8798, thus indicating that the response of the larvae to the two elliptical polarisations were statistically similar and also the same as their response to the unpolarised halogen light.

Light Regime	Mean	Standard Deviation	n
Horizontal Elliptical	1.029	0.1439	6
Vertical Elliptical	1.058	0.09525	6
Unpolarised Halogen Light	1.041	0.05098	8

Table 2.8: Proportion of larvae in the half of the ROI closer to the light source compared to the half further away for the two elliptical polarisation setups and the unpolarised light setup. The numbers are obtained after an arcsine transformation. The horizontal polarisation was obtained by placing the linear polarisation filter in the horizontal orientation, and vertical polarisation by placing the linear polarisation filter in the vertical orientation. There were $n = 8$ repeats for unpolarised halogen, and $n = 6$ for horizontal elliptical and vertical elliptical polarisations.

In Table 2.10, we display the proportions of the larvae in the ROI half closer to the light source compared to the half further away after an arcsine transformation, for left-handed and right-handed circular polarisations, as well as for unpolarised halogen light. Table 2.11 is the ANOVA table for the data obtained for Table 2.10 and we can see again from $F(2, 17) = 0.8498$ with $p = 0.4449$ that the larvae reacted the same to the left-handed and right-handed circular polarisations. They had the same reaction as for unpolarised halogen light. This shows that the larvae can detect elliptical and circular polarisations and do not show a preference for one of the elliptical polarisations nor for one of the circular polarisations.

Source of Variations	Sum of Squares	d.o.f	Mean Squares	F(DFn,DFd)	P value
Between Datasets	0.002537	2	0.001268	F(2,17) = 0.1290	0.8798
Within Datasets	0.1672	17	0.009833		
Total	0.1679	19			

Table 2.9: ANOVA test based on the data from Table 2.8. This shows that the larval response to elliptical polarisations are not statistically different from each other, nor are they different from unpolarised light.

Light Regime	Mean	Standard Deviation	n
Left-handed	0.9977	0.1240	6
Right-handed	1.084	0.1608	6
Unpolarised Halogen Light	1.041	0.05098	8

Table 2.10: Proportion of larvae for each light setup, after an arcsine transformation, in the half of the ROI closer to the light source compared to the half further away for left-handed and right-handed circularly polarised halogen light, as well as for unpolarised halogen light. There were $n = 8$ repeats for unpolarised halogen, and $n = 6$ for the circular polarisations.

Source of Variations	Sum of Squares	d.o.f	Mean Squares	F(DFn,DFd)	P value
Between Datasets	0.02243	2	0.01122	F(2,17) = 0.8498	0.4449
Within Datasets	0.2244	17	0.01320		
Total	0.2468	19			

Table 2.11: ANOVA test based on the data from Table 2.10. This is a comparison of distribution of sea urchin larvae to left-handed, right-handed and unpolarised light. We can see from the p value of 0.4449, there is no statistical difference in their response to each lighting regime.

Spectral Analysis

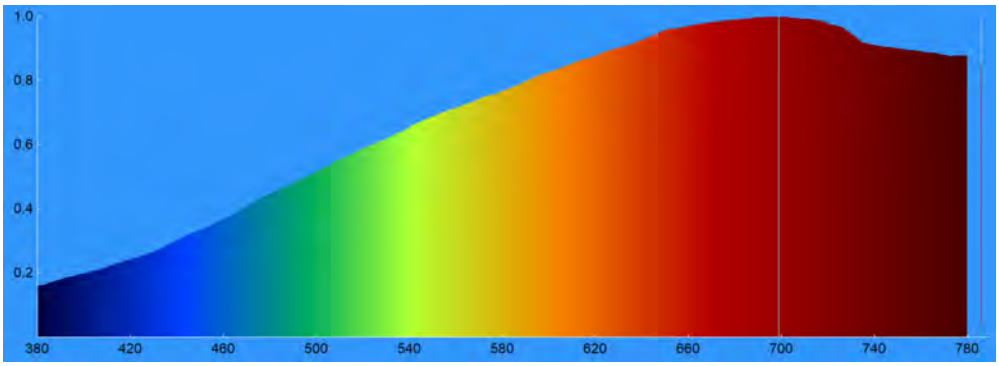

Figure 2.19: Spectra of the halogen lamp used.

Figure 2.19 shows the spectrum of the halogen lamp used. We have the intensity in counts on the y-axis and the wavelength in nanometres on the x-axis. The peak wavelength is around 640 nm. The shape of the spectrum nicely resembles the spectrum of sunlight on the surface of Earth.

Polarisation	Intensity (a.u.)	Cross Polarisation Intensity (a.u.)
Linear	565.07	6.99
Circular	846.62	8.10

Table 2.12: Measured intensities of light passing through the water chamber with a polariser and after a cross polariser.

Table 2.12 shows the measured intensities of the halogen lamp after passing through one polariser (linear and circular) and also the measured intensities after their respective cross polariser. A ratio of cross-polarisation intensity to polarisation intensity of 0.5 would mean that it has become completely depolarised, whilst a ratio of 0 would mean that it has retained all of its polarisation. We see that for linear polarisation, the ratio is 0.0124, which means that over 97% if light passing through the water chamber retained its linear polarisation. For circular polarisation, this ratio is 0.0096, which means that over 98% of the light retained its circular polarisation. This means that any depolarisation effects from the interactions of light to the glass and the water can be safely ignored.

2.5 Discussion

Here we showed that the larvae of the sea urchin (*C. rodgersii*) larvae were sensitive to white (halogen) light, exhibiting positive phototaxis. In contrast, the larvae sank to the bottom of the chamber or did not show a visible swimming response in the darkness (no light exposure). We also show that the polarisation of light matters to larvae swimming patterns. Positive phototaxis of larvae was observed when they were exposed to horizontally polarised light but

not to vertically polarised light. This trend does not appear to be the case when the light source was moved to a higher angle to mimic elliptical polarisation (which includes light that is polarised both in the horizontal and vertical directions). This indicates that the larvae responded to polarised light parallel to the ground, i.e. horizontally polarised light.

We also found no statistical difference in larvae distributions in response to horizontally polarised light and unpolarised light (p-value = 0.9947), nor were there any differences between vertically polarised light and dark (p-value = 0.4969). This suggests that the larvae have the same reaction to vertically polarised light as they do to no light exposure. This could mean that the photoreceptors of larvae are only responsive to horizontal polarisation.

There are a number of caveats to our study. For example, we tried to account for the counting of non-larval particles by setting criteria on particle sizes. However, this meant that some larvae towards the further side of the water chamber might not have been counted due to their smaller apparent size. In addition, larvae in the background were less lit up, so they also might not have been incorporated in the counts. We have assumed that any of the larvae that were not counted in the back due to the above reasons were in the same proportion as the larvae that were counted in the front, due to the symmetrical nature of the water chamber (i.e. we have assumed that the proportional distribution of the larvae within the ROI should be relatively unchanged), but this might not be the case. Furthermore, we note that the images that we took were not taken from the same perspective every time. This may impact the estimates of the larvae counts due to the projection of a 3 dimensional image onto a 2 dimensional plane. This should not impact the comparison of larvae counts in the left and right sides of the ROI for each individual image, but would be an issue if we wanted to compare the larvae counts across multiple images. It appears also that changing the comparison regions did not greatly impact the results as long as the analysis was done consistently. Furthermore, we note that changes in perspective were mainly due to changes in the vertical location of the camera (since the water chamber was centred in the frame with each image taken). As our study focused on the horizontal movement of the sea urchin larvae, vertical changes in perspective should not have a great impact on the comparison of horizontal larvae distributions. Thus, in general, we do not expect the changes in perspective to greatly affect our final results. We acknowledge that future experiments should have a fixed camera. Finally, we note that the circular polarisers used in our setups have a polarising efficiency of $> 99.9\%$. The fact that the efficiency is not perfect could mean that some larvae were exposed to unpolarised light. However, the corresponding flux would be extremely small, so the larvae would need to have extremely sensitive photoreceptors to detect it. In the future, experimental improvements could involve reducing the glare and contaminants, keeping a constant perspective for taking images, increasing the image quality for more accurate counting of the larvae, and increasing the number of runs. However, we do not expect the results to change dramatically.

Spectral analysis was also performed on the intensities after cross-polarisers for both linearly and circularly polarised light. 97 % of linearly polarised light and 98 % of circularly polarised light retained its polarisation after transmission through the water chamber. This shows that the depolarisation of light as a result of its interactions with glass and seawater is negligible and can be ignored. We can thus safely conclude that the responses of the sea urchins under the different polarisations of light are valid and not as an effect of depolarisation.

The water temperatures of the aquarium were not measured. Fluctuations in water temperature could have been caused by changes in climate between experimental runs, as well as differences in photon flux. Using a linear or circular polariser would effectively reduce the pho-

ton flux at the aquarium by half when compared to the unpolarised halogen runs. As a result, the water temperatures between the halogen, darkness, and polarised experimental runs could have differed. However, if the movement of the sea urchin larvae was caused by changes in water temperature, then the reactions of the larvae should have been the same when exposed to horizontally and vertically polarised light, as these runs would have delivered a similar photon flux to the aquarium. From our results, we observed that this was not the case, indicating that the differences were caused solely by the different polarisation modes.

To our knowledge, there is no documented case of cells being intrinsically sensitive to circularly polarised light [121]. For example, stromatopods are sensitive to circular polarisation but they posses specialised cells that act as quarter-waveplates that convert circularly polarised light into linearly polarised light [109]. The fact that sea urchin larvae seemed to display positive phototaxis after exposure to circularly polarised light but did not show a preference between left-handedhanded and right-handed circular polarisation suggests that they might possess an entirely new mechanism for detecting circular polarisation. This would warrant a dedicated study that includes an in-depth look at the morphology and orientation in the water column of sea urchin larvae, which may lead to exciting results.

2.6 Conclusion

In this work, we compared the swimming responses of larvae of the sea urchin species *C. rodgersii* after exposure to an unpolarised halogen, horizontally polarised halogen, vertically polarised halogen, and to darkness. We found that there was a positive phototaxis response after 10 min of exposure to unpolarised and horizontally polarised halogen light and no phototaxis after 10 min of exposure to vertically polarised halogen light and darkness. In fact, the larval response to unpolarised halogen and horizontally polarised halogen light was statistically equivalent, as well as the larval response to vertically polarised light, when compared to no light exposure. Our results suggest that not only do these sea urchin larvae have photoreceptors sensitive to light in the visible spectrum but also may have photo-receptors that are sensitive to horizontal polarisation (and not sensitive to vertical polarisation).

Photoreceptor cells usually contain the retinal molecule 11-cis retinal and a G-coupled protein receptor that forms the opsin protein. Upon a conformal change from 11-cis-retinal to all-trans-retinal, the opsin protein activates and sends a phototranducton cascade down the neurone [263, 264]. Photons with polarisation parallel to the double carbon-carbon bonds present in the retinal molecules are absorbed and converted to an electrical impulse [265]. Hence polarisation sensitivity can arise when groups of photoreceptors are aligned with each other in aligned microvilli [123]. Given that sea urchin larvae appear to possess Opsin2 [228] and are sensitive to horizontally polarised light, one may speculate that sea urchin larvae have photoreceptor cells that are aligned and preferentially horizontal.

The larvae also demonstrated a positive phototaxis response to circularly polarised light, indicating that they may possess a mechanism for circular polarisation detection. However, as these larvae did not show a preference between left-handed and right-handed circular polarisations, one should investigate whether sea urchin larvae possess cells similar to the quarter-waveplate cells of stromatopods. The absence of such cells would indicate a novel circular polarisation detection mechanism that could lead to the development of new technologies and possibly a new understanding of underwater vision.

Chapter 3

Adult Sea Urchins Seeing Polarisation

The following work is an adaptation of a submitted manuscript titled: "The response of the sea urchins *Echinus esculentus*, *Paracentrotus lividus* and *Psammechinus miliaris* to Different Light Intensities and Polarisation states" by Ben Li, Zhenxu Yang, Helena C. Reinardy, Julien Reboud, Filippo Menolascina, Ken-Tye Yong, Maria Byrne and Céline Bœhm.

Author Contributions:

- Ben Li: Conceptualisation (main), Methodology (main), Investigation (main), Data Analysis (main), Writing (original draft).
- Zhenxu Yang: Investigation (supporting), Writing (review).
- Helena C. Reinardy: Methodology (supporting), Sea Urchin housing (main), Writing (review and editing).
- Julien Reboud: Methodology (supporting), Writing (review and editing).
- Filippo Menolascina: Methodology (supporting).
- Ken-Tye Yong: Writing (review), Supervision (supporting)
- Maria Byrne: Conceptualisation (supporting), Methodology (supporting), Writing (review), Supervision (supporting).
- Céline Bœhm: Conceptualisation (supporting), Methodology (supporting), Writing (review and editing), Supervision (main).

This chapter outlines the work done following the studies conducted on the larvae of sea urchins. Based on previous results that sea urchin larvae possess the ability to detect light and have sensitivity towards horizontally polarised light, it was interesting to us whether adult sea urchins could possess the same abilities. As the larval and adult stages of the sea urchin life cycle are separated by a physical metamorphosis, we wondered whether the structural change affects their ability to sense light and polarisation. The following experiments are conducted with this question in mind; however, the species of sea urchins have changed due to seasonal restrictions. Nonetheless, the knowledge of potential polarisation sensitivity in adults would

clear the path to answering that question. This investigation was carried out at the facilities provided by the Scottish Association for Marine Science (SAMS) to allow multiple species of sea urchins to be tested at the same time.

The usefulness and importance of light polarisation have skyrocketed in recent times with applications found in biomedicine, imaging, characterisation of biological and chemical systems, and astrophysics just to name a few. Ecologically, more and more examples of flora and fauna are found to utilise the polarisation of light for growth, navigation, and communication, increasing the need for polarisation characterisation. Current polarimetric photodetectors for visible light generally use a polarising filter, which reduces their overall sensitivity and effectiveness. This motivates the search for better alternatives, both for linear and circular polarisations. In this work, we explore the possibility of polarisation detection via biomimicry by investigating the linear and circular polarisation sensitivity of the sea urchin species *Paracentrotus lividus*, *Echinus esculentus*, and *Psammechinus miliaris* through their phototactic responses under illumination of light. It was discovered that *P. miliaris* has the ability to differentiate between horizontally and vertically polarised halogen light, and additionally *P. lividus* potentially has the ability to differentiate circularly polarised light. These findings could lead to a novel mechanism of polarisation detection in the visible domain and a step toward a new technology or its determination. Such a detector would be simpler compared to current alternatives, making it cheaper and easier to produce, and it would also allow for direct detection of polarised light in the visible wavelengths.

3.1 Introduction

Polarisation is a fundamental property of visible light and all electromagnetic radiation, with applications spanning across many different fields of research, often interdisciplinary. It has implementations in biomedical and clinical imaging, to characterise complex tissue samples [140–143] and for diagnostics [144–146]. There are also potential therapeutic applications for the use of polarised light in tissue healing [147–150], immunomodulation [151] and photobiomodulation [152]. Outside the field of medicine, polarisation microscopy can reveal information very quickly about the orientations of molecules, including collagen fibres [153, 154], proteins, cellular structures [155] and liquid crystals [156]. Polarisation also has many everyday technological uses; such as improving the efficiency in liquid crystal displays (LCDs) [157, 158], increasing the contrast in photography in cameras but also in the retina [159] and reducing glare [160].

Recently, the importance of polarisation in the animal kingdom has increasingly come to the fore. From navigation in insects and arthropods [161–165] to communication in cephalopods and stromatopods [166] - the latter being currently the only species that appears to use circular rather than linear polarisation. In addition, polarisation is also used in the identification of predators and prey and in the responses in certain species of fish [167, 168]. Furthermore, it is used for the selection of habitat for semiaquatic insects [169], as well as to facilitate shore flight responses in water fleas [170]. Polarisation is significant in the study of plant development, resulting in better growth rates of maize and white lupin under linearly polarised light [171, 172] and higher germination rates of Arabidopsis and lettuce under circularly polarised light [173].

Realisation of the effects and applications of polarised light requires its characterisation. This is normally done via the use of polarisation detectors. Current detection methods of polarised electromagnetic waves spanning from infrared to visible to ultraviolet (UV) light generally include the use of polarisers or polarising filters. From Malus's law the transmitted intensity of polarised light through a linear polariser is:

$$I = I_0 \cos^2 \theta \tag{3.1}$$

where I is the transmitted intensity, I_0 is the intensity of incident polarised light, and θ is the angle between the direction of polarisation and the transmission axis of the polariser. In short, light with its polarisation parallel to the transmission axis is allowed through the polariser, and light with its polarisation perpendicular to the transmission axis is blocked. This can be used to characterise the polarisation of an unknown source by rotating the polariser until the measured intensity matches the incident intensity [199, 266]. For circularly polarised light, the inclusion of a quarter waveplate, which converts circularly polarised light to linearly polarised light [267], allows the determination of left-handed or right-handed polarisation states. However, such methods can only determine the polarisation state indirectly by measuring the intensity of light transmitted through a polariser. This additional optical filter adds to the complexity, size, and costs associated with such polarimetric photodetectors, and can also cause a loss of sensitivity and responsiveness of the photodetector [200]. This calls for methods of direct detection of polarisation to mitigate such restrictions. Current research on alternatives includes inorganic semiconductors [200, 201], carbon nanotubes [202, 203], and inorganic nanowires [204, 205].

In this work, we explore a novel method for the detection of polarisation using the biological mechanisms of animal sensitivity to polarisation. Polarisation sensitivity in some animals arises due to their photodetection mechanism, using chromophores. Chromophores are naturally dichroic, and polarisation sensitivity is due to the ordering of chromophore molecules [121,

123]. This mechanism can be exploited to possibly create a device that can directly detect the polarisation state of light, without the need to a separate filter, enhancing their sensitivity and resolution. Furthermore, the optical properties of chromophores have been well documented and studied, especially their peak wavelengths [128, 134, 206]. A polarimetric photodetector based on chromophores could potentially be extremely tunable to measure different wavelengths by switching out the base chromophore.

We were especially interested in sea urchins due to the calcite in their skeletons and tube feet [207, 208], where their photorecptors reside. Calcite interacts anisotropically with different polarisations of light [207] since calcite has high birefringent properties [209]. Coupled with the photoreceptors, this could potentially lead to linear and circular polarisation sensitivity in sea urchins, which uses both the birefringent properties of calcite and the polarisation sensitivity of aligned chromophores.

Here we study the sensitivity of three sea urchin species *Paracentrotus lividus*, *Echinus esculentus* and *Psammechinus miliaris* light and in particular towards both linearly and circularly polarised light. Certain species of sea urchins have already been shown to react to light, with an observed behaviour of both negative and positive phototaxis [268, 269], indicating that they possess photoreceptors. In fact, photoreceptor cells have been found in the tube feet of sea urchins [270, 271] and they are all interconnected to essentially form one large compound eye. Interestingly, juvenile sea urchins after metamorphosis [272] were found to have no phototaxis until their skeleton was completed after metamorphosis, suggesting that the skeleton is used as a photoreceptor cell screening device [270]. Any polarisation detection could pave the way to the possible development of a novel polarimetric photodetector. This would utilise the same mechanism that these sea urchins use to detect polarisation, which would not only directly measure the polarisation state of light, but would also help miniaturise the technology.

This chapter is divided into multiple sections. Section 3.2 showcases the experimental setup. The results can be found in Section 3.3. The discussion is in Section 3.4 and the conclusion can be found in Section 3.5.

3.2 Experimental set up

Species

For this experiment, three species of sea urchins were used; *P. lividus*, *E. esculentus* and *P. miliaris*. A specimen of the sea urchin *Paracentrotus lividus* can be seen in Figure 3.1. In particular one can see small tubular appendages protruding from the body which are used for locomotion, feeding, respiration, as well as for photo detection [273, 274]. In addition, specimens of all three species can be seen in Figure 3.2. We were especially interested in the locomotory response of the sea urchins to different lighting regimes. The sea urchins were obtained and housed at the Scottish Association for Marine Science (SAMS), and the experiments were carried out on site. We performed three separate experiments on each species. Firstly, each species were subjected to unpolarised halogen light to test for a phototactic response and varying the source to see if the behaviour of the sea urchins changed with different light intensities. A Thorlabs OSL2 halogen light source was chosen because its spectrum resembles the visible spectrum of sunlight. Once their response to light was established the sea urchins were subjected to different linear(horizontal and vertical) polarisations. We also tested their response to left-handed and right-handed circular polarisations.

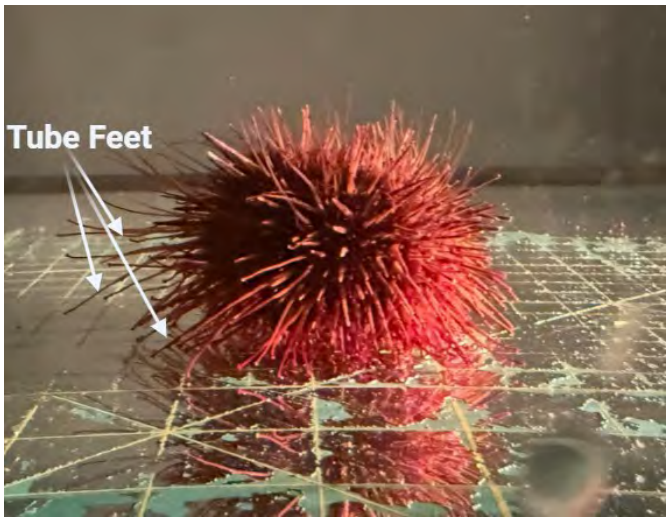

Figure 3.1: A specimen of the sea urchin species *Paracentrotus lividus*. We can see clearly the spines and rigid spines and the more flexible tube feet which they use for photo detection and also movement.

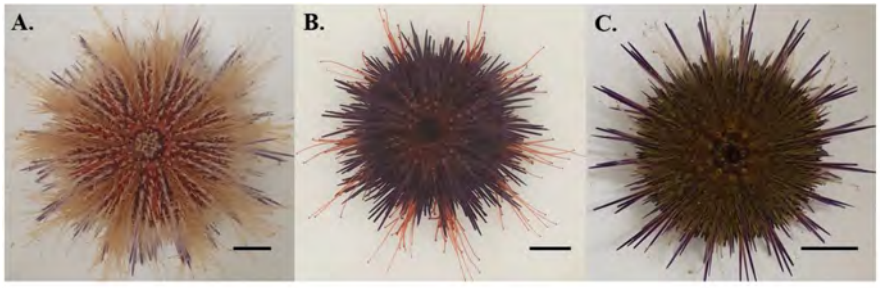

Figure 3.2: Specimens of the sea urchin (A) *Echinus esculentus*, (B) *Paracentrotus lividus* and (C) *Psammechinus miliaris* [275]. The scale bar shows 10 mm.

Intensity Test

To test for their response to illumination under unpolarised halogen light, an individual sea urchin was placed in the middle of a 50 cm $\times$ 50 cm $\times$ 30 cm acrylic tank filled with 1 micron filtered seawater. The halogen light source was initially placed on the right hand side of the tank and the light source switched on. The intensity and spectrum of the light source were measured at a distance of 1 metre from the lightbulb using an OHSP-350 series light meter, with the light passing through the tank and the water. A measuring grid, with spacings of 2 inches between lines, was also placed below the water tank to measure the scale of their movements. The sea urchins were chosen at random and were swapped out after one test to minimise the effects of exhaustion. They were initially placed in the middle of the tank and their movements recorded at 1080p and 24fps with a GoPro HERO10 Black, placed above the water tank, for a period of

5 minutes. The room temperature was kept at approximately 14° Celsius and the water was changed approximately every 4 hours for all the subsequent tests.

The experimental setup used can be seen in Figure 2. This was repeated 4 times for each light intensity. *P. lividus* was subjected to measured intensities of 100, 213, 471 and 1000 lux. *E. esculentus* was subjected to intensities of 100, 200, 500 and 1000 lux and *P. miliaris* was subjected to intensities of 100, 227, 515 and 1038 lux. Here the intensities were not exactly the same due to the sensitivity limitations of the tuning of the halogen light source.

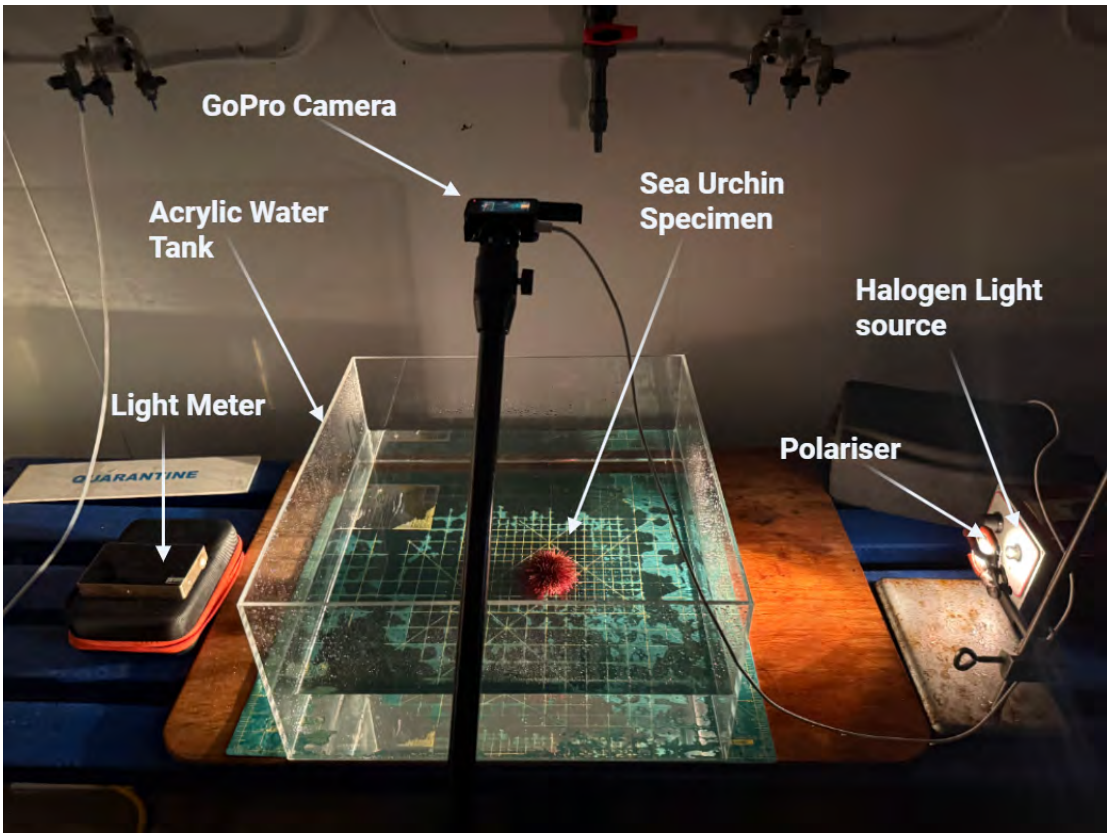

Figure 3.3: Experimental Setup of test for sea urchin sensitivity to light and polarisation. The sea urchins were placed in a 50 cm × 50 cm × 30 cm acrylic tank, filled with filtered sea water (1 μm). A halogen light source was used and, for polarisation tests, a polarising filter was placed in front of the light source.

Linear Polarisation Test

Each individual of the different species was illuminated with different linear polarisations. A Hoya 77 mm linear polarising filter was placed in front of the halogen light source, only allowing one mode of polarisation through. We tested both horizontal and vertical modes by rotating the filter in horizontal and vertical orientations with incident light laterally.

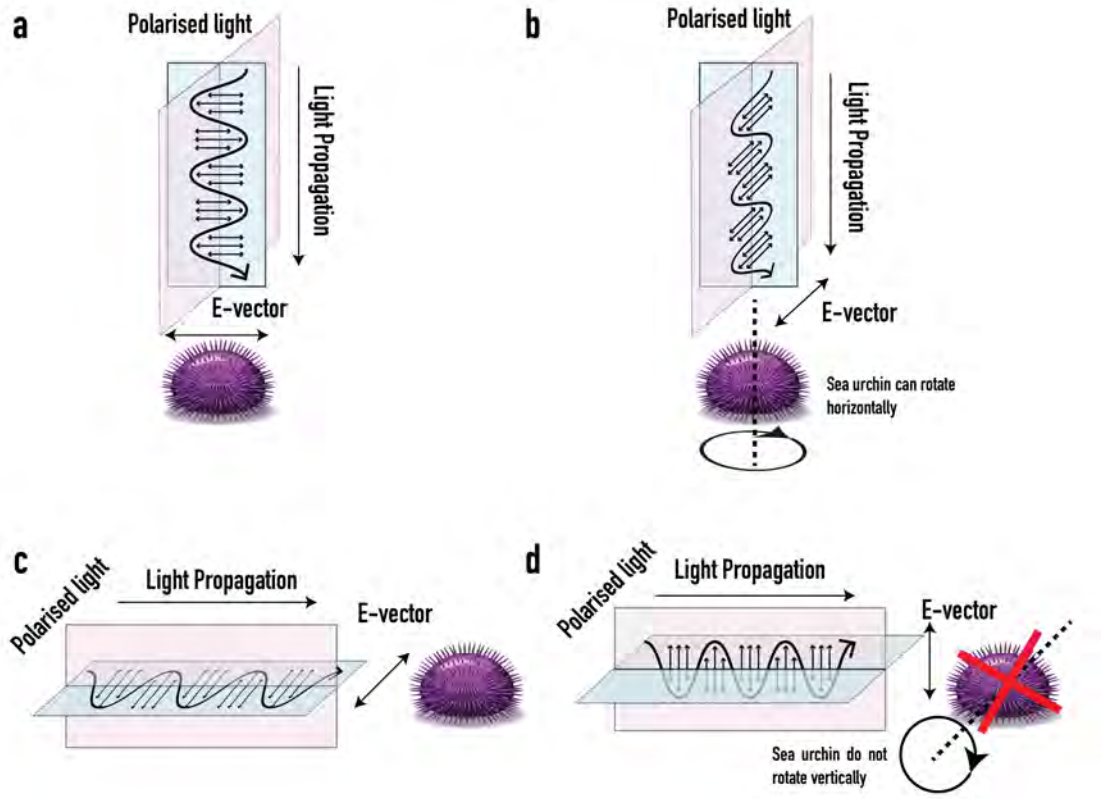

Figure 3.4: Sea urchins subjected to different polarisations of halogen light incident from above (a and b) and from the side (c and d). As the sea urchins are radial, they are free to rotate along the horizontal plane, we assume that they can detect the two polarisation states as the same after rotation. In images (c) & (d) we have sea urchins subjected to different polarisation modes of halogen light incident from the side. The sea urchins are not free to rotate along the vertical plane (i.e flip), thus they perceive the two polarisations as as fundamentally different. This allows for a test of their polarisation differentiation capabilities.

The intensity of light (measured at a distance of 1 m away) was set to 300 lux. We first tested for the degree of depolarisation of light by measuring the transmitted intensity under cross polarisers, using another linear polariser placed in front of the light meter and orientated perpendicularly to the original filter orientation. A lower transmitted intensity as a result of cross polarisation means that most of the light retained its polarisation.

Again, sea urchin individuals were chosen at random and placed in the middle of the water tank for locomotion testing. After one test, they were changed with another member of their species to minimise the effects of exhaustion. We repeated this procedure until all tests for that species were concluded. The order of the species tested was also randomised.

The response of individual sea urchins of each species was recorded over a 5 minute period for horizontally polarised light and vertically polarised light with repetitions (n = 8 for *P. lividus*,

n= 17 for *E. esculentus* and n = 10 for *P. Miliaris*).

Additionally, the response of sea urchins to polarised light was also tested for incident light from the left. This was done to make sure that, under illumination, the urchins had a consistent response that was only due to the light source and not to some other environmental factor of the room.

Circular Polarisation Test

Finally, each species was tested under left-handed and right-handed circular polarised light. This time, a circular polarising filter was placed in front of the halogen light source, one to test the left-handed polarisation and one for the right-handed polarisation. The polarisers used were the 50 mm CP42HE and CP42HER filters from Edmund Optics. The light intensity was once again set to 300 lux, and the movements of individual sea urchins of each species were recorded over a 5-minute period with repetitions (n=4 individuals for each species).

Data Analysis

For analysis of the movement speeds of sea urchins, frames were extracted from the video recordings at time stamps of 5 s, 60 s, 120 s, 180 s, 240 s, and 300 s. The distance of movement over the 300 second period was measured using the built-in measuring tool from the ImageJ software [276].

This measurement in pixels, was converted into cm using the measuring grid present in the images. Because we wanted to measure phototaxis, only the sea urchins movements towards or away from the light source was taken into account. Movement along the other axis were not used to judge phototaxis, as it is perpendicular to the direction of light incidence. The movement speed was then calculated and analysed for the different lighting regimes (unpolarised, linearly polarised, and circularly polarised) in GraphPad Prism (version 10.5.0 for Windows, GraphPad Software, Boston, Massachusetts USA) for each species. Statistical analysis on the movement speeds of sea urchins under horizontally polarised light was compared with their movement speeds under vertically polarised light using a t-test with Welch's correction, as the sample sizes were not the same. This was then also performed on the movement speeds under illumination of left-handed circularly polarised light compared to right-handed circularly polarised light.

3.3 Results

Halogen light spectra and polarisation.

The spectra of the halogen light source can be found in Appendix A, we confirm that it is a continuous spectrum in the visible wavelengths, similar to that of sunlight.

The measured depolarisation of light can be seen in Appendix B, and we obtained values of approximately 2 % that of horizontally polarised light and 4 % that of vertically polarised light were depolarised after passing through the glass and the water. This meant that for the polarised tests, the behaviour of the sea urchins was due to polarised light.

Intensity

An example composite image made from these extracted frames of the movement of a *Psammechinus miliaris* sea urchin exposed to 1000 lux of unpolarised halogen light, incident from the right, can be seen in Figure 3.5. The positions of the sea urchin are recorded with timestamps at 5 s, 60 s, 120 s, 180 s, 240 s, and 300 s. The first image was taken at 5 s to allow the water to settle after the placement of the sea urchin in the water tank. There is a progressive movement towards the left, away from the light source, which showcases negative phototaxis in this case. The complete data for the intensity tests for the three species can be found in Appendix C.

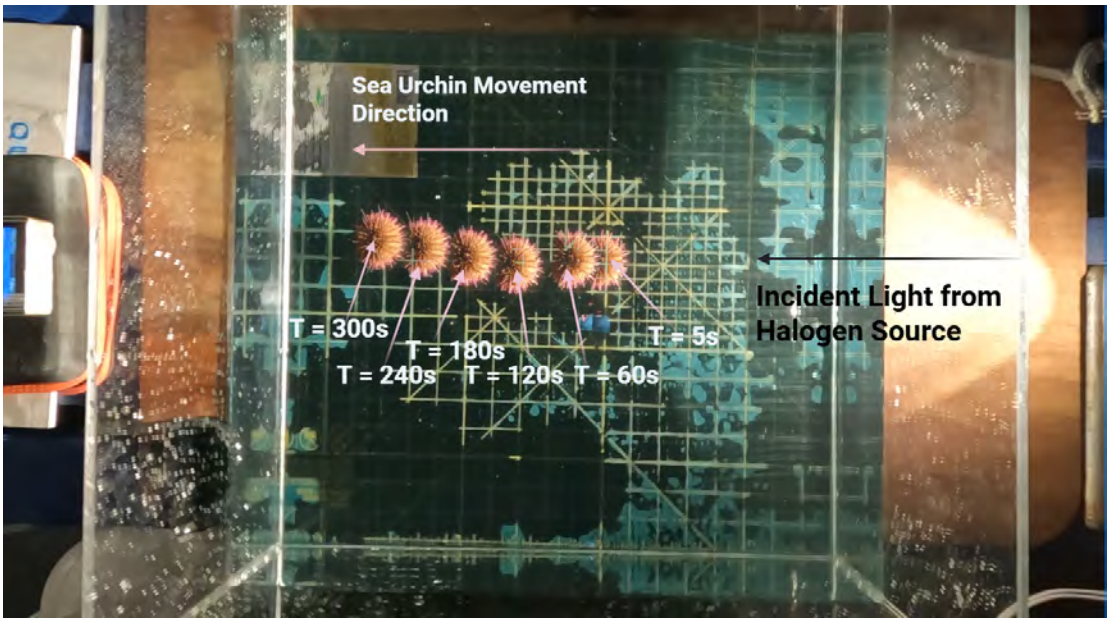

Figure 3.5: Movement of *Psammechinus miliaris* to 1000 Lux of unpolarised halogen light over a period of 5 min at 5 s, 60 s, 120 s, 180 s, 240 s and 300 s. The light source is incident from the right and the movement of the sea urchins are to the left. This showcases their negative phototaxis.

All species of sea urchins tested responded with negative phototaxis under illumination of unpolarised halogen light can be seen in Figure 3.6. It shows the negative phototactic velocities of *E. esculentus*, *P. lividus* and *P. miliaris* under different intensities. Here, we define negative phototaxis with positive velocities and positive phototaxis with negative velocities. There is a general trend of increased movement speeds under higher intensities for *P. lividus* and *P. miliaris*; however, a robust relation cannot be established due to the large error bars. Interestingly, in regards to the behaviour of *E. esculentus*, there does not seem to be an increase in the movement speed with higher intensities even though they also display a trend of negative phototaxis. However, this may be due to the fact that we have initially chosen larger and older individuals for clarity of the video recording. Indeed, observationally, larger individuals tend to have less movement, which could be due to their higher mass which may cause movements to be more difficult/slower. Thus, to mitigate this issue, further testing with *E. esculentus*, which is

the linear and circular polarisation tests, were performed with smaller individuals, which were more similar in sizes to the other species of sea urchins.

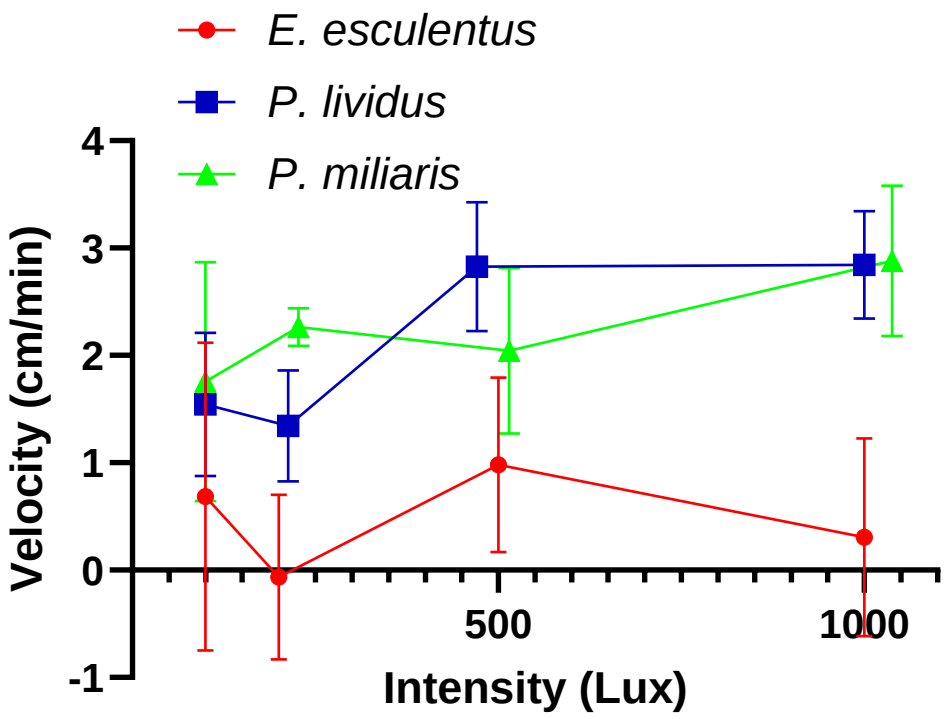

Figure 3.6: Negative phototactic response of *E. esculentus*, *P. lividus* and *P. miliaris* (n=4) to different intensities of unpolarised halogen light, showing the mean locomotive speeds and the standard error of the mean (SEM).

Examples of composite images of the sea urchin locations at 5 s (red) and 300 s (green) can be found for *E. esculentus* in Figure 3.7, for *P. lividus* in Figure 3.8 and for *P. miliaris* in Figure 3.9. All three species showcased negative phototaxis in general with some exceptions for some individuals of *E. esculentus* at 200 lux. However, overall, all species had consistent negative phototaxis from unpolarised halogen light.

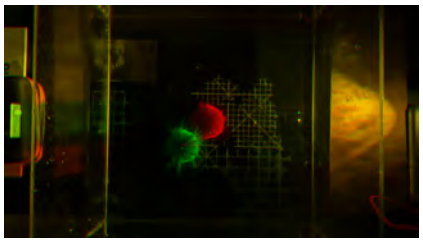

(a) 100 lux

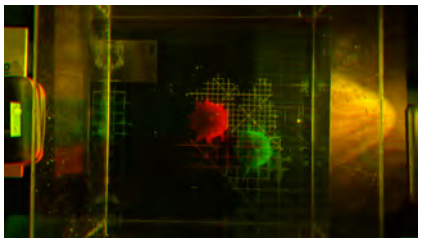

(b) 200 lux

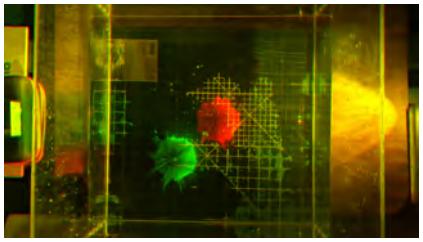

(c) 500 lux

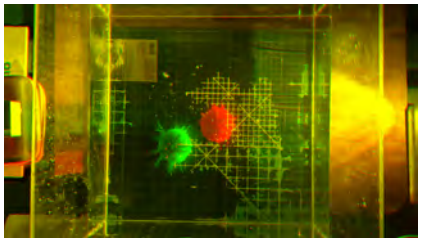

(d) 1000 lux

Figure 3.7: Composite images of the response of *E. esculentus* after 5 min of illumination of unpolarised halogen light of varying intensities; (a) 100 lux, (b) 200 lux, (c) 500 lux and (d) 1000 lux. Each image is a composite image of the positions of the sea urchin at 5 s (red) and 300 s (green) after the halogen light was switched on.

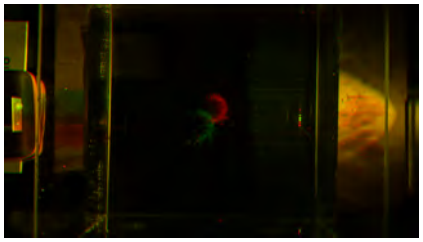

(a) 100 lux

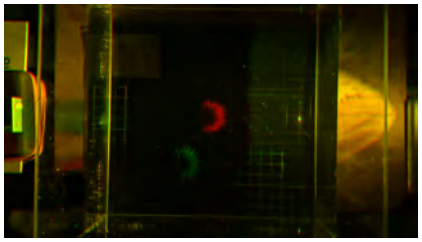

(b) 213 lux

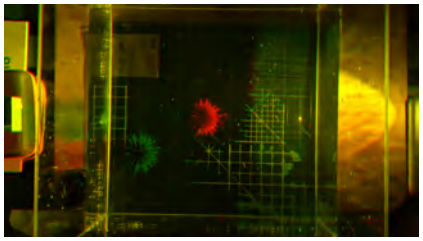

(c) 471 lux

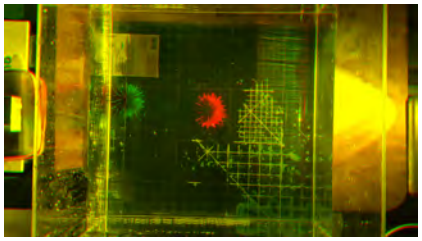

(d) 1000 lux

Figure 3.8: Composite images of the response of *P. lividus* after 5 min of illumination of unpolarised halogen light of varying intensities; (a) 100 lux, (b) 213 lux, (c) 471 lux and (d) 1000 lux. Each image is a composite image of the positions of the sea urchin at 5 s (red) and 300 s (green) after the halogen light was switched on.

(a) 100 lux

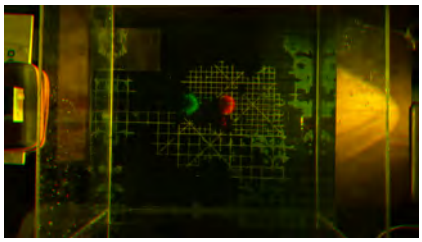

(b) 227 lux

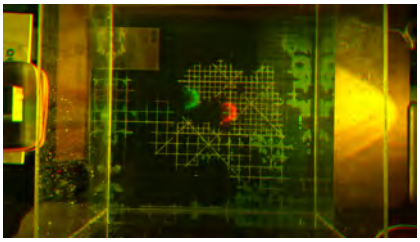

(c) 515 lux

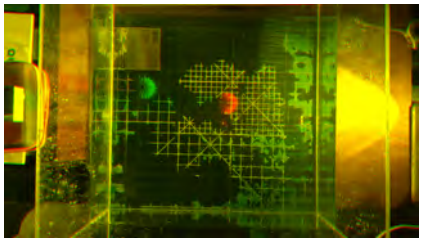

(d) 1038 lux

Figure 3.9: Composite images of the response of *P. miliaris* after 5 min of illumination of unpolarised halogen light of varying intensities; (a) 100 lux, (b) 227 lux, (c) 515 lux and (d) 1038 lux. Each image is a composite image of the positions of the sea urchin at 5 s (red) and 300 s (green) after the halogen light was switched on.

Linear Polarisation

The response of *P. lividus*, *E. esculentus* and *P. miliaris* under illumination of horizontally and vertically polarised halogen light can be seen in Figure 3.10. The complete results can be found in Appendix D.

We also confirmed that under the incidence of polarised light from both the right and left sides of the water tank, the sea urchins consistently responded with negative phototaxis. This confirms that not only do they have a mechanism of polarised light detection, but since they also consistently move away from the light source, their movements were caused by the incident light not due to some other environmental factor of the testing room where this experiment was performed. Table 3.1. shows the results of a t-test with Welch's correction, revealing the general trend of greater movement under horizontal polarisation compared to vertical polarisation for *P. lividus* and *E. esculentus*. But, it is not statistically significant with p-values of 0.2472 and 0.3220 respectively. However, *P. miliaris*, shows higher negative phototactic speeds under horizontal polarisation, compared to vertical polarisation with a p-value of 0.0282.

Once again, composite images of the merged frames extracted at 5 s (red) and 300 s (green) after illumination of linear polarised light can be seen for; *E. esculentus* in Figure 3.11, *P. lividus* in Figure 3.12 and, *P. miliaris* in Figure 3.13.

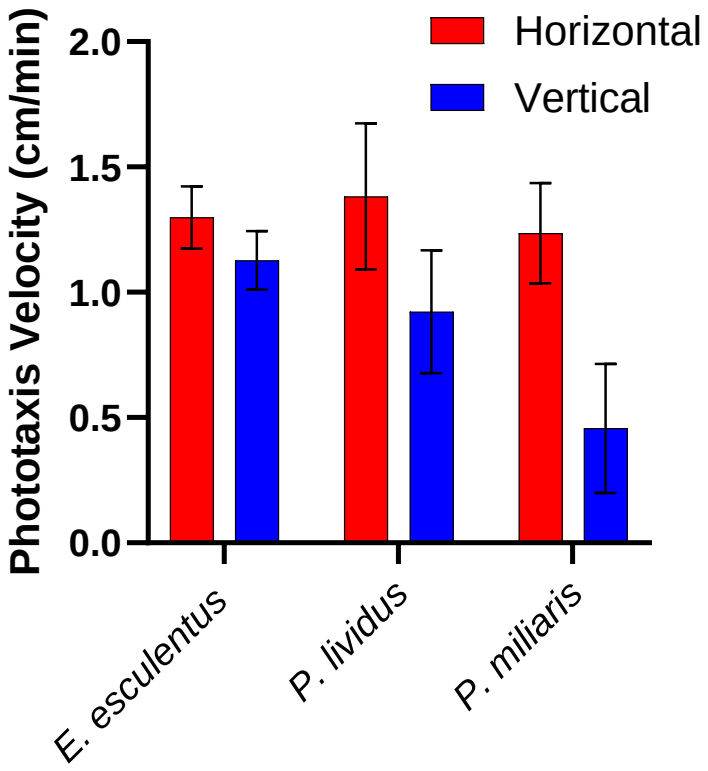

Figure 3.10: Response of *P. lividus*, *E. esculentus* and *P. miliaris* to horizontally and vertically polarised halogen light showing the average locomotive velocities and the SEM. On average, there is a larger phototaxis under horizontally polarised light than compared to the vertical polarisation.

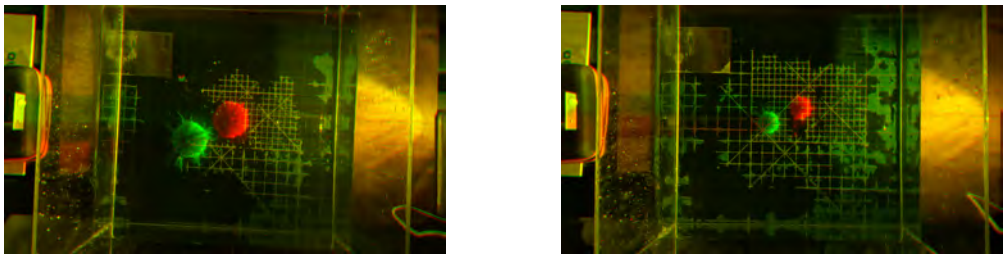

(a) Horizontal Polarisation (b) Vertical Polarisation

Figure 3.11: The response of *E. esculentus* after 300 seconds of polarised light illumination showing the initial (red) and final (green) positions of the sea urchins; (a) horizontal polarisation and (b) vertical polarisation. Again, we can see that their phototaxis is consistently negative for both polarisations and also similar in magnitude.

Species	p-value	z score
Paracentrotus lividus	0.2472	1.16 σ
Echinus esculentus	0.3220	0.99 σ
Psammechinus miliaris	0.0282	2.19 σ

Table 3.1: Statistical evaluation of the comparison of the movement speeds of phototaxis of the three species of sea urchins to horizontally polarised light compared to vertically polarised light.

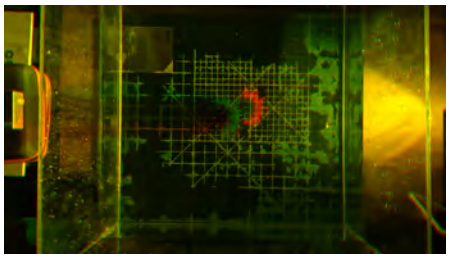

(a) Horizontal Polarisation

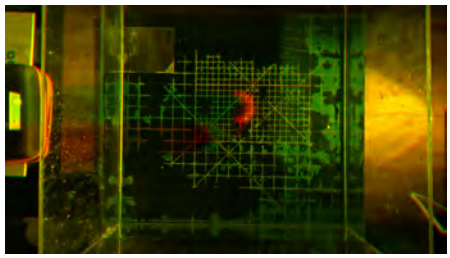

(b) Vertical Polarisation

Figure 3.12: The response of *P. lividus* after 300 seconds of polarised light illumination showing the initial (red) and final (green) positions of the sea urchins; (a) horizontal polarisation and (b) vertical polarisation. We can see that their phototaxis is consistently negative for both polarisations and also similar in magnitude.

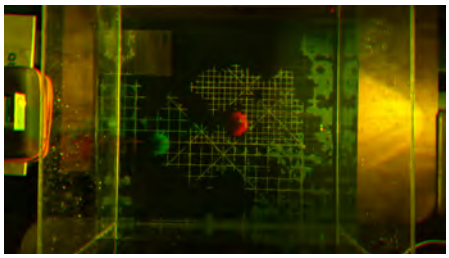

(a) Horizontal Polarisation

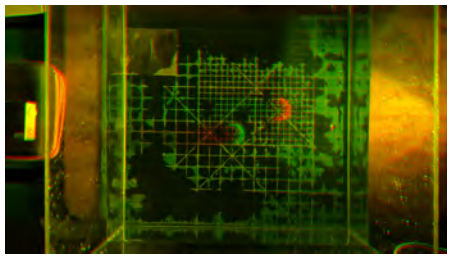

(b) Vertical Polarisation

Figure 3.13: The response of *P. miliaris* after 300 seconds of polarised light illumination showing the initial (red) and final (green) positions of the sea urchins; (a) horizontal polarisation and (b) vertical polarisation. Whilst there is negative phototaxis under both horizontal and vertical polarisations, this time, it appears that the movement is greater under horizontally polarised light when compared to vertically polarised light.

Circular Polarisation

Under circular polarisation, we also observed a negative phototaxis response for each of the sea urchin species, as shown in Figure 3.14. The complete results can be found in Appendix E.

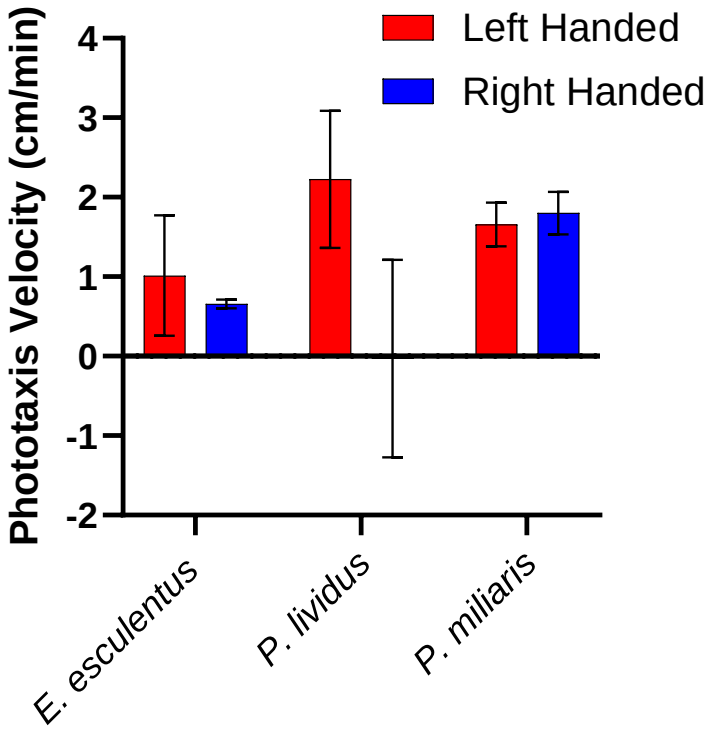

Figure 3.14: Response of *P. lividus*, *E. esculentus* and *P. miliaris* to left-handed and right-handed polarisations of light, showing the average and the SEM. There is a negative phototaxis under left-handed polarisation, however there does not seem to be an average direction under right-handed polarisation. This seems to indicate that they may not see right-handed polarised light.

Both *E. esculentus* and *P. miliaris* showcased negative phototaxis toward both circular polarisations. However, while *P. lividus* showed a clear negative phototactic response to left-handed polarised light, their response to right-handed polarised light appears random with a mean ca. 0.

Nonetheless, after performing a t-test with Welch's correction on the data sets for each species, there were no statistical differences between the responses of any species to left-handed and right-handed circular polarisations (see Table 3.2). The large errors were the result of the small sample size (n = 4), with more repetitions potentially clarifying if there is a difference in response, especially for *P. lividus*.

The merged composite images showing the initial (red) and final (green) positions of the sea urchins after 300 s of circular polarised light illumination can be seen for *E. esculentus* in Figure 3.15, for *P. lividus* in Figure 3.16 and for *P. miliaris* in Figure 3.19

Species	p-value	z score
Paracentrotus lividus	0.1923	1.30 σ
Echinus esculentus	0.6688	0.43 σ
Psammechinus miliaris	0.7230	0.35 σ

Table 3.2: Comparison of the movement speeds of phototaxis of the three species of sea urchins under illumination of left-handed circularly polarised light compared to right-handed circularly polarised light. None of the species had statistically significant different behaviours to illumination under left handed and right handed polarised light.

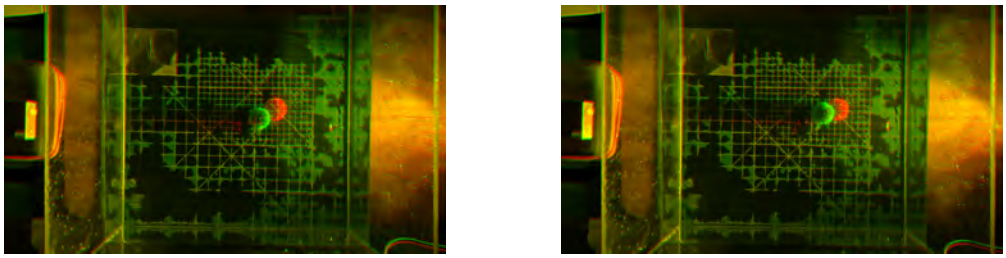

(a) Left-handed Polarisation (b) Right-handed Polarisation

Figure 3.15: The response of *E. esculentus* after 300 seconds of polarised light illumination showing the initial (red) and final (green) positions of the sea urchins; (a) left-handed and (b) right-handed polarised light. There is a consistent negative phototaxis for both circular polarisation states of light, and both degrees of phototaxis appear to be very similar.

3.4 Discussion

All three species of sea urchins tested; *P. lividus*, *E. esculentus* as well as *P. miliaris* exhibited negative phototaxis when exposed to unpolarised halogen light from the side. We note that in their natural habitats, the light source that the sea urchins would experience would mostly be from above, i.e., sunlight or moonlight. Although the lateral light setup does not mimic natural down-welling light, it is actually a common method used in echinoderm shade-seeking and shelter-location studies (e.g., Johnsen & Kier [277]). Here, a side-on lighting arrangement was chosen for several reasons. The first is that we wanted to test for phototaxis of the sea urchins as a response to the light source. If the light source was placed vertically above the sea urchins, the phototaxis direction would be along the vertical axis (z-axis). This was not feasible as the benthic adult sea urchins are unable to move down or swim up, rather, their movements are along the floor of the tank. Thus, to measure phototaxis, the light source had to be placed on the side. The second reason is due to the perceived polarisation modes of the sea urchins. Observationally, sea urchins have the ability to rotate along the z-axis (yaw), but not along the x-axis (roll) and the y-axis (pitch) [278]. This rotational freedom along the z-axis means that they have the ability to 'see' the two linear polarisation modes for light incident from above as the same.

The lack of rotational freedom along the x and y-axes also means that the two polarisation modes for light incident laterally would be fundamentally different from the point of view of the sea urchins. Finally, this geometry enhances contrast-based cues and was deliberately chosen to

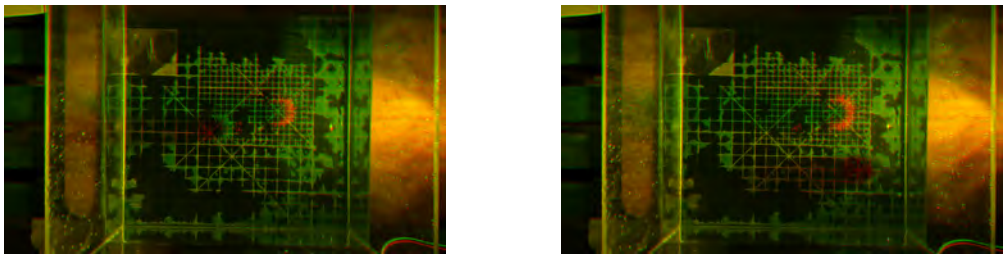

(a) Left-handed Polarisation (b) Right-handed Polarisation

Figure 3.16: The response of *P. lividus* after 300 seconds of polarised light illumination showing the initial (red) and final (green) positions of the sea urchins; (a) left-handed and (b) right-handed polarised light. Whilst there is negative phototaxis under left-handed polarised light, there is not a consistent negative phototaxis under right-handed polarised light. In fact, this example showcases positive phototaxis. The sporadic nature of their movement under right-handed polarisation indicates that their movements are not in response to the light and that they do not appear to be able to detect it or they can detect it but do not respond to it.

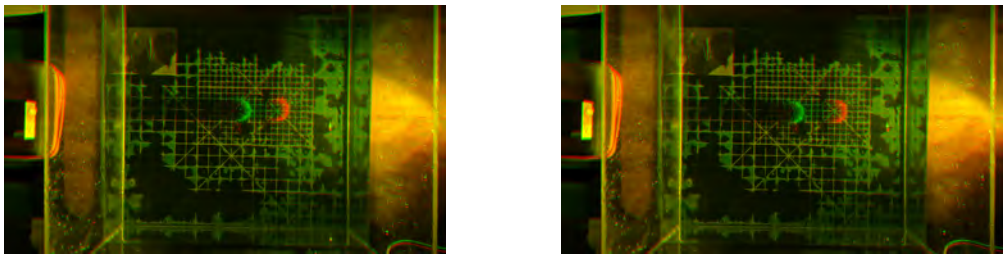

(a) Left-handed Polarisation (b) Right-handed Polarisation

Figure 3.17: The response of *P. miliaris* after 300 seconds of polarised light illumination showing the initial (red) and final (green) positions of the sea urchins; (a) left-handed and (b) right-handed polarised light. Once again, there is a consistent phototaxis for both circular polarisation states of light in both direction (negative) and magnitude.

maximise behavioural clarity under controlled lab conditions.

Since our analysis focused on gross displacement and directional response rather than fine kinematics, the low-resolution manual tracking is sufficient. The use of animal tracking software would not have enhanced the results in any significant way. In terms of their phototactic responses to varying intensities, both *Paracentrotus lividus* and *Psammechinus Miliaris* had a general trend of increased negative phototactic speeds for higher intensities. The avoidance of high intensities of light is consistent with Sun et al. [268] who discovered that under illumination of different intensities, the sea urchins spent more time in a region of lower intensity than in a region of higher intensity. Some proposed reasons for phototactic behaviour include protection against UV radiation, foraging for food, locating shelter, avoidance of predators, and embryonic development [268, 279–281]. Whilst *Echinus esculentus* also had a consistently negative phototactic response to the halogen light source, their movement speeds away from the light appeared

to be fairly consistent at different intensities. However, due to the small sample size (n=4), a robust conclusion about the relationship between intensity and movement speeds cannot be elucidated except for a general negative phototactic response.

For the linear polarisation tests, all three species showed negative phototaxis to both horizontal and vertical polarisations of light. Both *P. lividus* and *E. esculentus* did not have a statistically different response to the two polarisations, which is suggestive that they have the ability to detect but not differentiate between the two polarisation modes. We note that their mean velocities were higher under illumination of horizontally polarised light compared to vertically polarised light. An increase in the sample size could potentially reduce the error bars and separate the datasets.

However, the response of *P. miliaris* to horizontal and vertical polarisations was different, with a faster velocity under exposure to horizontally polarised light compared to that of vertical polarisation. This leads to the hypothesis that they have photodetectors capable of detecting both horizontally and vertically polarised light, but perhaps in unequal numbers or a biased distribution of tube feet. This might be the result of a greater number of their photoreceptors firing under illumination of horizontally polarised light compared to vertically polarised light and perceiving horizontal polarisations as brighter. This would also agree with their trend of increased movements under higher intensities seen previously.

Under the same assumption, one would also assume that *P. lividus* has an equal number of photoreceptors capable of detecting horizontal and vertical polarisations and that they see the two modes as equally bright, given their similar responses. However, the situation is more complex for *E. esculentus* , as they had no trend of increased phototaxis with increasing intensities. However, we note that the intensity tests for *E. esculentus* were performed with larger sea urchins that were more sluggish in their movements, and the polarisation tests were carried out with smaller urchins that resulted in greater movements overall. This warrants further testing for *E. esculentus*, especially under varying intensities with smaller individuals to elucidate a proper hypothesis on their photoreceptor arrangement.

One possible explanation for the differences in polarisation sensitivity between the three species is in their niche habitats, in particular the depths of water in which they live. Even though there is some overlap between the three species, generally both *P. lividus* and *E. esculentus* are found subtidally [282, 283] and *P. miliaris* are found more intertidally [284]. This means that, in particular, *P. miliaris* lives in shallower waters and is exposed to more sunlight. Whilst, the degree of polarisation decreases with increasing depth of water [248, 285, 286], increasing the path distance of light through seawater increases the probability of its interaction and subsequent depolarisation. Therefore, it is entirely possible that the detection of linear polarisation would be more useful for *P. miliaris* than for *P. lividus* and *E.s esculentus* given the abundance of linearly polarised light in shallower waters. Furthermore, due to how light enters underwater through refraction characterised by Snell's window, there is more horizontally polarised light than vertically polarised light [249, 287]. This could potentially explain the greater sensitivity of *P. miliaris* to horizontally polarised light.

One thing to note is that even though there is more of an abundance of horizontally polarised light than compared to vertically polarised light in shallower waters, in our experiment we assumed that the sea urchins do have the ability to rotate along the z-axis i.e yaw. However, the ocean floor is not flat like in our experiment tank, and the sea urchins exist in a variety of orientations, sometimes climbing up vertical surfaces. This effectively allows them to 'rotate' along the z-axis and see vertically polarised light as horizontally polarised light. Thus, this may

be a plausible explanation for why, whilst *Psammechinus miliaris* can differentiate between the two linear polarisations given the more abundant horizontally polarised light, they still have the ability to see vertically polarised light.

Under illumination of left-handed and right-handed circular polarisations, all three species displayed negative phototaxis for at least one polarisation mode. We did not find any statistically significant differences between the responses to the two polarisation modes for any species. However, looking specifically at the movement of *P.lividus* under exposure to right-handed polarised light, we can see that the mean movement velocity is quite close to 0. This is suggestive that their movements under right handed polarised light are random and not influenced by the light at all. This means that they do not have the ability to detect right-handed polarised light and the statistical similarities between their response to left-handed and right-handed polarisation are due to the relatively low sample size (n=4). Further testing with a larger size would be needed to determine if, in fact, they do have the ability to detect right-handed polarisations or not. If they do not, it would be a very interesting result, since the ability to differentiate between circular polarisations has only been observed so far in one other species in mantis shrimp [109].

We note that while our sample sizes are small, this is consistent with precedent studies on sea urchin behaviour under photo-irradiation (e.g. Sun et al. [268]), which have used similar group sizes. Due to the exploratory nature of this work, a conscious choice was made where we wanted to test for as many different polarisation modes on as many sea urchin species as possible at the detriment of large sample sizes. However the results of this work will lead to more focused future work, targetting the species that are potentially sensitive to polarisation.

Furthermore, whilst using cross polarisers meant that total depolarisation at the end of the tank was small ($\leq 4\%$), this does not preclude any spatial variations for depolarisation. However, if spatial variations did exist, it would be consistent between all trials, and thus any differences in behaviours would be initiated by the polarisation of light. As our experiment is designed as exploratory, our results give an indication of potential light and polarisation sensitivity. Additional follow up experiments should include a more comprehensive analysis of the spatial polarisation distribution throughout the tank, as well as more in depth study into the effects of the interactions between the light and the glass tank as well as the water. However, our initial results warrants the need for further exploration into the orientation and ordering of the photoreceptors of sea urchins.

3.5 Conclusion

In this chapter, we investigated the sensitivity of three sea urchin species, namely *P. lividus*, *E. esculentus* , and *P. miliaris*, to halogen light of varying intensities, as well as their sensitivity to linear and circular polarisation, with light incident laterally.

We recorded their phototactic responses to the different lighting regimes over a period of 5 minutes and measured their locomotive speeds under different illuminations. The three species showed a trend of increased negative phototaxis, but only *P. lividus* and *P. miliaris* appeared to be sensitive to the light intensity.

These three species also seem sensitive to linear polarisation, though only *P. miliaris* seems to posses the ability to differentiate between the two linear polarisation states, with a higher

negative phototaxis under illumination of horizontal polarisation compared to vertical polarisation.

Compared to the other two species, *P. miliaris* generally lives in shallower waters. Not only does this mean that there will be a higher degree of polarisation seen by these sea urchins but due to the mechanism of how light enters sea water through Snell's window, there will be a higher abundance of horizontally polarised light. Thus, this may explain why *P. miliaris* could have the ability to differentiate polarisation, including a greater sensitivity to horizontal polarisation.

When illuminated under circularly polarised light, the three species also display negative phototaxis. However none of the three species of *P. lividus*, *E. esculentus* and *P. miliaris* displayed the ability to differentiate between the two circular polarisation states from a statistical standpoint. However, under closer examination of *P. lividus*, it can be seen that they had no average phototaxis under right handed polarised light whilst left handed polarisation led to negative phototaxis. Statistical similarities were then due to a small sample size resulting in large error bars. If this behaviour is consistent under more testing, then it could be possible that *P. lividus* has the rare ability to differentiate between circular polarisations of light.

Polarisation sensitivity in other species arises due to a specific ordering of photoreceptor cells, and in particular an alignment of chromophores [121, 123]. This results in a higher detection of photons with their polarisation direction in the same direction as the aligned chromophores, allowing for a sensitivity to polarisation. A subsequent investigation into the ordering of the photoreceptors of the sea urchins, especially in *P. miliaris* may reveal specific mechanisms. Furthermore, as their photoreceptors are encased in calcite, a birefringent material. In particular, a deeper investigation is needed in their photoreceptive mechanisms in how their skeletal structures interacts with polarisation. This is particularly interesting as calcite structures are already theorised to affect polarisation sensitivity in brittlestars [288].

This would pave the way for the development of a novel polarisation detection method at visible wavelengths that mimics the polarisation sensitivity of these sea urchins. A new detector developed on this mechanism would not only have the ability to detect polarisation directly but would also be of much smaller size with greater ease of production in both costs and scale.

3.6 Appendix

Appendix A: Spectral Analysis

We have chosen a light source that was representative of sunlight in terms of spectral composition. The spectrum of the halogen light source can be seen in Figure 3.18. We can see that it has a continuous spectrum over the visible wavelengths (400-700 nm). While all visible wavelengths of sunlight are present in the spectrum of the halogen light source, we note that sunlight peaks at approximately 500 nm or green light, whereas halogen light peaks at 650 nm or red light

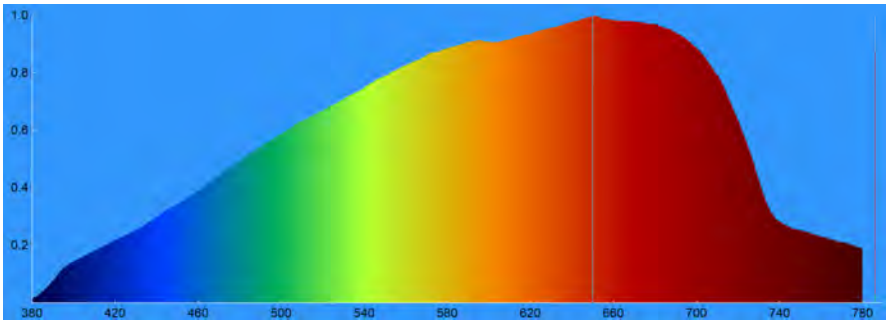

Figure 3.18: Spectrum of the Halogen light source with the x-axis being the wavelength(nm) and the y-axis being the intensity(a.u.).

Appendix B: Cross Polarisation

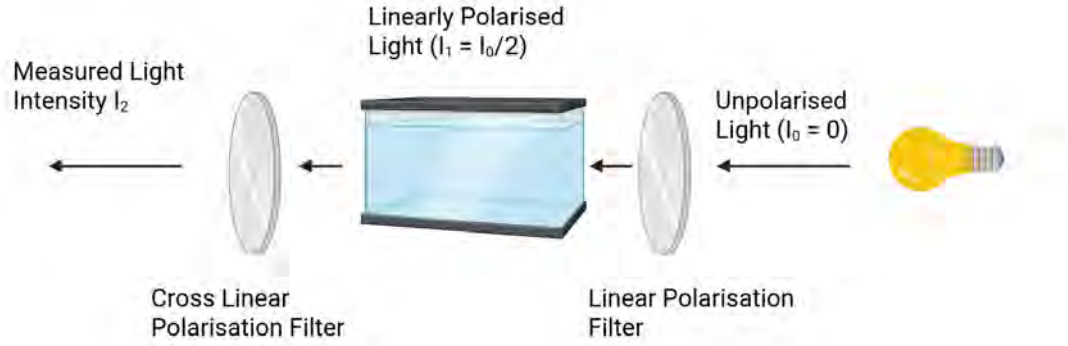

Figure 3.19: Cross polarisation test for depolarisation of the incident light in the experimental setup to measure potential depolarisation of light as it traverses through the water tank.

The cross polarisation test is outlined in Figure 3.19. Without any filters, the unpolarised halogen source would have an intensity of I_0. A linear polariser only lets through light with polarisation that is parallel to the orientation of the filter. This would cut the intensity of unpolarised light in half to be $I_1 = I_2/2$. We can measure any potential depolarisation by using a cross polariser (a linear filter that is orientated orthogonally to the first filter). This would block all the now polarised light such that $I_2 = 0$. However, any depolarisation due to the experimental setup would allow for light to still pass through. Full depolarisation would mean that, once again the intensity would be cut in half such that $I_2 = I_0/4$ with the ratio $I_2 : I_1 = 1 : 2$. Therefore it is possible to determine the amount of light that retains it polarisation after passing through the water tank with:

$$\text{Polarisation } \% = \left(1 - 2\frac{I_2}{I_1}\right) \times 100 \tag{3.2}$$

The results of the cross polarisation tests can be seen in Table 3.3, which shows that 98% of horizontally polarised halogen light and 96% of vertically polarised halogen light retained its polarisation vector. Thus we can safely say that the sea urchins were subjected to polarised light, with the polarisation vectors being in the orientations claimed.

Polarisation	Intensity	X-Polariser Intensity	Intensity Ratio	Polarisation %
Horizontal	243.43	2.86	0.012	98%
Vertical	232.92	4.45	0.019	96%

Table 3.3: Measured intensities of the halogen light source after one linear filter and after its subsequent cross polarising filter. 100 % depolarisation will result in a ratio of 0.5 and no depolarisation will result in a ratio of 0.

Appendix C: Intensity

The complete data for sea urchin phototaxis under different intensities of unpolarised halogen light can be seen for *E. esculentus*(n=4) in Table 3.4, for *P. lividus*(n=4 for 100 & 471 lux and n=3 for 213 & 1000 lux)[1] in Table 3.5 and for *P. miliaris*(n=4) in Table 3.6.

Intensity (Lux)	100	200	500	1000
Test 1	0.620458015	0.294455	-1.35659	-0.18929
Test 2	-3.039192651	1.188335	2.019118	-2.04015
Test 3	1.219883555	0.546844	1.093689	2.20841
Test 4	3.933072843	-2.29254	2.176861	1.240916
Mean	0.6836	-0.06573	0.9833	0.3050
SEM	1.435	0.7657	0.8157	0.9239

Table 3.4: Raw data for movement velocities (cm/min) of *E. esculentus* at different intensities (lux). Positive values indicate negative phototaxis and negative values indicate positive phototaxis.

[1]This was due to data one test being unusable at 213 and 1000 lux.

Intensity (Lux)	100	213	471	1000
Test 1	2.511206	2.226534	3.9752289	2.013031187
Test 2	0.081335	1.372521	3.751558	3.944727781
Test 3	0.752345	0.437173	1.606358	3.436386572
Test 4	2.836544	N/A	1.982531	N/A
Mean	1.545	1.345	2.829	3.131
SEM	0.6691	0.5167	0.6039	0.5781

Table 3.5: Raw data for movement velocities (cm/min) of *P. lividus* at different intensities (lux). Positive values indicate negative phototaxis and negative values indicate positive phototaxis.

Intensity (Lux)	100	227	515	1038
Test 1	3.454504	2.348228	0.688813559	4.112008
Test 2	-0.48008	1.742907	1.826399589	1.377627
Test 3	3.871967	2.473467	4.247683616	4.038952
Test 4	0.177422	2.49434	1.419373395	1.993385
Mean	1.756	2.265	2.046	2.880
SEM	1.113	0.1769	0.7708	0.7014

Table 3.6: Raw data for movement velocities (cm/min) of *P. miliaris* at different intensities (lux). Positive values indicate negative phototaxis and negative values indicate positive phototaxis.

Appendix D: Linear Polarisation

The complete data for sea urchin phototaxis under horizontal and vertical linear polarisations of halogen light with an intensity of 300 lux can be found for *E. esculentus*(n=17) in Table 3.7, for *P. lividus*(n=8) in Table 3.8 and for *P. miliaris*(n=12 for horizontal and n=10 for vertical)[2] in Table 3.9.

[2] 2 videos of vertical polarisation response rendered unusable.

Polarisation	Horizontal	Vertical
Test 1	0.609942	0.5784
Test 2	1.977053	1.1883
Test 3	0.746653	0.7572
Test 4	1.346078	0.6520
Test 5	1.545887	1.3881
Test 6	0.546844	0.7361
Test 7	1.608984	1.4723
Test 8	1.367111	1.5143
Test 9	1.493306	1.6195
Test 10	1.125237	0.5784
Test 11	1.104205	1.3671
Test 12	0.967494	0.4417
Test 13	2.37667	1.9140
Test 14	0.820267	0.9990
Test 15	2.019118	1.9665
Test 16	1.051624	0.7887
Test 17	1.36974	1.2094
Mean	1.299	1.128
SEM	0.1237	0.1165

Table 3.7: Raw data for movement velocities (cm/min) of *E. esculentus* under horizontal and vertical polarisations.

Polarisation	Horizontal	Vertical
Test 1	0.589676	0.740231
Test 2	1.596191	1.596191
Test 3	0.41684	0.41684
Test 4	1.53519	1.53519
Test 5	1.006516	0.904847
Test 6	1.891029	1.911363
Test 7	1.026849	0.050834
Test 8	2.999213	0.22367
Mean	1.383	0.9224
SEM	0.2919	0.2444

Table 3.8: Raw data for movement velocities (cm/min) of *P. lividus* under horizontal and vertical polarisations.

Polarisation	Horizontal	Vertical
Test 1	1.221078582	-0.636630714
Test 2	1.388063688	0.647067283
Test 3	3.141407293	0.511391885
Test 4	1.294134566	1.5863585
Test 5	1.043656908	-0.584447869
Test 6	1.221078582	0.605321007
Test 7	1.054093477	0
Test 8	1.189768875	1.868145865
Test 9	1.523739086	0.062619414
Test 10	0.500955316	0.510947776
Test 11	0.90798151	N/A
Test 12	0.34440678	N/A
Mean	1.236	0.4571
SEM	0.1995	0.2577

Table 3.9: Raw data for movement velocities (cm/min) of *P. miliaris* under horizontal and vertical polarisations.

Appendix E: Circular Polarisation

The complete data of sea urchin phototaxis under left handed and right handed circular polarisations of halogen light with an intensity of 300 lux can be found for *E. esculentus*(n=4) in Table 3.10, for *P. lividus*(n=4) in Table 3.11 and for *P. miliaris*(n=4) in Table 3.12.

Polarisation	Left Handed	Right Handed
Test 1	-0.3891	0.799234
Test 2	0.525812	0.546844
Test 3	3.154871	0.599426
Test 4	0.767685	0.683555
Mean	1.236	0.4571
SEM	0.1995	0.2577

Table 3.10: Raw data for movement velocities (cm/min) of *E. esculentus* under left and right handed circular polarisations.

Polarisation	Left Handed	Right Handed
Test 1	3.882404	2.306481767
Test 2	2.556959	1.763780175
Test 3	-0.19829	-1.283697997
Test 4	2.661325	-2.911802773
Mean	2.226	-0.03131
SEM	0.8622	1.243

Table 3.11: Raw data for movement velocities (cm/min) of *P. lividus* under left and right handed circular polarisations.

Polarisation	Left Handed	Right Handed
Test 1	2.431721	1.889019004
Test 2	1.315008	1.857709296
Test 3	1.669851	2.37953775
Test 4	1.210642	1.074966615
Mean	1.657	1.800
SEM	0.2764	0.2697

Table 3.12: Raw data for movement velocities (cm/min) of *P. miliaris* under left and right handed circular polarisations.

Chapter 4

Probing High Energy Polarisation With Gold Nanorods

The following project presented in this chapter is adapted from the submitted manuscript titled "Towards a Novel Method of X-ray Polarimetry with Aligned Gold Nanorods" by Ben Li, Livia Salvati Manni, Zhenxu Yang, Alex Yin, Ken-Tye Yong, Gregory Warr and Céline Bœhm.

Author Contributions:

- Ben Li: Conceptualisation (main), Methodology (main), Investigation (main), Data Analysis (main), Writing (original draft).
- Livia Salvati Manni: Conceptualisation (supporting), Methodology (supporting), Investigation (supporting), Writing(review and editing).
- Zhenxu Yang: Investigation (supporting), Writing(review and editing), Gold Nanorod Synthesis (supporting).
- Alex Yin: Gold Nanorod Synthesis (Main).
- Ken-Tye Yong: Writing (review), Supervision (supporting).
- Gregory Warr: Methodology (supporting), Writing (review), Supervision (supporting).
- Céline Bœhm: Methodology (supporting), Investigation (supporting), Writing(review and editing), Supervision (main).

The work done in the previous chapters outline work towards the development of linear and circular polarimetry in the IR, visible, and potentially the UV domains of light. However, there is much interest, particularly in the astroparticle physics community, to detect polarisation for higher energy photons. These photons would be outside the scope of any detectors developed using biological mechanisms due to damage caused by high energy photons to biological matter. This chapter is influenced by the desire to rectify this problem.

Motivation for this work stems from the fact that there has been much effort to develop sensitive high energy (X-ray and γ-ray) polarisation detector recently, with potential applications for a wide variety of fields such as cosmology, particle physics, astrophysics, medical science,

material science and high energy imaging. However, current technology is constrained both in the energy range and availability due to size, costs, and production difficulties. In this work, we propose a novel mechanism for detecting X-ray polarisation that could mitigate these issues. We showed that aligned gold nanorods in liquid crystals led to an anisotropic response when exposed to polarised X-rays under small-angle X-ray scattering (SAXS), which can be exploited to reconstruct the polarisation of the incident X-rays. The scattered X-rays directional differences that arise can be used in the development of novel detectors that would be on a much smaller scale, more cost effective and much easier to manufacture compared to current and proposed options.

4.1 Introduction

Polarised X-rays are at the heart of many X-ray imaging techniques such as magnetic X-ray diffraction [174], magnetic Compton scattering [175] and X-ray circular dichroism [176] which are used to study materials interacting with a magnetic field. Additionally, X-ray polarisation can also be used to study the magnetic sublevels of charged particle collisions [177–179]. At higher energies, the polarisation of γ-rays is also relevant in astrophysics in order to understand the nature of astrophysical sources [180, 181], the origin of cosmic rays [182], the nature of black holes and their role in the evolution of galaxies [183–185] amongst many other uses.

Despite the importance of polarisation, there are currently very limited options for its detection at high energy. Generally speaking, current X-ray and γ-ray polarimetry detection can be classified into two main techniques. The first relies on the dependence of polarisation on the direction of photoelectron emission [89]. The direction distributions of the ejected photoelectrons are dependent on the polarisation vector (E-vector) of the incident X-ray. Thus, their reconstruction can be used to determine the polarisation of the incident X-ray. This method is used by the IXPE (Imaging X-ray Polarimetry Explorer) [210, 211], which is currently the only X-ray polarisation detector in use. There are several proposals [212, 213] including the HypeX project which uses the same concept with improved resolution and effective X-ray energy range which is currently in development [214].

The second method uses the anisotropy of Compton scattering [215, 216]. The cross section (interaction rate) of Compton scattering is dependent on the polarisation of the incident photon and the azimuthal scattering angle [91]. The mapping of the distribution of the scattered photons can lead to a reconstruction of the polarisation of the incident photons. Current γ-ray polarisation detection projects includes; Polar-2 [217], GAP [218], Astrosat-CZTI (Cadmium-Zinc-Telluride Imager) [219], COSI (Compton Spectrometer and Imager) [220] and INTEGRAL (INTErnational Gamma-Ray Astrophysics Laboratory) [221].

The photoelectron detection method has difficulties associated with the sensitivity of the instrument and the reconstruction of photoelectron tracks [90]. The Compton detection method requires detailed comparison to Monte Carlo simulations, in which the projected azimuthal scattering angle is highly dependent on the orientation of the instrument as well as on multiple scattering events. Thus, instruments which utilises one of these two techniques are generally quite large and have complex electronics to achieve the sensitivity required to accurately determine the polarisation of the incident photons. Furthermore, both the photoelectric effect and Compton scattering are effective at different energies [222, 223]. This means that the current and proposed detectors mentioned above are limited in ranges for incident photon energies; and that one detector that is effective in one energy range would not be in the other energy range. Additionally, there is no current instrument capable of high-energy γ-ray polarimetry (> 10 MeV). Methods such as the one by Wojtsekhowski et al. [224] are proposed which make use of the E-vector dependence of pair production. In pair production, the directions of the created electron and positron are sensitive to the polarisation of the photon, their plane tending to be parallel to the polarisation vector of the incident photon [95]. However, multiple scattering of the produced particles need to be considered to accurately determine the photon polarisation and this presents a tremendous challenge [93].

In this work, we show that the polarisation of an incident X-ray beam can be measured through its scattering pattern off aligned gold nanorods, thus paving the way for the development of a novel polarisation detector that would be sensitive to all energies where Thomson and

Compton scatterings occur. To this end, we used the small-angle X-ray scattering (SAXS) beamline at the Australian Synchrotron as a source of polarised X-rays. We set up an experiment to measure the azimuthal anisotropy of scattered X-rays off align gold nanorods (AuNRs), utilising cetyltrimethylammonium bromide (CTAB) for alignment. To do this, we investigated the scattering images as a function of the angle subtended by the polarisation vector of the X-ray and the long axis of the AuNRs. The dependence would allow for the reverse engineering of the polarisation of an unknown source of photons.

This chapter is presented in the following way: I give a brief introduction to small angle X-ray scattering in Section 4.2. In Section 4.3, we discuss some X-rays interactions relevant to this work, including the mathematical framework of Thomson and Compton scattering of polarised photons and free electrons. Section 4.4 . In Section 4.5 we outline the experimental setup. Section 4.6 showcases the results. The discussion and conclusion can be seen in Section 4.7 and Section 4.8 respectively.

4.2 Small Angle X-ray Scattering (SAXS)

Small angle X-ray scattering (SAXS) is an imaging method used for the study of systems of small particles, usually in solution. It is commonly used to provide low-resolution information on the shape, size, structure state, composition, orientation, and dynamics of biological macromolecules such as proteins, nucleic acids, amino acids, and polypeptides [195]. Like microscopy, SAXS utilities the scattering and absorption interactions of photons and matter and the resulting contrast created by those interactions. However, unlike microscopy, SAXS uses X-ray interactions instead of visible light. X-rays are electromagnetic waves (EM) on the electromagnetic spectrum, taking a range of wavelengths between 0.01 nm and 10 nm. X-rays, like all other types of electromagnetic radiation, have a polarisation defined by the direction of their electric field oscillation.

However, because of the short wavelengths of X-rays, SAXS can also be used to resolve systems on a much smaller scale than compared to miscroscopy, such as systems of nanoparticles[289]. Recently, SAXS has also been useful in characterising the structure of surfactants and their macromolecular interactions [290].

Typically in SAXS, the scattering angle of the X-rays, $\theta \leq 5^{\circ}$. The intensity $I(q)$ is compared with the scattering vector, q, in linear reductions [291], but we will also compare it as a function of the azimuthal angle, ϕ, around the sample. Because the X-rays are monochromatic, the scattering can be coherent, which also allows interference patterns to be seen in the scattering results arising from the constructive and destructive interference of X-rays interacting with different layers of the sample.

Although SAXS is generally used to study the structures and shapes of systems of small particles, this work aims to do something different. Rather than having a predetermined system of small biological macromolecules of unspecified sizes and shapes, we will introduce specific nanoparticles of known shapes and sizes and will also be setting their arrangement. This allows us to predetermine the expected scattering pattern under X-ray interactions. Using this knowledge, this project therefore aims to study the effects of changing the polarisation of the incident X-rays on the expected scattering pattern of SAXS. X-rays interact with matter in two main fashions: absorption and scattering. Both interactions mainly involve the interaction of the X-ray and atomic electrons in the materials being exposed to the X-rays. Absorption of

X-rays results in the photoelectric effect whilst scattering of X-rays can be inelastic (Compton) or elastic (Rayleigh or Thomson) [292].

SAXS technical details

At the heart of SAXS are the interactions between X-rays and the atomic electrons of the sample. When atoms inside a sample are bombarded with X-rays, they will scatter the incident radiation in all directions, giving the background radiation. There will also be additional scattering of the X-rays due to the arrangement, density, shapes, and type of atoms that make up the particles. Particles similar to the sizes of X-ray wavelengths will interact more strongly with the incident X-rays, resulting in more scattered photons. By measuring the intensity distribution of the scattered radiation against the background, conclusions about the macroscopic and microscopic structures of the sample can be drawn.

Per the name, SAXS utilises scattering of X-rays off the sample. When the incident X-ray energy is high[1], the interaction is Compton and when the energy is low, the interaction is Thomson. The scattering X-rays can then be detected via an absorption of the scattered photon. There are several types of detectors including; solid state detectors [293], gas filled detectors [294] and scintillation detectors [295].

In solid-state detectors, electron-hole pairs are created when incident X-rays ionise electrons into the conduction band of the semiconductor [296]. Electrodes create an electric field which moves the electron-hole pair and creates an electric pulse. Gas-filled detectors contain an inert gas such as Argon or Xenon which has relatively high first ionisation energies[2]. An X-ray can then ionise the gas, which creates a negative electron and a positive ion pair. An applied electric field can then create an electric pulse from these charged particles [297]. Scintillation detectors use a scintillating material such as Sodium Iodide (NaI) or Caesium Iodide(CsI) which are excited when an X-ray is absorbed. When the molecule de-excites, a photon[3] is released [298] and this secondary emitted photon is subsequently detected. In all detection mechanisms, the signal is amplified, and the pulses created as an effect of X-ray absorption are counted.

SAXS uses the deflection of X-rays by bound electrons in atoms. When X-rays are elastically scattered at atoms via Thomson scattering, each atom acts as a source of X-rays emanating waves radially outward in the shape of a sphere (3 dimensional) or a circle (2 dimensional). Thomson scattering results in coherent waves, thus the scattering X-rays can form interference patterns, with constructive interference for waves in phase and destructive interference for waves out of phase [299]. These interference patterns depend on the path difference of the X-rays and also their wavelengths. When two X-rays with a path difference of integer wavelengths interact, the effect is constructive interference, and when the path difference is half integer wavelengths, destructive interference occurs (see Equation 4.1).

$$PD = d_1 - d_2 = \begin{cases} m\lambda, & \text{for constructive interference} \\ \left(m - \frac{1}{2}\right)\lambda, & \text{for destructive interference} \end{cases} \tag{4.1}$$

Here PD is the path difference of the X-rays, d_1 and d_2 are the paths taken by the two X-rays, m is an integer and λ is the X-ray wavelength. The path difference also depends on the

[1] $\gtrapprox$ 500 KeV for scattering off electrons
[2] 10-20 eV
[3] Usually in the visible/UV wavelengths

orientation of the sample, the scattering angle θ, and the distance between the atoms on the sample. This method is the basis for X-ray crystallography[300], and it follows Bragg's law of diffraction. When incident X-rays strike a lattice with lattice spacing d, at an angle of θ the path length between X-rays striking different layers of the lattice is $2d\sin\theta$. Therefore constructive interference occurs when $2d\sin\theta = m\lambda$ and destructive interference occurs when $2d\sin\theta = (m - 1/2)\lambda$ (see Figure 4.1).

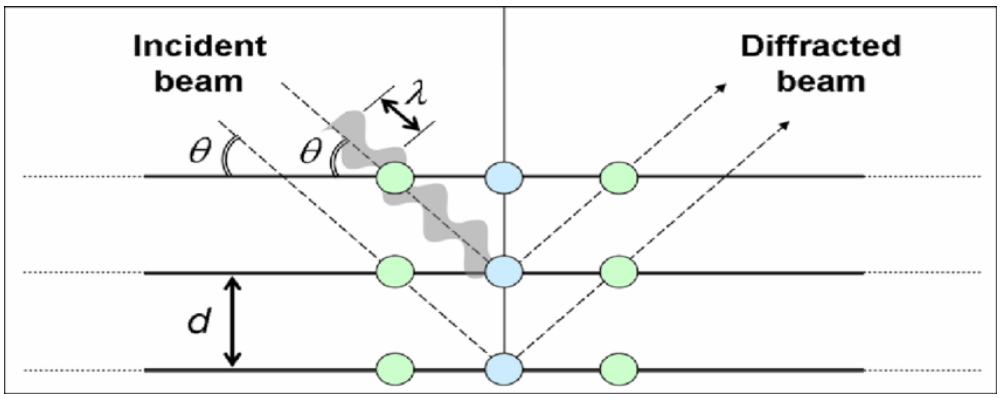

Figure 4.1: X-ray diffraction in a lattice. X-rays scattering off atoms in different layer of the lattice will have different path lengths depending on the angle of incidence θ and the lattice spacing d. Credit: N. Venkatathri et al [301]

The scattered radiation is then recorded by the detector, whilst the direct beam is usually stopped [302]. Scattered X-rays are characterised by their momentum transfer or scattering vector q:

$$q = \frac{4\pi \sin\theta}{\lambda} \tag{4.2}$$

where θ is half the angle between the scattered and incident X-rays and λ is the wavelength of the monochromatic X-rays. q has units of $[\text{Length}]^{-1}$ which details the structure in reciprocal space. Due to this reciprocal nature of q, the low-q region shows the overall size and shape of the sample whilst the high-q region shows the smaller structural features [303].

The scattering vector is also defined to be the difference between the wave vector of the scattered X-ray and the initial X-ray. The wavenumber (magnitude of the wave vector) is defined to be:

$$k = \frac{2\pi}{\lambda} \tag{4.3}$$

The momentum of a photon is defined to be:

$$\begin{aligned} p &= \frac{E}{c} \\ &= \frac{hf}{c} \\ &= \frac{h}{\lambda} \end{aligned} \tag{4.4}$$

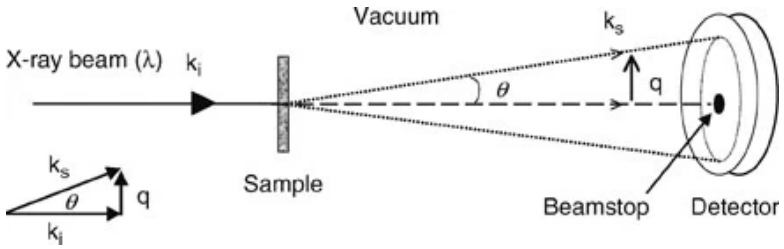

Figure 4.2: Schematic layout of SAXS, showing the incident and scattered X-rays as well as the q-vector [291].

Combining Equation 4.3 and Equation 4.4 we can see that:

$$k = \frac{p}{2\pi h} \tag{4.5}$$

Or in other words, the wave vector is also a measure of the momentum of a wave. The scattering vector q is

$$q = k_s - k_i \tag{4.6}$$

where k_s is the wave-vector of the scattered X-ray and k_i is the wave-vector of the incident X-ray. Thus, q is the change in momentum of the X-ray. The X-ray scatters off an electron and, by conservation of momentum, the change in momentum in the X-ray is also equal to the opposing change in momentum in the electron. Therefore, the scattering vector is also a measure of momentum transfer from X-ray to electron[4]. Figure 4.2 depicts a schematic layout of SAXS, showing the incident X-ray with momentum k_i, the scattered X-ray with momentum k_s and the scattering vector q. The image formed by the detector shows a count of X-rays as a function of the scattering vector, $I(q)$ vs. q. Small values of q are scattered X-rays with small momentum transfer and large values of q are scattered X-rays with a large momentum transfer.

The interference pattern of the sample is determined by summing up the interactions of X-rays with every electron inside the sample. The overall pattern is characteristic for the shape of the particle that the X-rays interact with; this is known as the form factor [304]. In a sample with numerous particles, the scattering pattern corresponds to the form factor of a single particle if:

1. The particles are all identical in shape and size, i.e. a monodisperse sample.
2. The particles are far away from each other, i.e. a dilute sample.

A dilute sample is one such that the distances between particles in the sample are larger than the wavelength of the X-rays. For a sample with varying particle sizes or polydisperse samples, the form factor of all particles must be summed to obtain the total scattering pattern. Samples that are not dilute, i.e. concentrated, if they have the distances between particles on the same order of magnitude as the X-ray wavelengths. For such samples, the interference pattern contains contributions from their neighbouring particles as well. This is known as the structure factor,

[4]Or vice versa

and it contains information about the positions of the particles with respect to each other. In a highly ordered and periodic structure, this results in a Bragg peak and it shows the distance between layers of aligned particles with Bragg's law [305]:

$$d = \frac{2\pi}{q_{\text{peak}}} \tag{4.7}$$

where d is the distance between the ordered layers of particles and q_{peak} is the q-value of the peak location.

When the sample develops long range ordering of particle packing, it develops a lattice structure and has crystal symmetry. There are several types of crystal symmetry including

- Lamellar symmetry, which are simple layers.
- Cubic symmetry, where the crystal has repeating unit cells in the shape of a cube.
- Hexagonal symmetry, where the crystal has repeating unit cells in the shape of hexagons.

The distance between the layers depends on the structure and the angle at which you view the structure, which gives different ratios of the Bragg peaks. The ratios are as follows:

- 1, 2, 3, 4, 5,... for lamellar symmetry.
- 1, $\sqrt{2}$, $\sqrt{3}$, 2, $\sqrt{5}$,...for cubic symmetry.
- 1, $\sqrt{3}$, 2, $\sqrt{7}$, 3,... for hexagonal symmetry.

Therefore, the type of ordering of a sample can be determined from the ratios of the peak locations on a scattering image.

The orientation of the particles in the sample can also be determined from the scattering image. When the sample is randomly oriented, the scattering pattern will be concentric circles with equal intensities at each point along the circle [303]. This is because there is no preferred scattering direction or azimuthal angle ϕ. An orientated sample will have a preferred scattering direction, and thus will result in intensity modulations, where there will be regions of high intensity and regions of low intensity depending on the orientation of the sample.

Rheology and RheoSAXS

Rheology is the study of the deformation and flow behaviour of materials [306]. One focus of rheology is the study of shear stress on viscous liquids. Viscosity is the resistance to flow due to internal friction, as particles and molecules in a liquid are forced to slide along each other.

Shear is applied to a sample when there is a shear force at the interface between the sample and the material touching the sample or between two layers of a sample. This may be caused by friction between the two materials as the sample flows along, or between two layers of the sample with different flow rates [307]. The shear stress is defined as:

$$\tau = \frac{F}{A} \tag{4.8}$$

where τ is the shear stress, F is the shear force and A is the shear area. The units for τ are in N/m^2 or Pa (see Figure 4.3).

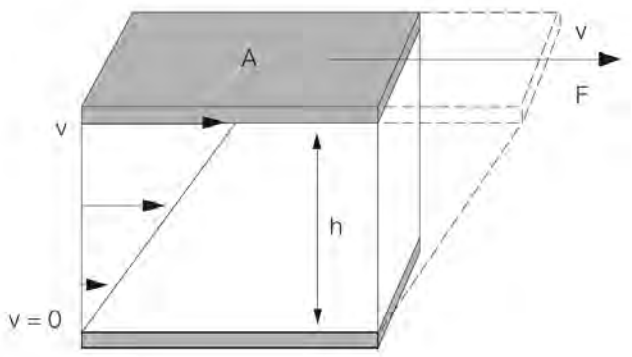

Figure 4.3: Shear being applied to a sample, showing the shear force F, the shear gap h, the fluid flow velocity v and the shear area A. Credit: AntonPaar [266]

The shear rate is the rate of change in velocity at which one layer of fluid passes over an adjacent layer [308]. The shear rate $\dot{\gamma}$ is defined to be:

$$\dot{\gamma} = \frac{v}{h} \tag{4.9}$$

where v is the difference in velocity between layers and h, the shear gap, is the distance between layers (see Figure 4.6). The shear rate has units of reciprocal seconds or s^{-1}.

Viscosity, η, can be defined in terms of the shear stress and the shear rate:

$$\eta = \frac{\tau}{\dot{\gamma}} \tag{4.10}$$

We can see that for more viscous liquids, a greater shear stress is needed for the same shear rate and vice versa for less viscous liquids.

Shear force is applied for the flow of nematic and hexagonal liquid crystals as they flow down a capillary. Shear force is caused by friction between the liquid crystal and the capillary walls, as well as between the different layers. This shear force will align the nematic liquid crystals in the direction of the shear [309]. The shear rate is defined as the difference in flow velocities between the layers; the largest shear rate is going to be the interface between the liquid crystal and the capillary wall, as the capillary wall is stationary, decreasing to 0 at the centre of the liquid crystal flow, with a nonlinear gradient. Therefore, the maximum shear stress, and thus the alignment of the liquid crystals, will occur at the walls of the capillary with poor alignment in the centre of the capillary (see Figure 4.4).

A rheometer can be used for the application of a continuous shear stress on a sample. This allows for a consistent and reliable method of applying a shear to a nematic liquid crystal. Using this technique, a method can be achieved for aligning the reliability of the liquid crystals consistently in both directions and degree can be achieved. In RheoSAXS, SAXS images are taken while the sample is placed in the rheometer (see Figure 4.5. The bob on the rheometer is spun at a constant velocity to provide a constant shear force on the sample due to the difference in angular velocities between the bob and the walls of the sample holder. This allows for the

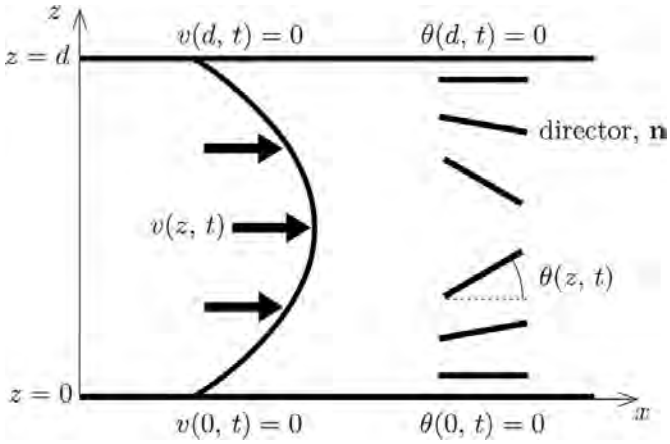

Figure 4.4: Flow of a nematic liquid crystal down a capillary. showing the flow velocity [310] The director, **n**, shows the average direction of flow. The maximum shear occurs at the interface between the liquid crystal and the capillary wall and the minimum shear rate occurs at the center of the flow.

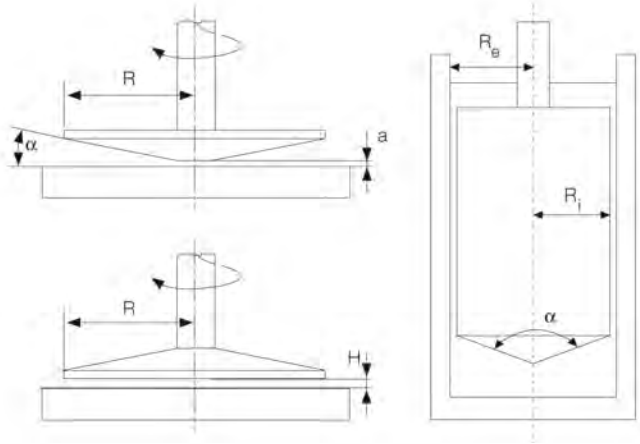

Figure 4.5: RheoSAXS, the sample is placed in a sample holder, and a bob(right) is spun at a constant velocity to provide a constant shear rate. Credit: AntonPaar [266].

reliable and consistent alignment of nematic liquid crystals and AuNRs whilst placed in an X-ray beam.

Synchrotron Radiation

Synchrotron radiation from the Australian Synchrotron is produced by accelerating a beam of electrons inside a circular vacuum chamber guided by strong electromagnets [311]. Deflection by the magnetic field causes electromagnetic radiation to be released, the energy of the generated

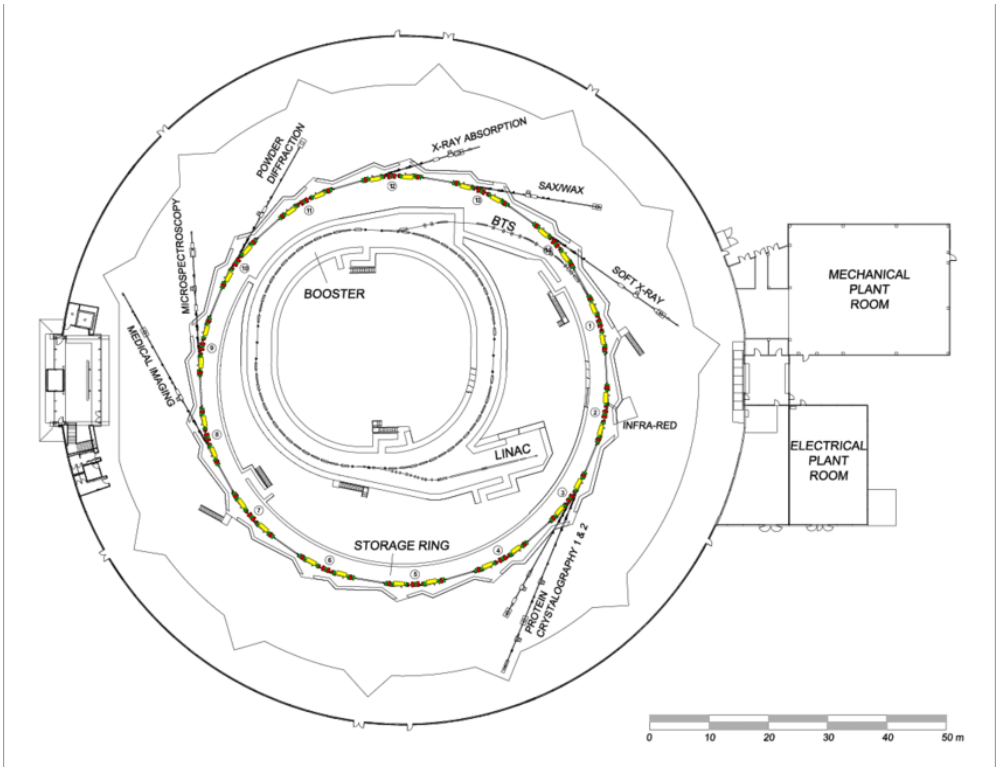

Figure 4.6: Layout of the Australian Synchrotron [314].

photon depends on the energy of the electron and the degree of bending of the electron [312]. A schematic of the Australian Synchrotron layout can be seen in Figure 4.6 The change in the velocity of the electron also determines the polarisation state of the electromagnetic wave [313]. As such, all synchrotron radiation is highly polarised. When observed in the plane of the electrons (as is the case at the Australian Synchrotron), the X-rays produced are linearly horizontally polarised.

4.3 X-ray interactions with matter

Photons also exist as electromagnetic radiation, which are orthogonal synchronised oscillating electric and magnetic fields propagating through space. Polarisation is a fundamental property of all electromagnetic waves, being defined as the direction of oscillation in their electric field. The interactions between light and matter, including absorption, emission, and scattering, have been studied extensively [36, 315–317], but the effects of polarisation have often been overlooked. Indeed, since other interactions such as reflection and refraction are inherently related to light polarisation [318], and even in some cases of light absorption by chromophores [319], one must consider how the polarisation of light might influence all light-matter interactions. As such, we consider the effects of polarisation in X-ray interactions.

X-rays are a form of electromagnetic radiation that is characterised by wavelengths between 0.01 nm and 10 nm, which in turn correspond to energies $E = hc/\lambda$, where h is Planck's constant, λ is the wavelength and c is the speed of light. Photons in the X-ray energies (100 eV - 100 keV) can interact with bound atomic electrons with elastic Rayleigh scattering [320], inelastic Compton scattering [215] where some energy is transferred from the photon to the electron and its low energy limit of elastic Thomson scattering [321], and the photoelectric effect where the photon is absorbed and all its energy is transferred to the electron [322].

Using the fundamentals of these interactions, many X-ray imaging techniques have been developed for use in radiography [186–188], radiotherapy [28, 189, 190], computed tomography (CT) scans [191, 192], X-ray diffraction [193, 194], small-angle X-ray scattering (SAXS), and wide-angle X-ray scattering (WAXS) [195–197].

X-ray Absorption

In SAXS we are interested mainly in two types of light-matter interactions; absorption and scattering. When X-ray photons strikes an object, some X-rays will be absorbed and transformed or remitted as other forms of energy such as heat [323], fluorescent radiation [324], photoelectrons[40] or auger electrons [325]. Auger electrons are emitted when an inner shell electron of an atom is ionised by an incident X-ray photon. This creates an electron hole which is then filled by an electron in an upper shell. Relaxation of the higher energy electron releases energy which can then be transferred to a valence electron and ionising it (see Figure 4.7). This release of a secondary electron is known as the Auger effect [326, 327]. This effect is more likely for lower energy X-rays (< 0.5 MeV) and for lighter atoms[5], as the atomic number and photon energy increases, the likelihood of the photoelectric effect begin to dominate. Alternatively, the relaxation of the higher energy electron can also release an photon, usually also in the X-ray regime.

The absorption of certain materials can increase sharply at certain X-ray energies. This is known as an X-ray absorption edge and is related to the production of a photoelectron. The energy corresponds to the energy required to eject a core electron into the LUMO (lowest unoccupied molecular orbital) state or to the continuum[6] [329]. The absorption discontinuities are known as X-ray absorption edges, with the K-edge being photoelectrons originating from the 1s orbital, an L-edge from photoelectrons from a 2s or 2p orbital, and M-edge causing photoelectrons from the 3s, 3p or the 3d orbitals and so on [330]. Figure 4.8) shows the K, L and M edges the absorption spectrum of gold[7]. Note the absorption edges where the absorption coefficient μ/ρ has a sharp increase.

X-ray Scattering

X-ray scattering is the deflection of X-rays off a sample or object. Changes in polarisation, wavelength, energy and flux of the scattered X-rays compared to incident X-rays can reveal information on the structure, composition, and atomic makeup of the sample. X-rays scatter off the electrons of the atoms that make up the sample, and thus, the more electrons that exist in the sample for the X-rays to interact with, the better the contrast. Therefore, X-ray scattering

[5] Z< 12
[6] free electron
[7] Z=79

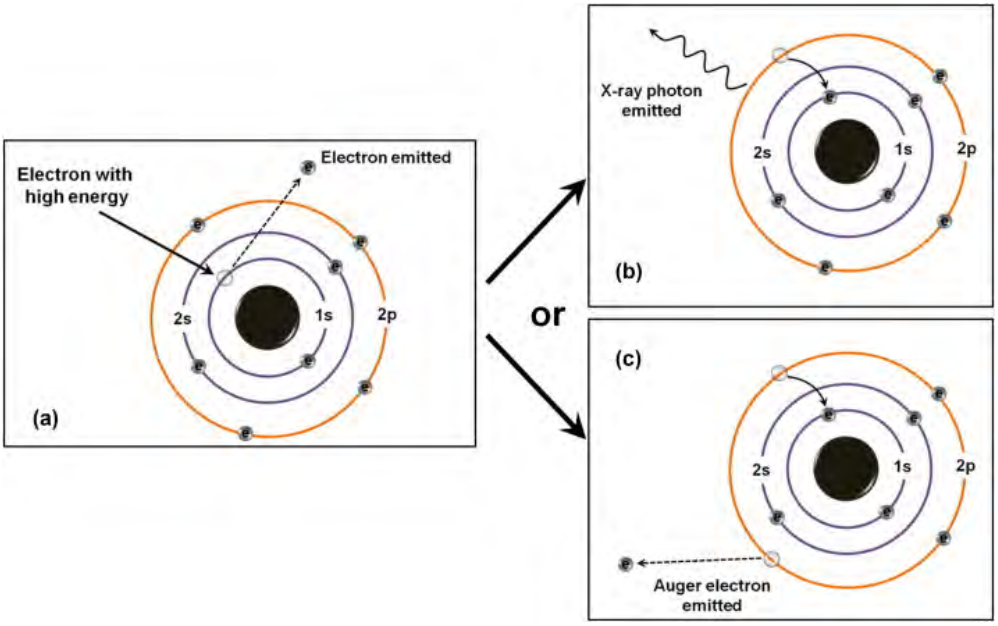

Figure 4.7: X-ray interactions with matter and the Auger effect mechanism [328]. After the emission of the photoelectron by the incident X-ray show in (a), a higher orbital electron will fall into the hole left by the ionised electron and this will be accompanied by the emission of an additional photon (b) or Auger electron (c).

is best suited for heavier elements such as gold, Au. Broadly speaking, X-ray scattering can be divided into two classes; elastic or inelastic scattering.

Elastic scattering, sometimes also known as coherent scattering, occurs when the energy of the scattered X-rays is identical to that of the incident X-rays[8]. The two main types of elastic scattering are; Rayleigh and Thompson scattering.

Inelastic scattering, or Compton scattering, occurs for high-energy X-rays. When the X-ray scatters off an object (generally a free electron), it transfers some of its energy to the electron, losing that same amount of energy[9]. Photon energy is inversely related to its wavelength:

$$E = \frac{hc}{\lambda} \tag{4.11}$$

where λ is the wavelength, h is Planck's constant and c is the speed of light. This means that the resultant change in photon energy from Compton scattering is associated with a change in wavelength called the Compton shift, as seen in Equation 4.12. Usually this results in a longer photon wavelength as the photon loses energy, but the inverse, where the photon gains energy called inverse Compton scattering, can also occur if the electron has more energy than

[8] identical frequencies and wavelengths
[9] Conservation of energy

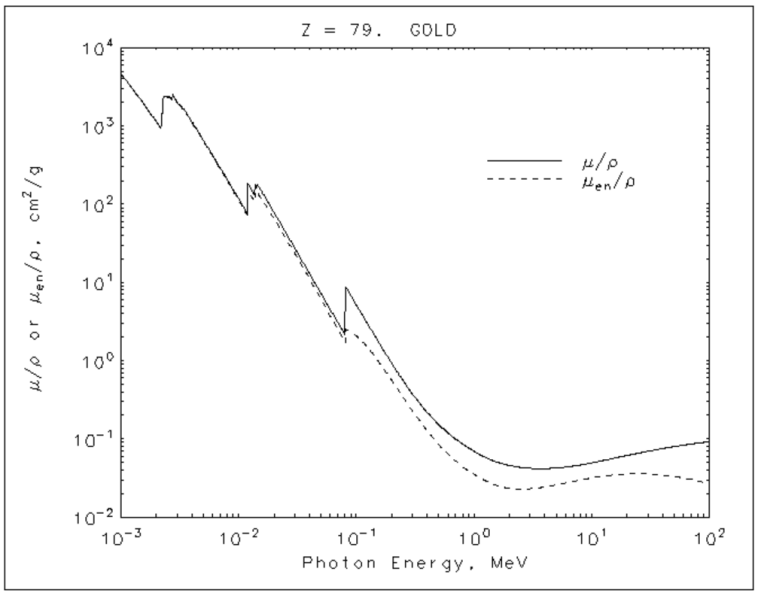

Figure 4.8: Gold X-ray absorption spectrum. The K-edges are approximately 10^{-1} MeV, the L-edges are approximately 10^{-2} MeV and the M-edges are approximately 10^{-3} MeV. Credit: Nist [331].

the photon with:

$$\begin{aligned} \lambda_f - \lambda_i &= \frac{h}{m_0 c}(1 - \cos\theta) \\ \Delta\lambda &= \lambda_c(1 - \cos\theta) \end{aligned} \tag{4.12}$$

Interactions Between Photons and Free Electrons

I have just given a more macroscopic view of X-ray interactions with matter. For the effects of polarisation and X-ray interactions, with the extension into γ ray photon interactions, we want to zoom in and see what happens in an individual interaction event. Classically, X-ray scattering is an interaction between the electric field of the photon and the electric field of the orbiting electrons in the atom. I will simply focus on the interactions between polarised photons and free electrons, since X-rays and γ rays have high enough energy to ionise electrons, providing a mathematical framework on why we believe that we may obtain an anisotropic scattering pattern between polarised X-rays and aligned gold nanorods. The following derivations of polarised Thomson and Compton scattering are adapted from Bœhm et al. [198]. I will go through their derivation of the result that suggests that Thomson and Compton scattering are polarisation dependent.

Thomson

The electric field of an electromagnetic wave can be expressed as:

$$\vec{E}(r,t) = E_0 e^{i(\omega t - k.r)} \tag{4.13}$$

- E_0 is the magnitude of the electric field
- $k = \dfrac{2\pi}{\lambda}$ is the wavenumber with λ being the wavelength
- $\omega = \dfrac{2\pi}{T}$ is the angular frequency with T being the period of oscillation

The polarisation state of a photon can be defined as the oscillation vector of the electric field of the electromagnetic wave and can be expressed by the Stokes parameters: I, Q, U and V where:

- I is the intensity.
- Q and U provides information about the linear polarisation. $Q = \pm 1$ for horizontally and vertically polarised light and $V = \pm 1$ for diagonally polarised light.
- V provides information about circular polarisation. $V = 0$ for linearly polarised light and $V = \pm 1$ for the two circular polarisations.

Thus for any polarisation plane we can choose two perpendicular polarisation basis vectors e_l, e_r s.t. the electric field can now be expressed as:

$$\vec{E}(r,t) = (E_l e_l + E_r e_r) e^{i(\omega t - \mathbf{k}.r)} \tag{4.14}$$

where $E_l e_l = a_l e^{i\delta_l}$ and $E_r e_r = a_r e^{i\delta_r}$ with a_r and a_r being the amplitudes and δ_r and δ_r being the phases of their respective electric fields. We can define two orthogonal vectors $\vec{\epsilon_l}$ and $\vec{\epsilon_r}$ which define the polarisation plane [10], with:

$$\vec{\epsilon_l} = \frac{1}{k_0 k_T}(k_x k_z, k_y k_z, -k_T^2) \tag{4.15}$$

$$\vec{\epsilon_r} = \frac{1}{k_T}(-k_y, k_x, 0) \tag{4.16}$$

where $\mathbf{k} = (k_x, k_y, k_z)$ is the 3-momentum of the photon and $k_T = \sqrt{k_x^2 + k_y^2}$. When $\delta_l = \delta_r$, the phases of the electric field components are the same and we say the EM wave is plane polarised, or linearly polarised, as it oscillates in the same plane. The electric field can now be expressed as:

$$\vec{E} = (a_r \vec{\epsilon_r} + a_l \vec{\epsilon_l}) e^{i\delta} e^{i(\omega t - \mathbf{k}.r)} \tag{4.17}$$

When the phases of the electric fields are offset by 90° s.t. $|\delta_l - \delta_r| = \pi/2$, and with the same amplitude i.e. $a_r = a_l = a$, then the electric field rotates around the direction of propagation and

[10] Plane spanned by the direction of propagation and the E-vector of the EM wave

the light is circularly polarised. Left-handedness and right-handedness depend on the difference between the phases being positive or negative and the electric field is:

$$\vec{E} = a(\vec{\epsilon_r} \pm i\vec{\epsilon_l})e^{i\delta_r}e^{i(\omega t - \mathbf{k}.r)} \tag{4.18}$$

If the amplitudes are not the same i.e. $a_l \neq a_r$, then the EM wave is elliptically polarised, with the electric field being:

$$\vec{E} = (a_r\vec{\epsilon_r} \pm ia_l\vec{\epsilon_l})e^{i\delta_r}e^{i(\omega t - \mathbf{k}.r)} \tag{4.19}$$

We can also define another set of orthogonal basis vectors $\vec{\epsilon_+}$ and $\vec{\epsilon_-}$ such that:

$$\vec{\epsilon_+} = \frac{1}{\sqrt{2}}(-\vec{\epsilon_l} - i\vec{\epsilon_r}) \tag{4.20}$$

$$\vec{\epsilon_-} = \frac{1}{\sqrt{2}}(\vec{\epsilon_l} - i\vec{\epsilon_r}) \tag{4.21}$$

The electric field in the $(\vec{\epsilon_+}, \vec{\epsilon_-})$ basis is:

$$E(\vec{r}, t) = (E_+\vec{\epsilon_+} + E_-\vec{\epsilon_-})e^{i(\omega t - \mathbf{k}.r)} \tag{4.22}$$

with $\vec{\epsilon_+}$ describing photons with positive helicity and $\vec{\epsilon_-}$ describing photons with negative helicity[11], with:

$$E_+ = -\frac{a_l e^{i\delta_l} - ia_r e^{-\delta_r}}{\sqrt{2}} \tag{4.23}$$

$$E_- = \frac{a_l e^{i\delta_l} + ia_r e^{-\delta_r}}{\sqrt{2}} \tag{4.24}$$

Stokes parameters can be defined using the $(\vec{\epsilon_l}, \vec{\epsilon_r})$ and the $(\vec{\epsilon_+}, \vec{\epsilon_-})$. In the $(\vec{\epsilon_l}, \vec{\epsilon_r})$ basis we have:

$$\begin{aligned} I &= |\vec{\epsilon_l} \cdot \vec{E}|^2 + |\vec{\epsilon_r} \cdot \vec{E}|^2 = a_l^2 + a_r^2 \\ Q &= |\vec{\epsilon_l} \cdot \vec{E}|^2 - |\vec{\epsilon_r} \cdot \vec{E}|^2 = a_l^2 - a_r^2 \\ U &= 2\mathrm{Re}[(\vec{\epsilon_r} \cdot \vec{E})^* \times (\vec{\epsilon_l} \cdot \vec{E})] = 2a_r a_l \cos(\delta_r - \delta_l) \\ V &= -2\mathrm{Im}[(\vec{\epsilon_r} \cdot \vec{E})^* \times (\vec{\epsilon_l} \cdot \vec{E})] = 2a_r a_l \sin(\delta_r - \delta_l) \end{aligned} \tag{4.25}$$

In the $(\vec{\epsilon_+}, \vec{\epsilon_-})$ basis we have:

$$\begin{aligned} I &= |\vec{\epsilon_+} \cdot \vec{E}|^2 + |\vec{\epsilon_-} \cdot \vec{E}|^2 = a_+^2 + a_-^2 \\ Q &= -2\mathrm{Re}[(\vec{\epsilon_+} \cdot \vec{E})^* \times (\vec{\epsilon_-} \cdot \vec{E})] = -2a_+ a_- \cos(\delta_+ - \delta_-) \\ U &= 2\mathrm{Im}[(\vec{\epsilon_+} \cdot \vec{E})^* \times (\vec{\epsilon_-} \cdot \vec{E})] = 2a_+ a_- \sin(\delta_+ - \delta_-) \\ V &= |\vec{\epsilon_+} \cdot \vec{E}|^2 - |\vec{\epsilon_-} \cdot \vec{E}|^2 = a_+^2 - a_-^2 \end{aligned} \tag{4.26}$$

[11] Here helicity corresponds to the circular polarisation states of a photon

With this in mind we can use Chandrasekhar's modified Stokes parameters: (I_l, I_r, U, V) with $I_r = a_r^2$ and $I_l = a_l^2$. Note that $I = I_l + I_r$ and $Q = I_l - I_r$

After a scattering event, the description of the radiative transfer can be given by the **R**-matrix for 2D or the **P**-matrix for 3D with the modified stokes parameters of the scattering photon being:

$$\begin{bmatrix} I_l \\ I_r \\ U \\ V \end{bmatrix}_S = \mathbf{R}_t \text{ or } \mathbf{P}_t \begin{bmatrix} I_l \\ I_r \\ U \\ V \end{bmatrix}_I \tag{4.27}$$

For low energy Thomson Scattering, i.e. energy and frequency of of the photon remains unchanged [332], the **R**-matrix is:

$$\mathbf{R}_t = \begin{bmatrix} \cos^2\theta & 0 & 0 & 0 \\ 0 & 1 & 0 & \\ 0 & 0 & \cos\theta & 0 \\ 0 & 0 & 0 & \cos\theta \end{bmatrix} \tag{4.28}$$

which gives us $I_{l,S} = I_{l,I}\cos^2\theta$ and $I_{r,S} = I_{r,I}$, with θ being the angle formed by the polarisation plane of the scattered photo and the polarisation plane of the incident photo.

In three dimensions, we must first fix a scattering plane and a polarisation plane. We can then define θ_I and θ_S to be the angle formed between the polarisation plane of the incident and scattered photos with the fixed initial polarisation plane. We can also define ϕ_I and ϕ_S to be the angle formed between the scattering plane of the incident and scattered photons and the fixed initial scattering plane. We then have:

$$\mathbf{P}_t = \begin{bmatrix} P_{11} & P_{12} & P_{13} & 0 \\ P_{21} & P_{22} & P_{23} & 0 \\ P_{31} & P_{32} & P_{33} & 0 \\ 0 & 0 & 0 & P_{44} \end{bmatrix} \tag{4.29}$$

with

$$
\begin{aligned}
P_{11} &= \left(\mu_1\mu_2 c_{12} + \sqrt{1-\mu_1^2}\sqrt{1-\mu_2^2}\right)^2 \\
P_{12} &= \mu_2^2 s_{12}^2 \\
P_{13} &= \frac{1}{2}\mu_2^2\mu_1 \sin 2(\theta_1-\theta_2) + \mu_2\sqrt{1-\mu_1^2}\sqrt{1-\mu_2^2}s_{12} \\
P_{21} &= \mu_1^2 s_{12}^2 \\
P_{22} &= c_{12} \\
P_{23} &= \mu_1 c_{12} s_{12} \\
P_{31} &= -\frac{1}{2}\mu_2\mu_1^2 \sin 2(\theta_1-\theta_2) - \mu_2\sqrt{1-\mu_1^2}\sqrt{1-\mu_2^2}s_{12} \\
P_{32} &= -2\mu_1 c_{12} s_{12} \\
P_{33} &= \sqrt{1-\mu_1^2}\sqrt{1-\mu_2^2}c_{12} + \mu_1\mu_2\cos 2(\theta_2-\theta_1) \\
P_{44} &= \sqrt{1-\mu_1^2}\sqrt{1-\mu_2^2}c_{12} + \mu_1\mu_2
\end{aligned}
$$

and $s_{12} = \sin(\theta_2 - \theta_1)$, $c_{12} = \cos(\theta_2 - \theta_1)$, $\mu_1 = \cos\phi_1$ and $\mu_2 = \cos\phi_2$. So our 3D radiative transfer of the scattered photon with respect to the incident photon is

$$
\begin{aligned}
I_{l,s} &= P_{11}I_{l,I} + P_{12}I_{r,I} + P_{13}U_I \\
I_{r,s} &= P_{21}I_{l,I} + P_{22}I_{r,I} + P_{23}U_I
\end{aligned}
\tag{4.30}
$$

As the polarisation vector of the incident photon, θ_1, would have an effect on both $I_{l,S}$ and $I_{r,s}$ (while keeping everything else fixed), we thus may expect that changing the angle between the polarisation vector and the long axis of the AuNRs with which it interacts may change the relative scattered intensities.

Compton

Compton scatterings between photons and free electrons are no longer elastic and thus change the energy and wavelength of the scattering photons according to Equation 4.12. In particular, when the initial is greater than the mass of the electron, i.e. $\sqrt{s} > m_e$ [12], the polarisation and the spin of the scattered photon can be affected by this interaction. As such, the Stokes parameters will depend on both the momentum and the energy of the incident photons. The derivation of the following Stokes parameter transformation matrix is beyond the scope of this work, but for the scattering of high-energy photons off AuNRs, Compton scattering must be considered. Using Chandrasekhar's modified Stokes parameters, (I_l, I_r, U, V) we have the following transformation under Compton scattering:

$$
\begin{bmatrix} I_l \\ I_r \\ U \\ V \end{bmatrix}_S = \mathbf{R}_c \begin{bmatrix} I_l \\ I_r \\ U \\ V \end{bmatrix}_I
\tag{4.31}
$$

[12] $\sqrt{s}$ is the centre of mass energy of the interaction

with [198]

$$\mathbf{R}_c = \frac{1}{2m_e}\begin{bmatrix} \sin^2\frac{\theta}{2}\Delta E_\gamma + 2m_e\cos^2\theta & \sin^2\frac{\theta}{2}\Delta E_\gamma & 0 & 0 \\ \sin^2\frac{\theta}{2}\Delta E_\gamma & \sin^2\frac{\theta}{2}\Delta E_\gamma + 2m_e & 0 & 0 \\ 0 & 0 & 2m_e\cos\theta & 0 \\ 0 & 0 & 0 & [2m_e + \Delta E_\gamma(1-\cos\theta)]\cos\theta \end{bmatrix} \tag{4.32}$$

Using Equation 4.32 and Equation 4.33 we have the following.

$$\begin{aligned} I_{l,s} &= \frac{1}{2m_e}[(\sin^2\frac{\theta}{2}\Delta E_\gamma + 2m_e\cos^2\theta)I_{l,I} + \sin^2\frac{\theta}{2}\Delta E_\gamma I_{r,I}] \\ I_{r,s} &= \frac{1}{2m_e}[\sin^2\frac{\theta}{2}\Delta E_\gamma I_{l,I} + (\sin^2\frac{\theta}{2}\Delta E_\gamma + 2m_e)I_{r,I}] \end{aligned} \tag{4.33}$$

The changes in intensities of the polarisation modes are now dependent on the change in energy of the photon and also the mass of the electron. For when the photon energy is low, we can neglect ΔE s.t $\Delta E_\gamma = 0$ we recover the Thomson scattering formula: $I_{l,s} = \cos^2\theta I_{l,I}$ and $I_{r,s} = I_{r,I}$.

For SAXS, the scattering angle is small, usually $< 5°$. For the Compton effect to have a significant impact, we would need $sin^2\frac{\theta}{2}\Delta E_\gamma$ to be on the order of the mass of the electron[13]. For $\theta = 5°$, $\sin^2(\theta/2)$ is approximately 0.002, which means that we need a change in photon energy close to 260 MeV. The change in energy of the scattered photon is as follows:

$$\begin{aligned} \Delta E_\gamma &= \Delta\frac{hc}{\lambda} \\ &= \frac{hc}{\lambda_f} - \frac{hc}{\lambda_i} \end{aligned} \tag{4.34}$$

Bremsstrahlung scattering and Synchrotron Radiation

Bremsstrahlung scattering or breaking radiation is the phenomenon of the emission of electromagnetic radiation produced by the deceleration of charge particles, in particular in a magnetic or electric field [38]. The deceleration of the charged particle results in a loss of kinetic energy. That energy converts into the energy of the photon (see Figure 4.9):

$$E = hf = \Delta KE \tag{4.35}$$

With KE being the kinetic energy. For relativistic particles, the kinetic energy is:

$$KE = (\gamma - 1)mc^2 \tag{4.36}$$

where m is the rest mass of the particle and γ is:

$$\gamma = \frac{1}{\sqrt{1 - \frac{v^2}{c^2}}} \tag{4.37}$$

[13] 0.511 MeV

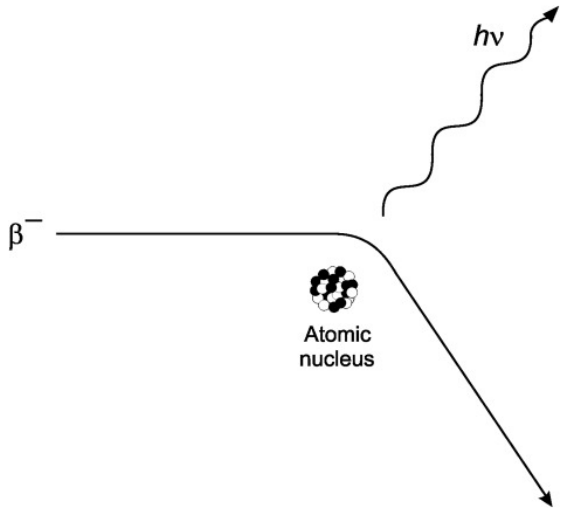

Figure 4.9: Emission of bremsstrahlung radiation from the deceleration of an electron caused by an atomic nucleus [334].

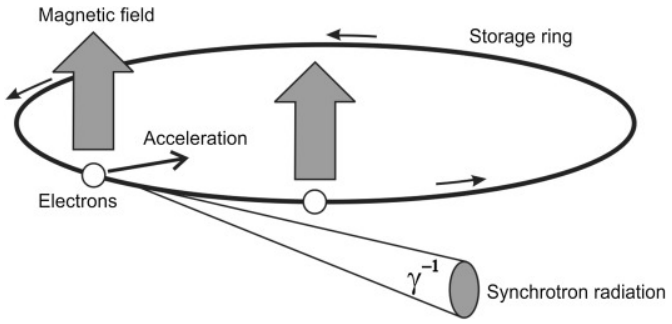

Figure 4.10: Synchrotron radiation from an accelerated beam of electrons deflected constantly by a magnetic field [334].

with v being the velocity of the particle. As such, no particle with nonzero rest mass can attain the speed of light. As the change in the kinetic energies of the decelerated charged particle has a continuous spectrum, so is the emitted bremsstrahlung radiation [333]. The production of X-ray γ ray beams at synchrotrons uses a technique similar to bremsstrahlung scattering. Instead of acceleration of charged particles caused by an electric (such as from a positive proton), synchrotron radiation uses a beam of relativistic charged particles, usually electrons, accelerated in a storage ring with a magnetic field. The magnetic field keeps the electrons travelling with a deflecting force. Each deflection causes the electrons to emit electromagnetic radiation, tangential to the deflection force [335]. The beam of emitted photons is highly collimated with an angular spread on the order of γ^{-1} in mrads[14] [336] (see Figure 4.10).

Synchrotron and cyclotron radiation, with cyclotron radiation being the non-relativistic limit

[14] milliradians

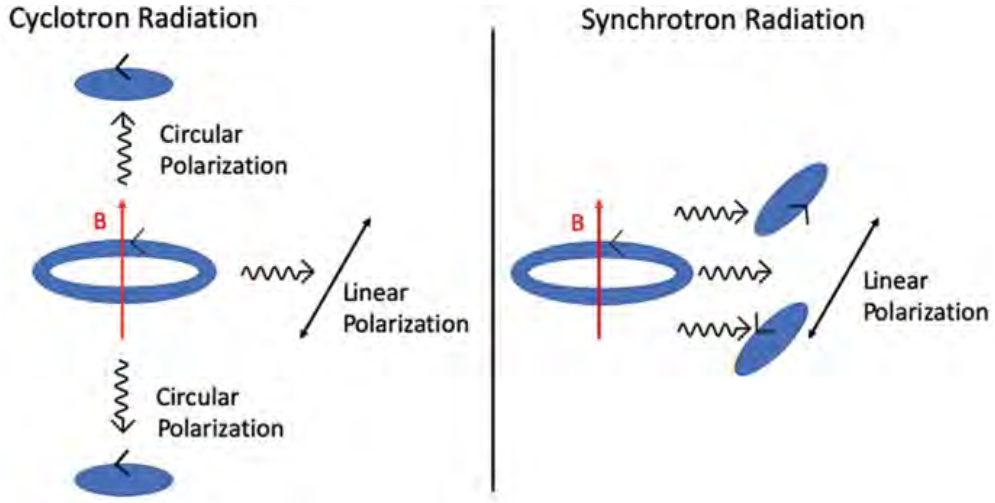

Figure 4.11: Synchrotron and cyclotron radiation produces polarised electromagnetic radiation [337] When viewed in the same plane of motion as the electrons, the emitted polarisation is linear. When view perpendicularly above or below, the polarisation is circular. Between the two exists elliptical polarisation.

of synchrotron radiation, can produce linear, circular, and elliptical polarisations. This depends on where one views the source of the radiation (see Figure 4.11). The emitted polarisation of the electromagnetic radiation has its electric field corresponding to the motion of the accelerating electrons. When viewed in the same plane as the electron's motion, the electrons seem to be moving linearly backward and forward, thus causing linear polarisation. When viewed perpendicularly above and below, the electrons trace our circles, either clockwise or counter-clockwise, which results in the two circular polarisation modes. At angles in between the two, the electrons trace out ellipses, which causes elliptical polarisation.

The interactions of X-rays and gold can ionize the atomic electrons of gold via the photoelectric effect. The free electrons are then able to produce bremsstrahlung radiation through interactions with bound electrons and nuclei of other Au atoms. Bremsstrahlung radiation scales with Z, or atomic number, for electron-electron interactions and with Z^2 for electron-nucleus interactions [338]. Au has an atomic number of $z = 79$, thus, we can ignore electron-electron bremsstrahlung interactions. The intensity of bremsstrahlung radiation produced via the nucleus is:

$$I_{bremmstralung} \propto \frac{Z^2 z^4 e^6}{M^2} \tag{4.38}$$

where z is the particle atomic number, 1 for electrons and protons, $e = 1.64.803 \times 10^{-10}$ esu[15], is the elementary charge and M is the mass of the scattering particle, or the electron in this case. We can see that the intensity increases quadratically as the atomic number Z increases, but also inversely to the particle mass M. Bremsstrahlung radiation will be much more intense

[15]Statcoulomb units, 1 csu to 4.44564×10^{-10} C

for electrons, $M = 0.0005485$ u[16], than for protons, $M = 1.007$ u, or alpha particles, $M = 4.001$ u.

4.4 Gold Nanorods and Liquid Crystals

One important aspect of some applications of X-ray interactions is to use materials where an interaction with high energy photons does not fully destroy the chemical bonds that bind the molecules together. It is thus useful to look towards metals for the suitability of such a material. Metals of the same element form a metallic lattice in the solid physical state, and unlike most ionic and covalent bonds, have electrons that exist in an 'electron ocean' [339]. This means that there are many electrons in the conduction band. These electrons are not used for chemical bonding and are free to move from atom to atom, which most usefully gives them the ability to conduct electricity. However, these electrons can also be ionised by an incoming high energy photon and leave the material entirely without compromising the metallic integrity. This allows some metals to have great scattering properties with X-rays and Gamma rays.

Gold

Gold is an extremely stable metal with an atomic number of 79. It has been called the noblest of all metals as a result of its low reactivity. This is because gold cannot form bonds with other atoms until they have broken their bonds with neighbouring gold atoms [340]. As there are few molecules that can make energetically favourable bonds with the electrons of gold, it is a fairly inert element [341]. The stability of gold and the abundance of electrons means that gold has a high cross section with light interactions and is especially potent with X-rays. Gold nanoparticles are additionally particularly potent in light absorption and scattering due to surface plasmon resonances (SPR).

Surface Plasmon Resonances

Surface plasmon resonance occurs when a photon is incident onto a metallic surface. At a specific angle of incidence, the energy from the photon is absorbed by the surface electrons of the gold and they are excited. This excitation leads to an oscillation of the electrons as they move parallel to the surface [342] (see Figure 4.12). The movement of electrons also causes an increased electromagnetic field on the surface and can lead to increased scattering and absorption events for incident photons [343]. As a result, gold nanoparticles have a much higher affinity for photon interactions compared to other non-plasmonic nanoparticles, and are used in many sensor technologies [344, 345]. SPRs are also inherently dependent on polarisation as the incident photon needs to have its polarisation parallel to the momentum of the plasmons due to conservation of momentum. Thus, p-polarised light (parallel to the plane of incidence) can create SPRs, while s-polarised light (perpendicular to the plane of incidence) cannot [347, 348]. Therefore, p-polarised and s-polarised photons have different interaction rates with gold nanoparticles (AuNPs).

However, SPRs are mainly caused by incident photons in the visible and near-infrared (NIR) wavelengths [349–351]. Gold coupled to a ZnSe semiconducting film was found to exhibit SPRs in

[16] u is the atomic mass unit with 1 u = 1.66×10^{-27} kg

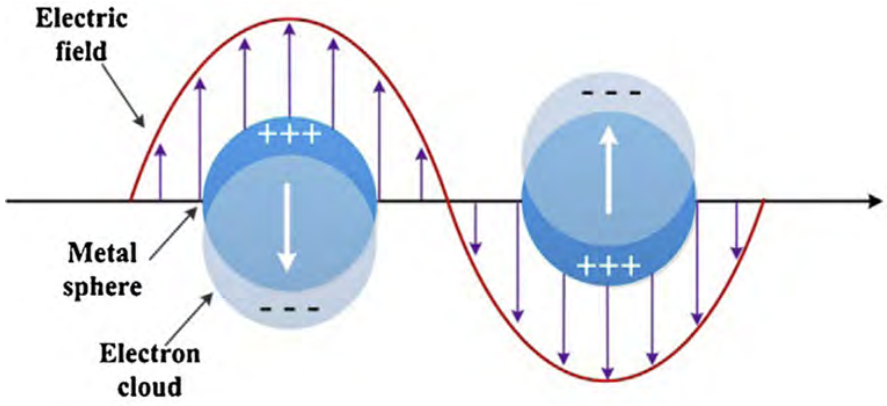

Figure 4.12: Excitation of electrons in surface plasmon resonance [346].

the soft X-ray energies. For hard X-ray energies of above 10 keV, the main interaction processes would be the photoelectric effect and Thomson/Compton Scattering. Given the large difference in ionisation energies for electrons bound to an Au atom and the energy of the incident X-rays, these interactions can be reasonability assumed to be between photons and free electrons. However, lower energy photons can be created via the Auger effect [352] or via Bremsstrahlung radiation, which is a continuous spectrum [353, 354]. As such these photons may induce SPRs in the AuNPs but should have negligible effects on the scattering results in SAXS because of the much higher flux of X-ray counts on the detector from the beamline as well as the small angle used, resulting in most of these secondary events not impacting the detector.

Aligned Gold Nanorods

Gold nanorods (AuNRs) also have properties different from those of AuNPs in how they interact with light. When AuNRs are aligned, the extinction coefficient of visible light is dependent on their polarisation [355–357]. The extinction coefficients of AuNRs were the highest when the incident light is polarised parallel to the long axis of the aligned AuNRs and decreased to the minimum when the polarisation was perpendicular. This change in extinction coefficient disappeared when the AuNRs are randomly orientated.

When the AuNRs are aligned magnetically, i.e., using magnetic nanoparticles to coat the AuNRs and aligning them with a magnetic field, there is an enhancement of the longitudinal SPR and a suppression for the transverse SPR for light polarised parallel to the magnetic field, and vice versa or light polarised perpendicularly to the magnetic field [356]. The sensitivity of the two SPRs to the polarisation of the incident photon, which corresponds to the oscillations of electrons along the long and short axes of the AuNRs, could be an explanation for their strong dependence on polarisation [358].

Gold is an excellent X-ray scatterer and has been used as an important tool for advanced X-ray imaging, especially gold nanoparticles [359]. Given the polarisation dependence of interactions between visible light and AuNRs, we would like to see if this extends into higher energies such as X-rays and γ rays, which would have important applications in astrophysics, particle

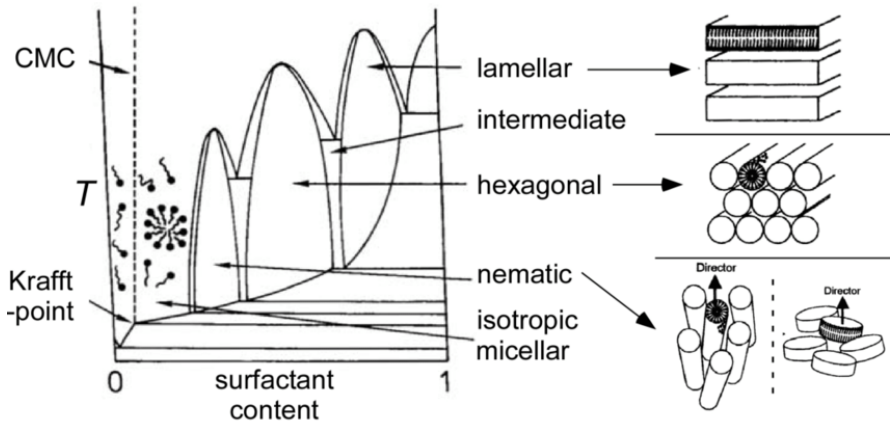

Figure 4.13: Liquid crystal phases [368].

physics, medical imaging, and radiotherapy.

Liquid Crystals

Liquid crystals are liquid-crystalline mesophases formed by a surfactant when mixed with water. They are constituted by parallel packed cylindrical micelles. There are several phases of liquid crystals that determine the arrangement of their molecules [360], including nematic and hexagonal (see Figure 4.13). The nematic phase is characterised by one-dimensional orientations of molecules along the long molecular axes [361]. The columnar phase is characterised by the liquid crystal molecules assembling into cylindrical structures with differently shaped lattices. The hexagonal shape is one example, with each micelle surrounded by six other micelles [362]. Both are highly orientable when a force is applied. Due to their anisotropic shape, they also exhibit birefringent properties [363]. AuNRs can be dispersed and aligned in a nematic liquid crystal through a shear force [357, 364, 365]. They can also be aligned in a hexagonal phase liquid crystal [366, 367]. Both methods can achieve a high level of ordering, and as only the alignment of AuNRs needed to be achieved for this work, one method was not favoured over the other.

Under an atmospheric pressure of approximately 101 kPa or 1 atm, the phase diagram of CTAB can be seen in Figure 4.14. The nematic phase is approximately between $20 - 30$ $wt\%$ with temperatures ranging from 280°K to 310°K. The phase change from the nematic phase to the hexagonal phase occurs at approximately 30 $wt\%$ of CTAB at temperatures above 290°K. The phase of CTAB will change from nematic to hexagonal if there is dehydration of the CTAB + water mixture, as the dehydration of the sample increases the percentage weight of CTAB.

Functionalisation of Gold Nanorods

Gold nanorods are usually prepared with hexadecyltrimethylammonium bromide (CTAB) capping [370], however, they are usually replaced with polyethylene glycol (PEG) caps due to their lower cytotoxicity [371]. However, for the purposes of this project, the impact of different func-

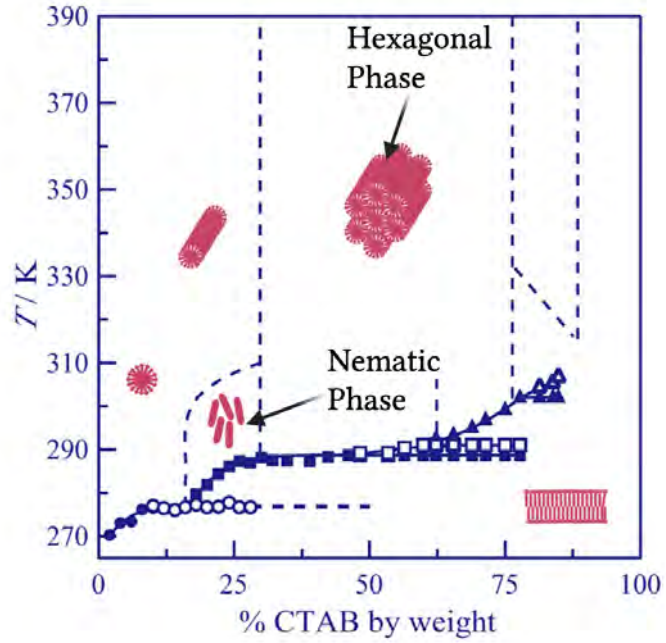

Figure 4.14: Liquid crystal phases, showcasing nematic and hexagonal phases with respect to the CTAB *wt*% and the temperature in Kelvin. Adopted from Yamamoto et al [369].

tionalisations of alignment quality on scattering must be considered. PEGs are a larger molecule compared to CTAB and increase the effective size of AuNRs [372, 373]. As a result, PEG-capped AuNRs can create more distorted ligand shells and alter the ordering and alignment of AuNRs in the liquid crystal [374].

Significance of Surface functionalisation on Gold Nanorods

Capping agents have been commonly used as stabilisers when producing gold nanoparticles (AuNPs). In addition to stabilising AuNPs in solution as a colloidal solution, different capping agents can also control the surface chemistry, morphology, and size distributions of the product [375–377]. The as-synthesised AuNRs were capped with CTAB, which is the nematic phase of choice in the experiment. To investigate whether capping agents may have different effects on the ability of the liquid crystal alignment, we used three types of PEGs, amine, methyl, and carboxylate groups, as functionalisations on the AuNRs.

4.5 Experimental Methods

The outline of the experimental method can be seen in Figure 4.15. We will provide more details in the following sections, but briefly AuNRs were synthesised with Cetyltrimethylammonium bromide (CTAB) functionalisation. We wanted to explore the alignment of AuNRs

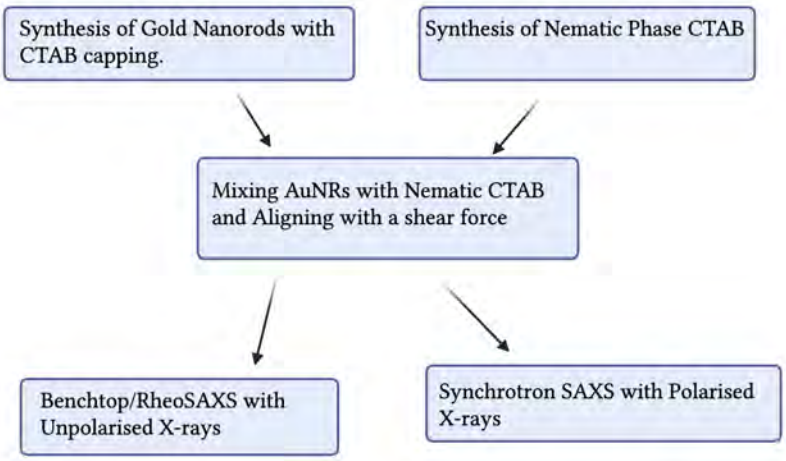

Figure 4.15: Flowchart of the experimental setup and methods. Firstly, gold nanorods were synthesised and functionalised with CTAB. At the same time, a nematic liquid crystal was made with CTAB. The two were mixed together and aligned in a capillary with a shear force. The now-aligned AuNR + nematic CTAB sample was tested with unpolarised X-rays at a benchtop SAXS and with polarised X-rays at the Australian Synchrotron.

with a nematic liquid crystal (NLC). With this in mind, a NLC was made with CTAB, and the possibility of their alignment was established. The two solutions were mixed together, and the final mixture was aligned with a shear force provided by inserting the solution into a capillary and placing the capillary into a centrifuge. This forces the solution to flow down the capillary and aligns the NLC and AuNRs solution. Its alignment was checked with a benchtop SAXS with unpolarised X-rays. Alignment of the AuNRS are characterised by an elongated scattering pattern. The benchtop SAXS was also used in conjuction with a rheometer at this point for a consistent shear force, and the relaxation time of the AuNRs was investigated, where their potential de-alignment was investigated to ensure the AuNRs remained aligned between measurements. Finally, the sample was taken to the Australian Synchrotron in order to perform SAXS with a source of polarised X-rays in order to establish the relationship between the anisotropic scattering of polarised X-rays and aligned gold nanorods.

Gold Nanorod synthesis

The synthesis of was done with the help of Alex Yin and Joseph Yang, from the University of Sydney.

The fundamental interaction that is being tested is Thomson scattering of free electrons [321]. In particular, we want to determine whether the distribution of scattered X-rays from Thomson scattered is dependent on the polarisation of the incident X-rays. As such, we needed

a material that not only has a high scattering interaction rate with X-rays but also many have loosely bound electrons to simulate free electrons and additionally be stable enough so that a high-energy, high-flux X-ray beam would not damage the material. With that in mind, we chose to use gold nanorods, which is very stable [341], has a high cross section with X-rays [359, 378], and has a high abundance of loosely bound electrons [379, 380], making it an ideal candidate for this project. In fact, gold nanoparticles have already many applications with X-ray interactions [359, 381–383].

Materials

To synthesis the AuNRS, we purchased chloroauric acid trihydrate ($HAuCl_4$), silver nitrate ($AgNO_3$), cetyltrimethylammonium bromide (CTAB), sodium borohydride ($NaBH_4$), ascorbic acid, and hydrochloric acid (HCl) (37 $wt\%$) from Sigma Aldrich.

Synthesis of Gold Nanorods

The synthesis of gold nanorods (AuNRs) was adopted from Scarabelli et al. [15]. AuNRs were synthesised via a seed-mediated procedure. Firstly, the seed solution is produced by rapidly injecting ice cold $NaBH_4$ (300 μL, 10 mM) into a solution of $HAuCl_4$ (25 μL, 50 mM) and CTAB (4.7 mL 0.1 M). The solution was stirred vigorously for 10 – 20 seconds and left to age for 30 minutes. Then, the seed solution is used for the synthesis of AuNRs and the reaction is kept at 30℃. CTAB (10 mL, 0.1 M), HCl (190 μL, 1 M), and $HAuCl_4$ (100 μL, 50 mM) were added and stirred for 5 mins in a reaction vial to a final pH of 1.5. Subsequently, $AgNO_3$ (120 μL, 10 mM) and ascorbic acid (200 μL, 100 mM) were added to the solution. After gentle shaking, the solution should turn colourless, where the seed solution (24 μ L) from the previous step was added to the mixture by stirring it rapidly for a few seconds and then left undisturbed for 2 hours.

The AuNRs were separated from excess CTAB and then purified from the by-products by centrifugation at 27°C to avoid the crystallisation of CTAB. The solution was centrifuged at 10,100 ×g for 30 minutes. The precipitates can be clearly seen at the bottom of the centrifuge tubes. The supernatant was then carefully removed, leaving a volume of approximately 50 μL solution with the precipitates. The pellets were resuspended with Milli-Q water (18.2 MΩ·cm @ 25°C), leading to a final volume of 1.5 mL. The isolated product from the first centrifugation was centrifuged again at 3,820 × g for 15 minutes. The supernatant, which contains the AuNRs, was finally carefully collected without disturbing the pellets (gold nanospheres and nanocubes).

Alignment of CTAB and AuNRs

To observe anisotropic scattering, we require an anisotropic system. Thus we have chosen to use gold nanorods instead of gold nanoparticles as their elongated shape will create an angular asymmetry. Alignment of AuNRs causes a global anisotropy, its aspect ratio (length of its long axis: length of its short axis) changes its interaction with light [384]. A system of aligned AuNRs has already been determined to be sensitive to polarisation in the visible wavelengths of light [355–358]. They observed that the absorption of light was maximal when the incident light was polarised parallel to the long axis of the aligned AuNRs and decreased to a minimal when the polarisation was perpendicular. In the visible spectrum the polarisation dependence

on the absorption of light by gold nanorods is due to surface plasmon resonances (SPR) that occur in gold [349–351]. SPRs are inherently sensitive to polarisation [347, 348]. However, at higher energies, SPRs would have little to no effect on AuNR-photon interactions as any photo-absorption would result in the electrons being ejected (photoelectric effect).

Liquid crystals such as CTAB are liquid crystalline mesophases formed by a surfactant when mixed with water. They are constituted by parallel packed cylindrical micelles. There are several phases of liquid crystals that determine the arrangement of their molecules [360], including nematic and hexagonal (see Fig.4.14). The nematic phase is characterised by one-dimensional orientations of molecules along the long molecular axes [361]. The hexagonal (columnar) phase is characterised by the liquid crystal molecules assembling into cylindrical structures with hexagonal lattices[362]. Both are highly orientable with the application of a shear force [385, 386]. Due to their anisotropic shape, they also exhibit birefringent properties [363]. AuNRs can be dispersed and aligned in a nematic liquid crystal through a shear force [357, 364, 365]. They can also be aligned in a hexagonal phase liquid crystal [366, 367]. Both methods can achieve a high level of ordering, and as only the alignment of AuNRs is needed to be achieved for this work, one method was not preferred over the other, i.e., nematic and hexagonal liquid crystal phases are both suitable.

Firstly, our goal was to recreate the alignment process of the nematic CTAB with a shear force. To do so, CTAB was made in the nematic state, using 0.2474 g of CTAB to 0.9976 g of Milli-Q water. This represented a 25 $wt\%$ ratio of CTAB at room temperature (approximately 25°C), which coincides with its nematic liquid crystal phase [369] (see Fig.4.14). The smeared and unsmeared nematic CTAB was then viewed under a polarising microscope, and the smearing was applied by sliding the cover slip and the microscope slide with the CTAB in between. As smearing provides a shear force, the smeared sample has the liquid crystals be aligned, whilst the unsmeared sample should not be ordered. This can be seen in Fig.4.16 with (a) the unaligned CTAB and (b) the aligned CTAB. As nematic CTAB is birefringent, the constructive inference wavelengths of polarised light as it traverses through the NLC is dependent on the orientation of the liquid crystals. Thus, aligned CTAB will be monochromatic under a polarising microscope whilst unaligned CTAB will look polychromatic.

SAXS

X-rays are a form of electromagnetic radiation that is characterised by wavelengths between 0.01 nm and 10 nm, which in turn correspond to energies between approximately 100 eV and 100 keV. They can interact with bound atomic electrons through elastic Rayleigh scattering [320], inelastic Compton scattering[17] [215] and elastic Thomson scattering [321]. In fact, Thomson scattering is the low energy limit of Compton scattering where the scattered photon has the same energy in Thomson but has a different energy in Compton. Additionally, X-rays can also interaction via the photoelectric effect where the photon is absorbed and all its energy is transferred to the electron [322].

Developments in X-ray interaction techniques have led to many important modern applications such as radiography [186–188], radiotherapy [28, 189, 190], computed tomography (CT) scans [191, 192], X-ray diffraction [193, 194], small-angle X-ray scattering (SAXS), and wide-

[17] Inelastic in the sense that the energy of the scattering photon is different from the energy of the incident photon.

angle X-ray scattering (WAXS) [195–197]. Since X-ray interactions change depending on their polarisation, it can be very important to consider and know the polarisation of X-rays as it can potentially fundamentally affect these applications.

SAXS uses the deflection of X-rays caused by their interactions with bound electrons in atoms. The scattered radiation is recorded by the detector, whereas the direct beam is usually stopped [302]. Scattered X-rays are characterized by their momentum transfer or scattering vector q:

$$q = \frac{4\pi \sin\theta}{\lambda} \tag{4.39}$$

where θ is half the angle between the scattered and incident X-rays and λ is the wavelength of the monochromatic X-rays. Typically in SAXS, $\theta \leq 5^{\circ}$ and the intensity of the scattered X-rays ,$I(q)$, is compared with the scattering vector q in linear reductions [291]. For our experiments, we will also compare the intensity of the scattered X-rays with the azimuthal angle around the sample, ϕ, (see Fig.4.24). This is done to study any potential differences in the angular distribution of the scattered X-rays due to the rotations of the aligned AuNRs.

As the X-rays are monochromatic, interference patterns can also be seen in the scattering results, arising from the constructive and destructive interference of X-rays interactions with different layers of the sample.

Benchtop/RheoSAXS

Prior to the exposure of the AuNR to polarised X-rays, we tested our capacity to align the AuNR in the NLCs solution as well as their relaxation time using the RhoSAXS at Sydney Analytical. This was done because RheoSAXS will grant a consistent shear force which will provide for a more consistent alignment of the NLCs and thus AuNRs, both in orientation and in population.

The RheoSAXS used consisted of an AntonPaar DSR 502 rheometer paired with an Anton Paar SAXSPoint benchtop SAXS system. The AntonPaar DSR 502 rheometer utilises a concentric cylinder geometry with polycarbonate cylinders with a 1 mm gap. The bob, which was 30 mm long and has a diameter of 20mm, was inserted into the cylinder and provided the shear force with rotations. The benchtop Anton Paar SAXSPoint system provided a copper microfocus 0.154 nm unpolarised X-ray source operating at 50 kV and 1 mA and a Dectris Eiger 1M detector with a pixel size of 75 µm x 75 µm.

We mixed the CTAB NLC with an AuNR solution so that the AuNR solution was 5.8% of the total weight. The solution was heated and then mixed to allow for a uniform distribution of the AuNRs. The final mixture was placed into the AntonPaar RheoSAXS setup outline previously and the AuNRs were aligned in the rheometer at a shear rate of 50 s^{-1}, and a SAXS image was taken. They were then allowed to relax for a period of 30 minutes by shutting the rheometer down, and another SAXS image was then taken. The two X-ray scattering images were compared to note any possible relaxation of the alignment of the AuNRs.

This preparation work was particularly important to ensure that the sample will remain aligned between subsequent irradiations at the Synchrotron and resistant to a change in orientation.

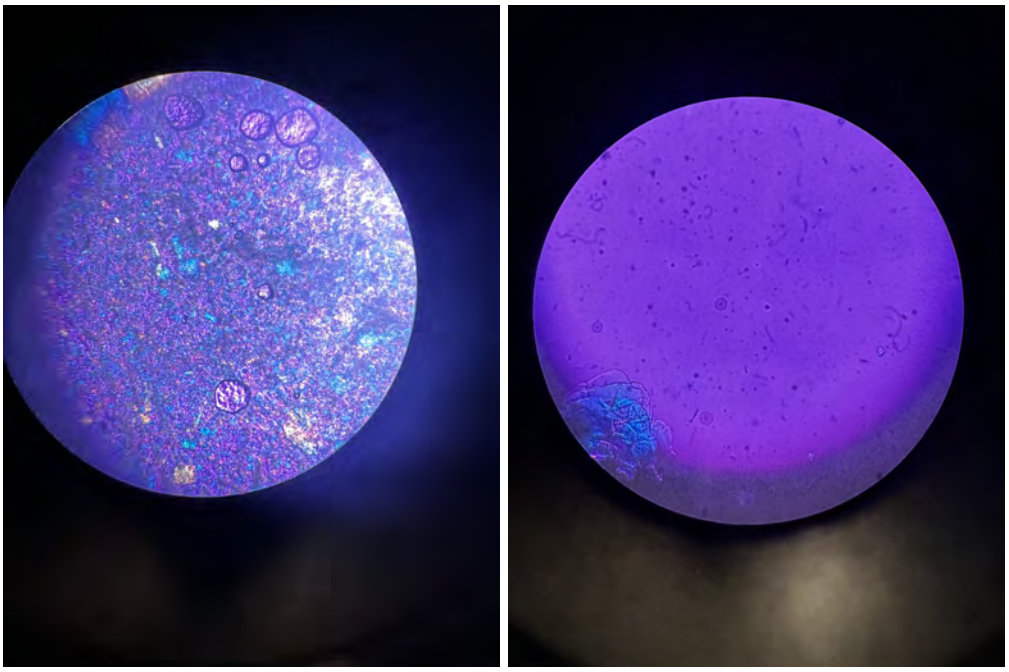

(a) Unaligned CTAB under a polarising microscope

(b) Aligned CTAB under a polarising microscope

Figure 4.16: Microscope images of (a) unaligned and (b) aligned CTAB in the nematic phase under a polarising microscope. Notice the homogeneous colour of CTAB when it is aligned, showcasing its birefringent properties.

Simulation

SAXS results were for aligned gold nanorods with dimensions of 40 nm ± 15 nm by 17 nm ± 2 nm with an angular (alignment) polydispersity of 30° were performed in SasView [387]. The incident X-rays were set to 12 keV (the X-ray energies at the synchrotron). For the purposes of the simulation of looking at X-ray scattering, the solution was set to be water, and it was set to have a negligible effect of the scattering image. The radial and angular X-ray intensities were compared between horizontally orientated and vertically orientated AuNRs for unpolarised incident X-rays.

4.6 Scattering Results

Aligned Nematic CTAB

In Figure 4.16 we see (a) unaligned CTAB and (b) aligned CTAB in the nematic phase under a polarizing microscope. The inhomogeneity of colour of the slide in (a) contrasts to the homogeneity in colour of the slide in (b), which clearly showcases the successful alignment of the CTAB liquid crystals because of their birefringent nature. The light from underneath the

sample is white i.e. all colours of the visible spectrum. The sample is viewed through cross polarisers, i.e. the light from underneath the sample is plane polarised and the eyepiece has a polarising filter that is orientated perpendicularly to the illuminating light [155]. This means that if the sample is all oriented in the same direction, so are the directions of ordinary and extraordinary waves, and thus also their velocities. Interference patterns between the ordinary and extraordinary waves will then happen similarly (at the same wavelengths) and thus the colour is homogenised. If the sample is not all oriented in the same direction, the ordinary waves and the extraordinary waves of the birefringent sample are all not going to be in the same directions either. Thus, interference patterns between those waves will happen at different wavelengths, depending on the orientation of the liquid crystal, giving us the different colours of the sample.

AuNR Synthesis

The AuNRs under a scanning electron microscope (SEM) can be seen in Fig.4.17 . The gold nanoparticles are generally rodlike with an average length of 40 nm and an average width of 16.9 nm, giving an aspect ratio of approximately 2.4 nm. As the asymmetric scattering image is the result of the difference in the length and width of the nanorods, a larger aspect ratio would result in great asymmetry. For our purposes, an aspect ratio of 2.4 is sufficient. Figure 4.18

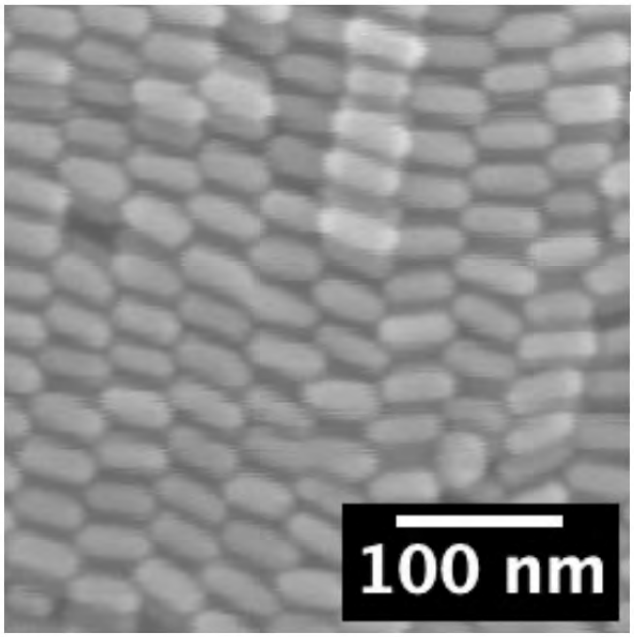

Figure 4.17: Scanning electron microscope (SEM) image of the gold nanorods. They have an average length of 40 nm and an average width of 16.9 nm, giving them an aspect ratio of 2.4.

shows the absorption spectra of the AuNRs with CTAB, carboxylate (CM), amine (NH_2) and methyl (MPEG) functionalisations. As they are rod like, 2 peaks are result, coming from the

two SPR, one transverse and one longitudinal. The first characteristic peaks for all AuNRs are at approximately 510 nm. And the second characteristic peak is at approximately 820 nm for CTAB functionalisation and 840 nm for CM, MPEG, and NH_2 functionalised AuNRs (a blue shift), a behavior similar to the report by Ablarghouthi et al. [388].

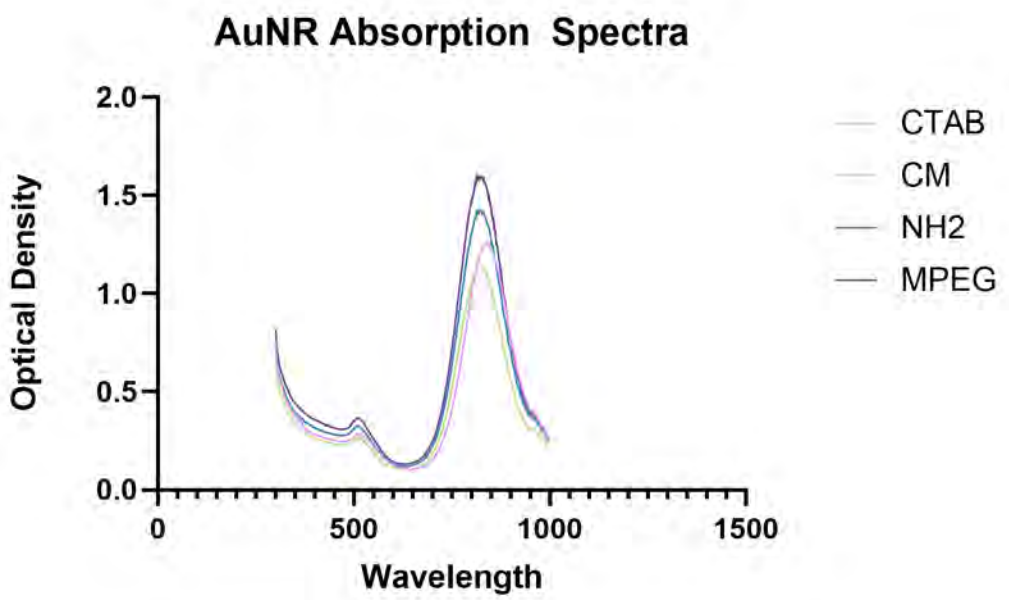

Figure 4.18: Absorption spectra of AuNR with CTAB, carboxylate (CM), amine (NH_2) and methyl (MPEG) functionalisations.

The absorption spectra for the AuNRs used are shown in Figure 4.19, characterised by two peaks at 510 nm and 840 nm as expected for nanorods, with spherical nanoparticles having only one peak. The peaks are as a result of the different SPR modes that arise as a result of the uneven dimensions of the nanorods. The 510 nm peak is as a result of transverse SPRs and it still fairly consistent with varying aspect ratios. The 840 nm peak is from the longitudinal SPR mode, traveling along the major axis of the AuNRs, and this increases with aspect ratio and with the dielectric constant of the AuNR, but also with its capping molecule (in this case CTAB) [384, 389]. Our absorption spectrum is consistent in shape with other AuNR spectra [390–392]. However, the longitudinal peak is higher than one would expect for nanorods with our aspect ratio of 2.4[393]. But, as the functionalisation of the nanorods (capping) changes its dielectric constant, it suggests that our nanorods have a higher than expected dielectric constant due to the CTAB capping.

As we are testing for Thomson scattering between AuNRs and X-rays, we wanted to ensure a high interaction rate. Therefore, we wanted a high concentration of AuNRs in our mixture. The concentration of the AuNRs can be approximated by their absorptance at 400 nm [394]:

$$[\mathrm{AuNR}]_{\mathrm{mM}} = 0.44 \times A_{400} \tag{4.40}$$

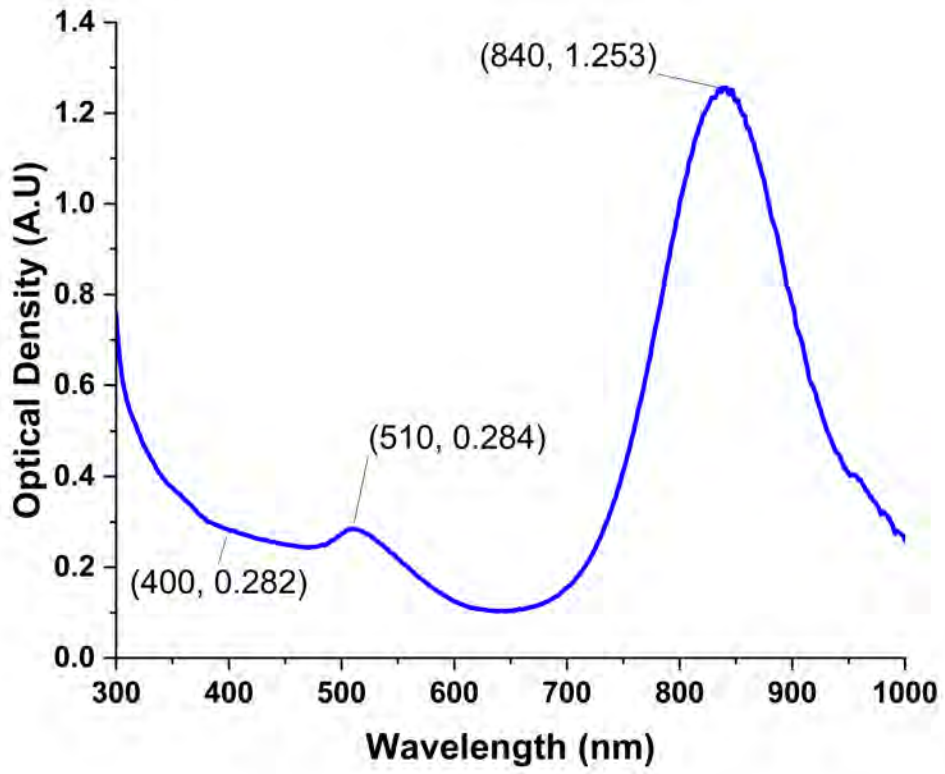

Figure 4.19: Absorption spectra of AuNR functionalised with CTAB, characterised by two peaks as a result of transverse and longitudinal SPRs. The first at 510 nm and the second at 840 nm.

where A_{400} is in units of optical density.

We tested the absorption of the AuNRs to light at 400 nm, which gave an optical density of 2.82. Using Equation 4.40, we then calculated the concentration of the AuNR solution to be approximately 1.24 mM. From Equation 4.39, we calculate the concentration of the AuNRs to be approximately: 0.124 mM with the CTAB functionalisation, 0.115 mM with the CM functionalisation, 0.139 mM with the NH_2 functionalisation and 0.157 mM with the MPEG functionalisation.

The sample used at the Australian Synchrotron consisted of 1.4 g of CTAB, 2.6 g of Milli-Q water and 1 g of 0.124 mM solution of AuNRs functionalised with CTAB, giving a total volume of approximately 3.6 mL and a therefore a concentration of 0.034 mM of AuNRs or approximately 2.05×10^{-19} AuNRs per litre. Nanorods of 40 nm long with a radius of 8.5 nm have a volume of approximately 9000 nm^3. This gives a volume fraction of $\Phi = 0.018$. This is above the colume fraction for non-interactive particles of $\Phi < 0.001$, but this shouldn't impact the alignment of the AuNRs.

Simulation

A model of the scattering pattern for unpolarised X-rays of 12 keV off aligned AuNRs of dimension 40 nm ± 5 nm by 17 nm ± 2 nm with an angular polydispersity of 30° to the alignment was done in SasView. The output for the 2D scattering intensity function for aligned cylinders is given by [395]:

$$I(q,a) = \frac{\Phi}{V} F^2(q,a) + \text{background} \tag{4.41}$$

where Φ is the volume fraction of the AuNRs[18], $V = \pi r^2 L$ is the volume of the cylinder and $F^2(q,a)$ is the form factor being:

$$F^2(q,a) = 2(\Delta\rho)V = \frac{\sin\frac{1}{2}qL\cos\alpha}{\frac{1}{2}\cos\alpha}\frac{J_1(qR\sin\alpha)}{R\sin\alpha} \tag{4.42}$$

where α is the angle between the axis of the cylinder and scattering vector q, L is the length of the cylinder, R is the radius of the cylinder, $\Delta\rho$ is the scattering length density(sld) difference between the scatterer and the solvent (sld of Au = 113 10^{-6} Å^{-2} and sld of CTAB and water being negligible compared to Au, this sld = 0 for the solvent.). and J_1 is the first order Bessel function.

Although individual AuNRs are expected to give an anisotropic SAXS image because of their asymmetrical and elongated shape, a population of unaligned AuNRs would still result in a symmetrical scattering pattern due to the scattering imaging being the summation of X-ray scattering off every AuNR. This can be seen in Figure 4.20(a). This is a simulation of the expected SAXS image done in SASView [387] for a beam of 12 keV X-rays on unaligned AuNRs, in water, of dimensions 40 nm × 17 nm with random alignment in azimuthal angle ϕ and also polar angle θ. We modelled AuNRs in water instead of CTAB as they are both low in contrast to the gold nanorods and thus are not expected to change the simulations overtly. As the CTAB is only there to facilitate the alignment of the nanorods, it can be ignored to visualise a scattering pattern because of the gold only, and this also saves computation time. If the AuNRs are aligned, the sum of the scattered X-ray counts (intensity) would result in an elongated shape that is the inverse of the rod shape. This can be seen in Figure 4.20(b) for horizontally aligned AuNRs and Figure 4.20(c) for vertically aligned AuNRs. As this model simulates a beam of unpolarised X-rays, the radial data reduction, which is a plot of the total counts of the scattered X-rays for each q-value (see Equation 4.39) or $I(q)$ vs. q, is identical regardless of the orientation of the AuNRs, as can be seen in Figure 4.21(a) after a radial reduction. Here reduction simply is the summation of the X-ray counts in the scattered image, and a reduction sums over a fixed radius (q-value) away from the centre, over a 2π range of the azimuthal angle ϕ (a complete circle). An angular reduction sums over a range of radii whilst keeping ϕ fixed. The radial data reduction, which is a plot of the total counts of scattered X-rays for each value of the azimuthal angle ϕ in degrees or $I(\phi)$ vs. ϕ, are also identical except for a shift of 90° between the two orientations as can be seen in Figure 4.21(b) . This is expected due to the 90° rotation. What we are aiming to test for is whether the angular reduction plot remains the same if the X-ray beam is polarised.

[18] $\Phi = 0.018$ for our experiment

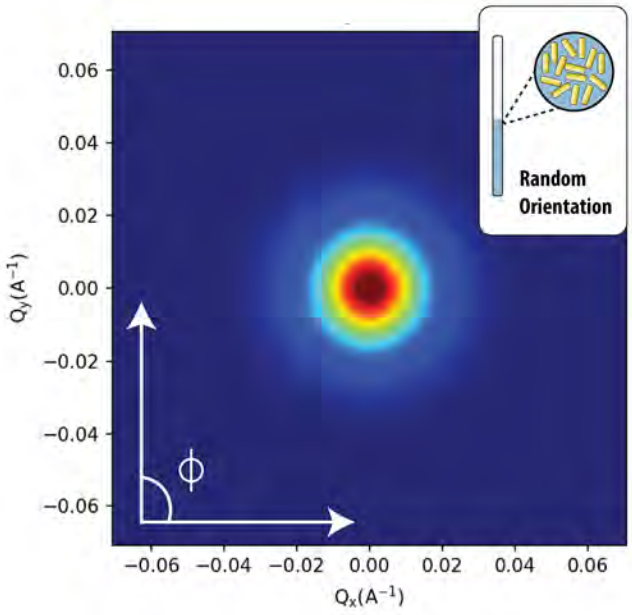

(a) Simulated scattering image of unaligned AuNRs and unpolarised 12 keV X-rays

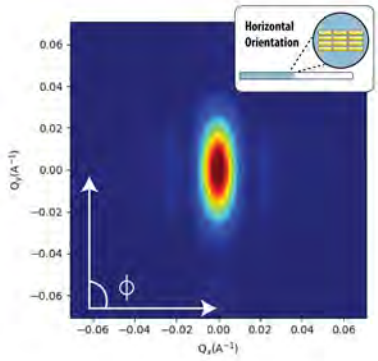

(b) Simulated scattering image of horizontally orientation AuNRs and unpolarised 12 keV X-rays

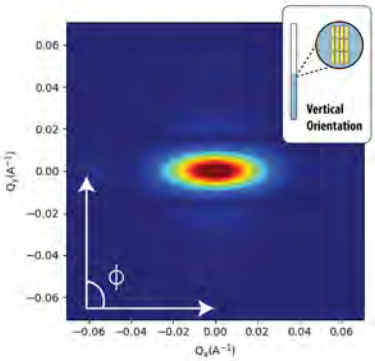

(c) Simulated scattering image of vertically orientation AuNRs and unpolarised 12 keV X-rays

Figure 4.20: SAXS model of unpolarised X-rays for (a) unaligned AuNRs (b) horizontally aligned AuNRs and (c) vertically aligned AuNRs. The scattering image of unaligned AuNRs results in a symmetric pattern. Aligned AuNRs results in an anisotropic shape.

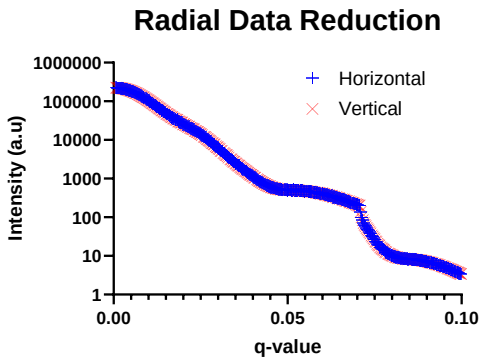

(a) Radial data reduction (Blue: horizontal, Orange: vertical)

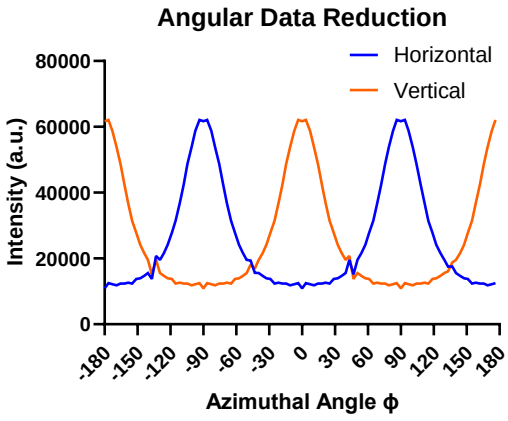

(b) Angular reduction (Blue: horizontal, Orange: vertical)

Figure 4.21: (a) Shows the radial data reduction (summation of X-ray counts radially outwards) and (b) shows the angular data reduction (summation of X-ray counts with azimuthal angle ϕ) of the horizontally and vertically aligned AuNRs. The radial data reduction has the horizontal and vertical intensity be exactly equal at every q, whilst the angular data reduction has the intensity plots being shifted by 90° due to the rotation of the AuNRs. However the peak intensities are still exactly the same.

Benchtop SAXS at varying AuNR concentrations

In Figure 4.22 we see the SAXS results of nematic CTAB with AuNRs for different concentrations by weight; (a) 1%. (b) 2.6%, (c) 5.8% and (d) 10.4%. The pattern is anisotropic because of the alignment of the AuNRs and their asymmetric (rod-like) shape. If the AuNRs were not aligned, the scattering pattern would have been a circle with layered rings. It was determined that around 5.8% by weight of the AuNR solution should be added to the CTAB to get the desired scattering pattern. Aligned nanorods would give an intensity peak perpendicular to their long axis, which is what we see in Figure 4.22(a), Figure 4.22(c) and Figure 4.22(d), however, there is some smearing and de-alignment of the AuNRs in Figure 4.22(a) and Figure 4.22(d) as can be seen from the shape of the central scattering pattern, as low q-values are scattered X-rays primarily from the gold. This could be caused by a changing of phase from nematic to hexagonal or a metastable gel phase[369] due to the drop in temperature or the dehydration of of the sample. Figure 4.22(b) also shows nice alignment but from the orientation of the peaks, the alignment seems to be vertical rather than horizontal. This could potentially be caused by the orientation of the capillary inside the centrifuge being not well aligned with the centrifugal force provided. This means that the solution did not flow evenly down the capillary, causing the AuNRs to be aligned not parallel to the capillary.

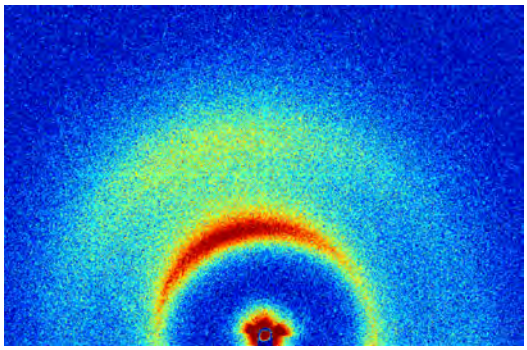

(a) SAXS pattern of nematic CTAB with 1% AuNR solution by weight.

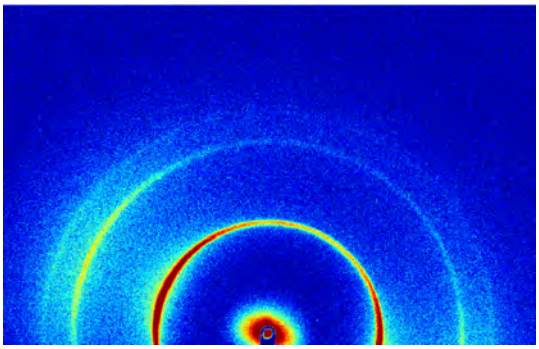

(b) SAXS pattern of nematic CTAB with 2.6% AuNR solution by weight.

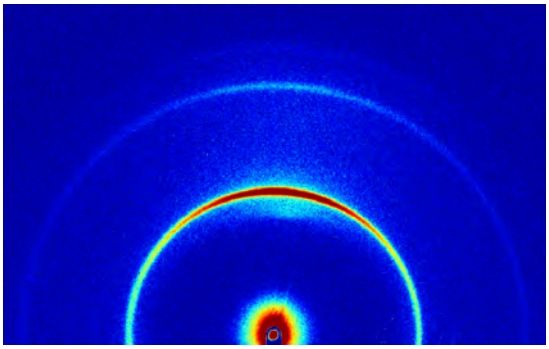

(c) SAXS pattern of nematic CTAB with 5.8% AuNR solution by weight.

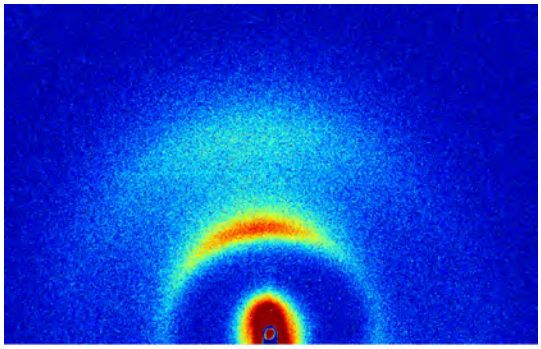

(d) SAXS pattern of nematic CTAB with 10.4% AuNR solution by weight.

Figure 4.22: SAXS of aligned nematic CTAB + AuNR at different concentrations.

RheoSAXS

In Figure 4.23 we can see the results of RheoSAXS of the nematic CTAB + AuNR at different shear rates of the rheometer; (a) 50 s^{-1}, (b) 250 s^{-1} and (c) 500 s^{-1}. There does not seem to be any significant difference between the three rotational speeds. However, the results are not as sharp as those of the centrifuge method, and this could be because the rheometer introduces air bubbles into the mixture because of the constant rotation of the bob.

We show the scattering image of aligned AuNRs in nematic CTAB obtained using the bench-top RheoSAXS at 50 s^{-1} can be seen in Figure 4.24(a) with Fig 4.24(b) being the SAXS image taken 30 min after stopping the rheometer. Due to the short sample-to-detector distance, the central scattering pattern of the gold is mostly blocked by the beamstop. However, we can still determine the alignment of the mixture from the first diffraction ring, as seen above and below the central bright spot in the image.

This is caused by the first order constructive interference pattern of the scattered X-rays off the layers of CTAB and gold. An unaligned sample would result in a homogeneous ring as their is preferred scattering direction. However, our scattering images show an asymmetry of the

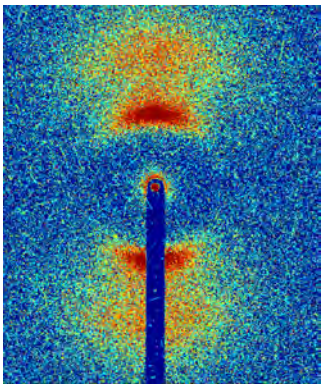

(a) RheoSAXS of nematic CTAB + AuNRs at 50 s^{-1}

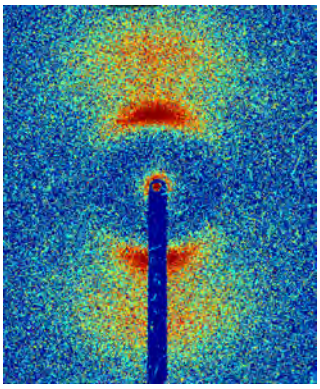

(b) RheoSAXS of nematic CTAB + AuNRs at 250 s^{-1}

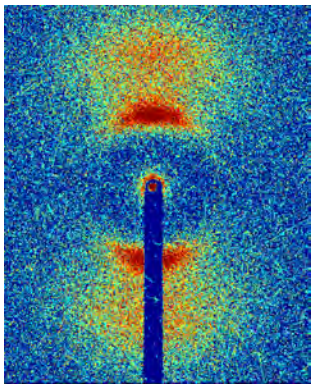

(c) RheoSAXS of nematic CTAB + AuNRs at 500 s^{-1}

Figure 4.23: RheoSAXS at different shear rates.

sample, indicating horizontal alignment. Furthermore, little to no loss of alignment can be seen after a 30 minute relaxation time. As the time between shots at the Australian Synchrotron is on the order of a few minutes at most, the AuNRs should retain their alignment.

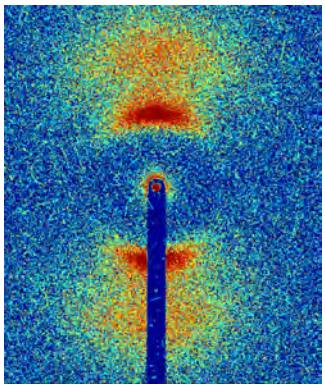

(a) RheoSAXS of nematic CTAB + AuNRs at 50 s^{-1}

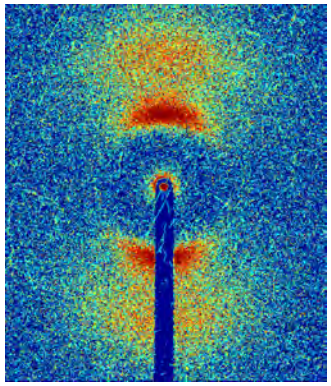

(b) SAXS of (a) after a 30min relaxation time

Figure 4.24: Scattering of (a) and (b) are very similar despite a 30 min relaxation time. This showcases that the AuNRs in NLC have a long relaxation time.

In Figure 4.25 we can see the RheoSAXS results of nematic CTAB and AuNRs with different capping; (a) CTAB cap, (b) CM cap, (c) NH_2 and (d) MPEG cap. From the scattering patterns it appears that the sharpest and clearest scattering results are from using either CTAB or MPEG capping and the best alignment are from using CM capping, but there isn't a significant difference between the 3. However, the NH_2 capping has the weakest results.

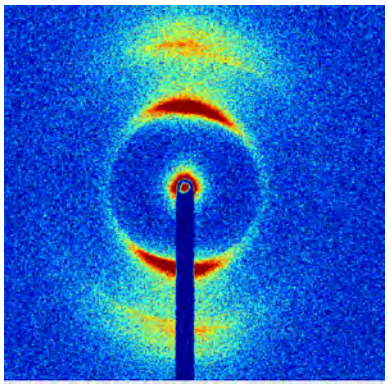

(a) RheoSAXS of nematic CTAB + CTAB capped AuNRs

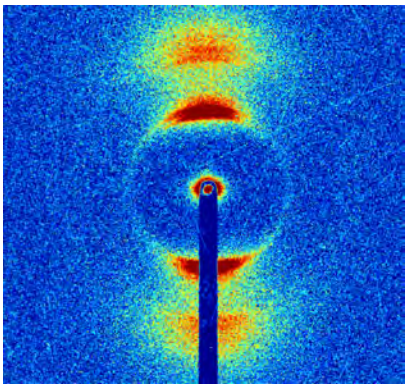

(b) RheoSAXS of nematic CTAB + CM capped AuNRs

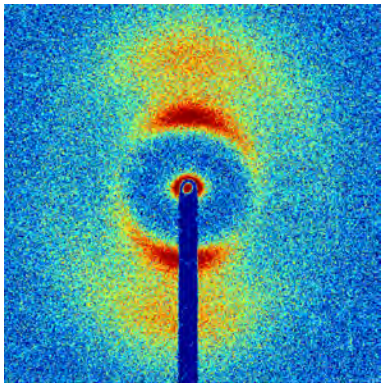

(c) RheoSAXS of nematic CTAB + NH_2 capped AuNRs

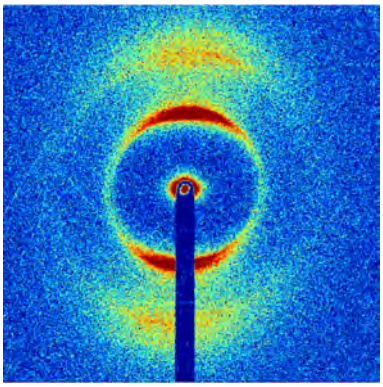

(d) RheoSAXS of nematic CTAB + MPEG capped AuNRs

Figure 4.25: RheoSAXS at of nematic CTAB and AuNRs with different cappings.

Polarised X-ray Interactions with Synchrotron Radiation

The scattering results of aligned AuNRs under polarised SAXS can be seen in Figure 4.26. The central bright spot (near q = 0) is due to direct scattering of the AuNRs, the asymmetric shape indicating their successful alignment. The rings around the central bright spot are due to the interference patterns of the scattered X-rays as a result of the spacings between the ordered AuNR and CTAB mixtures. The phase of the liquid crystal can be determined from the q-value ratio of the rings. However, since we are only concerned with aligned AuNRs, whether the liquid crystals are in a nematic or hexagonal phase should not have an impact on our results and conclusions. Figure 4.26(a) shows the scattering image for horizontally aligned AuNRs and Figure 4.26(b) shows the scattering image for vertically aligned AuNRs. As the gold interacts much more strongly with X-rays compared to the quartz capillary and the nematic CTAB solution, their contributions to the scattering intensity is negligible, and thus can be ignored when analysing the data. We can see that the anisotropic shape of the scattering image agrees with the simulation. There is a more rounded shape in the actual results when compared

with the simulated data. However, the simulations are for perfectly identical AuNRs with no variations in θ or ϕ. The actual nanorods would have some degree of polydispersity in the shape, size, and orientation, but we can see that they are still generally aligned. Firstly, we needed to determine whether the X-ray interaction spot between the two events remained consistent. This was done by looking at the radial data reduction of intensity of the scattered X-rays for every q-value, $I(q)$ vs. q. Data reduction was performed using the AntonParr SAXSanalysis software after exportation of the images obtained at the Australian Synchrotron. As we were only concerned with scattered X-rays from the nanorods and not about the interference patterns i.e. the ring structures, data reduction was chosen to be done from a q-value of 0.03 - 0.6. The lower limit is due to the fact that there being a beamstop protecting the detector from the high flux X-ray source and negating all the small q counts. The upper limit was chosen to maximise the counts of X-rays scattered from the AuNRs whilst also not counting X-rays undergoing interference (ring structures). The radial data reduction can be seen in Figure 4.26(c). Both orientations have a very similar $I(q)$ vs. q plot, which indicates a consistent sample.

Next, we wanted to see how a polarised beam of X-rays impacts the scattering pattern of the AuNRs in the horizontal and vertical orientations. In the simulations, the only difference between the two orientations was a 90∘ shift in the angular data reduction, with the same amplitudes. We wanted to see if polarised X-rays would also cause a change in the amplitudes of the data reduction, in addition to the angular shift. An angular data reduction was performed between the intensity of the scattered X-rays against the azimuthal angle ϕ, or $I(\phi)$ vs. ϕ, also choosing the same q-value ranges of 0.03 to 0.6. As the AuNR orientations were offset by 90 degrees from the rotation of the capillary, so were the angular scattering results, as seen in Figure 4.26(d)..

To compare the angular reduction directly, a 90 degree shift was applied. This can be seen in Figure 4.27). In the shifted angular reduction of $I(\phi)$ vs. ϕ, there is now a difference in the peak magnitudes, in contrast to the simulated results. The vertically aligned AuNRs resulted in a higher peak compared to the horizontally aligned AuNRs. This means that the scattered X-rays off the vertical AuNRs were distributed more sharply than the scattered X-rays off the horizontal AuNRs. As the only difference between the two samples was the angle subtended by the E-vector of the polarised X-rays, which were horizontal, and the alignment direction of the AuNRs, this indicates that polarisation of the X-rays influences their scattering direction.

Figure 4.28 shows another scattering result of aligned AuNRs and polarised X-rays from (a) horizontal orientation and (b) vertical orientation. Once again (c) shows the radial data reduction $I(q)$ vs. q and (d) shows the angular data reduction, $I(\phi)$ vs. ϕ. Once again the radial data reduction plots are nearly identical whilst the shifted angular plots (Figure 4.29) shows that the vertically aligned AuNRs have sharper peaks and troughs.

Figure 4.30 is another result of SAXS of aligned AuNRs at the Australian Synchrotron, with (a) horizontal orientation and (b) vertical orientation. (c) shows the radial data reduction $I(q)$ vs. q and (d) shows the angular data reduction, $I(\phi)$ vs. ϕ. The radial data reductions are once again identical, suggesting the sample remained the same after rotation, however, Figure 4.31, which shows the shifted angular data reduction, this time having the horizontally aligned AuNRs have slightly sharper peaks compared to the vertically aligned AuNRs. However, from Figures 4.30(a) and 4.30(b), the scattering pattern in the centre is more box-like and less rounded that compared to Figures 4.28(a) and 4.28(b) and Figures 4.26(a) and 4.26(b). This may suggest that the AuNRs are no longer perpendicular to the incident beam, but rather at a different angle. This effective changes their shape from the perspective of the X-rays, resulting in the

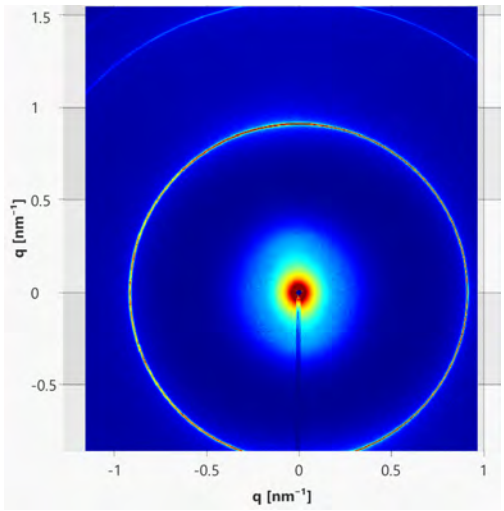

(a) Horizontal Orientation

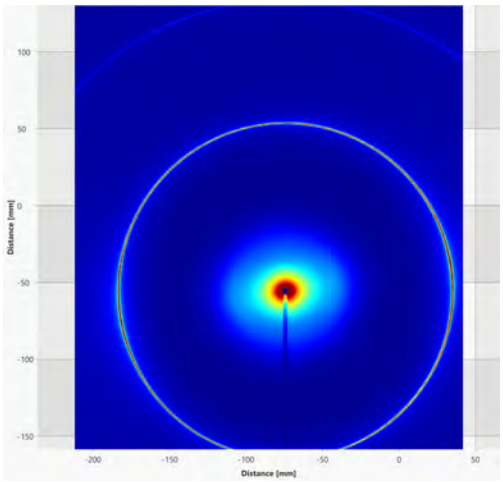

(b) Vertical Orientation

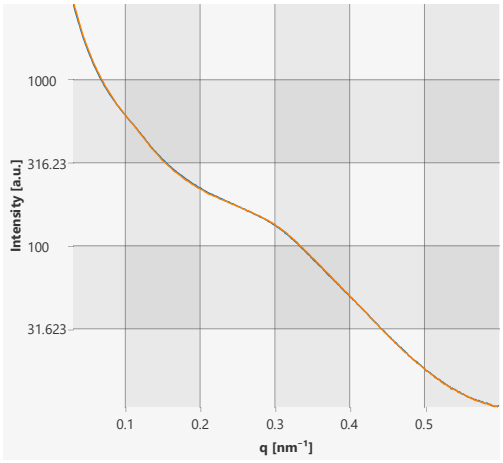

(c) Radial data reduction

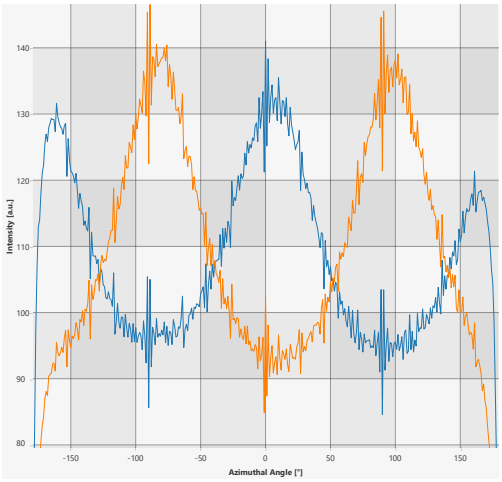

(d) Angular data reduction

Figure 4.26: SAXS results of horizontally polarised X-rays and aligned gold nanorods in the (a) vertical orientation and (b) horizontal orientation. (c) Radial data reduction of the counts of the scattering X-rays of the capillary in the horizontal and vertical orientations. The two nearly overlapping plots indicates the X-rays hit a consistent sample. (d) Angular data reduction of the same scattering images. The difference in peak magnitudes indicates a difference in the angular distribution of the scattered X-rays.

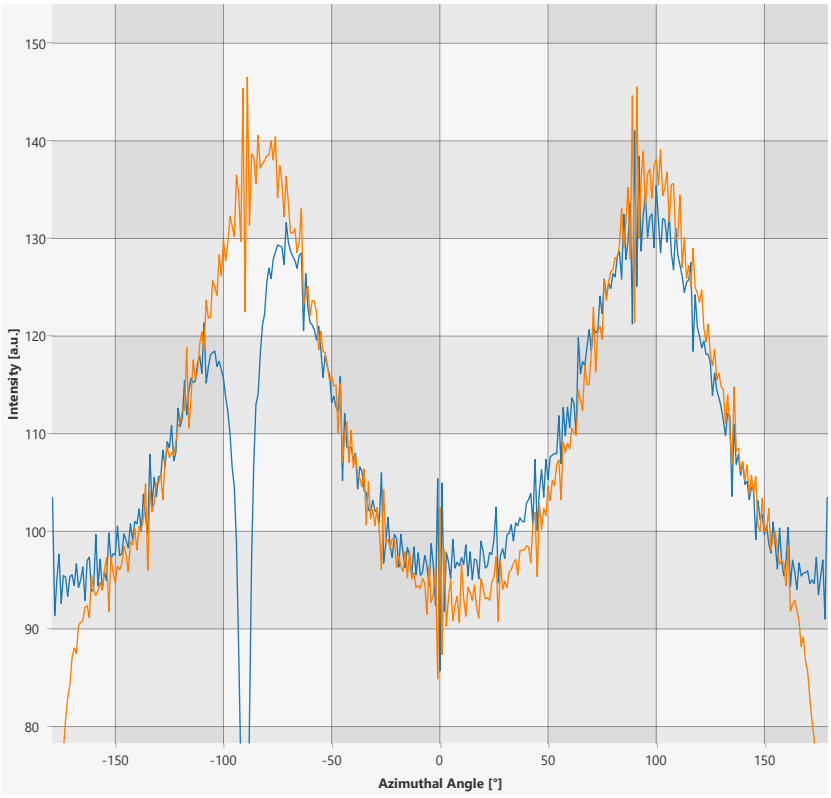

Figure 4.27: Shifted angular data reduction of the scattering images in Figure 4.26 (blue: horizontal, orange: vertical),. The difference in peak magnitudes indicates a difference in the angular distribution of the scattered X-rays.

differently shaped scattering pattern. This may be the cause of the change in behaviour of the scattered X-rays.

As we are investigating the impact of the angular scattering pattern of the angle between the polarisation vector of the X-rays and the orientation vector of the AuNRs after a rotation of the AuNRs, we also wanted to check to see if the differences in amplitudes obtained above remained if the gold nanorods were aligned at a 45° angle. In this scenario, a 90° rotation of the capillary would not result in a different angle of the polarisation of the X-rays and the AuNRs (as it would still be a 45° angle in both instances), and we expect the amplitudes of the scattering images to remain the same accordingly. The resulting scattering images of the aforementioned scenario can be seen in Figure 4.32(a) and Figure 4.32(b).

Once again, the radial data reduction $I(q)$ vs. q, are very similar (Figure 4.32(c)), showing that there were no disturbances in the sample after rotation. However, as seen in Figure 4.33, the shifted angular intensities are now also very similar despite a 90-degree rotation of the AuNRs, which means that the angular distributions of the scattered X-rays relative to the AuNRs remained the same. As the angles formed by the AuNRs and the E-vector of the X-rays are similar after a 90 degree rotation, with both being approximately 45°, this indicates that

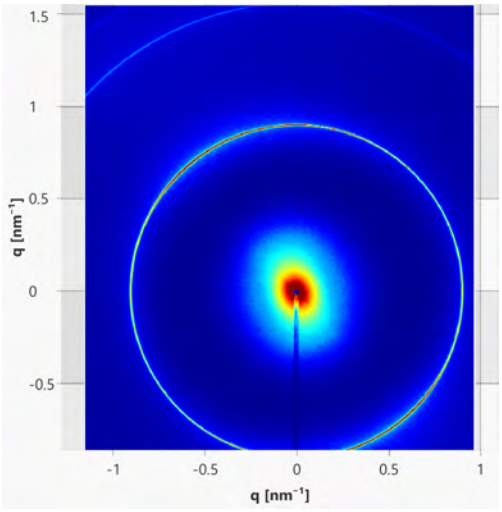

(a) Horizontal Orientation

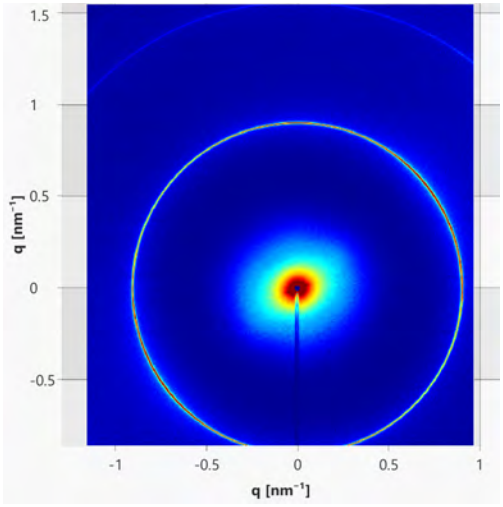

(b) Vertical Orientation

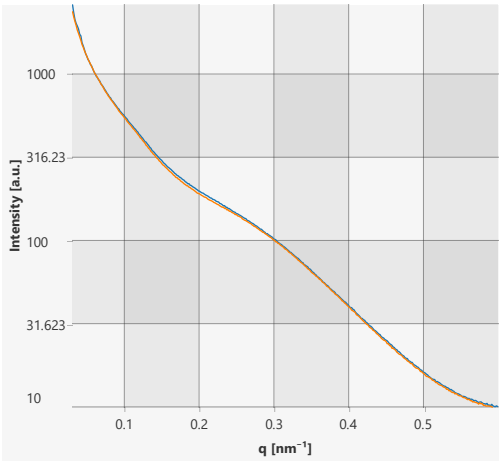

(c) Radial data reduction

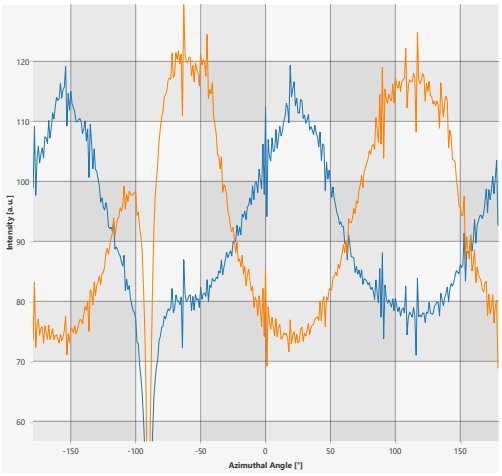

(d) Angular data reduction

Figure 4.28: SAXS results of the aligned gold nanorods with the alignment in the (a) horizontal orientation and (b) vertical orientation. (c) Radial data reduction (blue: horizontal, orange: vertical). (d) angular data reduction (blue: horizontal, orange: vertical)

.

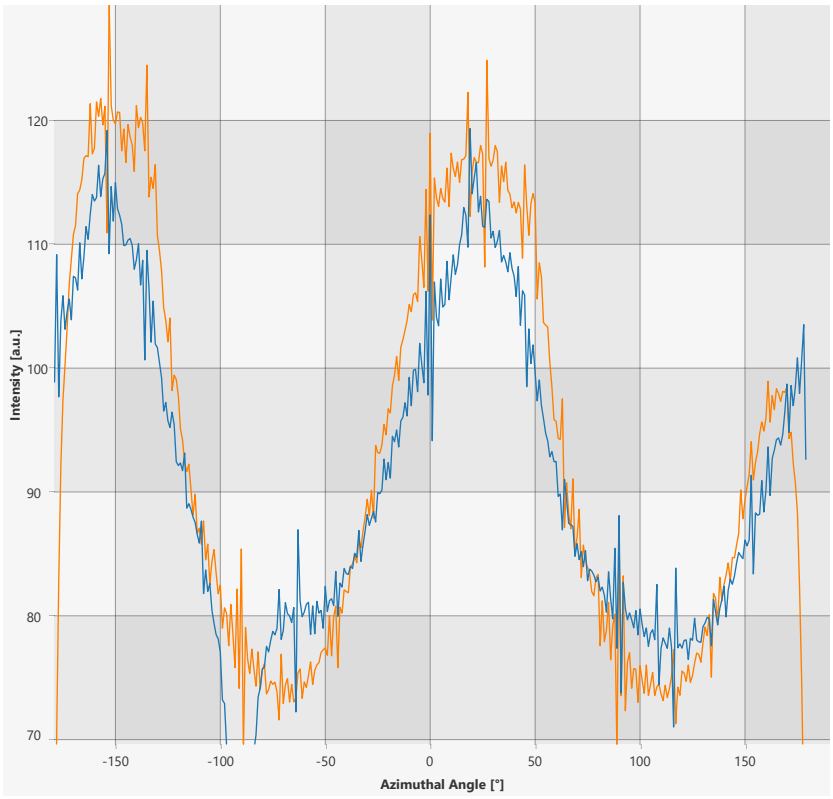

Figure 4.29: Shifted angular reduction for Figure 4.28 (blue: horizontal, orange: vertical), showing, once again, a higher peak and lower trough for the vertically aligned AuNRs compared to the horizontally aligned AuNRs.

the difference in angular scattering seen in Figure 4.27 and Figure 4.29 was not only caused by the rotation of the capillaries.

Furthermore, we also wanted to check the scattering results for unaligned or poorly aligned AuNRs to see if the polarisation dependence of the anisotropic scattered was an artefact of the SAXS instrumentation. Poorly aligned AuNRs in a quartz capillary was placed in the beamline in the horizontal and vertical orientations. The scattering images can be seen in Figure 4.34(a) and Figure 4.34(b). As the AuNRs are poorly aligned, the scattering image is much more symmetric. The radial reduction is shown in Figure 4.34(c), once again showing the intensity I(q) as a function of the q-value. The matching plots show that the sample was the same between the two shots and, moreover, that even partially aligned AuNRs have the same interaction rates with the polarised X-ray beam after rotation. The shifted angular data reduction is shown in Figure 4.35). There is actually a slight periodicity of the plot showing a partial alignment. We can see that partially aligned AuNRs also displayed very little difference in the angular scattering plots. This shows that the distribution or the direction of the scattered X-rays relative to the alignment of the AuNRs remained consistent in this case. This indicates that the difference seen in Figure 4.27 and Figure 4.29 was not the result related to the X-ray detector or an inherent

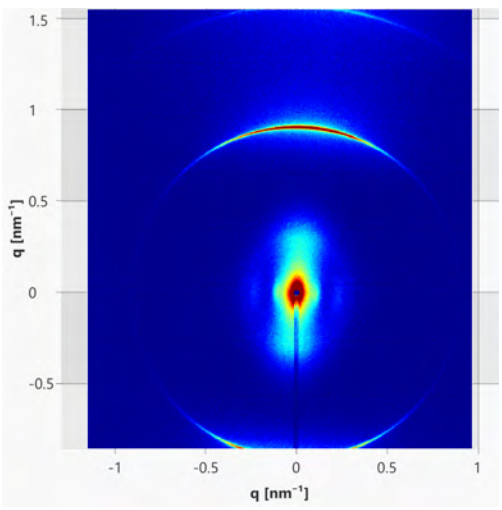

(a) Horizontal Orientaion

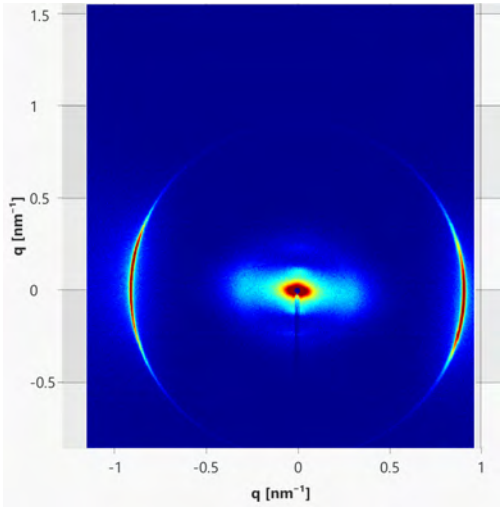

(b) Vertical Orientation

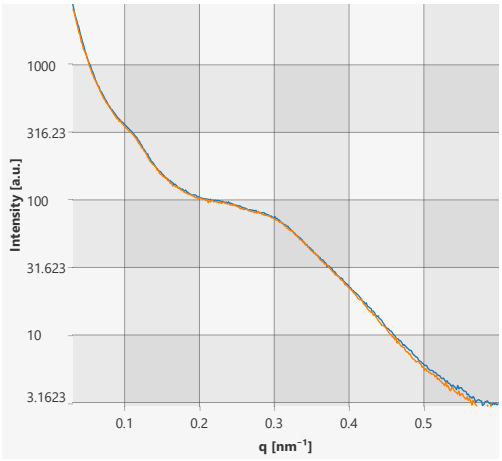

(c) Radial data reduction

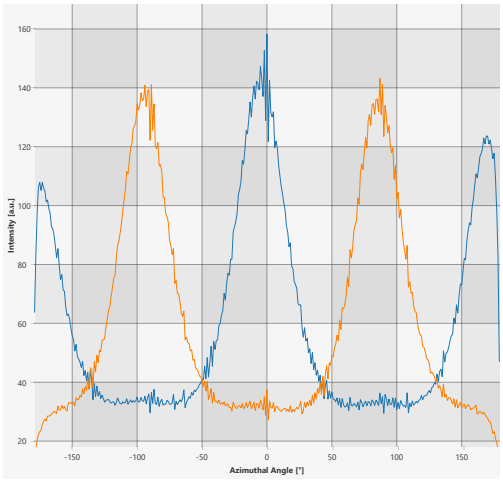

(d) Angular data reduction

Figure 4.30: Scattering results of SAXS of the align gold nanorods with the alignment in the (a) horizontal orientation and (b) vertical orientation. (c) shows the radial data reduction (blue: horizontal, orange: vertical) and (d) the angular data reduction (blue: horizontal, orange: vertical)

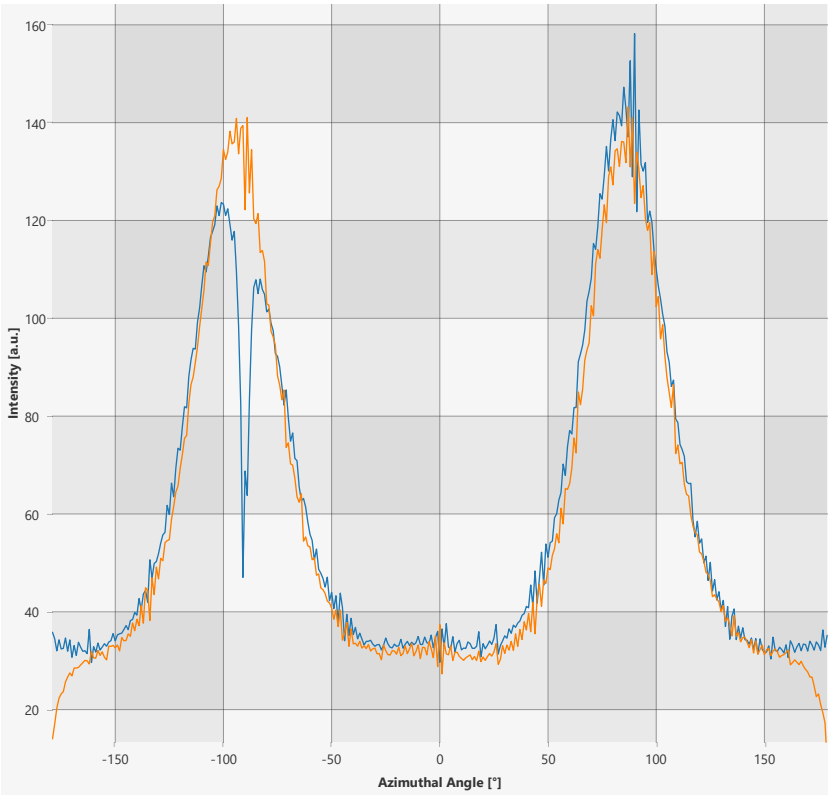

Figure 4.31: Shifted angular reduction for Figure 4.30 (blue: horizontal, orange: vertical). This time however, we can see there is a higher amplitude for the horizontally aligned nanorods instead of the vertically aligned nanorods.

artefact of the beamline, as that difference would also be present here. This reinforces the idea that the angle between the polarisation of the X-rays and the aligned AuNRs is the cause of the anisotropy in the angular scattering pattern that we observed.

4.7 Discussion

The results obtained at the Australian Synchrotron for SAXS of aligned AuNRs in a nematic CTAB solution and horizontally polarised X-rays showed that there was a difference in the angular distribution of the scattered X-rays when the alignment of the AuNRs was in the vertical and horizontal orientations. In fact, when the alignment of the AuNRs was perpendicular to the E-vector of the incident X-rays (horizontal), the angular scattering intensity produced higher peaks and lower troughs compared to the AuNRs oriented parallel to the X-ray E-vector. This meant that more of the scattered X-rays were in the direction directly perpendicular to the AuNRs and less in the direction directly parallel, changing the direction of the scattered X-rays relative to the orientation of the AuNRs. The differences were not caused by the X-rays striking

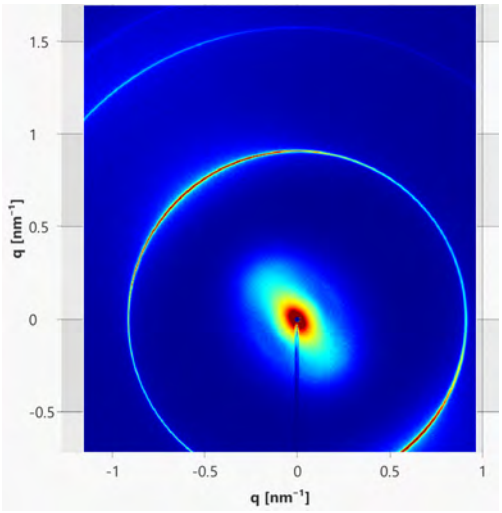

(a) Horizontal Orientaion

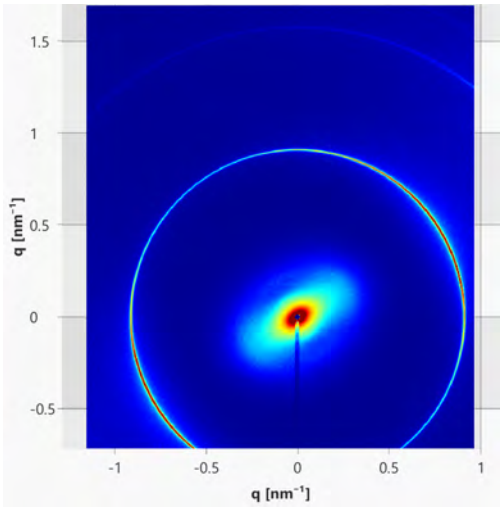

(b) Vertical Orientaion

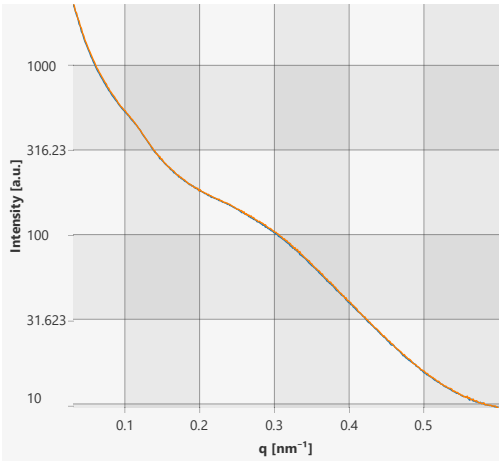

(c) Radial data reduction

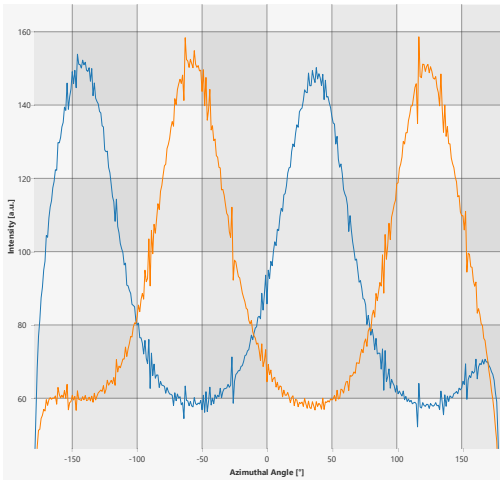

(d) Angular data reduction

Figure 4.32: Scattering results of SAXS of the align gold nanorods with the alignment in the (a) horizontal orientation and (b) vertical orientation. In this case the alignment of gold nanorods meant that under both vertical and horizontal orientations of the capillary, the angle subtend by aligned AuNRs and the x-ray E-vector remained the same. (c) Radial reduction of both images shows that the samples were still consistent in composition between shots. (d) Angular data reduction of both images (blue: horizontal, orange: vertical).

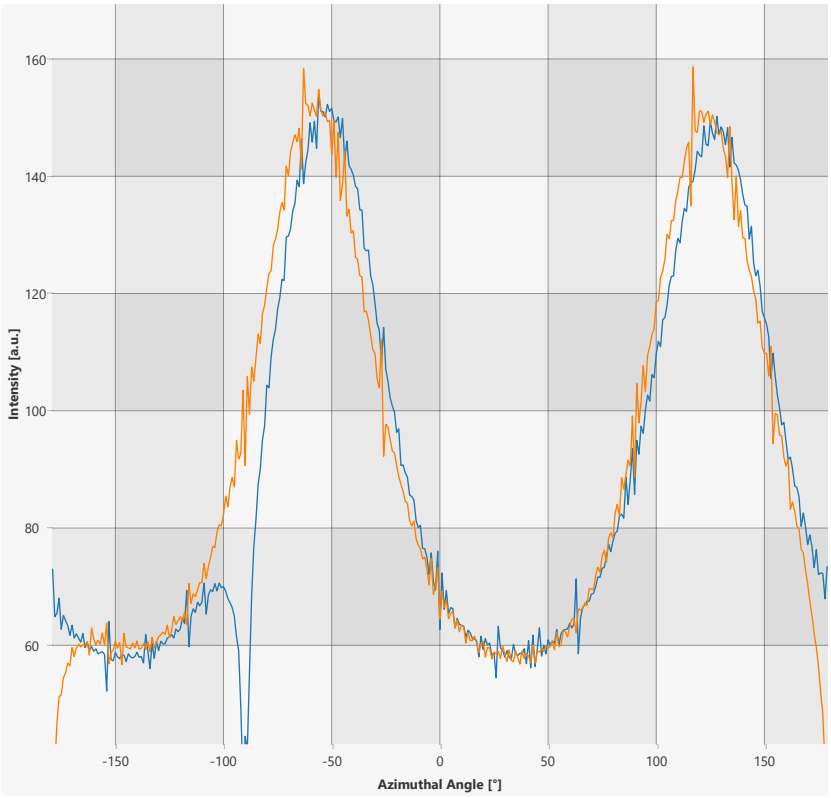

Figure 4.33: Shifted angular reduction for Figure 4.32 (blue: vertical, orange: horizontal), This time however, the two plots are much more similar. This meant in this case, the distribution of the scattered X-rays were the same for both orientations.

the capillary at a different location, differences in material, a change in phase of the nematic liquid crystal, or a change in path length of the X-rays through the material, because of the similarity of the radial plots at each q-value. Any instance of radiation damage or de-alignment of the AuNRs would have been seen in a change in the intensity plot of the radial reduction data. We also established that the relaxation time of the aligned AuNRs was not a factor as it is much longer than the time it took between shots.

Furthermore, when the alignment of the AuNRs was at 45° with the capillary, resulting in both orientations of the capillary having the same angular separation from the polarisation vector of the X-rays, the angular scattering patterns no longer showed any differences in intensity relative to the orientation. This suggests that the differences in the angular distribution of the scattered X-rays are not caused by the rotation of the capillary and that the angle subtended the orientation of the AuNRs and the X-ray polarisation is most likely the cause of the change. Additionally, when the AuNRs were poorly aligned or partially aligned, there were also no differences in the angular scattering pattern after rotation. This suggests that any differences detected in the scattering pattern were not due to the detection mechanism such as a fault in

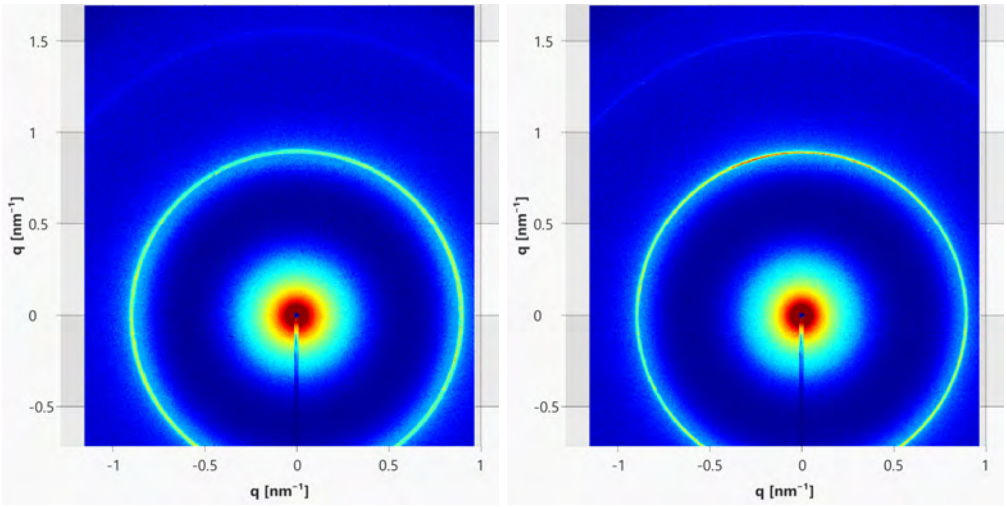

(a) Radial data reduction

(b) Angular data reduction

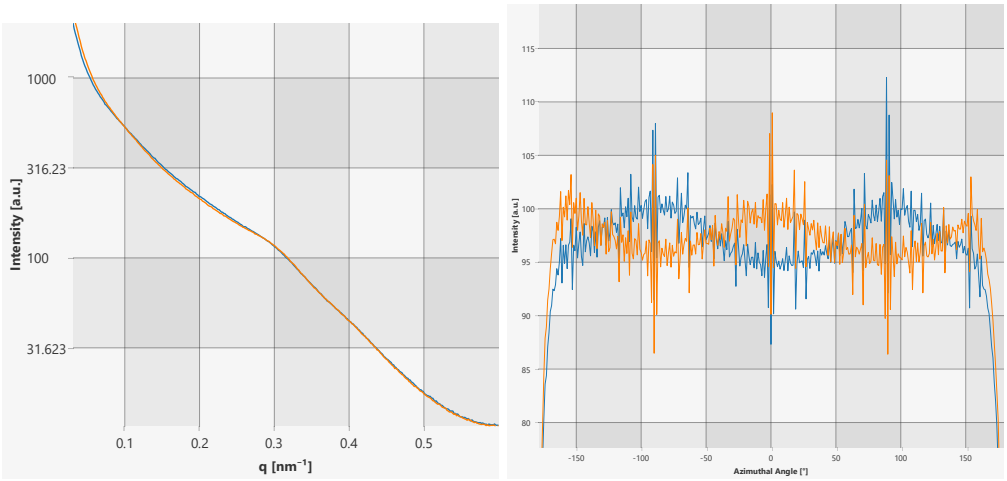

(c) Radial data reduction

(d) Angular data reduction

Figure 4.34: Scattering results of SAXS of poorly aligned AuNRs with the capillary in the (a) horizontal orientation and (b) vertical. In this instance, we obtained poorly aligned AuNRs which resulted in a more symmetric circular scattering pattern. (c) The radial data reduction are similar for the two orientations, indicating the same remained consistent between shots. (d) The angular data reduction.

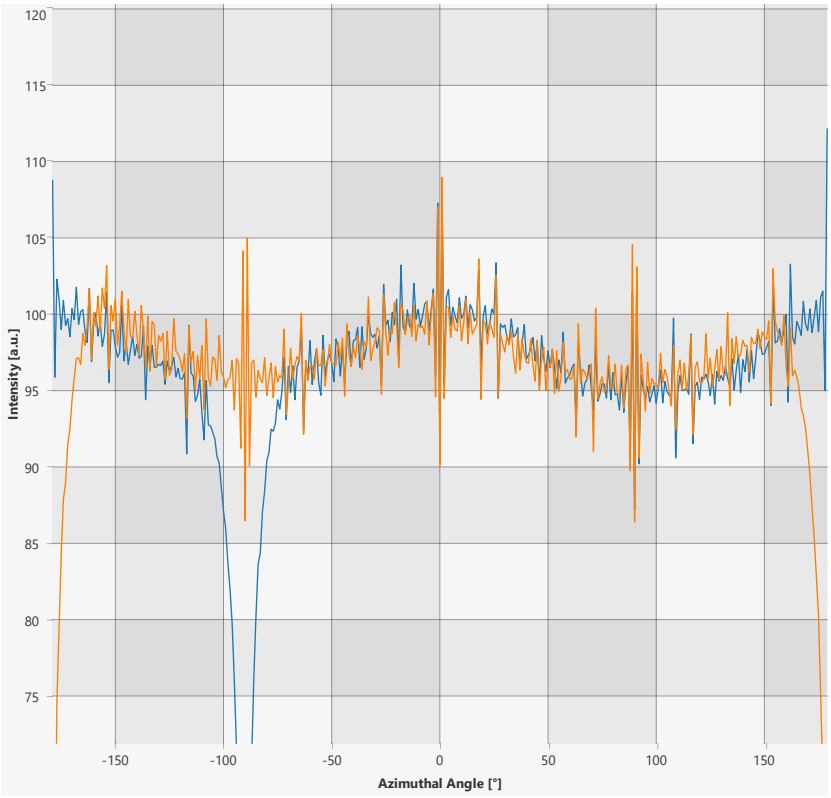

Figure 4.35: Shifted angular reduction for Figure 4.34 (blue: vertical, orange: horizontal), shows a slight periodicity which indicates partial alignment. However, once again the difference between the two plots are little to none.

the detector or a fault in the mounting mechanism. Neither was it an artefact of the beamline itself, as an angular intensity difference would still be present in this scenario.

The results relied heavily on the visual comparison of "shifted angular data reduction" plots. A more quantitative metric would be to compare the values of the intensity peaks between the horizontal and vertical orientations of the gold nanorods. However, as this work is exploratory and lacked many repetitions, observational results are sufficient to motivate future tests with larger sample sizes with rigorous statistical analysis. That is where the quantitative analysis would be more useful.

We note that some scattering results were more box-like rather than rounded such as in Figures 4.30(a) and 4.30(b). This may have arisen because the nanorods are no longer perfectly perpendicular to the X-ray beam (angular polydispersity). However, this should not overly impact the conclusions of our results for three reasons. Firstly, the simulations already accounted for an angular polydispersity of 30 degrees to the X-ray beam, i.e., some nanorods were simulated to not be perpendicular to the X-ray beam by up to 30 degrees. We can see that even in this case, the two intensity distributions were exactly the same and that any intensity differences are not the result of polydispersity. Secondly, polydispersity just changes the profile of the

nanorods from the perspective of the beam, i.e. changes their dimension ratio. As long as they are not aligned in the direction of X-ray propagation, then there is still an asymmetry to between their height and their width. Any discrepancies in the intensity profile are thus as a result of these differences and therefore from their orientation. Finally, as the rotation is completely perpendicular to the X-ray beam, the polydispersity in the horizontal orientation would be exactly the same as in the vertical orientation, and thus this variable would be fixed between tests of the same sample, with their orientation being the only independent variable.

It is worth mentioning that the theory behind anisotropic Thomson scattering of X-rays was calculated for free electrons. Although gold has relatively loosely bound electrons, their binding energies could still affect their X-ray interactions, albeit extremely minutely as the energy of the X-rays are much greater than the binding energy of the electrons. The difference in scattering intensities of the polarised X-rays could also arise from SPRs on the surface of gold nanoparticles, because they are also inherently dependent on polarisation. However, SPRs are not expected for interactions of such high energy, but could potentially be present from secondary interactions. However, once again, this should be negligible compared to the high flux of the X-ray beam. Another thing to consider is the alignment techniques used in this work, using nematic and hexagonal phase CTAB and providing a shear force using a centrifuge. This meant that their alignment was not always consistent in orientation and degree resulting in some polydispersity. CTAB in the nematic and hexagonal phases is also highly dependent on temperature. Excessive imaging under high flux synchrotron radiation could potentially cause radiation damage to the sample and change the phase. Thus, for this work, only orthogonal orientations of the AuNRs were tested under SAXS. Radiation damage was checked by reshooting the same spot at 0 and 90 degrees. However, a revisit to this experiment with better and more consistent alignment techniques should be done to test the scattering intensities at multiple AuNR orientations in between 0 and 90 degrees to get a more complete picture of the polarisation dependence of X-ray interactions. Moreover, this effect is expected to be more noticeable for Compton Scattering, which requires even higher energy photons (in the MeV or GeV range). To test for this, a more powerful beamline is required.

4.8 Conclusion

In this work, we demonstrate that it is possible to align gold nanorods in the nematic and hexagonal phase CTAB with a shear force. Aligned AuNRs resulted in an anisotropic X-ray scattering pattern under SAXS, as expected. The effects of the polarisations of the X-rays on their interactions with aligned AuNRs were examined. Samples of AuNRs in nematic CTAB were prepared in quartz capillaries, aligned using a centrifuge. The aligned samples were then put into a beam of horizontally polarised X-rays at the SAXS/WAXS beamline at the Australian Synchrotron. The capillaries were shot and then rotated 90° and again shot to see if there was a difference in the relative angular scattering pattern or the azimuthal angular distribution of the scattered X-rays. The radial counts of the detected x-rays of the vertical and horizontal orientated capillaries were the same, which indicates that the X-rays were scattering off the same sample makeup. However, the intensities were different in the intensity vs. azimuthal angle plot ($I(\phi)$ vs. ϕ, for horizontally and vertically aligned AuNRs. This suggests that the scattering patterns obtained from the different orientations of the AuNRs could be exploited to determine the initial polarisation mode of the incident X-rays.

Furthermore, when the alignment of the AuNRs is at a 45°, so that the horizontal and vertical orientations have the same angle subtended by the X-ray E-vector and the alignment axes of the AuNRs, the angular difference is no longer apparent. In addition, when the AuNRs are not well aligned, resulting in a more isotropic scattering pattern, the differences in intensities of $I(\phi)$ vs. ϕ of the scattered X-rays are also massively reduced, which indicates that the differences are not the result of instrumental error. Thus, this suggests that the angle subtended by the E-vector of the polarised X-rays and orientation of the aligned AuNRs are a factor in the intensity of angular distribution of the scattered X-rays. AuNRs aligned perpendicularly to the E-vector of the X-rays have more intense scattering in the direction perpendicular to their alignment. In contrast, AuNRS aligned parallel to the X-ray E-vector scattered more X-rays in the direction parallel to their alignment vector. These results indicate that the orientation of AuNRS can be used to determine the polarisation of X-rays through Thomson scattering, which would be used to design and develop a new type of X-ray polarisation detector. This novel detector would be much smaller in size, have greater cost-effectiveness, and be much easier to manufacture compared to current and proposed options. This could have long lasting applications in cosmology, astrophysics, medical science, and X-ray and γ ray imaging.

Chapter 5

Small Building Blocks

5.1 Introduction

This chapter outlines the work that was done that did not warrant an entire chapter in this thesis. Nevertheless, they helped with the conceptualisation, methodology, and motivation for the previously written chapters in this thesis. As such, I felt it was important to include the following.

For the work detailed here, I was not the main author of the work "Time-Resolved In Situ Small-Angle X-ray Scattering to Determine the Kinetics of Formation of Liquid Crystalline Structure in the Core of Polymeric Nanoparticles during and after Turbulent Mixing". My contribution to the project was solely in its investigation, namely carrying out the experiment at the Australian Synchrotron such as the making of the sample and taking measurements at the SAXS beamline. As such, I have included mainly the experimental method section of the manuscript[1]. The conceptualisation, methodology, and data analysis and interpretation were done by my coauthors, and I have only included such sections to contextualise the whole work. Nonetheless, my role in this project helped me gain an experience in the SAXS beamline at the Australian Synchrotron, which was key in the conceptualisation of the work done in Chapter 4.

I will go through the motivation for this work in Section 5.2, and give the background in Section 5.3. My main contribution is in the experimental and result gathering aspect, overviewed in Section 5.4 and Section 5.5, although I did not participate in the data analysis. Finally, a brief summary of the results can be found in Section 5.6.

For the full publication, see the article by Dasaro et al. [3].

5.2 Motivation of Work

The encapsulation of liquid crystalline phases, formed from biocompatible amphiphiles, into nanoparticles has emerged as a promising delivery strategy for hydrophilic and hydrophobic therapeutics. Strategies to characterise these delivery systems as a function of formulation parameters and aqueous environment postmanufacture are well-documented. A critical gap remains regarding the assembly kinetics and in situ dynamics of these systems using industrially

[1] Accepted by Nano Letters

relevant manufacturing techniques. Systematically investigating these characteristics is challenging: computational simulations are time-intensive and costly, while current in situ quantification techniques are limited in scalability and batch size. We here combine synchrotron small-angle X-ray scattering with Flash NanoPrecipitation, a scalable turbulent mixing technology, to capture time-resolved measurements of the formation of liquid crystal phases under nanoconfinement during and after nanoprecipitation. This technique reveals that self-assembly occurs in two steps, with internal liquid crystal self-assembly occurring on longer time scales (second to minutes) than initial nanoprecipitation (milliseconds) as a function of formulation parameters.

5.3 Background

In situ measurement techniques offer a comparably high-throughput path to obtaining real-time measurements of nanoscale self-assembled LC phases[396, 397]. Research in this area combines synchrotron small-angle X-ray scattering (SAXS) with a stop-flow apparatus or a microfluidic mixing device to quantify the behaviour of the LC phase in a time-resolved manner [398, 399]. SAXS is a robust, well-established method for identifying LC phases, and microfluidic mixing produces highly controllable and reproducible flow patterns[289, 400, 401]. The goal of this work was to quantify the time-resolved behaviour of an LC phase-based polymeric nanoparticle formulation prepared using an industrially relevant mixing technique. To do this, a confined impinging jets mixer (CIJ), a turbulent mixer used for the manufacture of lipid nanoparticles at the global scale by Pfizer, was used in conjunction with synchrotron SAXS[402]. CIJ mixers enable continuous reproducible turbulent mixing on a time scale of 1.53 ms [403]. When used for nanoprecipitation, termed Flash NanoPrecipitation (FNP), this rapid mixing results in nanoparticle self-assembly occurring via diffusion-limited aggregation[404]. We here utilise CIJ mixers to produce antibiotic-loaded coreshell polymeric nanoparticles (NPs) with liquid crystalline phases in the cores. These LC phases are comprised of hydrophobic ionic complexes formed between a cationic hydrophilic antibiotic peptide, polymyxin B (PMB), and an anionic hydrophobic counterion, sodium oleate (NaOL)[405]. An amphiphilic diblock copolymer, poly-(caprolactone)-*b*-poly(ethylene glycol), is used as the surface shell to provide steric colloidal stabilisation. Each block of the diblock copolymer was 5 kDa in molecular weight. The model PMB:OL PCL-*b*-PEG NP formulation process and assembly via FNP are provided in Figure 5.1

5.4 Experimental Setup

The flowthrough apparatus, depicted in Figure 5.2, consists of a CIJ mixer and a series of quartz capillaries inserted downstream of the mixer and connected in series to the mixer effluent. When the CIJ is run continuously, this setup enables measurement of LC phases in NPs under flow at selected times after fluid elements exit the mixer. A MATLAB script (provided in the Supporting Information) was used to remotely operate syringe pumps that fed solvent (50/50 Tetrahydrofuran (THF)/Methanol (MeOH), containing dissolved PCL-b-PEG and NaOL) and antisolvent (water, containing dissolved PMB sulfate) streams into the mixer at 60 mL/min per stream. Over the course of each 60s run (chosen to conserve material, though the CIJ can be run continuously), the platform anchored to the mixer-capillary system was moved vertically

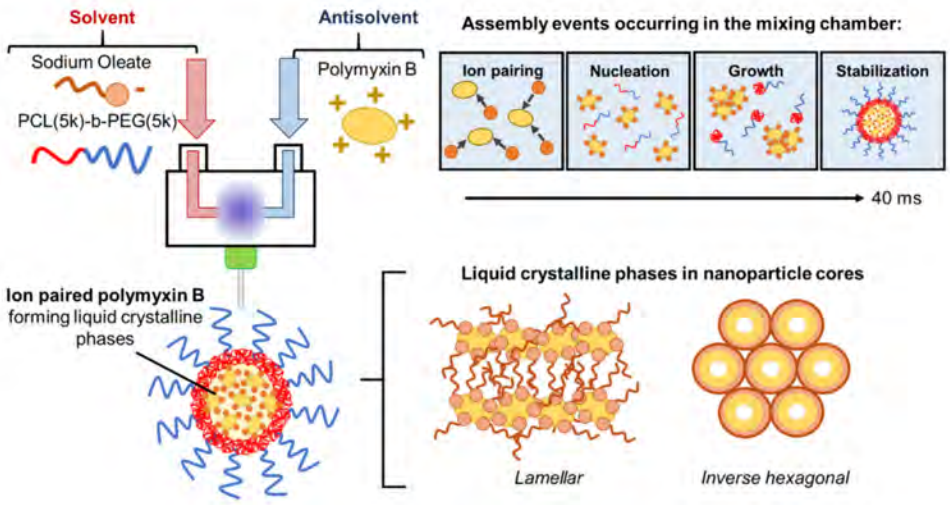

Figure 5.1: (Left) Schematic representation of the combined Flash NanoPrecipitation (FNP) and hydrophobic ion pairing process detailing formulation parameters used to validate the flowthrough apparatus. (Right) Overall time scale and order of events leading up to nanoparticle formation and diagram of potential liquid crystalline phases in nanoparticle cores.

through each of the four positions in Figure 5.2(A), and SAXS measurements (approximately 1.5 s per acquisition) were taken at each location. After 60 s, the flow was stopped and SAXS measurements were taken at position 3 every 90 s until significant changes in the LC phase were no longer observed over time. Initial shots at the outlet of the mixer were taken after 1 2 s after flow was initiated, allowing for the mixer to reach equilibrium. Slight vertical adjustments around position 3 were made after 5 min into the 'stopped flow' regime to avoid sample degradation due to repeated X-ray exposure.

The above setup enabled continuous characterisation on short time scales immediately after mixing. To completely characterise the system, including at the point of mixing, a custom-made modified CIJ was developed and inserted into the mixer-capillary system in Figure 5.2(A). This mixer, depicted in Figure 5.2(B) and Figure 5.2(C) contains a quartz window with optical access to the mixing chamber, allowing for SAXS measurements of the mixing event. Based on the volumetric flow rate through the mixer and the volume of the mixing chamber, the average residence time in the mixing chamber is calculated to be 32 ms. Therefore, accounting for the 1.5 3 ms mixing time, the measurements recorded from within the mixer chamber are representative of components that have had the opportunity to self-assemble for approximately 30 ms. A schematic of the experimental setup can be seen in Figure 5.3

5.5 Results

Figure 5.4 provides a representative snapshot of data collected from this mixer at this earliest time point in the mixing process, approx. 30 ms after mixing is complete. The upturn at lower q values of the averaged data, represented by the open circles, indicates definitive association

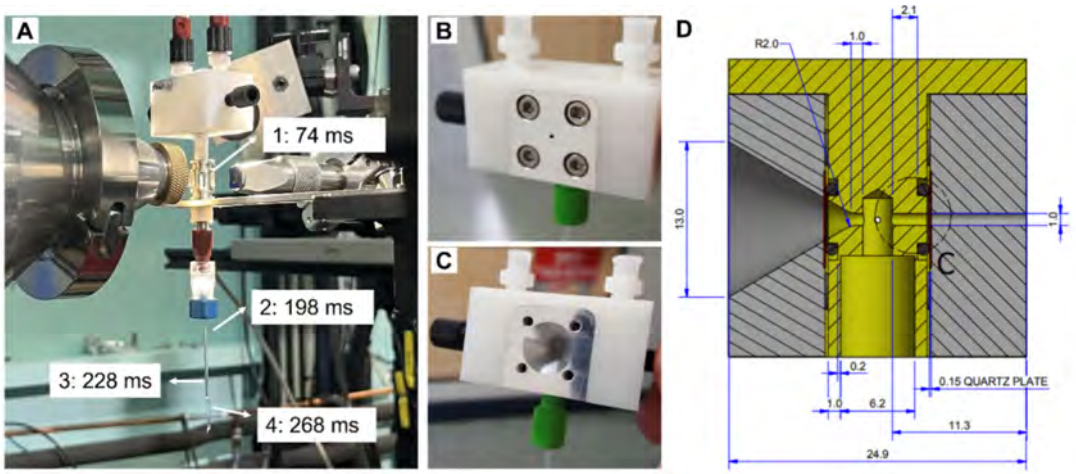

Figure 5.2: (A) Spatiotemporally resolved SAXS-CIJ configuration. Labels represent measurement locations and sample assembly time downstream of the mixer. Assembly time was based on a fluid element flowing through that location after exiting the mixing chamber determined from tubing length and diameter and liquid volumetric flow rate. (B) Front (beam-facing) and (C) back (detector-facing) views of the modified quartz window CIJ that allows for optical access into the mixing chamber and detection of scattered X-rays. (D) CAD design side view of the mixer detailing the specifications (in mm) and optical access points.

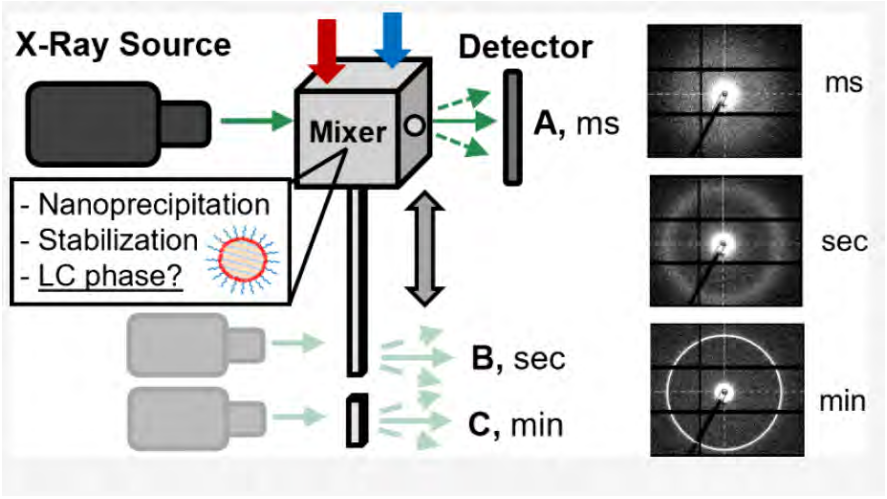

Figure 5.3: Schematic of the Experimental Setup. Nanoparticles are mixed in the CIJ mixing chamber and SAXS measurements are taken at different positions, which allows for time-resolved measurements

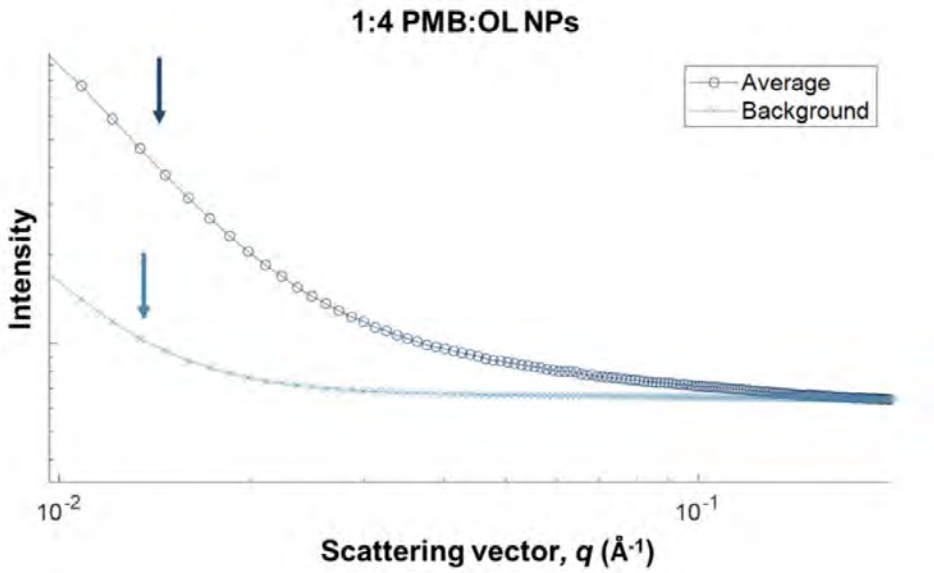

Figure 5.4: SAXS measurements from the CIJ mixing chamber after 30 ms of self-assembly suggesting the presence of nanoparticles (evident from increased scattering above background at low q values) but no LC phases. This suggests that formation of LC phases in NP cores likely occurs on a time scale longer than overall particle self-assembly. The average of three background subtracted measurements is represented by open circles and compared to a lipid-free, solvent-only blank run, plotted as ×. Arrows are provided to highlight the differences in the plot shapes at low q.

of molecular nanoparticle components, while the lack of prominent peaks suggests that quantifiable LC phase formation had not yet occurred[406]. The experimental setup was optimised specifically for LC phase quantification and thus there was not a robust population of low q data points that can be utilised to extrapolate size data, this will be the subject of future work.

For the same 1:4 PMB:OL formulation presented in Figure 5.4, broad but quantifiable higher-order peaks were identified immediately downstream of the mixer from SAXS-CIJ shots taken at positions 2 and 3. We present this evolution in liquid crystalline assembly over the course of 17 min for 1:4 PMB:OL NPs in Figure 5.5 (A). These results suggest that LC phase evolution continues under nanoconfinement once the nanoparticles exit the mixing chamber on a time scale that exceeds the expected assembly time for polymeric NPs. To investigate the sensitivity of the combined SAXS-CIJ system to changes in formulation parameters, NPs were prepared using the same 1:4 PMB:OL PCL-*b*-PEG formulation as the base, with an additional component, vitamin E acetate (25% of the total core) included in the organic solvent feed. Vitamin E is regularly used in FNP literature as a strongly hydrophobic small molecule that can act as a core material, serve as a nucleation site to promote precipitation of less hydrophobic species, or otherwise assist in core cohesion[407]. The LC phase kinetics for the 1:4 PMB:OL + vitamin E system over 17 min are presented as Figure 5.5 (B). A direct comparison between Figure 5.5 (A) and (B) reveals that the time for higher-order peaks to completely resolve in the presence

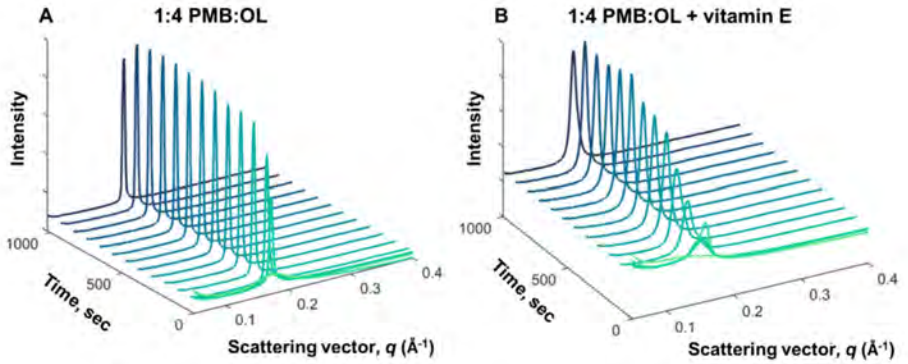

Figure 5.5: (A) Waterfall plot of the evolution of the internal structure of 1:4 PMB:OL NPs demonstrating a rapid increase in peak intensity over the first 100 ms postmixing. (B) Liquid crystalline assembly kinetics for 1:4 PMB:OL NPs in the presence of a strongly hydrophobic species (vitamin E). The final line on each plot represents an LC phase age of 17 min.

of vitamin E vs without is markedly different. Without vitamin E, the relative maximum peak intensity is achieved in less than 10 s. In the presence of vitamin E, the time taken to reach the relative maximum intensity was on the order of hundreds of seconds.

Conclusion

Our findings indicate that, for the model PMB:OL PCL-*b*-PEG NP system, the time scale of LC phase formation is longer than that of nanoparticle assembly, and that the presence of a hydrophobic cocore significantly affects these kinetics. The experimental apparatus (including the quartz window CIJ) is generalisable to other nanoparticle systems produced by antisolvent precipitation.

Chapter 6

Concluding Remarks

Ultimately, this project has been about the fundamental interactions light has with matter, in particular, with regard to detecting its polarisation. We started our journey with a brief dive into the fundamental properties of light that we have known throughout history and how it has shaped our understanding and modelling of light and its interactions. Currently, our best interpretation of light is by the quantum mechanical model where light behaves both as a wave and a particle, and it is through these behaviours that we must model light interactions.

One particular aspect of light that we focus on is the polarisation of light. Polarisation is a fundamental part of light, as cardinal as its energy, wavelength, frequency, and velocity. Every wave, every particle, has this aspect at its core and it must be considered when we deal with how light interacts with matter. Polarisation is present in both the classical and quantum-mechanical descriptions of light, and it can arise in many different ways. What we are most interested is in its detection, in particular creating novel methods in this pursuit, and use it to infer properties of its inception. Current detectors of polarisation exist in the visible domain, but direct detection requires intricate electronics, and they all suffer from size and cost complexities, which limits their mass production and general usage. What is missing is a small, easy to make polarisation detector that allows for a small, cost effective and easy to produce device that allows quick polarimetry of visible light.

To this end, we first started looking at some of the oldest known detectors of polarisation; animals. Animals, both terrestrial and aquatic, have been organically using polarisation to navigate and communicate in ways that we have not yet been able to fully master, or even discern. We began, in Chapter 2 by looking at the behaviour of the larvae of the sea urchin *Centrostephanus rodgersii*. We found that they responded to unpolarised halogen light with positive phototaxis, that is, they swam towards the light source. This was contrasted to their general apathy towards movement under no exposure to any light, indicating that they do, in fact, have photoreceptors, but also are responding to light stimulus. They also have impetus for polarised light. Positive phototaxis was shown under illumination of horizontally polarised light but not under vertically polarised light, which is suggestive that they have sensitivity to linear polarisation. The exact mechanism is unknown, but polarisation sensitivity arises in other animals due to an alignment of their photoreceptors. The light sensing molecules, chromophores, are inherently sensitive to polarisation, selectively absorbing light that has polarised parallel to the molecule. A global ordering of chromophores can give rise to polarisation contrast. For

marine species such as the sea urchin, there may also be some evolutionary pressure to be more sensitive to horizontal polarisation as well, as due to a combination of Rayleigh scattering and light refraction of Snell's Window, light underwater is more horizontally polarised than vertically polarised.

Additionally, we found that these larvae also had positive phototaxis under exposure to elliptical and circular polarisations of light. However, they either had no ability to differentiate between the two states of elliptical or circular polarisation, or they did not modify their behaviours between the two. This raises an interesting question about the nature of elliptical or circular polarisation in nature. Mathematically, such polarisations of light are just a rotating state of linear polarisations over time. There is a phase difference between the horizontal and vertical oscillations of the electric field in elliptical and circular polarisations; however, these 'linear' oscillations still exist. Would an animal who can normally see linear polarisation also see circular polarisation, or elliptical, as that is in fact the general polarisation state of light? This would be an interesting question to investigate and one that I hope to find an answer to in the future.

Nonetheless, this sensitivity to polarised light present in the larvae of sea urchins lead to another interesting question. Would this sensitivity also be present in adult sea urchins? Larvae undergo a physical metamorphosis to transition into the adult stage of their lifecycle, where many of their structures change. Whilst, the photo reception of larvae has not been extensively studied, the light detection capabilities of adult sea urchins are well known. Their photorecptors are located in their tube feet, surrounded by the birefringent material calcite, which may be cause of any potential polarisation sensitivity. They have many tube feet and, together they form a neural network, working like a compound eye. Unlocking the mechanism behind any polarisation sensitivity in adults, may also hint at how the larvae detect polarisation.

We tested the behaviour of three species of adult sea urchins to light and polarisation in Chapter 3; they were *Paracentrotus lividus*, *Echinus esculentus* and *Psammechinus miliaris*. All three species showed negative phototaxis under exposure to unpolarised halogen light, with the general trend of increased movement away from light as it became more intense. This was the same for when the light was polarised. Of the three, only one species showed any sensitivity to polarisation. *Psammechinus miliaris*, had greater phototaxis under illumination of horizontally polarised light compared to vertically polarised light. Unlike the larvae, which did not seem to respond at all to vertical polarisation, this species of adult sea urchin did respond to vertical polarised light, just to a lesser extent compared to horizontally polarised light. As they have greater phototaxis to higher intensities, this may mean that they see horizontal polarisation as brighter, meaning that they have more photoreceptors capable of seeing horizontal polarisation compared to vertical polarisation.

Furthermore, there were also indications of potential circular polarisation sensitivity in the species *Paracentrotus lividus*, where they had negative phototaxis for left-handed polarisations but not for right-handed polarisations. This is particularly interesting as there are currently very few documented cases of circular polarisation sensitivity. Further work into the exact mechanisms of light detection in these sea urchins could potentially unlock new ways of linear and circular polarisation detectors and pave the way into the development of novel technologies using our discovered polarisation detection method at visible wavelengths that mimics the polarisation sensitivity of these sea urchins. A new detector developed on this mechanism would not only have the ability to detect polarisation directly but would also be of much smaller size with greater ease of production in both costs and scale.

The detection of polarisation using the biological mechanisms of animal sensitivity to polarisation arises due to their photodetection mechanism, using chromophores. Chromophores are naturally dichroic, and polarisation sensitivity is due to the ordering of chromophore molecules [121, 123]. This mechanism can be exploited to possibly create a device that can directly detect the polarisation state of light, without the need to a separate filter, enhancing their sensitivity and resolution. Furthermore, the optical properties of chromophores have been well documented and studied, especially their peak wavelengths [128, 134, 206]. A polarimetric photodetector based on chromophores could potentially be extremely tunable to measure different wavelengths by switching out the base chromophore.

We were especially interested in sea urchins due to the calcite in their skeletons and tube feet [207, 208], where their photorecptors reside. Calcite interacts anisotropically with different polarisations of light [207] since calcite has high birefringent properties [209]. Coupled to the photoreceptors, this could potentially lead to both linear and circular polarisation sensitivity in sea urchins, which uses both the birefringent properties of calcite and polarisation sensitivity of aligned chromophores.

These new devices, which are based on organic compounds, would be feasible for the detection of polarisation of higher energy photons such as X-rays and γ-rays. For those, we would require another method capable of resisting the associated radiation damage. This brings us to Chapter 4, where we outline the work we have done to try to overcome this problem. Gold is an element that has already seen a lot of uses with X-rays because of its stability and high contrast under X-ray irradiation. Furthermore, aligned gold nanorods have a sensitivity to polarised light in the visible regime. Therefore, they would make a perfect candidate for this investigation. We wanted to test whether aligned gold nanorods also have sensitivity to X-ray polarisations. We performed SAXS with polarised X-ways from synchrotron radiation and found that they have anisotropic scattering of X-rays that were dependent on the polarisation direction of the X-rays relative to their orientation. When both were parallel, the X-rays had a sharper azimuthal distribution, scattering more perpendicularly to the nanorods, compared to the case when the polarisation was orthogonal to the orientation of the nanorods.

Thus, we showed that the polarisation of an incident X-ray beam can be measured through its scattering pattern off aligned gold nanorods. The differences in the scattered X-ray directions can be used in the development of a novel detector, capable of direction detection over a wider range of high energy photons. Additionally, the use of nanomaterials would miniaturise polarisation detection devices, which is a vast boon to utilisation in outer space where mass and volume are a premium. Furthermore, such devices would be more cost effective, and much easier to manufacture compared to current and proposed options.

This polarisation sensitivity of X-ray scattering in gold nanorods could lead to many applications. The primary being the progress into high energy polarimetry with applications in astro-particle physics, probing fundamental interactions of the weak force. However, there are several other applications of X-ray polarimetry and gold nanorods, one being in the field of oncology. The optical features of gold nanorods and their low cytotoxicity make them an ideal candidate for cancer therapy [408]. In radiation therapy, X-rays and γ-rays are used to kill cancer cells in the body, but one of the main concerns is always collateral damage to health cells around the cancer cells. Gold nanoparticles can be deposited in the cancer cells to mitigate this due to their high contrast with high energy photons, leading to a lower needed dose of radiation for the same effectiveness. This reduces the damage caused to the surrounding healthy cells. This can be improved with polarised X-rays. If we can increase the effectiveness of cancer treat-

ment with polarised X-rays, the dose can be lowered even further, reducing collateral damage even more.

X-rays are also currently widely used in a plethora of applications ranging from biomedical imaging, medical diagnostics and treatment to the characterisation of the structure of macromolecules, polymers and nanoparticles. They also play a key role in revealing the secrets of the universe. However, one of their properties has been underutilised so far: their polarisation. Not only can the inclusion of polarisation drastically improve image quality in PET and CT scans, but it can also enhance tissue characterisation such as for collagen fibres, which in turn may enable an earlier detection of cancer. Furthermore polarised X-rays can be used to study the magnetic and electronic properties of materials. This proposal aims to develop a device that is capable of detecting the polarisation of X-rays as well as producing them using anisotropic scattering of polarised X-rays and gold nanorods.

As this project has already provided the proof on concept for anisotropic scattering of polarised X-rays off aligned AuNrs, the next step is to optimise the alignment techniques for the gold nanorods that will be more robust under a flux of high energy photons as the current techniques are susceptible to the heating effects of the high energy photons. Some candidate techniques can potentially be applied to mitigate the structure deformation, such as growing gold nanorods in metal-organic frameworks (MOFs) with prealigned structures, depositing magnetic ferromagnetic nanoparticles (such as Fe_3O_4) onto the gold and aligning with a magnetic field, slotting gold nanorods in mesoporous silica (SBA-15) for alignment, or implement an active cooling system to stabilise the gold nanorod system.

All in all, this is the first step in an exciting movement towards the future of polarisation based technology both in the IR-UV range with chromophores and the high energy range with aligned AuNRs.

Bibliography

1. Li, B. *et al.* Response of the larvae of the sea urchin Centrostephanus rodgersii under light and polarization conditions. en. *Photochemistry and Photobiology* **n/a.** _eprint: https://onlinelibrary.wiley.com/doi/pdf/10.1111/php.70055. ISSN: 1751-1097. https://onlinelibrary.wiley.com/doi/abs/10.1111/php.70055 (2025).
2. Li, B. *et al.* Toward a Novel Method of X-Ray Polarimetry with Aligned Gold Nanorods. en. *Advanced Materials Technologies* **n/a,** e01811. ISSN: 2365-709X. https://onlinelibrary.wiley.com/doi/abs/10.1002/admt.202501811 (2026).
3. Dasaro, S. R. *et al.* Time-Resolved In Situ Small-Angle X-ray Scattering to Determine the Kinetics of Formation of Liquid Crystalline Structure in the Core of Polymeric Nanoparticles during and after Turbulent Mixing. *Nano Letters* **25.** Publisher: American Chemical Society, 7075–7080. ISSN: 1530-6984. https://doi.org/10.1021/acs.nanolett.5c01095 (2025) (Apr. 2025).
4. Feynman, R. P. Mathematical Formulation of the Quantum Theory of Electromagnetic Interaction. *Physical Review* **80.** Publisher: American Physical Society, 440–457. https://link.aps.org/doi/10.1103/PhysRev.80.440 (2025) (Nov. 1950).
5. Aspect, A. From Huygens' waves to Einstein's photons: Weird light. *Comptes Rendus Physique. Science in the making: The Comptes rendus de l'Académie des sciences throughout history* **18,** 498–503. ISSN: 1631-0705. https://www.sciencedirect.com/science/article/pii/S1631070517301032 (2025) (Nov. 2017).
6. Goldstein, D. H. *Polarized Light* en. Google-Books-ID: w6PMBQAAQBAJ. ISBN: 978-1-4398-3041-3 (CRC Press, Dec. 2017).
7. Huyghens, C. Traité de la Lumière. où Sont Expliquées les Causes de ce Qui Luy Arrive Dans la Reflexion, & Dans la Refraction. et Particulierement dans L'etrange Refraction du Criystal D'islande. *Pierre Vander AA: Leiden, The Netherlands* (1690).
8. Brezinski, M. E. in *Optical Coherence Tomography* (ed Brezinski, M. E.) 71–94 (Academic Press, Burlington, Jan. 2006). ISBN: 978-0-12-133570-0. https://www.sciencedirect.com/science/article/pii/B9780121335700500068 (2025).
9. Michelson, A. A. & Morley, E. W. On the relative motion of the Earth and the luminiferous ether. *American journal of science* **3,** 333–345 (1887).

10. Maxwell, J. C. VIII. A dynamical theory of the electromagnetic field. *Philosophical Transactions of the Royal Society of London* **155.** Publisher: Royal Society, 459–512. https://royalsocietypublishing.org/doi/10.1098/rstl.1865.0008 (2025) (Jan. 1997).

11. Griffiths, D. J. *Introduction to electrodynamics* (Pearson, 2013).

12. *Imagine the Universe!* https://imagine.gsfc.nasa.gov/features/yba/CygX1_mass/binary/spectra_info.html (2025).

13. Ranganath, G. S. Black-body radiation. en. *Resonance* **13,** 115–133. ISSN: 0973-712X. https://doi.org/10.1007/s12045-008-0028-7 (2025) (Feb. 2008).

14. Garrett, A. B. Quantum theory: Max Planck. *Journal of Chemical Education* **40.** Publisher: American Chemical Society, 262. ISSN: 0021-9584. https://doi.org/10.1021/ed040p262 (2025) (May 1963).

15. Scarabelli, L., Sánchez-Iglesias, A., Pérez-Juste, J. & Liz-Marzán, L. M. A "Tips and Tricks" Practical Guide to the Synthesis of Gold Nanorods. *The Journal of Physical Chemistry Letters* **6.** Publisher: American Chemical Society, 4270–4279. https://doi.org/10.1021/acs.jpclett.5b02123 (2025) (Nov. 2015).

16. Man, Z.-X., Xia, Y.-J. & An, N. B. Simultaneous observation of particle and wave behaviors of entangled photons. en. *Scientific Reports* **7.** Publisher: Nature Publishing Group, 42539. ISSN: 2045-2322. https://www.nature.com/articles/srep42539 (2025) (Feb. 2017).

17. Rab, A. S. *et al.* Entanglement of photons in their dual wave-particle nature. *Nature Communications* **8,** 915. ISSN: 2041-1723. https://www.ncbi.nlm.nih.gov/pmc/articles/PMC5688178/ (2025) (Oct. 2017).

18. Mairhofer, L. & Passon, O. Reconsidering the Relation Between "Matter Wave Interference" and "Wave–Particle Duality". en. *Foundations of Physics* **52,** 32. ISSN: 1572-9516. https://doi.org/10.1007/s10701-022-00544-2 (2025) (Feb. 2022).

19. Yoon, T. H. & Cho, M. Quantitative complementarity of wave-particle duality. *Science Advances* **7.** Publisher: American Association for the Advancement of Science, eabi9268. https://www.science.org/doi/10.1126/sciadv.abi9268 (2025) (Aug. 2021).

20. *IAU Office of Astronomy for Education* en. https://astro4edu.org/resources/diagram/8m97bG23XT57/ (2025).

21. Tse, D. & Viswanath, P. *Fundamentals of Wireless Communication* en. Google-Books-ID: GdsLAQAAQBAJ. ISBN: 978-1-139-44466-8 (Cambridge University Press, May 2005).

22. Zoughi, R. *Microwave Non-Destructive Testing and Evaluation Principles* en. ISBN: 978-0-412-62500-8 (Springer Science & Business Media, Feb. 2000).

23. Nikolova, N. K. Microwave Imaging for Breast Cancer. *IEEE Microwave Magazine* **12,** 78–94. ISSN: 1557-9581. https://ieeexplore.ieee.org/abstract/document/6031961 (2025) (Dec. 2011).

24. Sun, Q. *et al.* Recent advances in terahertz technology for biomedical applications. *Quantitative Imaging in Medicine and Surgery* **7,** 345–355. ISSN: 2223-4292. https://www.ncbi.nlm.nih.gov/pmc/articles/PMC5537133/ (2025) (June 2017).

25. Berger, M., Yang, Q. & Maier, A. en. in *Medical Imaging Systems: An Introductory Guide* (eds Maier, A., Steidl, S., Christlein, V. & Hornegger, J.) 119–145 (Springer International Publishing, Cham, 2018). ISBN: 978-3-319-96520-8. https://doi.org/10.1007/978-3-319-96520-8_7 (2025).

26. Sun, Z., Ng, K. & Ramli, N. Biomedical imaging research: a fast-emerging area for interdisciplinary collaboration. *Biomedical Imaging and Intervention Journal* **7,** e21. ISSN: 1823-5530. https://www.ncbi.nlm.nih.gov/pmc/articles/PMC3265193/ (2025) (July 2011).

27. Yerushalmi, A. *Localized, Non-Invasive Deep Microwave Hyperthermia for the Treatment of Prostatic Tumors: The First 5 Years* en. in *Application of Hyperthermia in the Treatment of Cancer* (eds Issels, R. D. & Wilmanns, W.) (Springer, Berlin, Heidelberg, 1988), 141–146. ISBN: 978-3-642-83260-4.

28. Baskar, R., Lee, K. A., Yeo, R. & Yeoh, K.-W. Cancer and Radiation Therapy: Current Advances and Future Directions. *International Journal of Medical Sciences* **9,** 193–199. ISSN: 1449-1907. https://www.ncbi.nlm.nih.gov/pmc/articles/PMC3298009/ (2025) (Feb. 2012).

29. Yun, S. H. & Kwok, S. J. J. Light in diagnosis, therapy and surgery. *Nature biomedical engineering* **1,** 0008. ISSN: 2157-846X. https://www.ncbi.nlm.nih.gov/pmc/articles/PMC5476943/ (2025) (2017).

30. Pastuszak, J. & Węgierek, P. Photovoltaic Cell Generations and Current Research Directions for Their Development. *Materials* **15,** 5542. ISSN: 1996-1944. https://www.ncbi.nlm.nih.gov/pmc/articles/PMC9414585/ (2025) (Aug. 2022).

31. Yadav, L. D. S. en. in *Organic Spectroscopy* (ed Yadav, L. D. S.) 1–6 (Springer Netherlands, Dordrecht, 2005). ISBN: 978-1-4020-2575-4. https://doi.org/10.1007/978-1-4020-2575-4_1 (2025).

32. Scotter, C. Use of near infrared spectroscopy in the food industry with particular reference to its applications to on/in-line food processes. *Food Control* **1,** 142–149. ISSN: 0956-7135. https://www.sciencedirect.com/science/article/pii/095671359090006X (2025) (July 1990).

33. Kolokolova, L. & Kimura, H. Effects of electromagnetic interaction in the polarization of light scattered by cometary and other types of cosmic dust. en. *Astronomy & Astrophysics* **513.** Publisher: EDP Sciences, A40. ISSN: 0004-6361, 1432-0746. https://www.aanda.org/articles/aa/abs/2010/05/aa13681-09/aa13681-09.html (2025) (Apr. 2010).

34. Lembessis, V. E. & Andrews, D. L. Forces in the Interaction of Light with Matter. en. *Applied Sciences* **14.** Number: 16 Publisher: Multidisciplinary Digital Publishing Institute, 7008. ISSN: 2076-3417. https://www.mdpi.com/2076-3417/14/16/7008 (2025) (Jan. 2024).

35. Boehm, C. *Dark Matter-Photon Interactions: Are They Allowed?* en. in *Dark Matter in Astro- and Particle Physics* (eds Klapdor-Kleingrothaus, H. V. & Viollier, R. D.) (Springer, Berlin, Heidelberg, 2002), 345–355. ISBN: 978-3-642-55739-2.

36. Saleem, A., Afzal, I., Javed, Y. & Jamil, Y. in *Modern Luminescence from Fundamental Concepts to Materials and Applications* (eds Sharma, S. K., Jacinto da Silva, C., Garcia, D. J. & Shrivastava, N.) 185–218 (Woodhead Publishing, Jan. 2023). ISBN: 978-0-323-89954-3. https://www.sciencedirect.com/science/article/pii/B9780323899543000090 (2025).

37. Dewar, M. J. S. & Dougherty, R. C. en. in *The PMO Theory of Organic Chemistry* (eds Dewar, M. J. S. & Dougherty, R. C.) 391–483 (Springer US, Boston, MA, 1975). ISBN: 978-1-4613-4404-9. https://doi.org/10.1007/978-1-4613-4404-9_6 (2025).

38. Schirrmacher, A. en. in *Compendium of Quantum Physics* (eds Greenberger, D., Hentschel, K. & Weinert, F.) 58–61 (Springer, Berlin, Heidelberg, 2009). ISBN: 978-3-540-70626-7. https://doi.org/10.1007/978-3-540-70626-7_18 (2025).

39. *cesar.esa.int/printable_section.php?Section=SSE_Composicion_de_las_estrellas_portada&Id=* https://cesar.esa.int/printable_section.php?Section=SSE_Composicion_de_las_estrellas_portada&Id= (2025).

40. Wheaton, B. R. en. in *Compendium of Quantum Physics* (eds Greenberger, D., Hentschel, K. & Weinert, F.) 472–475 (Springer, Berlin, Heidelberg, 2009). ISBN: 978-3-540-70626-7. https://doi.org/10.1007/978-3-540-70626-7_143 (2025).

41. Marghany, M. in *Synthetic Aperture Radar Imaging Mechanism for Oil Spills* (ed Marghany, M.) 41–60 (Gulf Professional Publishing, Jan. 2020). ISBN: 978-0-12-818111-9. https://www.sciencedirect.com/science/article/pii/B9780128181119000033 (2025).

42. Lockwood, D. J. en. in *Encyclopedia of Color Science and Technology* (ed Luo, M. R.) 1097–1107 (Springer, New York, NY, 2016). ISBN: 978-1-4419-8071-7. https://doi.org/10.1007/978-1-4419-8071-7_218 (2025).

43. Nieto-Vesperinas, M. in *Dielectric Metamaterials* (eds Brener, I., Liu, S., Staude, I., Valentine, J. & Holloway, C.) 39–72 (Woodhead Publishing, Jan. 2020). ISBN: 978-0-08-102403-4. https://www.sciencedirect.com/science/article/pii/B9780081024034000074 (2025).

44. Cox, A. J., DeWeerd, A. J. & Linden, J. An experiment to measure Mie and Rayleigh total scattering cross sections. en. *American Journal of Physics* **70,** 620–625. ISSN: 0002-9505, 1943-2909. https://pubs.aip.org/ajp/article/70/6/620/1040625/An-experiment-to-measure-Mie-and-Rayleigh-total (2025) (June 2002).

45. *Polarization by scattering – TikZ.net* en-US. Aug. 2021. https://tikz.net/optics_scattering/ (2025).

46. Gardiner, D. J. en. in *Practical Raman Spectroscopy* (eds Gardiner, D. J. & Graves, P. R.) 1–12 (Springer, Berlin, Heidelberg, 1989). ISBN: 978-3-642-74040-4. https://doi.org/10.1007/978-3-642-74040-4_1 (2025).

47. Robinson, A. L. Tunable Far IR Molecular Lasers Developed. *Science* **227.** Publisher: American Association for the Advancement of Science, 736–737. https://www.science.org/doi/10.1126/science.227.4688.736 (2025) (Feb. 1985).

48. Jones, R. R., Hooper, D. C., Zhang, L., Wolverson, D. & Valev, V. K. Raman Techniques: Fundamentals and Frontiers. *Nanoscale Research Letters* **14,** 231. ISSN: 1931-7573. https://www.ncbi.nlm.nih.gov/pmc/articles/PMC6626094/ (2025) (July 2019).

49. Nibler, J. W. & Knighten, G. V. en. in *Raman Spectroscopy of Gases and Liquids* (ed Weber, A.) 253–299 (Springer, Berlin, Heidelberg, 1979). ISBN: 978-3-642-81279-8. https://doi.org/10.1007/978-3-642-81279-8_7 (2025).

50. Huang, Z., Peng, J., Xu, L. & Liu, P. Development and Application of Surface-Enhanced Raman Scattering (SERS). en. *Nanomaterials* **14.** Number: 17 Publisher: Multidisciplinary Digital Publishing Institute, 1417. ISSN: 2079-4991. https://www.mdpi.com/2079-4991/14/17/1417 (2025) (Jan. 2024).

51. Enciso-Martinez, A. *et al.* Synchronized Rayleigh and Raman scattering for the characterization of single optically trapped extracellular vesicles. *Nanomedicine: Nanotechnology, Biology and Medicine* **24,** 102109. ISSN: 1549-9634. https://www.sciencedirect.com/science/article/pii/S1549963419301935 (2025) (Feb. 2020).

52. Itoh, Y. & Hasegawa, T. Polarization Dependence of Raman Scattering from a Thin Film Involving Optical Anisotropy Theorized for Molecular Orientation Analysis. *The Journal of Physical Chemistry A* **116.** Publisher: American Chemical Society, 5560–5570. ISSN: 1089-5639. https://doi.org/10.1021/jp301070a (2025) (June 2012).

53. Cajiao Vélez, F., Kamiński, J. Z. & Krajewska, K. Electron Scattering Processes in Non-Monochromatic and Relativistically Intense Laser Fields. en. *Atoms* **7.** Number: 1 Publisher: Multidisciplinary Digital Publishing Institute, 34. ISSN: 2218-2004. https://www.mdpi.com/2218-2004/7/1/34 (2025) (Mar. 2019).

54. Makarov, D. N. General quantum theory of Thomson scattering. *Results in Physics* **52,** 106790. ISSN: 2211-3797. https://www.sciencedirect.com/science/article/pii/S2211379723005831 (2025) (Sept. 2023).

55. Hussein, E. M. A. in *Radiation Mechanics* (ed Hussein, E. M. A.) 153–245 (Elsevier Science Ltd, Oxford, Jan. 2007). ISBN: 978-0-08-045053-7. https://www.sciencedirect.com/science/article/pii/B9780080450537500045 (2025).

56. Khalaf, M. & Kaminer, I. Compton scattering driven by intense quantum light. *Science Advances* **9,** eade0932. ISSN: 2375-2548. https://www.ncbi.nlm.nih.gov/pmc/articles/PMC9812390/ (2025).

57. Bichsel, H. & Schindler, H. en. in *Particle Physics Reference Library: Volume 2: Detectors for Particles and Radiation* (eds Fabjan, C. W. & Schopper, H.) 5–44 (Springer International Publishing, Cham, 2020). ISBN: 978-3-030-35318-6. https://doi.org/10.1007/978-3-030-35318-6_2 (2025).

58. Lee, R. N., Lyubyakin, A. A. & Smirnov, V. A. Total Born cross section of e+e-pair production by an electron in the Coulomb field of a nucleus. *Physics Letters B* **848,** 138408. ISSN: 0370-2693. https://www.sciencedirect.com/science/article/pii/S0370269323007414 (2025) (Jan. 2024).

59. Omer, M. & Hajima, R. *Geant4 Physics Process for Elastic Scattering of -Rays* June 2018.

60. Hubbell, J. H., Gimm, H. A. & O/verbo/, I. Pair, Triplet, and Total Atomic Cross Sections (and Mass Attenuation Coefficients) for 1 MeV-100 GeV Photons in Elements Z=1 to 100. *Journal of Physical and Chemical Reference Data* **9,** 1023–1148. ISSN: 0047-2689. https://doi.org/10.1063/1.555629 (2025) (Oct. 1980).

61. Bichsel, H. & Schindler, H. en. in *Particle Physics Reference Library* (eds Fabjan, C. W. & Schopper, H.) 5–44 (Springer International Publishing, Cham, 2020). ISBN: 978-3-030-35317-9 978-3-030-35318-6. http://link.springer.com/10.1007/978-3-030-35318-6_2 (2025).

62. Rochford, K. in *Encyclopedia of Physical Science and Technology (Third Edition)* (ed Meyers, R. A.) 521–538 (Academic Press, New York, Jan. 2002). ISBN: 978-0-12-227410-7. https://www.sciencedirect.com/science/article/pii/B0122274105005901 (2025).

63. Siblini, A. *Optimization of Antenna ARMA (Agile Matrix Antenna radiating by pixel elaborated with Meta-material) For beam forming for the RFID and Radar Applications* PhD thesis (Oct. 2017).

64. Stokes, G. G. On the Composition and Resolution of Streams of Polarized Light from different Sources. *Transactions of the Cambridge Philosophical Society* **9,** 399 (Jan. 1851).

65. Phuoc, G. H. & Pham, T. H. T. *Measuring the Stokes Polarization Parameters* en. in *6th International Conference on the Development of Biomedical Engineering in Vietnam (BME6)* (eds Vo Van, T., Nguyen Le, T. A. & Nguyen Duc, T.) (Springer, Singapore, 2018), 593–596. ISBN: 978-981-10-4361-1.

66. Malykin, G. B. Use of the poincare sphere in polarization optics and classical and quantum mechanics. Review. en. *Radiophysics and Quantum Electronics* **40,** 175–195. ISSN: 1573-9120. https://doi.org/10.1007/BF02676342 (2025) (Mar. 1997).

67. *Using the Poincare Sphere to Represent the Polarization State* en. https://www.thorlabs.com (2025).

68. Wyatt, C. L. in *Radiometric Calibration: Theory and Methods* (ed Wyatt, C. L.) 151–162 (Academic Press, Jan. 1978). ISBN: 978-0-12-766150-6. https://www.sciencedirect.com/science/article/pii/B9780127661506500189 (2025).

69. Schattschneider, P., Rubino, S. & Hébert, C. in *Encyclopedia of Materials: Science and Technology* (eds Buschow, K. H. J. *et al.*) 1–11 (Elsevier, Oxford, Jan. 2007). ISBN: 978-0-08-043152-9. https://www.sciencedirect.com/science/article/pii/B9780080431529021734 (2025).

70. Nordén, B., Rodger, A. & Dafforn, T. 1 Linear and circular dichroism spectroscopy: basic principles. en, 1–14. https://books.rsc.org/books/monograph/1760/chapter/1235894/1-Linear-and-circular-dichroism-spectroscopy-basic (2025) (Sept. 2010).

71. Land, E. H. Some Aspects of the Development of Sheet Polarizers*. EN. *JOSA* **41.** Publisher: Optica Publishing Group, 957–963. https://opg.optica.org/josa/abstract.cfm?uri=josa-41-12-957 (2025) (Dec. 1951).

72. G.V., V. B. R. *et al.* Exploring Liquid Crystal Texture Analysis Through Linear Dichroism. en. *Brazilian Journal of Physics* **54,** 120. ISSN: 1678-4448. https://doi.org/10.1007/s13538-024-01497-9 (2025) (May 2024).

73. Schattschneider, P., Rubino, S. & Hébert, C. in *Reference Module in Materials Science and Materials Engineering* (Elsevier, Jan. 2016). ISBN: 978-0-12-803581-8. https://www.sciencedirect.com/science/article/pii/B9780128035818034378 (2025).

74. Gao, W. Mueller matrix decomposition methods for tissue polarization tomography. *Optics and Lasers in Engineering* **147,** 106735. ISSN: 0143-8166. https://www.sciencedirect.com/science/article/pii/S0143816621002050 (2025) (Dec. 2021).

75. Feynman, R. P., Leighton, R. B. & Sands, M. *The Feynman lectures on physics Ch. 33: Polarization; New millennium ed.* Originally published 1963-1965. https://cds.cern.ch/record/1494701 (Basic Books, New York, NY, 2010).

76. Zhang, F. *et al.* An excellent deep-ultraviolet birefringent material based on [BO2] infinite chains. en. *Light: Science & Applications* **11.** Publisher: Nature Publishing Group, 252. ISSN: 2047-7538. https://www.nature.com/articles/s41377-022-00941-2 (2025) (Aug. 2022).

77. Bennis, N. *et al.* A high birefringence liquid crystal for lenses with large aperture. en. *Scientific Reports* **12.** Publisher: Nature Publishing Group, 14603. ISSN: 2045-2322. https://www.nature.com/articles/s41598-022-18530-z (2025) (Aug. 2022).

78. Van Vliet, A. H. F. & de Graauw, T. Quarter wave plates for submillimeter wavelengths. en. *International Journal of Infrared and Millimeter Waves* **2,** 465–477. ISSN: 1572-9559. https://doi.org/10.1007/BF01007414 (2025) (May 1981).

79. Hindi, S. Birefringence of bio-based liquid crystals. *BioCrystals Journal* **1,** 13–25 (Mar. 2016).

80. in. *Wave Fields in Real Media (Third Edition)* (ed Carcione, J. M.) 247–298 (Elsevier, Oxford, Jan. 2015). ISBN: 978-0-08-099999-9. https://www.sciencedirect.com/science/article/pii/B9780080999999000066 (2025).

81. Emery, W. & Camps, A. in *Introduction to Satellite Remote Sensing* (eds Emery, W. & Camps, A.) 43–83 (Elsevier, Jan. 2017). ISBN: 978-0-12-809254-5. https://www.sciencedirect.com/science/article/pii/B9780128092545000026 (2025).

82. *Waves in composites and metamaterials/Airy theory - Wikiversity* en. https://en.wikiversity.org/wiki/Waves_in_composites_and_metamaterials/Airy_theory (2025).

83. De Angelis, M. & Tino, G. M. in *Encyclopedia of Condensed Matter Physics* (eds Bassani, F., Liedl, G. L. & Wyder, P.) 159–175 (Elsevier, Oxford, Jan. 2005). ISBN: 978-0-12-369401-0. https://www.sciencedirect.com/science/article/pii/B012369401900499 27 (2025).

84. Davis, J. A. *et al.* Diffraction gratings generating orders with selective states of polarization. EN. *Optics Express* **24.** Publisher: Optica Publishing Group, 907–917. ISSN: 1094-4087. https://opg.optica.org/oe/abstract.cfm?uri=oe-24-2-907 (2025) (Jan. 2016).

85. Sobczak, M., Kurzynowski, P., Woźniak, W. A., Owczarek, M. & Drobczyński, S. Polarimeter for measuring the properties of birefringent media in reflective mode. EN. *Optics Express* **28.** Publisher: Optica Publishing Group, 249–257. ISSN: 1094-4087. https://opg.optica.org/oe/abstract.cfm?uri=oe-28-1-249 (2025) (Jan. 2020).

86. Monteiro, M., Stari, C., Cabeza, C. & Marti, A. C. The polarization of light and the Malus' law using smartphones. *The Physics Teacher* **55.** arXiv:1607.02659 [physics], 264–266. ISSN: 0031-921X, 1943-4928. http://arxiv.org/abs/1607.02659 (2025) (May 2017).

87. Black, K., Costa, E., Soffitta, P. & Zajczyk, A. en. in *Handbook of X-ray and Gamma-ray Astrophysics* (eds Bambi, C. & Santangelo, A.) 1–12 (Springer Nature, Singapore, 2022). ISBN: 978-981-16-4544-0. https://doi.org/10.1007/978-981-16-4544-0_172-1 (2025).

88. Costa, E. en. in *Handbook of X-ray and Gamma-ray Astrophysics* (eds Bambi, C. & Santangelo, A.) 1–20 (Springer Nature, Singapore, 2022). ISBN: 978-981-16-4544-0. https://doi.org/10.1007/978-981-16-4544-0_140-1 (2025).

89. Black, K. & Zajczyk, A. en. in *Handbook of X-ray and Gamma-ray Astrophysics* (eds Bambi, C. & Santangelo, A.) 841–875 (Springer Nature, Singapore, 2024). ISBN: 978-981-19-6960-7. https://doi.org/10.1007/978-981-19-6960-7_26 (2025).

90. Di Marco, A. *et al.* A Weighted Analysis to Improve the X-Ray Polarization Sensitivity of the Imaging X-ray Polarimetry Explorer. en. *The Astronomical Journal* **163.** Publisher: The American Astronomical Society, 170. ISSN: 1538-3881. https://dx.doi.org/10.3847/1538-3881/ac51c9 (2025) (Mar. 2022).

91. Go, S. *et al.* Demonstration of nuclear gamma-ray polarimetry based on a multi-layer CdTe Compton camera. en. *Scientific Reports* **14.** Publisher: Nature Publishing Group, 2573. ISSN: 2045-2322. https://www.nature.com/articles/s41598-024-52692-2 (2025) (Feb. 2024).

92. Del Monte, E., Fabiani, S. & Pearce, M. en. in *Handbook of X-ray and Gamma-ray Astrophysics* (eds Bambi, C. & Santangelo, A.) 1–42 (Springer Nature, Singapore, 2022). ISBN: 9789811645440. https://doi.org/10.1007/978-981-16-4544-0_27-1 (2025).

93. Bernard, D., Chattopadhyay, T., Kislat, F. & Produit, N. in. arXiv:2205.02072 [astro-ph], 1–42 (2022). http://arxiv.org/abs/2205.02072 (2025).

94. Ilie, C. Gamma Ray polarimetry; a new window for the non-thermal Universe. *Publications of the Astronomical Society of the Pacific* **131.** arXiv:1906.02824 [astro-ph], 111001. ISSN: 0004-6280, 1538-3873. http://arxiv.org/abs/1906.02824 (2025) (Nov. 2019).

95. Berlin, T. H. & Madansky, L. On the Detection of γ-Ray Polarization by Pair Production. *Phys. Rev.* **78,** 623–623. https://link.aps.org/doi/10.1103/PhysRev.78.623 (5 June 1950).

96. Boldyshev, V. F. & Peresunko, Y. P. Electron-positron pair photoproduction on electrons and analysis of photon beam polarization. *Yad. Fiz.* **14,** 1027–1032 (1971).

97. Eingorn, M. *et al.* A high energy photon polarimeter for astrophysics. *Journal of Astronomical Telescopes, Instruments, and Systems* **4** (Jan. 2015).

98. Gros, P. *et al.* Performance measurement of HARPO: a Time Projection Chamber as a gamma-ray telescope and polarimeter. *Astroparticle Physics* **97.** arXiv:1706.06483 [astro-ph], 10–18. ISSN: 09276505. http://arxiv.org/abs/1706.06483 (2025) (Jan. 2018).

99. Dacke, M., Nilsson, D.-E., Scholtz, C. H., Byrne, M. & Warrant, E. J. Insect orientation to polarized moonlight. en. *Nature* **424,** 33–33. ISSN: 0028-0836, 1476-4687. http://www.nature.com/articles/424033a (July 2003).

100. Dacke, M., Byrne, M. J., Scholtz, C. H. & Warrant, E. J. Lunar orientation in a beetle. *Proceedings of the Royal Society B: Biological Sciences* **271,** 361–365. ISSN: 0962-8452. https://www.ncbi.nlm.nih.gov/pmc/articles/PMC1691606/ (Feb. 2004).

101. Foster, J. J. *et al.* Orienting to polarized light at night—matching lunar skylight to performance in a nocturnal beetle. en. *Journal of Experimental Biology,* jeb.188532. ISSN: 1477-9145, 0022-0949. https://journals.biologists.com/jeb/article/doi/10.1242/jeb.188532/259555/Orienting-to-polarized-light-at-night-matching (2025) (Jan. 2018).

102. Heinze, S. in *Polarized Light and Polarization Vision in Animal Sciences, Second Edition* Journal Abbreviation: Polarized Light and Polarization Vision in Animal Sciences, Second Edition, 61–111 (Jan. 2014).

103. Heinze, S. & Reppert, S. M. Sun Compass Integration of Skylight Cues in Migratory Monarch Butterflies. en. *Neuron* **69,** 345–358. ISSN: 08966273. https://linkinghub.elsevier.com/retrieve/pii/S0896627310010731 (Jan. 2011).

104. Blum, M. & Labhart, T. Photoreceptor visual fields, ommatidial array, and receptor axon projections in the polarisation-sensitive dorsal rim area of the cricket compound eye. eng. *Journal of Comparative Physiology. A, Sensory, Neural, and Behavioral Physiology* **186,** 119–128 (Feb. 2000).

105. Zufall, F., Schmitt, M. & Menzel, R. Spectral and polarized light sensitivity of photoreceptors in the compound eye of the cricket (Gryllus bimaculatus). eng. *Journal of Comparative Physiology. A, Sensory, Neural, and Behavioral Physiology* **164,** 597–608 (Feb. 1989).

106. Hensgen, R., Zittrell, F., Pfeiffer, K. & Homberg, U. Performance of polarization-sensitive neurons of the locust central complex at different degrees of polarization. *Journal of Comparative Physiology. A, Neuroethology, Sensory, Neural, and Behavioral Physiology* **208,** 387–403. ISSN: 0340-7594. https://www.ncbi.nlm.nih.gov/pmc/articles/PMC9123078/ (2022).

107. Homberg, U. & Paech, A. Ultrastructure and orientation of ommatidia in the dorsal rim area of the locust compound eye. eng. *Arthropod Structure & Development* **30,** 271–280. ISSN: 1873-5495 (June 2002).

108. Cronin, T. W., Chiou, T.-H., Caldwell, R. L., Roberts, N. & Marshall, J. *Polarization signals in mantis shrimps* en. in (eds Shaw, J. A. & Tyo, J. S.) (San Diego, CA, Aug. 2009), 74610C. http://proceedings.spiedigitallibrary.org/proceeding.aspx?doi=10.1117/12.828492.

109. Chiou, T.-H. *et al.* Circular Polarization Vision in a Stomatopod Crustacean. *Current Biology* **18,** 429–434. ISSN: 0960-9822. https://www.sciencedirect.com/science/article/pii/S0960982208002522 (Mar. 2008).

110. Rüdiger, W. en. in *Photomorphogenesis in plants* 17–33 (Springer, Dordrecht, 1986). ISBN: 978-94-017-2624-5. https://link.springer.com/chapter/10.1007/978-94-017-2624-5_2 (2025).

111. Zhong, M., Kawaguchi, R., Kassai, M. & Sun, H. Retina, Retinol, Retinal and the Natural History of Vitamin A as a Light Sensor. *Nutrients* **4,** 2069–2096. ISSN: 2072-6643. https://www.ncbi.nlm.nih.gov/pmc/articles/PMC3546623/ (2025) (Dec. 2012).

112. Wolf, G. The visual cycle of the cone photoreceptors of the retina. eng. *Nutrition Reviews* **62,** 283–286. ISSN: 0029-6643 (July 2004).

113. Lehninger, A. L., Nelson, D. L. & Cox, M. M. *Lehninger Principles of Biochemistry* en. Google-Books-ID: 7chAN0UY0LYC. ISBN: 978-0-7167-4339-2 (W. H. Freeman, 2005).

114. Jastrzebska, B., Debinski, A., Filipek, S. & Palczewski, K. Role of membrane integrity on G protein-coupled receptors: Rhodopsin stability and function. eng. *Progress in Lipid Research* **50,** 267–277. ISSN: 1873-2194 (July 2011).

115. Yoshizawa, T. & Wald, G. Photochemistry of Iodopsin. en. *Nature* **214.** Publisher: Nature Publishing Group, 566–571. ISSN: 1476-4687. https://www.nature.com/articles/214566a0 (2025) (May 1967).

116. *retinalandrhodopsin* https://www.sas.upenn.edu/~tareilaj/retinalandrhodopsin.html (2025).

117. Yokoyama, S., Tada, T. & Yamato, T. Modulation of the Absorption Maximum of Rhodopsin by Amino Acids in the C-terminus. *Photochemistry and photobiology* **83,** 236–241. ISSN: 0031-8655. https://www.ncbi.nlm.nih.gov/pmc/articles/PMC2572076/ (2025) (2007).

118. Mannu, G. S. Retinal phototransduction. *Neurosciences* **19,** 275–280. ISSN: 1319-6138. https://www.ncbi.nlm.nih.gov/pmc/articles/PMC4727664/ (2025) (Oct. 2014).

119. Foroni, F., Pergola, G. & Rumiati, R. I. Food color is in the eye of the beholder: the role of human trichromatic vision in food evaluation. en. *Scientific Reports* **6.** Publisher: Nature Publishing Group, 37034. ISSN: 2045-2322. https://www.nature.com/articles/srep37034 (2025) (Nov. 2016).

120. Al-Bahadly, I. & BERNDT, R. LED-based color sensing system. *Sens. Transducers J.* **114,** 132–150 (Mar. 2010).

121. Marshall, J. & Cronin, T. W. Polarisation vision. *Current Biology* **21,** R101–R105. ISSN: 0960-9822. https://www.sciencedirect.com/science/article/pii/S0960982210015988 (Feb. 2011).

122. Purschke, G., Arendt, D., Hausen, H. & Müller, M. C. M. Photoreceptor cells and eyes in Annelida. eng. *Arthropod Structure & Development* **35,** 211–230. ISSN: 1873-5495 (Dec. 2006).

123. Roberts, N. W., Porter, M. L. & Cronin, T. W. The molecular basis of mechanisms underlying polarization vision. *Philosophical Transactions of the Royal Society B: Biological Sciences* **366,** 627–637. ISSN: 0962-8436. https://www.ncbi.nlm.nih.gov/pmc/articles/PMC3049014/ (2025) (Mar. 2011).

124. Bradbury, J. W. & Vehrencamp, S. L. *Principles of animal communication, 2nd ed* Pages: xiv, 697. ISBN: 978-0-87893-045-6 (Sinauer Associates, Sunderland, MA, US, 2011).

125. Buenzli, E., Schmid, H. M. & Joos, F. Polarization Models for Rayleigh Scattering Planetary Atmospheres. en. *Earth, Moon, and Planets* **105,** 153–157. ISSN: 1573-0794. https://doi.org/10.1007/s11038-009-9312-0 (2025) (Sept. 2009).

126. Suhai, B. & Horváth, G. How well does the Rayleigh model describe the E-vector distribution of skylight in clear and cloudy conditions? A full-sky polarimetric study. EN. *JOSA A* **21.** Publisher: Optica Publishing Group, 1669–1676. ISSN: 1520-8532. https://opg.optica.org/josaa/abstract.cfm?uri=josaa-21-9-1669 (2025) (Sept. 2004).

127. Wrighton, K. H. And then there was light. en. *Nature Reviews Molecular Cell Biology* **10.** Publisher: Nature Publishing Group, 814–814. ISSN: 1471-0080. https://www.nature.com/articles/nrm2808 (2025) (Dec. 2009).

128. Linsley, C. S., Quach, V. Y., Agrawal, G., Hartnett, E. & Wu, B. M. Visible light and near infrared-responsive chromophores for drug delivery-on-demand applications. *Drug delivery and translational research* **5,** 611–624. ISSN: 2190-393X. https://www.ncbi.nlm.nih.gov/pmc/articles/PMC5016096/ (2025) (Dec. 2015).

129. Xu, X.-Q., He, Y. & Wang, Y. Near-infrared organic chromophores with pH-sensitive, non-radiative emission for intelligent disease treatment. *Cell Reports Physical Science* **2,** 100433. ISSN: 2666-3864. https://www.sciencedirect.com/science/article/pii/S2666386421001284 (2025) (May 2021).

130. Wang, Y., Huang, Y.-Y., Wang, Y., Lyu, P. & Hamblin, M. R. Red (660 nm) or near-infrared (810 nm) photobiomodulation stimulates, while blue (415 nm), green (540 nm) light inhibits proliferation in human adipose-derived stem cells. en. *Scientific Reports* **7.** Publisher: Nature Publishing Group, 7781. ISSN: 2045-2322. https://www.nature.com/articles/s41598-017-07525-w (2025) (Aug. 2017).

131. Lei, X., Pan, J. & Devlin, A. T. Characteristics of Absorption Spectra of Chromophoric Dissolved Organic Matter in the Pearl River Estuary in Spring. *Remote Sensing* **11.** ISSN: 2072-4292. https://www.mdpi.com/2072-4292/11/13/1533 (2019).

132. Souroullas, K., Manoli, A., Itskos, G., Apostolou, T. & Papademas, P. Fluorescence of Intrinsic Milk Chromophores as a Novel Verification Method of UV-C Treatment of Milk. *Foods* **13.** ISSN: 2304-8158. https://www.mdpi.com/2304-8158/13/18/2887 (2024).

133. Szymczyk, M. en. in *Encyclopedia of Color Science and Technology* (ed Shamey, R.) 154–159 (Springer International Publishing, Cham, 2023). ISBN: 978-3-030-89862-5. https://doi.org/10.1007/978-3-030-89862-5_440 (2025).

134. Joung, J. F., Han, M., Jeong, M. & Park, S. Experimental database of optical properties of organic compounds. en. *Scientific Data* **7.** Publisher: Nature Publishing Group, 295. ISSN: 2052-4463. https://www.nature.com/articles/s41597-020-00634-8 (2025) (Sept. 2020).

135. Garman, E. F. & Weik, M. Radiation damage to biological samples: still a pertinent issue. *Journal of Synchrotron Radiation* **28,** 1278–1283. ISSN: 0909-0495. https://www.ncbi.nlm.nih.gov/pmc/articles/PMC8415327/ (2025) (Sept. 2021).

136. en. in *The Materials Science of Semiconductors* (ed Rockett, A.) 395–453 (Springer US, Boston, MA, 2008). ISBN: 978-0-387-68650-9. https://doi.org/10.1007/978-0-387-68650-9_9 (2025).

137. Zhang, M. *et al.* Organic Semiconductor-Based Polarized Photodetectors for Next-Generation Optoelectronics. en. *Advanced Functional Materials* **n/a,** 2423932. ISSN: 1616-3028. https://onlinelibrary.wiley.com/doi/abs/10.1002/adfm.202423932 (2025).

138. Iwata, T. *et al.* Development of the X-ray polarimeter using CMOS imager: Polarization sensitivity of a 1.5m pixel CMOS sensor. *Nuclear Instruments and Methods in Physics Research Section A: Accelerators, Spectrometers, Detectors and Associated Equipment* **1065,** 169487. ISSN: 0168-9002. https://www.sciencedirect.com/science/article/pii/S0168900224004133 (2025) (Aug. 2024).

139. Bernards, D. A., Owens, R. M. & Malliaras, G. G. *Organic Semiconductors in Sensor Applications* en. Google-Books-ID: uz_KbsPZq1cC. ISBN: 978-3-540-76314-7 (Springer Science & Business Media, Feb. 2008).

140. He, H. *et al.* Mueller matrix polarimetry—an emerging new tool for characterizing the microstructural feature of complex biological specimen. *Journal of Lightwave Technology* **37,** 2534–2548 (2018).

141. Ghosh, N. & Vitkin, A. I. Tissue polarimetry: concepts, challenges, applications, and outlook. *Journal of Biomedical Optics* **16.** Publisher: SPIE, 110801. ISSN: 1083-3668, 1560-2281. https://www.spiedigitallibrary.org/journals/journal-of-biomedical-optics/volume-16/issue-11/110801/Tissue-polarimetry-concepts-challenges-applications-and-outlook/10.1117/1.3652896.full (2025) (Nov. 2011).

142. Gurjar, R. S. *et al.* Imaging human epithelial properties with polarized light-scattering spectroscopy. en. *Nature Medicine* **7.** Publisher: Nature Publishing Group, 1245–1248. ISSN: 1546-170X. https://www.nature.com/articles/nm1101-1245 (2025) (Nov. 2001).

143. Qi, J. & Elson, D. S. Mueller polarimetric imaging for surgical and diagnostic applications: a review. *Journal of biophotonics* **10,** 950–982 (2017).

144. Qiu, L. *et al.* Multispectral scanning during endoscopy guides biopsy of dysplasia in Barrett's esophagus. *Nature medicine* **16,** 603–606 (2010).

145. Tuchin, V. V. Polarized light interaction with tissues. *Journal of biomedical optics* **21,** 071114–071114 (2016).

146. Groner, W. *et al.* Orthogonal polarization spectral imaging: a new method for study of the microcirculation. *Nature medicine* **5,** 1209–1212 (1999).

147. M Allam, N., Eladl, H. M. & Eid, M. M. Polarized Light Therapy in the Treatment of Wounds: A Review. eng. *The International Journal of Lower Extremity Wounds* **24,** 288–293. ISSN: 1552-6941 (June 2025).

148. Shiryan, G. T., Amin, F. S. & Embaby, E. A. Effectiveness of polarized polychromatic light therapy on myofascial trigger points in chronic non-specific low back pain: a single blinded randomized controlled trial. *Bulletin of Faculty of Physical Therapy* **27,** 33. ISSN: 2536-9660. https://doi.org/10.1186/s43161-022-00085-9 (2025) (Aug. 2022).

149. Feehan, J. *et al.* Therapeutic applications of polarized light: Tissue healing and immunomodulatory effects. *Maturitas* **116,** 11–17. ISSN: 0378-5122. https://www.sciencedirect.com/science/article/pii/S0378512218303888 (2025) (Oct. 2018).

150. Monstrey, S. *et al.* The effect of polarized light on wound healing. en. *European Journal of Plastic Surgery* **24,** 377–382. ISSN: 1435-0130. https://doi.org/10.1007/s00238-001-0305-0 (2025) (Feb. 2002).

151. Feehan, J. *et al.* Polarized light therapy: Shining a light on the mechanism underlying its immunomodulatory effects. *Journal of Biophotonics* **13,** e201960177. ISSN: 1864-063X. https://www.ncbi.nlm.nih.gov/pmc/articles/PMC7065605/ (2025) (Mar. 2020).

152. Tripodi, N. *et al.* The effects of polarized photobiomodulation on cellular viability, proliferation, mitochondrial membrane potential and apoptosis in human fibroblasts: Potential applications to wound healing. *Journal of Photochemistry and Photobiology B: Biology* **236,** 112574. ISSN: 1011-1344. https://www.sciencedirect.com/science/article/pii/S1011134422001889 (2025) (Nov. 2022).

153. Yang, B. *et al.* Instant polarized light microscopy for imaging collagen microarchitecture and dynamics. *Journal of biophotonics* **14,** e202000326. ISSN: 1864-063X. https://www.ncbi.nlm.nih.gov/pmc/articles/PMC7887070/ (2025) (Feb. 2021).

154. Keikhosravi, A. *et al.* Real-time polarization microscopy of fibrillar collagen in histopathology. en. *Scientific Reports* **11.** Publisher: Nature Publishing Group, 19063. ISSN: 2045-2322. https://www.nature.com/articles/s41598-021-98600-w (2025) (Sept. 2021).

155. KOIKE-TANI, M., TANI, T., MEHTA, S. B., VERMA, A. & OLDENBOURG, R. Polarized Light Microscopy in Reproductive and Developmental Biology. *Molecular reproduction and development* **82,** 548–562. ISSN: 1040-452X. https://www.ncbi.nlm.nih.gov/pmc/articles/PMC4979313/ (2025) (2015).

156. Ramanathan, K. V. & Sinha, N. en. in *Current Developments in Solid State NMR Spectroscopy* (eds Müller, N. & Madhu, P. K.) 55–68 (Springer, Vienna, 2003). ISBN: 978-3-7091-3715-4. https://doi.org/10.1007/978-3-7091-3715-4_3 (2025).

157. Matioli, E. *et al.* High-brightness polarized light-emitting diodes. en. *Light: Science & Applications* **1.** Publisher: Nature Publishing Group, e22–e22. ISSN: 2047-7538. https://www.nature.com/articles/lsa201222 (2025) (Aug. 2012).

158. Rodriguez, N. A. *et al.* Use of wire grid polarizers with liquid crystal display for large-volume stereolithography. *Additive Manufacturing* **52,** 102641. ISSN: 2214-8604. https://www.sciencedirect.com/science/article/pii/S2214860422000471 (2026) (Apr. 2022).

159. Rossi, A. *et al.* Preserving polarization maintaining photons for enhanced contrast imaging of the retina. *Biomedical Optics Express* **14,** 5932–5945. ISSN: 2156-7085. https://www.ncbi.nlm.nih.gov/pmc/articles/PMC10659774/ (2025) (Oct. 2023).

160. Mercatelli, L. Examining polarizing and non-polarizing filters for road sports. *Frontiers in Sports and Active Living* **5,** 1236473. ISSN: 2624-9367. https://www.ncbi.nlm.nih.gov/pmc/articles/PMC10441776/ (2025) (Aug. 2023).

161. Dacke, M., Doan, T. A. & O'Carroll, D. C. Polarized light detection in spiders. *Journal of Experimental Biology* **204,** 2481–2490 (2001).

162. Dacke, M., Nordström, P., Scholtz, C. & Warrant, E. A specialized dorsal rim area for polarized light detection in the compound eye of the scarab beetle Pachysoma striatum. *Journal of Comparative Physiology A* **188,** 211–216 (2002).

163. Dacke, M., Nilsson, D.-E., Scholtz, C. H., Byrne, M. & Warrant, E. J. Insect orientation to polarized moonlight. *Nature* **424,** 33–33 (2003).

164. Reppert, S. M., Zhu, H. & White, R. H. Polarized light helps monarch butterflies navigate. eng. *Current biology: CB* **14,** 155–158. ISSN: 0960-9822 (Jan. 2004).

165. Shashar, N., Sabbah, S. & Aharoni, N. Migrating locusts can detect polarized reflections to avoid flying over the sea. *Biology Letters* **1,** 472–475. ISSN: 1744-9561. https://www.ncbi.nlm.nih.gov/pmc/articles/PMC1626356/ (2025) (Dec. 2005).

166. Mäthger, L. M. & Hanlon, R. T. Anatomical basis for camouflaged polarized light communication in squid. *Biology Letters* **2,** 494–496. ISSN: 1744-9561. https://www.ncbi.nlm.nih.gov/pmc/articles/PMC1834008/ (2025) (Dec. 2006).

167. Novales Flamarique, I. Swimming behaviour tunes fish polarization vision to double prey sighting distance. en. *Scientific Reports* **9.** Publisher: Nature Publishing Group, 944. ISSN: 2045-2322. https://www.nature.com/articles/s41598-018-37632-1 (2025) (Jan. 2019).

168. Pignatelli, V. *et al.* Behavioural relevance of polarization sensitivity as a target detection mechanism in cephalopods and fishes. *Philosophical Transactions of the Royal Society B: Biological Sciences* **366,** 734–741. ISSN: 0962-8436. https://www.ncbi.nlm.nih.gov/pmc/articles/PMC3049012/ (Mar. 2011).

169. Šigutová, H. *et al.* Specialization directs habitat selection responses to a top predator in semiaquatic but not aquatic taxa. en. *Scientific Reports* **11.** Publisher: Nature Publishing Group, 18928. ISSN: 2045-2322. https://www.nature.com/articles/s41598-021-98632-2 (2025) (Sept. 2021).

170. Schwind, R. Polarization vision in water insects and insects living on a moist substrate. *Journal of Comparative Physiology A* **169,** 531–540 (1991).

171. Kulchin, Y. N. *et al.* The Linearly Polarized Light Effect on Maize Development. en. *Bulletin of the Russian Academy of Sciences: Physics* **87,** S409–S415. ISSN: 1934-9432. https://doi.org/10.1134/S1062873823705950 (2025) (Dec. 2023).

172. Macht, D. I. CONCERNING THE INFLUENCE OF POLARIZED LIGHT ON THE GROWTH OF SEEDLINGS. *The Journal of General Physiology* **10,** 41–52. ISSN: 0022-1295. https://www.ncbi.nlm.nih.gov/pmc/articles/PMC2140871/ (2025) (Sept. 1926).

173. Lkhamkhuu, E. *et al.* Effect of circularly polarized light on germination, hypocotyl elongation and biomass production of arabidopsis and lettuce: Involvement of phytochrome B. *Plant Biotechnology* **37,** 57–67. ISSN: 1342-4580. https://www.ncbi.nlm.nih.gov/pmc/articles/PMC7193831/ (2025) (Mar. 2020).

174. Rollason, A. J. in *Polarized Electron/Polarized Photon Physics* (eds Kleinpoppen, H. & Newell, W. R.) 311–330 (Springer US, Boston, MA, 1995). ISBN: 978-1-4899-1418-7. https://doi.org/10.1007/978-1-4899-1418-7_23.

175. Cooper, M. J., Shenton-Taylor, C., Duffy, J. A., Steer, C. A. & Blaauw, L. V. A short history of magnetic Compton scattering. *Nuclear Instruments and Methods in Physics Research Section A: Accelerators, Spectrometers, Detectors and Associated Equipment. Proceedings of the 10 th International Symposium on Radiation Physics* **580,** 1–7. ISSN: 0168-9002. https://www.sciencedirect.com/science/article/pii/S0168900207008480 (2025) (Sept. 2007).

176. Baudelet, F. in *Neutron and X-ray Spectroscopy* (eds Hippert, F., Geissler, E., Hodeau, J. L., Lelièvre-Berna, E. & Regnard, J.-R.) 103–130 (Springer Netherlands, Dordrecht, 2006). ISBN: 978-1-4020-3337-7. https://doi.org/10.1007/1-4020-3337-0_3.

177. Fritzsche, S., Surzhykov, A., Jentschura, U. D. & Stöhlker, T. Angular and polarization analysis of x-rays emitted from highly-charged, few-electron ions. en. *Journal of Physics: Conference Series* **88,** 012018. ISSN: 1742-6596. https://dx.doi.org/10.1088/1742-6596/88/1/012018 (2025) (Nov. 2007).

178. Ma, K., Wang, S.-X., Zhu, L.-F., Tang, Z.-M. & Xie, L.-Y. Multipole mixing effects on the angular distribution and polarization of dielectronic hypersatellite lines from highly charged helium-like ions. *Physics Letters A* **475,** 128852. ISSN: 0375-9601. https://www.sciencedirect.com/science/article/pii/S0375960123002323 (2025) (July 2023).

179. Yang, Z. *et al.* Effect of the configuration mixing on the polarization and angular distribution of x-ray line emissions following electron-impact excitation of Ne-like ions. eng. *Optics Express* **32,** 9877–9889. ISSN: 1094-4087 (Mar. 2024).

180. Zhang, S.-N. *et al.* Detailed polarization measurements of the prompt emission of five gamma-ray bursts. en. *Nature Astronomy* **3.** Publisher: Nature Publishing Group, 258–264. ISSN: 2397-3366. https://www.nature.com/articles/s41550-018-0664-0 (2025) (Mar. 2019).

181. Oswald, L. S. *et al.* Pulsar polarization: a broad-band population view with the Parkes Ultra-Wideband receiver. *Monthly Notices of the Royal Astronomical Society* **520,** 4961–4980. ISSN: 0035-8711. https://doi.org/10.1093/mnras/stad070 (2025) (Apr. 2023).

182. Korchak, A. A. Polarization of Cosmic X-Rays. en. *Nature* **213.** Publisher: Nature Publishing Group, 1209–1210. ISSN: 1476-4687. https://www.nature.com/articles/2131209a0 (2025) (Mar. 1967).

183. Chen, S., Wang, M. & Jing, J. Polarization effects in Kerr black hole shadow due to the coupling between photon and bumblebee field. en. *Journal of High Energy Physics* **2020,** 54. ISSN: 1029-8479. https://doi.org/10.1007/JHEP07(2020)054 (2025) (July 2020).

184. Gußmann, A. Polarimetric signatures of the photon ring of a black hole that is pierced by a cosmic axion string. en. *Journal of High Energy Physics* **2021,** 160. ISSN: 1029-8479. https://doi.org/10.1007/JHEP08(2021)160 (2025) (Aug. 2021).

185. Cattaneo, A. *et al.* The role of black holes in galaxy formation and evolution. *Nature* **460,** 213–219. ISSN: 1476-4687. https://doi.org/10.1038/nature08135 (July 2009).

186. Törnroos, S., Leino-Kilpi, H. & Metsälä, E. Phenomena of radiography science - A scoping review. *Radiography* **27,** 1231–1240. ISSN: 1078-8174. https://www.sciencedirect.com/science/article/pii/S1078817421000857 (2025) (Nov. 2021).

187. Arnold, B. A., Kereiakes, J. G. & Thomas, S. R. en. in *Digital Radiography: Selected Topics* (eds Kereiakes, J. G., Thomas, S. R. & Orton, C. G.) 1–11 (Springer US, Boston, MA, 1986). ISBN: 978-1-4684-5068-2. https://doi.org/10.1007/978-1-4684-5068-2_1 (2025).

188. Kamm, K.-F. & Onnasch, D. G. W. en. in *Diagnostics of Vascular Diseases: Principles and Technology* (eds Lanzer, P. & Lipton, M.) 63–98 (Springer, Berlin, Heidelberg, 1997). ISBN: 978-3-642-60512-3. https://doi.org/10.1007/978-3-642-60512-3_5 (2025).

189. Mehta, S., Suhag, V., Semwal, M. & Sharma, N. Radiotherapy: Basic Concepts and Recent Advances. *Medical Journal, Armed Forces India* **66,** 158–162. ISSN: 0377-1237. https://www.ncbi.nlm.nih.gov/pmc/articles/PMC4920949/ (2025) (Apr. 2010).

190. Tamura, M., Ito, H. & Matsui, H. Radiotherapy for cancer using X-ray fluorescence emitted from iodine. en. *Scientific Reports* **7.** Publisher: Nature Publishing Group, 43667. ISSN: 2045-2322. https://www.nature.com/articles/srep43667 (2025) (Mar. 2017).

191. Patel, P. R. & De Jesus, O. eng. in *StatPearls* (StatPearls Publishing, Treasure Island (FL), 2025). http://www.ncbi.nlm.nih.gov/books/NBK567796/ (2025).

192. Booij, R., Budde, R. P. J., Dijkshoorn, M. L. & van Straten, M. Technological developments of X-ray computed tomography over half a century: User's influence on protocol optimization. *European Journal of Radiology* **131,** 109261. ISSN: 0720-048X. https://www.sciencedirect.com/science/article/pii/S0720048X20304502 (2025) (Oct. 2020).

193. Artioli, G. en. in *Encyclopedia of Geoarchaeology* (ed Gilbert, A. S.) 1019–1025 (Springer Netherlands, Dordrecht, 2017). ISBN: 978-1-4020-4409-0. https://doi.org/10.1007/978-1-4020-4409-0_29 (2025).

194. Smyth, M. S. & Martin, J. H. J. x Ray crystallography. *Molecular Pathology* **53,** 8–14. ISSN: 1366-8714. https://www.ncbi.nlm.nih.gov/pmc/articles/PMC1186895/ (2025) (Feb. 2000).

195. Kikhney, A. G. & Svergun, D. I. A practical guide to small angle X-ray scattering (SAXS) of flexible and intrinsically disordered proteins. *FEBS Letters. Dynamics, flexibility, and intrinsic disorder in protein assemblies* **589,** 2570–2577. ISSN: 0014-5793. https://www.sciencedirect.com/science/article/pii/S0014579315007279 (2025) (Sept. 2015).

196. Liu, L., Boldon, L., Urquhart, M. & Wang, X. Small and Wide Angle X-Ray Scattering Studies of Biological Macromolecules in Solution. *Journal of Visualized Experiments : JoVE,* 4160. ISSN: 1940-087X. https://www.ncbi.nlm.nih.gov/pmc/articles/PMC3671599/ (2025) (Jan. 2013).

197. Makowski, L. Characterization of Proteins with Wide-angle X-ray Solution Scattering (WAXS). *Journal of structural and functional genomics* **11,** 9–19. ISSN: 1345-711X. https://www.ncbi.nlm.nih.gov/pmc/articles/PMC3057577/ (2025) (Mar. 2010).

198. Boehm, C., Campo, A. O.-D., Ramirez-Quezada, M. & Zhou, Y.-l. Polarisation of high energy gamma-rays after scattering. *Journal of Cosmology and Astroparticle Physics* **2019.** arXiv:1903.11074 [hep-ph], 041–041. ISSN: 1475-7516. http://arxiv.org/abs/1903.11074 (2025) (Dec. 2019).

199. *What is Polarimeter? A Comprehensive Guide to Optical Activity and Applications | Torontech* en-US. Section: Analytical Labs. Jan. 2025. https://torontech.com/what-is-polarimeter/ (2025).

200. Gao, Y. *et al.* High Performance Polarization-Resolved Photodetectors Based on Intrinsically Stretchable Organic Semiconductors. en. *Advanced Science* **10,** 2204727. ISSN: 2198-3844. https://onlinelibrary.wiley.com/doi/abs/10.1002/advs.202204727 (2025) (2023).

201. Sen, P. *et al.* Panchromatic All-Polymer Photodetector with Tunable Polarization Sensitivity. en. *Advanced Optical Materials* **7,** 1801346. ISSN: 2195-1071. https://onlinelibrary.wiley.com/doi/abs/10.1002/adom.201801346 (2025) (2019).

202. He, X. *et al.* Photothermoelectric p–n Junction Photodetector with Intrinsic Broadband Polarimetry Based on Macroscopic Carbon Nanotube Films. *ACS Nano* **7.** Publisher: American Chemical Society, 7271–7277. ISSN: 1936-0851. https://doi.org/10.1021/nn402679u (2025) (Aug. 2013).

203. Hao, J. *et al.* Direct Detection of Circularly Polarized Light Using Chiral Copper Chloride–Carbon Nanotube Heterostructures. *ACS Nano* **15.** Publisher: American Chemical Society, 7608–7617. ISSN: 1936-0851. https://doi.org/10.1021/acsnano.1c01134 (2025) (Apr. 2021).

204. Zhao, K. *et al.* Direct Polarimetric Image Sensor and Wide Spectral Response Based on Quasi-1D Sb2S3 Nanowire. en. *Advanced Functional Materials* **31,** 2006601. ISSN: 1616-3028. https://onlinelibrary.wiley.com/doi/abs/10.1002/adfm.202006601 (2025) (2021).

205. Casadei, A. *et al.* Polarization response of nanowires à la carte. en. *Scientific Reports* **5.** Publisher: Nature Publishing Group, 7651. ISSN: 2045-2322. https://www.nature.com/articles/srep07651 (2025) (Jan. 2015).

206. Heim, R. & Tsien, R. Y. Engineering green fluorescent protein for improved brightness, longer wavelengths and fluorescence resonance energy transfer. *Current Biology* **6,** 178–182. ISSN: 0960-9822. https://www.sciencedirect.com/science/article/pii/S0960982202004505 (2025) (Feb. 1996).

207. Herman, A., Addadi, L. & Weiner, S. Interactions of sea-urchin skeleton macromolecules with growing calcite crystals— a study of intracrystalline proteins. en. *Nature* **331.** Publisher: Nature Publishing Group, 546–548. ISSN: 1476-4687. https://www.nature.com/articles/331546a0 (2025) (Feb. 1988).

208. Hoerl, S. *et al.* Evaluating the single crystallinity of sea urchin calcite. *Acta Biomaterialia* **198,** 334–355. ISSN: 1742-7061. https://www.sciencedirect.com/science/article/pii/S174270612500220X (2025) (May 2025).

209. Ulian, G. & Valdrè, G. Study of the variation of the optical properties of calcite with applied stress, useful for specific rock and material mechanics. en. *Scientific Reports* **12.** Publisher: Nature Publishing Group, 299. ISSN: 2045-2322. https://www.nature.com/articles/s41598-021-04471-6 (2025) (Jan. 2022).

210. Weisskopf, M. C. *et al.* The Imaging X-ray Polarimetry Explorer (*IXPE*). *Results in Physics* **6,** 1179–1180. ISSN: 2211-3797. https://www.sciencedirect.com/science/article/pii/S221137971630448X (2025) (Jan. 2016).

211. Doroshenko, V. *et al.* Determination of X-ray pulsar geometry with IXPE polarimetry. en. *Nature Astronomy* **6.** Publisher: Nature Publishing Group, 1433–1443. ISSN: 2397-3366. https://www.nature.com/articles/s41550-022-01799-5 (2025) (Dec. 2022).

212. Soffitta, P. *et al.* XIPE: the X-ray imaging polarimetry explorer. en. *Experimental Astronomy* **36,** 523–567. ISSN: 1572-9508. https://doi.org/10.1007/s10686-013-9344-3 (2025) (Dec. 2013).

213. André, P. *et al.* PRISM (Polarized Radiation Imaging and Spectroscopy Mission): an extended white paper. en. *Journal of Cosmology and Astroparticle Physics* **2014,** 006. ISSN: 1475-7516. https://dx.doi.org/10.1088/1475-7516/2014/02/006 (2025) (Feb. 2014).

214. Fiorina, D. *et al. HypeX: high yield polarimetry experiment in x-rays* in *X-Ray, Optical, and Infrared Detectors for Astronomy XI* **13103** (SPIE, Aug. 2024), 497–503. https://www.spiedigitallibrary.org/conference-proceedings-of-spie/13103/1310318/HypeX-high-yield-polarimetry-experiment-in-x-rays/10.1117/12.3021559.full (2025).

215. Harding, G. Inelastic photon scattering: Effects and applications in biomedical science and industry. *Radiation Physics and Chemistry. Inelastic Scattering of X-Rays and Gamma Rays* **50,** 91–111. ISSN: 0969-806X. https://www.sciencedirect.com/science/article/pii/S0969806X97000261 (2025) (July 1997).

216. Del Monte, E., Fabiani, S. & Pearce, M. en. in *Handbook of X-ray and Gamma-ray Astrophysics* 1–42 (Springer, Singapore, 2023). ISBN: 978-981-16-4544-0. https://link.springer.com/rwe/10.1007/978-981-16-4544-0_27-1 (2025).

217. Hulsman, J. *et al. POLAR-2: a large scale gamma-ray polarimeter for GRBs* in *Space Telescopes and Instrumentation 2020: Ultraviolet to Gamma Ray* arXiv:2101.03084 [astro-ph] (Dec. 2020), 314. http://arxiv.org/abs/2101.03084 (2025).

218. Yonetoku, D. *et al.* Gamma-Ray Burst Polarimeter (GAP) aboard the Small Solar Power Sail Demonstrator IKAROS. *Publications of the Astronomical Society of Japan* **63.** _eprint: https://academic.oup.com/pasj/article-pdf/63/3/625/54692470/pasj_63_3_625.pdf, 625–638. ISSN: 0004-6264. https://doi.org/10.1093/pasj/63.3.625 (June 2011).

219. Vadawale, S. V. *et al.* Hard X-ray polarimetry with Astrosat-CZTI. en. *Astronomy & Astrophysics* **578.** Publisher: EDP Sciences, A73. ISSN: 0004-6361, 1432-0746. https://www.aanda.org/articles/aa/abs/2015/06/aa25686-15/aa25686-15.html (2025) (June 2015).

220. Tomsick, J. A., Lowell, A., Lazar, H., Sleator, C. & Zoglauer, A. in. arXiv:2204.00027 [astro-ph], 1–24 (2022). http://arxiv.org/abs/2204.00027 (2025).

221. Chauvin, M., Roques, J. P., Clark, D. J. & Jourdain, E. POLARIMETRY IN THE HARD X-RAY DOMAIN WITH INTEGRAL SPI*. en. *The Astrophysical Journal* **769.** Publisher: The American Astronomical Society, 137. ISSN: 0004-637X. https://dx.doi.org/10.1088/0004-637X/769/2/137 (2025) (May 2013).

222. Almahwasi, A. *"Does Hadron Therapy Offer Enough Effectiveness in Treating Cancer to be Worth the Cost?"* Dec. 2016.

223. Kierans, C., Takahashi, T. & Kanbach, G. in *Handbook of X-ray and Gamma-ray Astrophysics* 1–72 (Springer Nature Singapore, Sept. 2022). ISBN: 9789811645440. http://dx.doi.org/10.1007/978-981-16-4544-0_46-1.

224. Wojtsekhowski, B., Tedeschi, D. & Vlahovic, B. A pair polarimeter for linearly polarized high-energy photons. *Nuclear Instruments and Methods in Physics Research Section A: Accelerators, Spectrometers, Detectors and Associated Equipment* **515,** 605–613. ISSN: 0168-9002. https://www.sciencedirect.com/science/article/pii/S0168900203023143 (2025) (Dec. 2003).

225. Do Hung Dang, V., Fong, C.-L., Shiu, J.-H. & Nozawa, Y. Grazing effects of sea urchin Diadema savignyi on algal abundance and coral recruitment processes. en. *Scientific Reports* **10.** Publisher: Nature Publishing Group, 20346. ISSN: 2045-2322. https://www.nature.com/articles/s41598-020-77494-0 (Nov. 2020).

226. Miller, K. I. & Shears, N. T. The efficiency and effectiveness of different sea urchin removal methods for kelp forest restoration. en. *Restoration Ecology* **31,** e13754. ISSN: 1526-100X. https://onlinelibrary.wiley.com/doi/abs/10.1111/rec.13754 (2023).

227. Soars, N., Prowse, T. & Byrne, M. Overview of phenotypic plasticity in echinoid larvae, 'Echinopluteus transversus' type vs. typical echinoplutei. *Marine Ecology Progress Series* **383,** 113 (May 2009).

228. Yaguchi, S., Taniguchi, Y., Suzuki, H., Kamata, M. & Yaguchi, J. Planktonic sea urchin larvae change their swimming direction in response to strong photoirradiation. en. *PLOS Genetics* **18.** Publisher: Public Library of Science, e1010033. ISSN: 1553-7404. https://journals.plos.org/plosgenetics/article?id=10.1371/journal.pgen.1010033 (Feb. 2022).

229. Yaguchi, J. & Yaguchi, S. Sea urchin larvae utilize light for regulating the pyloric opening. *BMC Biology* **19,** 64. ISSN: 1741-7007. https://doi.org/10.1186/s12915-021-00999-1 (Apr. 2021).

230. Valencia, J. E., Feuda, R., Mellott, D. O., Burke, R. D. & Peter, I. S. Ciliary photoreceptors in sea urchin larvae indicate pan-deuterostome cell type conservation. *BMC Biology* **19,** 257. ISSN: 1741-7007. https://doi.org/10.1186/s12915-021-01194-y (Dec. 2021).

231. Okazaki, K. & Inoué, S. Crystal Property of the Larval Sea Urchin Spicule*. en. *Development, Growth & Differentiation* **18,** 413–434. ISSN: 1440-169X. https://onlinelibrary.wiley.com/doi/abs/10.1111/j.1440-169X.1976.00413.x (1976).

232. Marshall, N. J. *et al.* Polarisation signals: a new currency for communication. en. *Journal of Experimental Biology* **222,** jeb134213. ISSN: 1477-9145, 0022-0949. https://journals.biologists.com/jeb/article/222/3/jeb134213/20737/Polarisation-signals-a-new-currency-for (Feb. 2019).

233. Wehner, R. Polarization vision–a uniform sensory capacity? eng. *The Journal of Experimental Biology* **204,** 2589–2596. ISSN: 0022-0949 (July 2001).

234. Daly, I. M. *et al.* Dynamic polarization vision in mantis shrimps. en. *Nature Communications* **7.** Bandiera_abtest: a Cc_license_type: cc_by Cg_type: Nature Research Journals Number: 1 Primary_atype: Research Publisher: Nature Publishing Group Subject_term: Animal behaviour;Pattern vision Subject_term_id: animal-behaviour;pattern-vision, 12140. ISSN: 2041-1723. https://www.nature.com/articles/ncomms12140 (July 2016).

235. Gagnon, Y. L., Templin, R. M., How, M. J. & Marshall, N. J. Circularly Polarized Light as a Communication Signal in Mantis Shrimps. *Current Biology* **25,** 3074–3078. ISSN: 0960-9822. https://www.sciencedirect.com/science/article/pii/S096098221501310X (Dec. 2015).

236. Sweeney, A., Jiggins, C. & Johnsen, S. Polarized light as a butterfly mating signal. en. *Nature* **423.** Publisher: Nature Publishing Group, 31–32. ISSN: 1476-4687. https://www.nature.com/articles/423031a (2025) (May 2003).

237. Beck, M., Althaus, V., Pegel, U. & Homberg, U. Neurons sensitive to non-celestial polarized light in the brain of the desert locust. eng. *Journal of Comparative Physiology. A, Neuroethology, Sensory, Neural, and Behavioral Physiology* **209,** 907–928. ISSN: 1432-1351 (Nov. 2023).

238. Horváth, G., Barta, A. & Hegedüs, R. en. in *Polarized Light and Polarization Vision in Animal Sciences* (ed Horváth, G.) 367–406 (Springer, Berlin, Heidelberg, 2014). ISBN: 978-3-642-54718-8. https://doi.org/10.1007/978-3-642-54718-8_18.

239. Flamarique, I. N. & Hárosi, F. I. Visual pigments and dichroism of anchovy cones: a model system for polarization detection. eng. *Visual Neuroscience* **19,** 467–473. ISSN: 0952-5238 (2002).

240. Hawryshyn, C. W., Moyer, H. D., Allison, W. T., Haimberger, T. J. & McFarland, W. N. Multidimensional polarization sensitivity in damselfishes. eng. *Journal of Comparative Physiology. A, Neuroethology, Sensory, Neural, and Behavioral Physiology* **189,** 213–220. ISSN: 0340-7594 (Mar. 2003).

241. Parkyn, D. C. & Hawryshyn, C. W. Polarized-light sensitivity in rainbow trout (Oncorhynchus mykiss): characterization from multi-unit responses in the optic nerve. en. *Journal of Comparative Physiology A* **172,** 493–500. ISSN: 1432-1351. https://doi.org/10.1007/BF00213531 (May 1993).

242. Sabbah, S., Barta, A., Gál, J., Horváth, G. & Shashar, N. Experimental and theoretical study of skylight polarization transmitted through Snell's window of a flat water surface. EN. *JOSA A* **23.** Publisher: Optica Publishing Group, 1978–1988. ISSN: 1520-8532. https://opg.optica.org/josaa/abstract.cfm?uri=josaa-23-8-1978 (Aug. 2006).

243. Zhou, G., Wang, J., Xu, W., Zhang, K. & Ma, Z. Polarization Patterns of Transmitted Celestial Light under Wavy Water Surfaces. en. *Remote Sensing* **9.** Number: 4 Publisher: Multidisciplinary Digital Publishing Institute, 324. ISSN: 2072-4292. https://www.mdpi.com/2072-4292/9/4/324 (Apr. 2017).

244. Cheng, H., Chu, J., Zhang, R., Tian, L. & Gui, X. Underwater polarization patterns considering single Rayleigh scattering of water molecules. *International Journal of Remote Sensing* **41,** 4947–4962. ISSN: 0143-1161. https://doi.org/10.1080/01431161.2019.1685725 (July 2020).

245. Cheng, H., Chu, J., Zhang, R., Tian, L. & Gui, X. Turbid Underwater Polarization Patterns Considering Multiple Mie Scattering of Suspended Particles. *Photogrammetric Engineering & Remote Sensing* **86,** 737–743 (Dec. 2020).

246. Cheng, H., Chu, J., Zhang, R. & Zhang, P. Simulation and measurement of the effect of various factors on underwater polarization patterns. *Optik* **237,** 166637. ISSN: 0030-4026. https://www.sciencedirect.com/science/article/pii/S0030402621003582 (July 2021).

247. Cheng, H., Guo, X., Bai, H., Li, G. & Su, C. The Research on Ocean Polarized Light Fields at Different Depths for Polarization Navigation. *IEEE Access* **11.** Conference Name: IEEE Access, 137702–137708. ISSN: 2169-3536. https://ieeexplore.ieee.org/document/10347220 (2023).

248. Lerner, A., Sabbah, S., Erlick, C. & Shashar, N. Navigation by light polarization in clear and turbid waters. *Philosophical Transactions of the Royal Society B: Biological Sciences* **366.** Publisher: Royal Society, 671–679. https://royalsocietypublishing.org/doi/10.1098/rstb.2010.0189 (Mar. 2011).

249. Cronin, T. W. & Marshall, J. Patterns and properties of polarized light in air and water. *Philosophical Transactions of the Royal Society B: Biological Sciences* **366.** Publisher: Royal Society, 619–626. https://royalsocietypublishing.org/doi/10.1098/rstb.2010.0201 (Mar. 2011).

250. Horváth, G. & Kriska, G. Polarization vision in aquatic insects and ecological traps for polarotactic insects. *Aquatic insects: challenges to populations. Royal Entomological Society* 204–229. ISSN: 9781845933968. https://www.cabidigitallibrary.org/doi/10.1079/9781845933968.0204 (Jan. 2008).

251. Shashar, N. *et al.* Underwater linear polarization: physical limitations to biological functions. *Philosophical Transactions of the Royal Society B: Biological Sciences* **366.** Publisher: Royal Society, 649–654. https://royalsocietypublishing.org/doi/10.1098/rstb.2010.0190 (Mar. 2011).

252. Waterman, T. H. Reviving a neglected celestial underwater polarization compass for aquatic animals. en. *Biological Reviews* **81,** 111–115. ISSN: 1469-185X. https://onlinelibrary.wiley.com/doi/abs/10.1017/S1464793105006883 (2006).

253. Ivanoff, A. & Waterman, T. Factors, mainly depth and wavelength, affecting the degree of underwater light polarization. *Journal of Marine Research* **16.** https://elischolar.library.yale.edu/journal_of_marine_research/898 (Jan. 1958).

254. Wynberg, H. *et al.* Circular polarization observed in bioluminescence. en. *Nature* **286.** Publisher: Nature Publishing Group, 641–642. ISSN: 1476-4687. https://www.nature.com/articles/286641a0 (Aug. 1980).

255. Horváth, G. & Varjú, D. en. in *Polarized Light in Animal Vision: Polarization Patterns in Nature* (eds Horváth, G. & Varjú, D.) 100–103 (Springer, Berlin, Heidelberg, 2004). ISBN: 978-3-662-09387-0. https://doi.org/10.1007/978-3-662-09387-0_15.

256. Rhode, S. C., Pawlowski, M. & Tollrian, R. The impact of ultraviolet radiation on the vertical distribution of zooplankton of the genus Daphnia. eng. *Nature* **412,** 69–72. ISSN: 0028-0836 (July 2001).

257. Williamson, C. E., Fischer, J. M., Bollens, S. M., Overholt, E. P. & Breckenridge, J. K. Toward a more comprehensive theory of zooplankton diel vertical migration: Integrating ultraviolet radiation and water transparency into the biotic paradigm. en. *Limnology and Oceanography* **56,** 1603–1623. ISSN: 1939-5590. https://onlinelibrary.wiley.com/doi/abs/10.4319/lo.2011.56.5.1603 (2024) (2011).

258. Wheeler, J. D., Chan, K. Y. K., Anderson, E. J. & Mullineaux, L. S. Ontogenetic changes in larval swimming and orientation of pre-competent sea urchin Arbacia punctulata in turbulence. *The Journal of Experimental Biology* **219,** 1303–1310. ISSN: 0022-0949. https://www.ncbi.nlm.nih.gov/pmc/articles/PMC4874563/ (May 2016).

259. Seow, Y., Rashidi, C., Aljunid, S., Ali, N. & Endut, R. 20 Mb/s Experimental Demonstration Using Modulated 460 nm Blue LED for Underwater Wireless Optical Communications (UOWC). *Journal of Physics: Conference Series* **1878,** 012069 (May 2021).

260. Dacke, M., Byrne, M. J., Baird, E., Scholtz, C. H. & Warrant, E. J. How dim is dim? Precision of the celestial compass in moonlight and sunlight. *Philosophical Transactions of the Royal Society B: Biological Sciences* **366.** Publisher: Royal Society, 697–702. https://royalsocietypublishing.org/doi/full/10.1098/rstb.2010.0191 (Mar. 2011).

261. Schneider, C. A., Rasband, W. S. & Eliceiri, K. W. NIH Image to ImageJ: 25 years of image analysis. *Nat Meth* **9,** 671–675. ISSN: 15487091. http://dx.doi.org/10.1038/nmeth.2089 (July 2012).

262. Lin, L. & Xu, C. Arcsine-based transformations for meta-analysis of proportions: Pros, cons, and alternatives. en. *Health Science Reports* **3,** e178. ISSN: 2398-8835. https://onlinelibrary.wiley.com/doi/abs/10.1002/hsr2.178 (2020).

263. Kono, M., Goletz, P. W. & Crouch, R. K. 11-cis and all-trans retinols can activate rod opsin: Rational design of the visual cycle. *Biochemistry* **47,** 7567–7571. ISSN: 0006-2960. https://www.ncbi.nlm.nih.gov/pmc/articles/PMC2561911/ (July 2008).

264. Terakita, A., Kawano-Yamashita, E. & Koyanagi, M. Evolution and diversity of opsins. en. *Wiley Interdisciplinary Reviews: Membrane Transport and Signaling* **1,** 104–111. ISSN: 2190-4618. https://onlinelibrary.wiley.com/doi/abs/10.1002/wmts.6 (2012).

265. Helfrich-Förster, C. Polarization Vision: Targets of Polarization-Sensitive Photoreceptors in the Drosophila Visual System. English. *Current Biology* **29.** Publisher: Elsevier, R839–R842. ISSN: 0960-9822. https://www.cell.com/current-biology/abstract/S0960-9822(19)30877-2 (Sept. 2019).

266. *Basics of polarimetry | Anton Paar Wiki* en. https://wiki.anton-paar.com/kr-en/basics-of-polarimetry/ (2025).

267. *Choosing a Wave Plate* en. https://www.thorlabs.com (2025).

268. Sun, J. *et al.* Light intensity regulates phototaxis, foraging and righting behaviors of the sea urchin Strongylocentrotus intermedius. *PeerJ* **7,** e8001. ISSN: 2167-8359. https://www.ncbi.nlm.nih.gov/pmc/articles/PMC6844242/ (2025) (Nov. 2019).

269. Salazar, M. H. Phototaxis in the deep-sea urchin *Allocentrotus fragilis* (Jackson). *Journal of Experimental Marine Biology and Ecology* **5,** 254–264. ISSN: 0022-0981. https://www.sciencedirect.com/science/article/pii/0022098170900043 (2025) (Nov. 1970).

270. Ullrich-Lüter, E. M., Dupont, S., Arboleda, E., Hausen, H. & Arnone, M. I. Unique system of photoreceptors in sea urchin tube feet. *Proceedings of the National Academy of Sciences of the United States of America* **108,** 8367–8372. ISSN: 0027-8424. https://www.ncbi.nlm.nih.gov/pmc/articles/PMC3100952/ (2025) (May 2011).

271. Li, T., Kirwan, J., Arnone, M. I., Nilsson, D.-E. & La Camera, G. A model of decentralized vision in the sea urchin *Diadema africanum*. *iScience* **26,** 106295. ISSN: 2589-0042. https://www.sciencedirect.com/science/article/pii/S2589004223003723 (2025) (Apr. 2023).

272. Okazaki, K. en. in *The Sea Urchin Embryo: Biochemistry and Morphogenesis* (ed Czihak, G.) 177–232 (Springer, Berlin, Heidelberg, 1975). ISBN: 978-3-642-65964-5. https://doi.org/10.1007/978-3-642-65964-5_9 (2025).

273. Lesser, M. P., Carleton, K. L., Böttger, S. A., Barry, T. M. & Walker, C. W. Sea urchin tube feet are photosensory organs that express a rhabdomeric-like opsin and PAX6. *Proceedings of the Royal Society B: Biological Sciences* **278,** 3371–3379. ISSN: 0962-8452. https://www.ncbi.nlm.nih.gov/pmc/articles/PMC3177635/ (2025) (Nov. 2011).

274. Narvaez, C. A., Stark, A. Y. & Russell, M. P. Morphological and Mechanical Tube Feet Plasticity among Populations of Sea Urchin (Strongylocentrotus purpuratus). *Integrative Organismal Biology* **6,** obae022. ISSN: 2517-4843. https://doi.org/10.1093/iob/obae022 (2025) (Jan. 2024).

275. Liu, F. *Hydrogen peroxide-induced genotoxicity and transgenerational implications in sea urchins* en. 2023. https://pure.uhi.ac.uk/en/studentTheses/hydrogen-peroxide-induced-genotoxicity-and-transgenerational-impl (2025).

276. Schneider, C. A., Rasband, W. S. & Eliceiri, K. W. NIH Image to ImageJ: 25 years of image analysis. en. *Nature Methods* **9.** Publisher: Nature Publishing Group, 671–675. ISSN: 1548-7105. https://www.nature.com/articles/nmeth.2089 (2025) (July 2012).

277. Johnsen, S. & Kier, W. M. Shade-seeking behaviour under polarized light by the brittlestar *Ophioderma Brevispinum* (Echinodermata: Ophiuroidea). en. *Journal of the Marine Biological Association of the United Kingdom* **79,** 761–763. ISSN: 0025-3154, 1469-7769. https://www.cambridge.org/core/product/identifier/S0025315498000940/type/journal_article (2025) (Aug. 1999).

278. Yoshimura, K., Iketani, T. & Motokawa, T. Do regular sea urchins show preference in which part of the body they orient forward in their walk? en. *Marine Biology* **159,** 959–965. ISSN: 1432-1793. https://doi.org/10.1007/s00227-011-1874-5 (2026) (May 2012).

279. Dumont, C. P., Drolet, D., Deschênes, I. & Himmelman, J. H. Multiple factors explain the covering behaviour in the green sea urchin, *Strongylocentrotus droebachiensis*. *Animal Behaviour* **73,** 979–986. ISSN: 0003-3472. https://www.sciencedirect.com/science/article/pii/S0003347207000796 (2025) (June 2007).

280. Kirwan, J. D. *et al.* The sea urchin Diadema africanum uses low resolution vision to find shelter and deter enemies. *Journal of Experimental Biology* **221,** jeb176271 (2018).

281. Li, Y.-Y., Su, F.-J., Hsieh, Y.-J., Huang, T.-C. & Wang, Y.-S. Embryo Development and Behavior in Sea Urchin (Tripneustes gratilla) Under Different Light Emitting Diodes Condition. *Frontiers in Marine Science* **8,** 684330 (June 2021).

282. Comely, C. A. & Ansell, A. D. Population density and growth of *Echinus esculentus* L. on the Scottish west coast. *Estuarine, Coastal and Shelf Science* **27,** 311–334. ISSN: 0272-7714. https://www.sciencedirect.com/science/article/pii/0272771488900595 (2025) (Sept. 1988).

283. Boudouresque, C. F. & Verlaque, M. in *Developments in Aquaculture and Fisheries Science* (ed Lawrence, J. M.) 447–485 (Elsevier, Jan. 2020). https://www.sciencedirect.com/science/article/pii/B9780128195703000263 (2025).

284. Kelly, M. S., Hughes, A. D. & Cook, E. J. in *Developments in Aquaculture and Fisheries Science* (ed Lawrence, J. M.) 329–336 (Elsevier, Jan. 2013). https://www.sciencedirect.com/science/article/pii/B9780123964915000228 (2025).

285. Shashar, N., Sabbah, S. & Cronin, T. W. Transmission of linearly polarized light in seawater: implications for polarization signaling. *Journal of Experimental Biology* **207,** 3619–3628. ISSN: 0022-0949. https://doi.org/10.1242/jeb.01187 (2025) (Sept. 2004).

286. Liu, F., Li, X., Han, P. & Shao, X. Advanced Visualization Polarimetric Imaging: Removal of Water Spray Effect Utilizing Circular Polarization. *Applied Sciences* **11,** 2996 (Mar. 2021).

287. Horváth, G. & Varjú, D. en. in *Polarized Light in Animal Vision: Polarization Patterns in Nature* (eds Horváth, G. & Varjú, D.) 95–99 (Springer, Berlin, Heidelberg, 2004). ISBN: 978-3-662-09387-0. https://doi.org/10.1007/978-3-662-09387-0_14 (2025).

288. Johnsen, S. Extraocular sensitivity to polarized light in an echinoderm. eng. *The Journal of Experimental Biology* **195,** 281–291. ISSN: 0022-0949 (Oct. 1994).

289. Li, T., Senesi, A. J. & Lee, B. Small Angle X-ray Scattering for Nanoparticle Research. *Chemical Reviews* **116.** Publisher: American Chemical Society, 11128–11180. ISSN: 0009-2665. https://doi.org/10.1021/acs.chemrev.5b00690 (2025) (Sept. 2016).

290. Chen, R. *et al.* Developments in small-angle X-ray scattering (SAXS) for characterizing the structure of surfactant-macromolecule interactions and their complex. eng. *International Journal of Biological Macromolecules* **251,** 126288. ISSN: 1879-0003 (Nov. 2023).

291. Narayanan, T. en. in *Soft Matter Characterization* (eds Borsali, R. & Pecora, R.) 899–952 (Springer Netherlands, Dordrecht, 2008). ISBN: 978-1-4020-4465-6. https://doi.org/10.1007/978-1-4020-4465-6_17 (2025).

292. Bushberg, J. T. The AAPM/RSNA physics tutorial for residents. X-ray interactions. eng. *Radiographics: A Review Publication of the Radiological Society of North America, Inc* **18,** 457–468. ISSN: 0271-5333 (1998).

293. Heath, R. L. en. in *Advances in X-Ray Analysis: Volume 15* (eds Heinrich, K. F. J., Barrett, C. S., Newkirk, J. B. & Ruud, C. O.) 1–35 (Springer US, Boston, MA, 1972). ISBN: 978-1-4613-9966-7. https://doi.org/10.1007/978-1-4613-9966-7_1 (2025).

294. Veloso, J. F. C. A. & Silva, A. L. M. Gaseous detectors for energy dispersive X-ray fluorescence analysis. *Nuclear Instruments and Methods in Physics Research Section A: Accelerators, Spectrometers, Detectors and Associated Equipment. Radiation Imaging Techniques and Applications* **878,** 24–39. ISSN: 0168-9002. https://www.sciencedirect.com/science/article/pii/S016890021730966X (2025) (Jan. 2018).

295. Xu, L.-J., Lin, X., He, Q., Worku, M. & Ma, B. Highly efficient eco-friendly X-ray scintillators based on an organic manganese halide. en. *Nature Communications* **11.** Publisher: Nature Publishing Group, 4329. ISSN: 2041-1723. https://www.nature.com/articles/s41467-020-18119-y (2025) (Aug. 2020).

296. Leroy. C, P.-G. R. in *Principles of Radiation Interaction in Matter and Detection* 689–811 (WORLD SCIENTIFIC, Apr. 2014). ISBN: 978-981-4603-18-8. https://www.worldscientific.com/doi/abs/10.1142/9789814603195_0010 (2025).

297. Titov, M. en. in *Handbook of Particle Detection and Imaging* (eds Grupen, C. & Buvat, I.) 239–264 (Springer, Berlin, Heidelberg, 2012). ISBN: 978-3-642-13271-1. https://doi.org/10.1007/978-3-642-13271-1_11 (2025).

298. Nikl, M. Scintillation detectors for x-rays. en. *Measurement Science and Technology* **17,** R37–R54. ISSN: 0957-0233, 1361-6501. https://iopscience.iop.org/article/10.1088/0957-0233/17/4/R01 (2025) (Apr. 2006).

299. Changizi, V., Kheradmand, A. A. & Oghabian, M. A. Application of small-angle X-ray scattering for differentiation among breast tumors. *Journal of Medical Physics / Association of Medical Physicists of India* **33,** 19–23. ISSN: 0971-6203. https://www.ncbi.nlm.nih.gov/pmc/articles/PMC2786093/ (2025) (2008).

300. Thomas, J. M. The birth of X-ray crystallography. en. *Nature* **491.** Publisher: Nature Publishing Group, 186–187. ISSN: 1476-4687. https://www.nature.com/articles/491186a (2025) (Nov. 2012).

301. Adepu, A. & Venkatathri, N. *Development of Porous Titanosilicate - Based hybrid Nanocomposites for Photocatalytic Applications under UV and Solar light irradiation* PhD thesis (Jan. 2018).

302. Jacques, D. A. & Trewhella, J. Small-angle scattering for structural biology—Expanding the frontier while avoiding the pitfalls. en. *Protein Science* **19,** 642–657. ISSN: 1469-896X. https://onlinelibrary.wiley.com/doi/abs/10.1002/pro.351 (2025) (2010).

303. Byer, A. S., Pei, X., Patterson, M. G. & Ando, N. Small-angle X-ray scattering studies of enzymes. *Current Opinion in Chemical Biology* **72,** 102232. ISSN: 1367-5931. https://www.sciencedirect.com/science/article/pii/S136759312200117X (2025) (Feb. 2023).

304. Grishaev, A. Sample preparation, data collection and preliminary data analysis in biomolecular solution X-ray scattering. *Current protocols in protein science / editorial board, John E. Coligan ... [et al.]* **CHAPTER,** Unit17.14. ISSN: 1934-3655. https://www.ncbi.nlm.nih.gov/pmc/articles/PMC3523188/ (2025) (Nov. 2012).

305. Malanovic, N. *et al.* Small-Angle X-ray Scattering (SAXS) Used for the Identification of Nicomorphine Polymorphic Changes at the Early Stage to Avoid Varied Stability and Possible Side Effects. *Pharmaceuticals* **17,** 375. ISSN: 1424-8247. https://www.ncbi.nlm.nih.gov/pmc/articles/PMC10975358/ (2025) (Mar. 2024).

306. Leblanc, J. L. Rubber–filler interactions and rheological properties in filled compounds. *Progress in Polymer Science* **27,** 627–687. ISSN: 0079-6700. https://www.sciencedirect.com/science/article/pii/S0079670001000405 (2025) (May 2002).

307. Pyke, K. E. & Tschakovsky, M. E. The relationship between shear stress and flow-mediated dilatation: implications for the assessment of endothelial function. *The Journal of Physiology* **568,** 357–369. ISSN: 0022-3751. https://www.ncbi.nlm.nih.gov/pmc/articles/PMC1474741/ (2025) (Oct. 2005).

308. Krishna, K. V., Swathi, K., Hemalatha, M. & Mohan, S. V. in *Microbial Electrochemical Technology* (eds Mohan, S. V., Varjani, S. & Pandey, A.) 117–141 (Elsevier, Jan. 2019). ISBN: 978-0-444-64052-9. https://www.sciencedirect.com/science/article/pii/B9780444640529000066 (2025).

309. Van Horn, B. L. & Winter, H. H. Dynamics of shear aligning of nematic liquid crystal monodomains. en. *Rheologica Acta* **39,** 294–300. ISSN: 1435-1528. https://doi.org/10.1007/s003970000111 (2025) (Aug. 2000).

310. Walton, J., McKay, G., Grinfeld, M. & Mottram, N. Pressure-driven changes to spontaneous flow in active nematic liquid crystals. *The European Physical Journal E* **43** (Aug. 2020).

311. Synchrotron, A. *How it works* https://www.ansto.gov.au/facilities/australian-synchrotron.

312. Wiedemann, H. en. in *Synchrotron Light Sources and Free-Electron Lasers: Accelerator Physics, Instrumentation and Science Applications* (eds Jaeschke, E. J., Khan, S., Schneider, J. R. & Hastings, J. B.) 3–49 (Springer International Publishing, Cham, 2016). ISBN: 978-3-319-14394-1. https://doi.org/10.1007/978-3-319-14394-1_1 (2025).

313. Westfold, K. C. The Polarization of Synchrotron Radiation. *Astrophysical Journal* **130,** 241. https://ui.adsabs.harvard.edu/abs/1959ApJ...130..241W/abstract (2025) (1959).

314. Jackson, A. *The Australian Synchrotron Project-Update* in (June 2005), 102–106. ISBN: 0-7803-8859-3.

315. Gutzler, R., Garg, M., Ast, C. R., Kuhnke, K. & Kern, K. Light–matter interaction at atomic scales. en. *Nature Reviews Physics* **3.** Publisher: Nature Publishing Group, 441–453. ISSN: 2522-5820. https://www.nature.com/articles/s42254-021-00306-5 (2025) (June 2021).

316. Stenzel, O. *Light–Matter Interaction: A Crash Course for Students of Optics, Photonics and Materials Science* en. ISBN: 978-3-030-87143-7 978-3-030-87144-4. https://link.springer.com/10.1007/978-3-030-87144-4 (2025) (Springer International Publishing, Cham, 2022).

317. Weight, B. M., Li, X. & Zhang, Y. *Theory and modeling of light-matter interactions in chemistry: current and future* arXiv:2303.10111 [physics]. Aug. 2023. http://arxiv.org/abs/2303.10111 (2025).

318. Brewster, D. On the laws of the polarization of light by refraction. *Abstracts of the Papers Printed in the Philosophical Transactions of the Royal Society of London* **2.** Publisher: Royal Society, 394–395. https://royalsocietypublishing.org/doi/10.1098/rspl.1815.0388 (2024) (Jan. 1997).

319. Empedocles, S. A., Neuhauser, R. & Bawendi, M. G. Three-dimensional orientation measurements of symmetric single chromophores using polarization microscopy. en. *Nature* **399.** Publisher: Nature Publishing Group, 126–130. ISSN: 1476-4687. https://www.nature.com/articles/20138 (2024) (May 1999).

320. Roy, S. C., Pratt, R. H. & Kissel, L. Rayleigh scattering by energetic photons: Development of theory and current status. *Radiation Physics and Chemistry* **41,** 725–738. ISSN: 0969-806X. https://www.sciencedirect.com/science/article/pii/0969806X9390320T (2025) (Apr. 1993).

321. Xia, B. *et al.* Evaluation and simulations of a Thomson scattering X-ray source based on ray tracing methods. en. *Laser and Particle Beams* **22,** 355–365. ISSN: 1469-803X, 0263-0346. https://www.cambridge.org/core/journals/laser-and-particle-beams/article/evaluation-and-simulations-of-a-thomson-scattering-xray-source-based-on-ray-tracing-methods/90ECB763B51BB2761EC495C34CD0F3B9 (2025) (July 2004).

322. Seibert, J. A. & Boone, J. M. X-Ray Imaging Physics for Nuclear Medicine Technologists. Part 2: X-Ray Interactions and Image Formation. en. *Journal of Nuclear Medicine Technology* **33.** Publisher: Society of Nuclear Medicine Section: CONTINUING EDUCATION, 3–18. ISSN: 0091-4916, 1535-5675. https://tech.snmjournals.org/content/33/1/3 (2025) (Mar. 2005).

323. Kim, J. & Nam, K. H. X-ray-Induced Heating in the Vicinity of the X-ray Interaction Point. en. *Applied Sciences* **13.** Number: 2 Publisher: Multidisciplinary Digital Publishing Institute, 717. ISSN: 2076-3417. https://www.mdpi.com/2076-3417/13/2/717 (2025) (Jan. 2023).

324. Alikunju, R. P. *et al.* Effect of different scintillator choices on the X-ray imaging performance of CMOS sensors. *Nuclear Instruments and Methods in Physics Research Section A: Accelerators, Spectrometers, Detectors and Associated Equipment* **1050,** 168136. ISSN: 0168-9002. https://www.sciencedirect.com/science/article/pii/S0168900223001262 (2025) (May 2023).

325. Howell, R. W. Auger processes in the 21st century. *International journal of radiation biology* **84,** 959–975. ISSN: 0955-3002. https://www.ncbi.nlm.nih.gov/pmc/articles/PMC3459331/ (2025) (Dec. 2008).

326. Auger, P. *Sur les rayons [beta] secondaires prodiuts dans un gaz par des rayons x* (Gauthier-Villars, 1925).

327. Meitner, L. Das -Strahlenspektrum von UX1 und seine Deutung. de. *Zeitschrift für Physik* **17,** 54–66. ISSN: 0044-3328. https://doi.org/10.1007/BF01328663 (2025) (Dec. 1923).

328. Wang, H. & Chu, P. K. in *Characterization of Biomaterials* (eds Bandyopadhyay, A. & Bose, S.) 105–174 (Academic Press, Oxford, Jan. 2013). ISBN: 978-0-12-415800-9. https://www.sciencedirect.com/science/article/pii/B9780124158009000048 (2025).

329. Yano, J. & Yachandra, V. K. X-ray absorption spectroscopy. *Photosynthesis Research* **102,** 241–254. ISSN: 0166-8595. https://www.ncbi.nlm.nih.gov/pmc/articles/PMC2777224/ (2025) (2009).

330. Penner-Hahn, J. E. 1.59 CCC01063.0005 X-ray Absorption Spectroscopy. en.

331. *NIST: X-Ray Mass Attenuation Coefficients - Gold* https://physics.nist.gov/PhysRefData/XrayMassCoef/ElemTab/z79.html (2025).

332. Chen, S.-y., Maksimchuk, A. & Umstadter, D. Experimental observation of relativistic nonlinear Thomson scattering. en. *Nature* **396,** 653–655. ISSN: 0028-0836, 1476-4687. https://www.nature.com/articles/25303 (2025) (Dec. 1998).

333. L'Annunziata, M. F. in *Radioactivity (Third Edition)* (ed L'Annunziata, M. F.) 709–746 (Elsevier, Boston, Jan. 2023). ISBN: 978-0-323-90440-7. https://www.sciencedirect.com/science/article/pii/B9780323904407000053 (2025).

334. L'Annunziata, M. F. in *Radioactivity (Second Edition)* (ed L'Annunziata, M. F.) 269–302 (Elsevier, Boston, Jan. 2016). ISBN: 978-0-444-63489-4. https://www.sciencedirect.com/science/article/pii/B9780444634894000083 (2025).

335. Elder, F. R., Langmuir, R. V. & Pollock, H. C. Radiation from Electrons Accelerated in a Synchrotron. *Phys. Rev.* **74,** 52–56. https://link.aps.org/doi/10.1103/PhysRev.74.52 (1 July 1948).

336. Terasawa, M. & Kihara, M. in *Analytical Spectroscopy Library* (eds Saisho, H. & Gohshi, Y.) 1–78 (Elsevier, Jan. 1996). https://www.sciencedirect.com/science/article/pii/S0926434596800022 (2025).

337. Pannuti, T. G. en. in *The Physical Processes and Observing Techniques of Radio Astronomy: An Introduction* (ed Pannuti, T. G.) 69–114 (Springer International Publishing, Cham, 2020). ISBN: 978-3-319-16982-8. https://doi.org/10.1007/978-3-319-16982-8_3 (2025).

338. Tessier, F. & Kawrakow, I. Calculation of the electron–electron bremsstrahlung cross-section in the field of atomic electrons. *Nuclear Instruments and Methods in Physics Research Section B: Beam Interactions with Materials and Atoms* **266,** 625–634. ISSN: 0168-583X. https://www.sciencedirect.com/science/article/pii/S0168583X07017454 (2025) (Feb. 2008).

339. Carr, J. J. in *The Technician's EMI Handbook* (ed Carr, J. J.) 5–21 (Newnes, Woburn, Jan. 2000). ISBN: 978-0-7506-7233-7. https://www.sciencedirect.com/science/article/pii/B9780750672337500028 (2025).

340. Hammer, B. & Norskov, J. K. Why gold is the noblest of all the metals. en. *Nature* **376.** Publisher: Nature Publishing Group, 238–240. ISSN: 1476-4687. https://www.nature.com/articles/376238a0 (2025) (July 1995).

341. Lipkin, R. *What makes gold such a noble metal? - Free Online Library* July 1995. https://www.thefreelibrary.com/What+makes+gold+such+a+noble+metal%3F-a017352490 (2025).

342. Nguyen, H. H., Park, J., Kang, S. & Kim, M. Surface Plasmon Resonance: A Versatile Technique for Biosensor Applications. *Sensors (Basel, Switzerland)* **15,** 10481–10510. ISSN: 1424-8220. https://www.ncbi.nlm.nih.gov/pmc/articles/PMC4481982/ (2025) (May 2015).

343. Su, Y.-H., Ke, Y.-F., Cai, S.-L. & Yao, Q.-Y. Surface plasmon resonance of layer-by-layer gold nanoparticles induced photoelectric current in environmentally-friendly plasmon-sensitized solar cell. en. *Light: Science & Applications* **1.** Publisher: Nature Publishing Group, e14–e14. ISSN: 2047-7538. https://www.nature.com/articles/lsa201214 (2025) (June 2012).

344. Theodosiou, M. *et al.* Amino acid driven synthesis of gold nanoparticles: A comparative study on their biocompatibility. *Materials Chemistry and Physics* **319,** 129260. ISSN: 0254-0584. https://www.sciencedirect.com/science/article/pii/S0254058424003857 (2025) (June 2024).

345. Lee, J.-H., Cho, H.-Y., Choi, H. K., Lee, J.-Y. & Choi, J.-W. Application of Gold Nanoparticle to Plasmonic Biosensors. en. *International Journal of Molecular Sciences* **19.** Number: 7 Publisher: Multidisciplinary Digital Publishing Institute, 2021. ISSN: 1422-0067. https://www.mdpi.com/1422-0067/19/7/2021 (2025) (July 2018).

346. Sun, L. *et al.* en. in *Applications of Molecular Spectroscopy to Current Research in the Chemical and Biological Sciences* (IntechOpen, Oct. 2016). ISBN: 978-953-51-2681-2. https://www.intechopen.com/chapters/51493 (2025).

347. Che, Z. *et al.* Surface plasmon resonance sensor based on polarization parameter SPR imaging. EN. *Optics Express* **31.** Publisher: Optica Publishing Group, 41569–41581. ISSN: 1094-4087. https://opg.optica.org/oe/abstract.cfm?uri=oe-31-25-41569 (2025) (Dec. 2023).

348. Zeng, S. *et al.* Size dependence of Au NP-enhanced surface plasmon resonance based on differential phase measurement. en. *Sensors and Actuators B: Chemical* **176,** 1128–1133. ISSN: 09254005. https://linkinghub.elsevier.com/retrieve/pii/S0925400512009860 (2025) (Jan. 2013).

349. Borah, R., Ninakanti, R., Bals, S. & Verbruggen, S. W. Plasmon resonance of gold and silver nanoparticle arrays in the Kretschmann (attenuated total reflectance) vs. direct incidence configuration. en. *Scientific Reports* **12.** Publisher: Nature Publishing Group, 15738. ISSN: 2045-2322. https://www.nature.com/articles/s41598-022-20117-7 (2025) (Sept. 2022).

350. Ghosh, S. K. & Pal, T. Interparticle Coupling Effect on the Surface Plasmon Resonance of Gold Nanoparticles: From Theory to Applications. *Chemical Reviews* **107.** Publisher: American Chemical Society, 4797–4862. ISSN: 0009-2665. https://doi.org/10.1021/cr0680282 (2025) (Nov. 2007).

351. Huang, X. & El-Sayed, M. A. Gold nanoparticles: Optical properties and implementations in cancer diagnosis and photothermal therapy. *Journal of Advanced Research* **1,** 13–28. ISSN: 2090-1232. https://www.sciencedirect.com/science/article/pii/S2090123210000056 (2025) (Jan. 2010).

352. McMahon, S. J. *et al.* Biological consequences of nanoscale energy deposition near irradiated heavy atom nanoparticles. en. *Scientific Reports* **1.** Publisher: Nature Publishing Group, 18. ISSN: 2045-2322. https://www.nature.com/articles/srep00018 (2025) (June 2011).

353. Li, W. *et al.* Intercomparison of dose enhancement ratio and secondary electron spectra for gold nanoparticles irradiated by x-rays calculated using multiple Monte Carlo simulation codes. *Physica medica : PM : an international journal devoted to the applications of physics to medicine and biology : official journal of the Italian Association of Biomedical Physics (AIFB)* **69,** 147–163. ISSN: 1120-1797. https://www.ncbi.nlm.nih.gov/pmc/articles/PMC7446940/ (2025) (Jan. 2020).

354. Wu, D., Yu, W., Zhao, Y. T., Fritzsche, S. & He, X. T. Characteristics of X/-ray radiations by intense laser interactions with high-Z solids: The role of bremsstrahlung and radiation reactions. *Matter and Radiation at Extremes* **3,** 293–299. ISSN: 2468-080X. https://www.sciencedirect.com/science/article/pii/S2468080X18300438 (2025) (Nov. 2018).

355. Ming, T. *et al. Strong Polarization Dependence of Plasmon-Enhanced Fluorescence on Single Gold Nanorods* EN. rapid-communication. Archive Location: world Publisher: American Chemical Society. Sept. 2009. https://pubs.acs.org/doi/pdf/10.1021/nl902095q (2025).

356. Rizvi, M. H. *et al.* Magnetic Alignment for Plasmonic Control of Gold Nanorods Coated with Iron Oxide Nanoparticles. en. *Advanced Materials* **34,** 2203366. ISSN: 1521-4095. https://onlinelibrary.wiley.com/doi/abs/10.1002/adma.202203366 (2025) (2022).

357. Wang, Y. L., Chen, L. Y., Liu, Q. K., Cai, F. H. & Qian, J. The ordering alignment of gold nanorods in liquid crystals and its applications to polarization-sensitive SERS. en. *Journal of Physics: Conference Series* **680.** Publisher: IOP Publishing, 012021. ISSN: 1742-6596. https://dx.doi.org/10.1088/1742-6596/680/1/012021 (2025) (Jan. 2016).

358. Chen, L. *et al.* Sensing the Moving Direction, Position, Size, and Material Type of Nanoparticles with the Two-Photon-Induced Luminescence of a Single Gold Nanorod. en. *The Journal of Physical Chemistry C* **117,** 20146–20153. ISSN: 1932-7447, 1932-7455. https://pubs.acs.org/doi/10.1021/jp405403g (2025) (Oct. 2013).

359. Ahn, S., Jung, S. Y. & Lee, S. J. Gold Nanoparticle Contrast Agents in Advanced X-ray Imaging Technologies. *Molecules* **18,** 5858–5890. ISSN: 1420-3049. https://www.ncbi.nlm.nih.gov/pmc/articles/PMC6270207/ (2025) (May 2013).

360. Andrienko, D. Introduction to liquid crystals. *Journal of Molecular Liquids. Special Issue Dedicated to the Memory of Professor Y. Reznikov* **267,** 520–541. ISSN: 0167-7322. https://www.sciencedirect.com/science/article/pii/S016773221735314X (2025) (Oct. 2018).

361. Bruce, D. W., Deschenaux, R., Donnio, B. & Guillon, D. in *Comprehensive Organometallic Chemistry III* (eds Mingos, D. M. P. & Crabtree, R. H.) 195–293 (Elsevier, Oxford, Jan. 2007). ISBN: 978-0-08-045047-6. https://www.sciencedirect.com/science/article/pii/B0080450474001709 (2025).

362. Tadros, T. en. in *Encyclopedia of Colloid and Interface Science* (ed Tadros, T.) 682–683 (Springer, Berlin, Heidelberg, 2013). ISBN: 978-3-642-20665-8. https://doi.org/10.1007/978-3-642-20665-8_115 (2025).

363. Meier, G. en. in *Applications of Liquid Crystals* (eds Meier, G., Sackmann, E. & Grabmaier, J. G.) 1–20 (Springer, Berlin, Heidelberg, 1975). ISBN: 978-3-642-80954-5. https://doi.org/10.1007/978-3-642-80954-5_1 (2025).

364. Kuang, Z.-Y. *et al.* Alignment Control of Nematic Liquid Crystal using Gold Nanoparticles Grafted by the Liquid Crystalline Polymer with Azobenzene Mesogens as the Side Chains. *ACS Applied Materials & Interfaces* **10.** Publisher: American Chemical Society, 27269–27277. ISSN: 1944-8244. https://doi.org/10.1021/acsami.8b07483 (2025) (Aug. 2018).

365. Qi, H. & Hegmann, T. Multiple Alignment Modes for Nematic Liquid Crystals Doped with Alkylthiol-Capped Gold Nanoparticles. *ACS Applied Materials & Interfaces* **1.** Publisher: American Chemical Society, 1731–1738. ISSN: 1944-8244. https://doi.org/10.1021/am9002815 (2025) (Aug. 2009).

366. Liu, Q. *et al.* Self-Alignment of Plasmonic Gold Nanorods in Reconfigurable Anisotropic Fluids for Tunable Bulk Metamaterial Applications. *Nano Letters* **10.** Publisher: American Chemical Society, 1347–1353. ISSN: 1530-6984. https://doi.org/10.1021/nl9042104 (2025) (Apr. 2010).

367. Feng, X. *et al.* Discotic Liquid Crystal-Functionalized Gold Nanorods: 2- and 3D Self-Assembly and Macroscopic Alignment as well as Increased Charge Carrier Mobility in Hexagonal Columnar Liquid Crystal Hosts Affected by Molecular Packing and – Interactions. en. *Advanced Functional Materials* **25,** 1180–1192. ISSN: 1616-3028. https://onlinelibrary.wiley.com/doi/abs/10.1002/adfm.201401844 (2025) (2015).

368. Schymura, S. *Liquid Crystalline Carbon Nanotube Suspensions - From Unique Challenges to Unique Properties* PhD thesis (July 2013).

369. Yamamoto, T. *et al.* Metastable and stable phase diagrams and thermodynamic properties of the cetyltrimethylammonium bromide (CTAB)/water binary system. *Colloids and Surfaces A: Physicochemical and Engineering Aspects* **625,** 126859. ISSN: 0927-7757. https://www.sciencedirect.com/science/article/pii/S0927775721007287 (2025) (Sept. 2021).

370. Wei, M.-Z., Deng, T.-S., Zhang, Q., Cheng, Z. & Li, S. Seed-Mediated Synthesis of Gold Nanorods at Low Concentrations of CTAB. *ACS Omega* **6.** Publisher: American Chemical Society, 9188–9195. https://doi.org/10.1021/acsomega.1c00510 (2025) (Apr. 2021).

371. Kotkowiak, M., Tim, B., Kotkowiak, M., Musiał, J. & Błaszkiewicz, P. The Role of the Polyethylene Glycol in the Organization of Gold Nanorods at the Air–Water and Air–Solid Interfaces. *Langmuir* **40.** Publisher: American Chemical Society, 14561–14569. ISSN: 0743-7463. https://doi.org/10.1021/acs.langmuir.4c01427 (2025) (July 2024).

372. Kopwitthaya, A. *et al.* Functionalized Plasmonic Anisotropic Nanocrystals for Multimodal Imaging of Cancer Cells. en. *Plasmonics* **8,** 313–318. ISSN: 1557-1963. https://doi.org/10.1007/s11468-012-9391-z (2025) (June 2013).

373. Centi, S. *et al.* In vitro assessment of antibody-conjugated gold nanorods for systemic injections. *Journal of Nanobiotechnology* **12,** 55. ISSN: 1477-3155. https://doi.org/10.1186/s12951-014-0055-3 (2025) (Dec. 2014).

374. Singh, B. P. *et al.* Chemically Functionalized Gold Nanosphere-Blended Nematic Liquid Crystals for Photonic Applications. *ACS Omega* **8.** Publisher: American Chemical Society, 2315–2327. https://doi.org/10.1021/acsomega.2c06718 (2025) (Jan. 2023).

375. Li, C.-C., Chang, S.-J., Su, F.-J., Lin, S.-W. & Chou, Y.-C. Effects of capping agents on the dispersion of silver nanoparticles. *Colloids and Surfaces A: Physicochemical and Engineering Aspects* **419,** 209–215. ISSN: 0927-7757. https://www.sciencedirect.com/science/article/pii/S0927775712008497 (2025) (Feb. 2013).

376. Niu, Z. & Li, Y. Removal and Utilization of Capping Agents in Nanocatalysis. *Chemistry of Materials* **26.** Publisher: American Chemical Society, 72–83. ISSN: 0897-4756. https://doi.org/10.1021/cm4022479 (2025) (Jan. 2014).

377. Kanelidis, I. & Kraus, T. The role of ligands in coinage-metal nanoparticles for electronics. eng. *Beilstein Journal of Nanotechnology* **8,** 2625–2639. ISSN: 2190-4286 (2017).

378. McMahon, S. J. & Currell, F. J. in *Frontiers of Nanoscience* (ed Summers, H.) 65–93 (Elsevier, Jan. 2013). https://www.sciencedirect.com/science/article/pii/B9780080983387000030 (2025).

379. Ndione, P. D., Weber, S. T., Gericke, D. O. & Rethfeld, B. Nonequilibrium band occupation and optical response of gold after ultrafast XUV excitation. en. *Scientific Reports* **12.** Publisher: Nature Publishing Group, 4693. ISSN: 2045-2322. https://www.nature.com/articles/s41598-022-08338-2 (2025) (Mar. 2022).

380. Kolwas, K. & Derkachova, A. Impact of the Interband Transitions in Gold and Silver on the Dynamics of Propagating and Localized Surface Plasmons. *Nanomaterials* **10,** 1411. ISSN: 2079-4991. https://www.ncbi.nlm.nih.gov/pmc/articles/PMC7407753/ (2025) (July 2020).

381. Konefał, A. *et al.* Influence of a shape of gold nanoparticles on the dose enhancement in the wide range of gold mass concentration for high-energy X-ray beams from a medical linac. *Reports of Practical Oncology & Radiotherapy* **25,** 579–585. ISSN: 1507-1367. https://www.sciencedirect.com/science/article/pii/S1507136720300833 (2025) (July 2020).

382. Hara, D. *et al.* Prostate Cancer Targeted X-Ray Fluorescence Imaging via Gold Nanoparticles Functionalized With Prostate-Specific Membrane Antigen (PSMA). *International Journal of Radiation Oncology*Biology*Physics* **111,** 220–232. ISSN: 0360-3016. https://www.sciencedirect.com/science/article/pii/S0360301621004594 (2025) (Sept. 2021).

383. Van Ballegooie, C. *et al.* Gold–Protein Composite Nanoparticles for Enhanced X-ray Interactions: A Potential Formulation for Triggered Release. en. *Pharmaceutics* **13.** Number: 9 Publisher: Multidisciplinary Digital Publishing Institute, 1407. ISSN: 1999-4923. https://www.mdpi.com/1999-4923/13/9/1407 (2025) (Sept. 2021).

384. Kumar, R. *et al.* Determination of the Aspect-ratio Distribution of Gold Nanorods in a Colloidal Solution using UV-visible absorption spectroscopy. en. *Scientific Reports* **9.** Publisher: Nature Publishing Group, 17469. ISSN: 2045-2322. https://www.nature.com/articles/s41598-019-53621-4 (2025) (Nov. 2019).

385. Rienäcker, G. & Hess, S. Orientational dynamics of nematic liquid crystals under shear flow. *Physica A: Statistical Mechanics and its Applications* **267,** 294–321. ISSN: 0378-4371. https://www.sciencedirect.com/science/article/pii/S0378437198006694 (2025) (May 1999).

386. Richtering, W., Laeuger, J. & Linemann, R. Shear Orientation of a Micellar Hexagonal Liquid Crystalline Phase: A Rheo and Small Angle Light Scattering Study. *Langmuir* **10.** Publisher: American Chemical Society, 4374–4379. ISSN: 0743-7463. https://doi.org/10.1021/la00023a073 (2025) (Nov. 1994).

387. SasView. *SasView* en. https://sasview.github.io/ (2025).

388. Albarghouthi, N., Chotoye, S. a. B. & Brosseau, C. L. An Exploration of Cysteamine as a Subphase Additive for the Fabrication of Uniform Gold Nanorod Arrays using Langmuir-Blodgett Deposition. en. *ChemPhysChem* **25,** e202400146. ISSN: 1439-7641. https://onlinelibrary.wiley.com/doi/abs/10.1002/cphc.202400146 (2025) (2024).

389. Link, S., Mohamed, M. B. & El-Sayed, M. A. Simulation of the Optical Absorption Spectra of Gold Nanorods as a Function of Their Aspect Ratio and the Effect of the Medium Dielectric Constant. *The Journal of Physical Chemistry B* **103.** Publisher: American Chemical Society, 3073–3077. ISSN: 1520-6106. https://doi.org/10.1021/jp990183f (2025) (Apr. 1999).

390. Mishra, N., Liu, M., Fang, Y. & Kulkarni, S. Study of adsorption behavior of aminothiophenols on gold nanorods using surface-enhanced Raman spectroscopy. *Journal of Nanophotonics* **5,** 053513 (July 2011).

391. Feng, L. *et al.* Preparation of gold nanorods with different aspect ratio and the optical response to solution refractive index. *Journal of Experimental Nanoscience* **10.** Publisher: Taylor & Francis _eprint: https://doi.org/10.1080/17458080.2013.824619, 258–267. https://doi.org/10.1080/17458080.2013.824619 (2015).

392. Muskens, O. L. *et al.* Quantitative Absorption Spectroscopy of a Single Gold Nanorod. *The Journal of Physical Chemistry C* **112.** Publisher: American Chemical Society, 8917–8921. ISSN: 1932-7447. https://doi.org/10.1021/jp8012865 (2025) (June 2008).

393. *Gold Nanorods* en. https://nanocomposix.com/pages/gold-nanorods (2025).

394. Khlebtsov, N. G., Khlebtsov, B. N., Kryuchkova, E. V., Zarkov, S. V. & Burov, A. M. Universal Determination of Gold Concentration in Colloids with UV–vis Spectroscopy. *The Journal of Physical Chemistry C* **126.** Publisher: American Chemical Society, 19268–19276. ISSN: 1932-7447. https://doi.org/10.1021/acs.jpcc.2c05843 (2025) (Nov. 2022).

395. Guinier, A. & Fournet, G. *Small-angle Scattering of X-rays* ISBN: 978-0-598-66993-3. https://books.google.com.au/books?id=5zRRAAAAMAAJ (Wiley, 1955).

396. Ilhan-Ayisigi, E., Yaldiz, B., Bor, G., Yaghmur, A. & Yesil-Celiktas, O. Advances in microfluidic synthesis and coupling with synchrotron SAXS for continuous production and real-time structural characterization of nano-self-assemblies. eng. *Colloids and Surfaces. B, Biointerfaces* **201,** 111633. ISSN: 1873-4367 (May 2021).

397. Kuang, Q. *et al.* Lamellar structure change of waxy corn starch during gelatinization by time-resolved synchrotron SAXS: *Food Hydrocolloids* **62,** 43–48 (July 2016).

398. Yu, H. *et al.* Real-Time pH-Dependent Self-Assembly of Ionisable Lipids from COVID-19 Vaccines and In Situ Nucleic Acid Complexation. eng. *Angewandte Chemie (International Ed. in English)* **62,** e202304977. ISSN: 1521-3773 (Aug. 2023).

399. Gilbert, J. *et al.* Evolution of the structure of lipid nanoparticles for nucleic acid delivery: From in situ studies of formulation to colloidal stability. eng. *Journal of Colloid and Interface Science* **660,** 66–76. ISSN: 1095-7103 (Apr. 2024).

400. Chu, B. & Hsiao, B. S. Small-Angle X-ray Scattering of Polymers. *Chemical Reviews* **101.** Publisher: American Chemical Society, 1727–1762. ISSN: 0009-2665. https://doi.org/10.1021/cr9900376 (2025) (June 2001).

401. Petoukhov, M. V. & Svergun, D. I. Applications of small-angle X-ray scattering to biomacromolecular solutions. eng. *The International Journal of Biochemistry & Cell Biology* **45,** 429–437. ISSN: 1878-5875 (Feb. 2013).

402. Sealy, A. *Manufacturing moonshot: How Pfizer makes its millions of Covid-19 vaccine doses* en. Apr. 2021. https://www.cnn.com/2021/03/31/health/pfizer-vaccine-manufacturing/index.html (2025).

403. Devos, C. *et al.* Impinging jet mixers: A review of their mixing characteristics, performance considerations, and applications. en. *AIChE Journal* **71,** e18595. ISSN: 1547-5905. https://onlinelibrary.wiley.com/doi/abs/10.1002/aic.18595 (2025) (2025).

404. Johnson, B. & Prud'homme, R. Flash NanoPrecipitation of Organic Actives and Block Copolymers using a Confined Impinging Jets Mixer. *Australian Journal of Chemistry* **56,** 1021–1024 (Sept. 2003).

405. Pagels, R. F., Edelstein, J., Tang, C. & Prud'homme, R. K. Controlling and Predicting Nanoparticle Formation by Block Copolymer Directed Rapid Precipitations. eng. *Nano Letters* **18,** 1139–1144. ISSN: 1530-6992 (Feb. 2018).

406. Pedersen, J., Svaneborg, C., Almdal, K., Hamley, I. & Young, R. A small-angle neutron and X-ray contrast variation scattering study of the structure of block copolymer micelles: Corona shape and excluded volume interactions. English. *Macromolecules* **36,** 416–433. ISSN: 0024-9297 (2003).

407. Tang, C. & Prud'homme, R. K. en. in *Polymer Nanoparticles for Nanomedicines: A Guide for their Design, Preparation and Development* (eds Vauthier, C. & Ponchel, G.) 55–85 (Springer International Publishing, Cham, 2016). ISBN: 978-3-319-41421-8. https://doi.org/10.1007/978-3-319-41421-8_3 (2025).

408. Kesharwani, P. *et al.* Gold nanoparticles and gold nanorods in the landscape of cancer therapy. *Molecular Cancer* **22,** 98. ISSN: 1476-4598. https://doi.org/10.1186/s12943-023-01798-8 (2025) (June 2023).